Fundamentals and Applications of N-pulse Particle Image Velocimetry-accelerometry: Towards Advanced Measurements of Complex Flows and Turbulence

by

Liuyang Ding

A Dissertation Presented in Partial Fulfillment
of the Requirements for the Degree
Doctor of Philosophy

Approved Janurary 2018 by the
Graduate Supervisory Committee:

Ronald J. Adrian, Chair
David Frakes
Marcus Herrmann
Huei-Ping Huang
Yulia Peet

ARIZONA STATE UNIVERSITY

May 2018

ABSTRACT

Over the past three decades, particle image velocimetry (PIV) has been continuously growing to become an informative and robust experimental tool for fluid mechanics research. Compared to the early stage of PIV development, the dynamic range of PIV has been improved by about an order of magnitude (Adrian, 2005; Westerweel *et al.*, 2013). Further improvement requires a breakthrough innovation, which constitutes the main motivation of this dissertation. N-pulse particle image velocimetry-accelerometry (N-pulse PIVA, where $N \geq 3$) is a promising technique to this regard. It employs bursts of N pulses to gain advantages in both spatial and temporal resolution. The performance improvement by N-pulse PIVA is studied using particle tracking (i.e. N-pulse PTVA), and it is shown that an enhancement of at least another order of magnitude is achievable. Furthermore, the capability of N-pulse PIVA to measure unsteady acceleration and force is demonstrated in the context of an oscillating cylinder interacting with surrounding fluid. The cylinder motion, the fluid velocity and acceleration, and the fluid force exerted on the cylinder are successfully measured. On the other hand, a key issue of multi-camera registration for the implementation of N-pulse PIVA is addressed with an accuracy of 0.001 pixel. Subsequently, two applications of N-pulse PTVA to complex flows and turbulence are presented. A novel 8-pulse PTVA analysis was developed and validated to accurately resolve particle unsteady drag in post-shock flows. It is found that the particle drag is substantially elevated from the standard drag due to flow unsteadiness, and a new drag correlation incorporating particle Reynolds number and unsteadiness is desired upon removal of the uncertainty arising from non-uniform particle size. Next, the estimation of turbulence statistics utilizes the ensemble average of 4-pulse PTV data within a small domain of an optimally determined size. The estimation of mean velocity, mean velocity gradient and isotropic dissipation rate are presented and discussed by

means of synthetic turbulence, as well as a tomographic measurement of turbulent boundary layer. The results indicate the superior capability of the N-pulse PTV based method to extract high-spatial-resolution high-accuracy turbulence statistics.

ACKNOWLEDGMENTS

At the time of finishing the dissertation, my heart is full of appreciation to those who have played important roles during my PhD study. First of all, I am truly and deeply grateful to my advisor, Dr. Ronald J. Adrian, without whom I could not become who I am today. He is the one who led me into the wonderful world of experimental fluid mechanics, and guided me through the completion of PhD degree. I always remember those fruitful and inspiring discussions between us on a variety of research topics, many of which turned out to be the motivations and driving forces of my research accomplishments. I am also very thankful for his strong support of the start-up of my scientific career.

Many thanks are due to Dr. Rafeed Chaudhury, Heather Zunino and Dr. Blair Johnson. It has been a memorable period of my life to work in the same laboratory with them for years, discussing and sharing our research experiences. It is my pleasure to become not only co-workers but good friends with them.

I also wish to acknowledge Dr. Stefano Discetti, Dr. Brandon Wilson, Dr. John Charonko and Dr. Sivaram Gogineni, all of whom I learned from through different collaborations/projects. In addition, it is worth to mention the time when I was visiting the Universität der Bundeswehr Müchen and closely working with Dr. Thomas Fuchs and Dr. Christian Kähler. I consider working with them was a very precious experience for me to broaden my horizons on advanced measurement techniques. In fact, many colleagues and seniors I have met, not limited to those listed above, have been helping and encouraging me to pursue my goals.

Lastly, and most importantly, I sincerely thank my parents for their endless love and understanding.

TABLE OF CONTENTS

CHAPTER Page

CHAPTER Page

APPENDIX

LIST OF TABLES

LIST OF FIGURES

INTRODUCTION

Since its invention about 35 years ago (Adrian, 1984), particle image velocimetry (PIV) has been continuously and substantially improved in almost all aspects, along with the advances in laser and camera technologies. In the initial stage of PIV development, experimentalists faced numerous options in light source, recording strategy, particle type, and interrogation (Adrian, 1986). With the considerations in velocity fidelity of tracer particles, image signal-to-noise ratio, and robustness of interrogation algorithms, the practice with pulsed Nd:YAG lasers, micron-sized tracer particles (a few microns for gas and a few tens of microns for liquid), and statistical correlation analysis stood out among other options to become the basic standard form of dual-pulse PIV. In early years, PIV images were recorded on photographic films that possessed extremely high spatial resolution, but the data analysis often required a tedious procedure. In this regard, the later development of digital PIV really enhanced the usability and popularity of the technique (Willert and Gharib, 1991; Westerweel, 1993). The fast development of camera technology in terms of pixel resolution, data transfer speed and signal-to-noise ratio made PIV with digital imaging become the standard starting in mid-1990s.

Aside from correlation-based analysis, the interest of performing interrogation by tracking individual particles also has a long history. Such analysis scheme is conventionally termed as particle tracking velocimetry (PTV). The very early motivation of doing PTV was probably its low computational cost considering the limited computer capabilities in late 1980s. Subsequent advances in PTV demonstrated its capability of measuring 3-D flow fields by triangulation of 3-D particle positions from multiple cameras (Nishino *et al.*, 1989; Malik *et al.*, 1993), or by inferring depth from defocused and modulated particle images (Willert and Gharib, 1992). One important advantage of PTV is the spatial resolu-

tion of each measured velocity vector is comparable to the size of a particle image (20-50 microns), which is considerably finer than what is achievable from correlation-based PIV. However, as low seeding density was preferred for reliable triangulations as well as correct pairing of particles in two successive frames, PTV once suffered low data yield making it not informative about flow structures. Valuable works towards high data yield of planar PTV were reported (Keane *et al.*, 1995; Ohmi and Li, 2000), but the accuracy was still not satisfactory due to the high noise level imbedded in individual particle images. Therefore, PTV appeared to reach a bottleneck in early 2000s (Stanislas *et al.*, 2005, 2008). Meanwhile, the vast development of PIV techniques enabled it to be a dominant tool for accurate, time-resolved and volumetric flow field measurement.

Early practice of PIV correlation was in the form of auto-correlation as the camera interframe time was not short enough for singe-exposure, double-frame recording. As a result, the dynamic range, given by the ratio between the maximum velocity and the smallest resolvable velocity in the field (Adrian, 1997), was severely limited (below 10:1), which prevented PIV from being applied in serious fluid mechanics research. The issue was then partially compensated when cross-correlation became the standard procedure with the development of frame-straddling PIV cameras. Since then, numerous interrogation algorithms emerged to significantly improve the accuracy and dynamic range of PIV, including window shift (Westerweel *et al.*, 1997; Gui and Wereley, 2002), image deformation (Scarano, 2001), etc. Further improvement of PIV performance was achieved by virtue of enhanced camera framing rate that allowed time-resolved measurement of liquid flows with low to moderate velocity. Several interrogation algorithms for time-revolved PIV data were developed to optimize the separation between two images being correlated to thus increase the overall dynamic range (Hain and Kähler, 2007; Sciacchitano *et al.*, 2012). Besides the attempts on accuracy, efforts were also made

towards measuring high-spatial-resolution turbulence statistics by correlation-based PIV (Meinhart *et al.*, 2000; Westerweel *et al.*, 2004; Kähler *et al.*, 2006).

Another remarkable improvement of PIV was the capability of measuring fully 3-dimension 3-component (3D3C) velocity fields in densely seeded flows. Precedent works aiming at more than two velocity components in a plane included stereoscopic PIV (Arroyo and Greated, 1991; Prasad, 2000), multi- and dual-plane PIV (Kähler and Kompenhans, 2000; Ganapathisubramani *et al.*, 2005), and holographic PIV (Sheng *et al.*, 2006, 2008). The wide application of PIV for fully 3D3C velocity measurement was then initiated by the groundbreaking tomographic PIV work of Elsinga *et al.* (2006), followed by a series of development for reconstruction techniques (Atkinson and Soria, 2009; Novara *et al.*, 2010; Discetti and Astarita, 2012c) and 3-D interrogation algorithm (Discetti and Astarita, 2012a). Tomographic PIV stimulated a continuously increasing interest in 3D flow measurements, which led to new insights into turbulence coherent structures (Scarano and Poelma, 2009; Elsinga *et al.*, 2010; Schröder *et al.*, 2011), as well as a few other 3D flow measurement techniques (Cierpka *et al.*, 2010; Belden *et al.*, 2010; Fahringer *et al.*, 2015).

While the advances of PIV in accuracy and 3-D accessibility have been sensational, the limitations in further improved accuracy, spatial resolution and capability of measuring higher-order flow quantities and turbulence statistics were also well recognized. The hindrance of further achievement in accuracy lay in the conventional way of estimating particle motion using a straight trajectory with constant velocity (Boillot and Prasad, 1996; Westerweel *et al.*, 2013). The limited spatial resolution is a nature of PIV, i.e. velocity is averaged over all particles within the interrogation spot. Another factor that presents the spatial resolution from being further improved is the positioning accuracy of a velocity vector is not satisfactory with the straight trajectory approximation, especially in highly vortical flows. For tomographic PIV, the spatial resolution is restricted by the maximum

number of particles an image sensor can hold, which results in the trade-off between the measurement volume thickness and the smallest achievable interrogation volumes size. The constraints of velocity accuracy and spatial resolution make the dynamic range of current PIV systems hardly beyond 100:1 (Adrian, 2005). Consequently, it makes PIV not very attractive for higher-order flow quantities (acceleration, force, pressure, etc.) and turbulence statistics (Reynolds stress, dissipation, etc.), considering the errors are amplified during differentiations and multiplications.

In the regard of improving PIV performance with innovative ideas and techniques, N-pulse particle image velocimetry-accelerometry (N-pulse PIVA, where $N \geq 3$) becomes a promising candidate. The fundamental advantage of N-pulse PIVA comes from that, by estimating the trajectory of a single particle or a group of particles from more than two pulses, curvature and velocity variation are taken into account to yield more accurate velocity estimate and vector positioning. The extent to which PIV performance is improved by additional pulses motivates the theoretical study described in Chapter 1, which is also an extension of the author's Master thesis (Ding, 2014). The study uses PTV as a logical starting point, which suggestively treats a group of particles as a single 'super particle' whose deformation is accounted for by common image deformation methods. High temporal resolution is another advantage of N-pulse PIVA from the practical point of view. An N-pulse PIVA system employs multiple independently triggered lasers and multiple cameras to record particle images in fast bursts (which distinguishes N-pulse PIVA from time-resolved PIV with continuous, slow and equidistant pulses). Combined with enhanced accuracy, the sufficient temporal resolution enables reliable estimation of flow acceleration and force. This is demonstrated in Chapter 2 in the context of unsteady flow-structure interaction. In N-pulse PIVA, the use of multiple cameras is the consequence of insufficient framing rate of current video cameras. The challenge in setting up

multiple cameras is that small misalignment could cause significant bias in acceleration. Such issue is discussed and addressed in Chapter 3.

Besides the strategy of multiple pulsing, other attempts to break through the limitations of PIV turned out to move the focus back to PTV. This is not a surprise given enhanced camera quantum efficiency and advanced algorithms for 3-D particle position identification (Schanz *et al.*, 2012; Wieneke, 2012), both of which reduced the uncertainty in locating individual particles and thus improved the overall accuracy. Therefore, the theoretical advantage of high spatial resolution possessed by PTV became more realistic (Kähler *et al.*, 2012a) without the sacrifice in noise level. In addition, the final gap between the theory and applications of PTV, i.e. the low data yield in 3-D flow measurements and the high percentage of ghost particles, was filled by the outstanding work of Schanz *et al.* (2016) and a successor (Novara *et al.*, 2016). Given the above, PTV is growing to be more attractive than ever before.

In virtue of the promising advances in PTV techniques, Chapter 4 and 5 concern applications of N-pulse PTVA to investigating particle-shock physics and turbulence. A special 8-pulse measurement of particle dynamics in a post-shock flow constitutes Chapter 4, in which it will become evident N-pulse analysis can be even more powerful when it is possible to adopt a fitting model incorporating particle dynamics. On the other hand, the desire of estimating turbulence statistics with high spatial resolution, comparable to or even better than that of hot-wire anemometry (HWA) and laser-Doppler velocimetry (LDV), stimulates the work in Chapter 5. The method is an extension of the ensemble PTV analysis reported previously (Kähler *et al.*, 2012b; Discetti *et al.*, 2015), utilizing recent achievements in volumetric PTV.

Chapter 1

OPTIMIZATION OF N-PULSE PARTICLE TRACKING VELOCIMETRY-ACCELEROMETRY[1]

ABSTRACT

N-pulse particle tracking velocimetry-accelerometry (N-P PTVA, where $N \geq 3$) extends conventional 2-pulse PTV by employing three or four laser pulses in a burst, aiming at more accurately resolving particle trajectories and thus improving the performance of current PIV systems. Simultaneous velocity and acceleration are obtained by differentiating the particle trajectory estimated by polynomial curve fitting. We conducted a theoretical study of 3- and 4-P PTVA to thoroughly understand the behaviors of rms errors in position, velocity and acceleration in a 4-D space consisted of four non-dimensional parameters – normalized time, normalized displacement (sweeping angle), normalized particle locating noise, and acceleration factor. The normalized rms errors were computed with respect to a reference trajectory assumed to be a circular pathline with constant angular acceleration. Elevated rms errors occur when increasing the normalized displacement and the acceleration factor. The 4-pulse analysis with interpolation produces the least bias error but the largest random error, whereas the 3-pulse method and the 4-pulse with least squares are capable to reduce the random error. It is also showed that the acceleration field tends to be much noisier than the simultaneous velocity field. To achieve the best performance, cost functions taking into account the vector

[1]This chapter is reformatted from a manuscript prepared for publication in Measurement Science and Technology.

positioning uncertainty were used to find the optimal times to evaluate velocity and acceleration. Furthermore, we calculated the dynamic range ratios between N-P and 2-P PTVA to quantify the performance improvement. The results indicate that N-P PTVA is able to improve the overall performance by 10 to 50 times, which could be even better when the development in camera technology allows a further reduction of the locating noise. The dynamic ranges for acceleration measurement were also calculated using example numbers. This work demonstrates the great potential of N-P PTVA/PIVA as the next-generation PIV to enhance the performance of existing PIV systems, and provides guidances for experimentalists to optimize their measurement accuracies.

Keywords: particle tracking velocimetry-accelerometry (PTVA), particle image velocimetry-accelerometry (PIVA), N-P PTVA/PIVA, optimization, uncertainty, dynamic range

1.1 Introduction

Particle image velocimetry (PIV) is a dominant technique for accurate fluid velocity field measurements. The performance of PIV has been continuously enhanced over the past 30 years thanks to the advances in camera technology and PIV algorithms (Adrian, 2005; Adrian and Westerweel, 2011). However, further improvements require fundamental innovations from the traditional 2-pulse method, which has recently motivated the use of more than two fast pulses to sample the flow field (Adrian, 2010; Westerweel *et al.*, 2013). When the displacement of a small group of particles is measured by cross-correlation analysis of N successive frames, this type of analysis is referred to as N-P PIVA. Its superior capability for measuring higher order quantities (e.g. acceleration, force, pressure, etc.) was demonstrated by Ding and Adrian (2016); Lynch and Scarano

(2014); Liu and Katz (2006), among others. When statistical cross-correlation is replaced by tracking individual particles, it is referred to as N-P PTVA. The advantage of high spatial resolution of particle tracking, combined with better resolving velocity variation and trajectory curvature, makes the improvement of performance by N-P PTVA become promising.

Before we discuss the performance of a PIV system, it is useful to first distinguish the measurement error from the measurement uncertainty. The measurement error is the differential between a measured value and the true value. In contrast, an uncertainty is given by a range with a confidence level (percentage) indicating the probability of the true value to fall in that range. For realistic measurements, while absolute errors are difficult to calculate from unknown true values, the root mean square (rms) of a measured quantity at identical (or nearly identical) experimental conditions is often representative of the measurement uncertainty. Herein, the rms, sometimes termed 'rms error', is calculated with respect the true value, and it can be decomposed into bias (or systematic) error and random error. Mathematically, the square of rms error is the sum of squares of bias and random error:

$$\sigma_\xi^2 = \sigma_{\text{bias},\xi}^2 + \sigma_{\text{rnd},\xi}^2 \tag{1.1}$$

wherein $\sigma_{\text{bias},\xi}^2 = (\langle\xi\rangle - \xi_{\text{true}})^2$ and $\sigma_{\text{rnd},\xi}^2 = \langle(\xi - \langle\xi\rangle)^2\rangle$ for a measured quantity ξ with $\langle\,\rangle$ denoting ensemble averaging.

One way to characterize the performance of a PIVA/PTVA system for measuring velocity is the dynamic velocity range (*DVR*), given by the ratio of the full-scale velocity to the velocity rms error (Adrian, 1997),

$$DVR = \frac{u_{max}}{\sigma_u} \tag{1.2}$$

Many factors influence σ_u, including but not limited to particle image size, seeding density, velocity gradient, curved streamline and interrogation algorithm. There has been

a history of investigators extensively studying the uncertainty to optimize correlation-based PIV by simulations using synthetic particle images (Keane and Adrian, 1992; Willert, 1996; Huang *et al.*, 1997; Scarano and Riethmuller, 2000; Foucaut *et al.*, 2004, among others). In recent years, *a posteriori* uncertainty quantification ((UQ) methods have erupted (Timmins *et al.*, 2012; Sciacchitano *et al.*, 2013; Charonko and Vlachos, 2013; Wieneke, 2015), and a benchmark experimental database was established to assess their performances (Neal *et al.*, 2015; Sciacchitano *et al.*, 2015).

In contrast, relatively few studies focused on the uncertainty of PTV in the past. It is probably because the robustness of PTV was limited by low data yield and large rms error (Stanislas *et al.*, 2005, 2008). The low data yield of triangulation-based 3-D PTV mostly attributes to the difficulty in searching for particle correspondences from multiple cameras when the seeding density is high (Nishino *et al.*, 1989; Robinson and Rockwell, 1993; Virant and Dracos, 1997). In addition, the percentage of spurious matching elevates when tracking particle pairs in densely seeded flows. In this regard, substantial efforts have been increasingly reported thanks to enhanced camera signal-to-noise ratio, pixel resolution and framing rate. Predictions using flow temporal information and neighboring particles were used to track particles in high seeding density with high reliability (Malik *et al.*, 1993; Keane *et al.*, 1995; Ohmi and Li, 2000; Fuchs *et al.*, 2017). Wieneke (2012) developed an iterative particle reconstruction (IPR) method to accurately determine particle 3-D positions utilizing locally varying optical transfer functions (OTFs) (Schanz *et al.*, 2012). Schanz *et al.* (2016) extended the IPR algorithm by adding the dimension of time to eliminate ghost particles in tomographic reconstructions, opening the way to resolving turbulence small scale motions using PTV (Kähler *et al.*, 2016). With these considerations, one can expect the performance of PTV approaches or even surpasses PIV, increasing the importance of investigating PTV uncertainty.

In this work, we consider three sources contributing to the uncertainty of N-P PTVA: (i) particle locating noise, (ii) curved streamlines and (iii) particle in-line acceleration. It is conceptually obvious that N-P PTVA promises improvements since it allows a longer time delay to reduce the relative locating noise and meanwhile addresses trajectory curvature and velocity variation. However, there is still lacking the quantification of rms error reduction. Moreover, as the additional pulses enable an estimate of time-dependent particle velocity, whether or not there exists an optimal time to evaluate the velocity needs to be answered.

In addition to the velocity uncertainty, the vector positioning uncertainty (position rms error) is an equally important issue and must be addressed in PIV measurements. In other words, measured vectors need to be correctly assigned to Eulerian positions in the field to faithfully represent the flow. The vector positioning uncertainty also relates to the dynamic spatial range (*DSR*, or more precisely, velocity-*DSR*, *VDSR*), which characterizes the capability of a PIV system to resolve motions of different scales in turbulence (Adrian, 1997). On the basis that two independent vectors should not be located closer than the positioning uncertainty (two or three rms), quantification of the positioning uncertainty provides an upper bound for *DSR*. Such way to interpret *DSR* is especially suitable for ensemble PTV measurements (Discetti *et al.*, 2015; Kähler *et al.*, 2012b) in which the data spacing of turbulence statistics is not limited by particle overlaps but rather by the particle locating uncertainty and the vector positioning uncertainty. The optimization of vector positioning of 2-pulse PTV/PIV was investigated in several early works. Adrian (1995) and Wereley and Meinhart (2001) proposed to assign velocity vectors to the midpoints of particle displacement vectors to achieve second-order accuracy; Scharnowski and Kähler (2013) showed further improvement of the positioning error by estimating the streamline

curvature from neighboring vectors. The quantification and optimization of the vector positioning uncertainty of N-P PTVA is the scope of the present work.

The above discussion on the velocity and position uncertainty can be easily extended to the measurement of acceleration using N-P PTVA. Correspondingly, we can define dynamic acceleration range (*DAR*) and acceleration-*DSR* (*ADSR*). Early investigations on the rms errors in position, velocity, and acceleration of N-P PTVA include Haranandani (2011); Ding (2014), both of which preliminarily showed reduced rms errors. We follow this direction in this work to thoroughly study the performances of 3- and 4-P PTVA. Section 1.2 introduces the methodology of our N-P PTVA simulation, followed by the behaviors of rms errors in Section 1.3 and the optimization of evaluating velocity and acceleration in Section 1.4. With these results, Section 1.5 focuses on the improvement of dynamic ranges by N-P PTVA.

1.2 Methodology

In our N-P PTVA analysis, we estimate a particle trajectory by fitting a curve to three or four measured particle locations, and differentiate the curve to obtain particle velocity and acceleration. The study compares the difference between an estimated trajectory and the reference (ground truth) assumed to be a circular pathline with a radius of curvature R. In realistic flows, the circular pathline represents a local segment of a long-time particle trajectory, or the strong swirling flow near a vortex core. If we further assume the reference trajectory has a constant angular acceleration, $\ddot{\vartheta}_0$, then the angular displacement profile $\vartheta(t')$ is

$$\vartheta(t') = \dot{\vartheta}_0 t' + \frac{1}{2}\ddot{\vartheta}_0 t'^2, \tag{1.3}$$

wherein $\dot{\vartheta}_0 = \dot{\vartheta}(0)$ and $\ddot{\vartheta}_0 = \ddot{\vartheta}(0)$ are the initial angular velocity and acceleration, respectively. Hereafter, the prime notation indicates the variable is referenced to the beginning time. For instance, $t' = t - t_0$, $t' \in [0, \Delta t]$, where Δt is the time delay from the first to the last pulse. Given Equation (1.3), the reference particle trajectory $\boldsymbol{X}'_p(t')$ is

$$\boldsymbol{X}'_p(t') = R\left[1 - cos(\dot{\vartheta}_0 t' + \frac{1}{2}\ddot{\vartheta}_0 t'^2)\right]\boldsymbol{i} + Rsin(\dot{\vartheta}_0 t' + \frac{1}{2}\ddot{\vartheta}_0 t'^2)\boldsymbol{j}, \tag{1.4}$$

We investigated three analysis methods – the 3-pulse analysis interpolates a quadratic curve to three measured particle locations, whereas the 4-pulse analysis either interpolates a cubic curve or fits a quadratic curve with least squares using four measured particle locations. In the following discussions, we use abbreviations '3-P', '4-P INT' and '4-P LSQ' to distinguish them. Explicit forms of the rms errors for 3-P and 4-P INT are derived in Section 1.2.1 and 1.2.2, respectively. The study of 4-P LSQ employed a Monte Carlo simulation, which is described in Section 1.2.3.

1.2.1 3-P PTVA

A 3-pulse measurement records three particle locations at $t' = 0, \alpha\Delta t, \Delta t$. Suppose the three random particle locating errors are $\delta\boldsymbol{X}_{pi}$, $i = 1,2,3$. Then the three measured particle locations are

$$\boldsymbol{X}'_{p1,m} = \boldsymbol{X}'_p(0) + \delta\boldsymbol{X}_{p1} = \delta\boldsymbol{X}_{p1}, \quad \boldsymbol{X}'_{p2,m} = \boldsymbol{X}'_p(\alpha\Delta t) + \delta\boldsymbol{X}_{p2}, \quad \boldsymbol{X}'_{p3,m} = \boldsymbol{X}'_p(\Delta t) + \delta\boldsymbol{X}_{p3}, \tag{1.5}$$

wherein the subscript 'm' denotes measured quantities with errors. An estimate of the particle trajectory, $\hat{\boldsymbol{X}}'_p(t')$, is then obtained by fitting a quadratic curve to $\boldsymbol{X}'_{pi,m}$:

$$\hat{\boldsymbol{X}}'_p(t') = \delta\boldsymbol{X}_{p1} + (\boldsymbol{c}_i \cdot \boldsymbol{t}^{*3\mathrm{P}})\boldsymbol{X}'_{pi,m}, \quad i = 1,2,3, \tag{1.6}$$

with $\boldsymbol{t}^{*3\mathrm{P}} = \left(\dfrac{t'}{\Delta t}, \dfrac{t'^2}{\Delta t^2}\right) = \left(t^*, t^{*2}\right)$ and coefficient vectors

$$\boldsymbol{c}_1 = \left(-\frac{1+\alpha}{\alpha}, \frac{1}{\alpha}\right), \quad \boldsymbol{c}_2 = \left(\frac{1}{\alpha(1-\alpha)}, -\frac{1}{\alpha(1-\alpha)}\right), \quad \boldsymbol{c}_3 = \left(-\frac{\alpha}{1-\alpha}, \frac{1}{1-\alpha}\right)$$

The difference between Equations (1.6) and (1.4) defines the position error for any t' along the trajectory. Thereby, the position rms error, $\sigma_{X_p}(t')$, with respect to the reference is given by

$$\sigma^2_{X_p}(t') = \left\langle \left| \hat{\boldsymbol{X}}'_p(t') - \boldsymbol{X}'_p(t') \right|^2 \right\rangle. \tag{1.7}$$

wherein the angle brackets indicate ensemble averaging. Likewise, we can calculate the rms errors in velocity and acceleration as

$$\sigma^2_{\dot{X}_p}(t') = \left\langle \left| \dot{\hat{\boldsymbol{X}}}'_p(t') - \dot{\boldsymbol{X}}'_p(t') \right|^2 \right\rangle, \quad \sigma^2_{\ddot{X}_p}(t') = \left\langle \left| \ddot{\hat{\boldsymbol{X}}}'_p(t') - \ddot{\boldsymbol{X}}'_p(t') \right|^2 \right\rangle. \tag{1.8}$$

wherein $\dot{()}$ and $\ddot{()}$ denote the derivatives with respect to t'. For generality, we normalize the rms errors using the characteristic scales. The position error is normalized using the total length of the trajectory $R\vartheta(\Delta t)$,

$$\sigma^*_{X_p} = \frac{\sigma_{X_p}}{R\vartheta(\Delta t)}; \tag{1.9}$$

the velocity error using the time-averaged velocity $\dfrac{1}{\Delta t}\displaystyle\int_0^{\Delta t} |\dot{\boldsymbol{X}}'_p| dt' = \frac{R\vartheta(\Delta t)}{\Delta t}$,

$$\sigma^*_{\dot{X}_p} = \frac{\sigma_{\dot{X}_p} \Delta t}{R\vartheta(\Delta t)}; \tag{1.10}$$

and the acceleration error using a convenient and reasonable acceleration scale $\dfrac{2R\vartheta(\Delta t)}{\Delta t^2}$,

$$\sigma^*_{\ddot{X}_p} = \frac{\sigma_{\ddot{X}_p} \Delta t^2}{2R\vartheta(\Delta t)}. \tag{1.11}$$

Justification of choosing this acceleration scale is explained in Section 1.2.5. Substituting (1.3)–(1.8) into (1.9)–(1.11) and organizing terms, it is found that the total rms error

comprises two components – the bias error arising from the 3-pulse interpolator and the random error arising from $\delta \boldsymbol{X}_{pi}$. We also assume $\delta \boldsymbol{X}_{pi}$ is zero-mean and statistically independent with identical probability density profile, i.e.

$$\langle \delta \boldsymbol{X}_{pi} \rangle = \boldsymbol{0}, \quad \langle \delta \boldsymbol{X}_{pi} \cdot \delta \boldsymbol{X}_{pj} \rangle = \langle \left| \delta \boldsymbol{X}_{p} \right|^2 \rangle \delta_{ij}, \quad i,j = 1,2,3, \tag{1.12}$$

Then we can write the normalized bias error in terms of three non-dimensional parameters, namely the normalized time,

$$t^* = t'/\Delta t, \tag{1.13}$$

the normalized particle displacement (or the total sweeping angle),

$$\vartheta(\Delta t) = R\vartheta(\Delta t)/R = \dot{\vartheta}_0 \Delta t + \frac{1}{2}\ddot{\vartheta}_0 \Delta t^2, \tag{1.14}$$

and the acceleration factor,

$$\zeta = \frac{\frac{1}{2}\ddot{\vartheta}_0 \Delta t^2}{\dot{\vartheta}_0 \Delta t} = \frac{\ddot{\vartheta}_0 \Delta t}{2\dot{\vartheta}_0}. \tag{1.15}$$

We can also write the normalized random error in terms of t^* and the normalized particle locating noise,

$$\delta^* = \frac{\langle \left| \delta \boldsymbol{X}_{p} \right|^2 \rangle^{1/2}}{R\vartheta(\Delta t)}. \tag{1.16}$$

Consequently, the square of the rms error is the sum of squares of the bias error and the random error,

$$\left(\sigma_q^{*3\mathrm{P}}\right)^2 = \left[\sigma_{\mathrm{bias},q}^{*3\mathrm{P}}\left(t^*, \vartheta(\Delta t), \zeta; \alpha\right)\right]^2 + \left[\sigma_{\mathrm{rnd},q}^{*3\mathrm{P}}\left(t^*, \delta^*; \alpha\right)\right]^2, \tag{1.17}$$

wherein the subscript $q = X_p$, $\dot{X}_p$ and $\ddot{X}_p$ denoting position, velocity and acceleration, respectively. The complete form of (1.17) is provided in Appendix A.

1.2.2 4-P PTVA with Interpolation

The derivation of the rms errors of 3-P can be easily extended to the case of four pulses. 4-P PTVA measures four particle locations at $t' = 0, \beta\Delta t, \gamma\Delta t, \Delta t$:

$$\boldsymbol{X}'_{p1,m} = \delta\boldsymbol{X}_{p1}, \quad \boldsymbol{X}'_{p2,m} = \boldsymbol{X}'_p(\beta\Delta t)+\delta\boldsymbol{X}_{p2}, \quad \boldsymbol{X}'_{p3,m} = \boldsymbol{X}'_p(\gamma\Delta t)+\delta\boldsymbol{X}_{p3}, \quad \boldsymbol{X}'_{p4,m} = \boldsymbol{X}'_p(\Delta t)+\delta\boldsymbol{X}_{p4} \tag{1.18}$$

The particle trajectory is then estimated by fitting a cubic curve to the four measured particle locations:

$$\hat{\boldsymbol{X}}'_p(t') = \delta\boldsymbol{X}_{p1} + (\boldsymbol{d}_i \cdot \boldsymbol{t}^{*4\text{P INT}})\boldsymbol{X}'_{pi,m}, \quad i = 1,2,3,4 \tag{1.19}$$

with $\boldsymbol{t}^{*4\text{P INT}} = \left(\dfrac{t'}{\Delta t}, \dfrac{t'^2}{\Delta t^2}, \dfrac{t'^3}{\Delta t^3}\right) = \left(t^*,\ t^{*2},\ t^{*3}\right)$ and the coefficient vectors

$$\boldsymbol{d}_1 = \frac{1}{\beta\gamma}\left(-\beta\gamma-\beta-\gamma, 1+\beta+\gamma, -1\right), \quad \boldsymbol{d}_2 = \frac{1}{\beta(1-\beta)(\gamma-\beta)}\left(\gamma, -\gamma-1, 1\right),$$
$$\boldsymbol{d}_3 = \frac{1}{\gamma(1-\gamma)(\gamma-\beta)}\left(-\beta, \beta+1, -1\right), \quad \boldsymbol{d}_4 = \frac{1}{(1-\beta)(1-\gamma)}\left(\beta\gamma, -\beta-\gamma, 1\right).$$

Subtracting (1.4) from (1.19) and normalizing in the same way as in (1.9)–(1.11), we obtain the rms errors of 4-P INT with similar forms to (1.17),

$$\left(\sigma_q^{*4\text{P INT}}\right)^2 = \left[\sigma_{\text{bias},q}^{*4\text{P INT}}\left(t^*, \vartheta(\Delta t), \zeta; \beta, \gamma\right)\right]^2 + \left[\sigma_{\text{rnd},q}^{*4\text{P INT}}\left(t^*, \delta^*; \beta, \gamma\right)\right]^2, \tag{1.20}$$

wherein $q = X_p$, $\dot{X}_p$ and $\ddot{X}_p$. The complete form of (1.20) is provided in Appendix A.

1.2.3 4-P PTVA with Least Squares

4-P LSQ fits a quadratic curve to the four measured particle positions given in (1.18). While the least-square solutions are analytically obtainable, the equations are too complicated to be presented here. Instead, we performed a Monte Carlo simulation that

generated 50,000 Gaussian-distributed random locating error for each pulse. The standard deviation of the Gaussian distribution was set to be $\delta^* R\vartheta(\Delta t)$. The computation was implemented on a GPU (NVIDIA GeForce GTX 645) to significantly reduce the processing time by parallelization. The equivalence between a Monte Carlo simulation and an analytical study was validated by Haranandani (2011).

1.2.4 Parameter Space

We studied the rms errors in a 4-D space spanned by four non-dimensional parameters – t^*, $\vartheta(\Delta t)$, ζ and δ^*. The parameter space was selected to cover a wide range of flow conditions and experimental conditions. Apparently, $t^* = \dfrac{t'}{\Delta t} \in [0,1]$. The normalized particle displacement, $\vartheta(\Delta t)$, can be alternatively interpreted as the sweeping angle a particle travels over with respect to the center of curvature. Considering a N-pulse experiment with an optimal Δt to have a total particle displacement of 10-50 pixels, a very small $\vartheta(\Delta t)$ implies a nearly straight trajectory, whereas a large $\vartheta(\Delta t)$ corresponds to a strongly curved pathline. We set $\vartheta(\Delta t) \in (0,3]$ to cover trajectories from a straight line to almost a half circle. The acceleration factor, ζ, is the ratio of the displacement arising from the angular acceleration, $\ddot{\vartheta}_0$, to the displacement arising from the initial angular velocity, $\dot{\vartheta}_0$. We choose -0.5 for the lower bound, when the particle decelerates to zero velocity at $t' = \Delta t$, and 0.5 for the upper bound, when the particle accelerates to twice of its initial speed at the end. The noise level in locating the particle, δ^*, is the ratio of the locating rms error to the total particle displacement, $R\vartheta(\Delta t)$. Depending on the image quality and the algorithm, the rms locating error is typically of the order of 5%-10% of the particle diameter (Adrian and Westerweel 2011, Section 7.3.3). This implies a maxium rms locating error of about 1.5 pixels, if we allow a particle image diameter up to 15

Parameter	t^*	$\vartheta(\Delta t)$	ζ	δ^*
Range	[0, 1]	(0, 3]	[-0.5, 0.5]	[0, 0.2]

Table 1.1: Parameter space for 3- and 4-P PTVA simulations.

pixels, which is possible for experiments with high magnification. On the other hand, an optimally designed N-pulse experiment should have a total displacement of at least 8-10 pixels to reduce the percentage of random error. These considerations in effect suggest an upper limit of approximately 0.2 for δ^*. Table 1.1 summarizes the ranges of all parameters. Our study only considers equal time spacing, i.e. $\alpha = \frac{1}{2}$ for 3-P PTVA, and $\beta = \frac{1}{3}$, $\gamma = \frac{2}{3}$ for 4-P PTVA.

While we choose [0, 0.2] for δ^* without loss of generality, for most experiments the locating noise may be much lower than 0.2. Note that the way we define δ^* in (1.16) enables us to relate it to the *DVR* in a 2-pulse measurement:

$$DVR^{2\mathrm{P}} \approx \frac{\Delta X_{p,max}}{\sigma_{\Delta X}} = \frac{R\vartheta(\Delta t)_{max}}{\sqrt{2}\langle \left|\delta \boldsymbol{X}_p\right|^2 \rangle^{1/2}} = \frac{1}{\sqrt{2}\delta^*} \tag{1.21}$$

The above '≈' results from the approximations $u_{\max} \approx \frac{\Delta X_{p,max}}{M_0 \Delta t}$ and $\sigma_u \approx \frac{\sigma_{\Delta_X}}{M_0 \Delta t}$ if we consider in 2-pulse PIV each particle trajectory is approximated by a straight line with constant velocity. Usually, the time delay of a 2-pulse PIV experiment is properly selected so that the straight lines are good estimates. Westerweel *et al.* (2013) reviewed some benchmark 2-pulse PIV measurements of turbulent flows, in which most *DVR*s ranged from 59 to 122 corresponding to $\delta^{*2\mathrm{P}}$ = 0.005 ... 0.012, which is representative of the performance of current 2-pulse PIV systems. In Section 1.5, we discuss the improvement of *DVR* and *DSR* by N-P PTVA for $\delta^{*2\mathrm{P}}$ = 0.001 ... 0.01, covering current 2-pulse PIV

systems and envisioning the future when camera technology allows the reduction of δ^* by a factor of $4 \sim 5$.

1.2.5 Acceleration Scale

Given the parameter space in Table 1.1, we are now able to reconsider the acceleration scale used in (1.11). As a matter of fact, two orthogonal components contribute to the acceleration scale – the tangential acceleration, $R\ddot{\vartheta}_0$, and the averaged centripetal acceleration, $\frac{R\vartheta^2(\Delta t)}{\Delta t^2}$. Thus, the total acceleration is

$$\frac{R\vartheta(\Delta t)}{\Delta t^2}\left[\vartheta^2(\Delta t)+\left(\frac{\ddot{\vartheta}_0\Delta t^2}{\vartheta(\Delta t)}\right)^2\right]^{\frac{1}{2}} = \frac{R\vartheta(\Delta t)}{\Delta t^2}\left[\vartheta^2(\Delta t)+\left(\frac{2\zeta}{1+\zeta}\right)^2\right]^{\frac{1}{2}} \tag{1.22}$$

In a flow field measured by PIV, while the length scale $R\vartheta(\Delta t)$ and the velocity scale $\frac{R\vartheta(\Delta t)}{\Delta t}$ typically vary within a decade, the acceleration scale (1.22) could range over several decades. Extremely high accelerations occur, for instance, near vortex cores (Lynch and Scarano, 2014) or stagnation points (Ding, 2014), whereas the rest of the field exhibit very small acceleration. Thus, using (1.22) to normalize the acceleration rms error could result in extremely high $\sigma^*_{\ddot{X}_p}$, even though the absolute error may be insignificant relative to the maximum acceleration. In this regard, it would be more reasonable to use an acceleration scale in the same order of magnitude as the maximum acceleration. We chose $\frac{2R\vartheta(\Delta t)}{\Delta t^2}$ considering $\left[\vartheta^2(\Delta t)+\left(\frac{2\zeta}{1+\zeta}\right)^2\right]^{\frac{1}{2}}$ is in the range of $(0, 3.6]$ according to Table 1.1. It is worth mentioning that $\left[\vartheta^2(\Delta t)+\left(\frac{2\zeta}{1+\zeta}\right)^2\right]^{\frac{1}{2}}$ is independent of t^*. Replacing it with a constant does not change the optimal t^* minimizing the rms error.

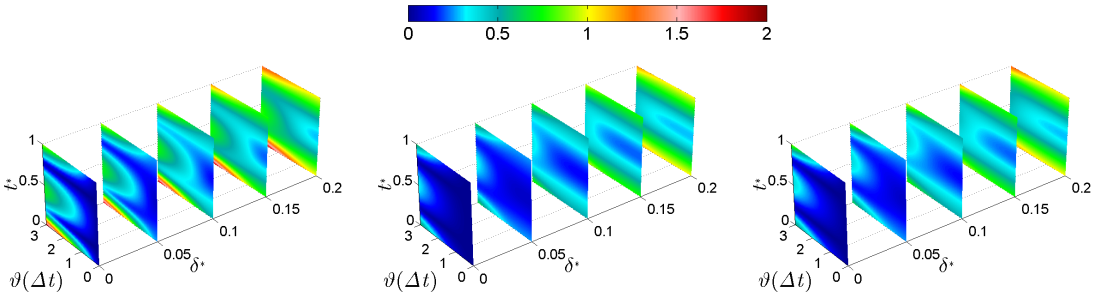

(a) $\zeta = -0.5$ (b) $\zeta = 0$ (c) $\zeta = 0.5$

Figure 1.1: Velocity rms error of 3-P.

1.3 Behaviors of Rms Errors

Figure 1.1 presents the velocity rms error of 3-P, $\sigma^{*3P}_{\dot{X}_p}$, with $\zeta = -0.5, 0, 0.5$. For each ζ, t^*–$\vartheta(\Delta t)$ planes are displayed at $\delta^* = 0$, 0.05, ..., 0.2. It is evident that large rms error shows when the trajectory is strongly curved, i.e. $\vartheta(\Delta t)$ is large. Velocity variations, acceleration (Figure 1.1(c)) and especially deceleration (Figure 1.1(a)), cause the elevation of rms error , which is consistent with the conclusion by Boillot and Prasad (1996). It is also observed that the rms error of $\zeta = -0.5$ is more noticeable compared to that of $\zeta = 0.5$. This is related to the position of the middle particle image, which is schematically illustrated in Figure 1.2. When a particle decelerates, the middle image deviates more significantly from the axis of symmetry compared to an accelerating particle with the same $|\zeta|$. Thereby, the polynomial representation becomes less accurate for negative ζ.

The color contours in Figure 1.1 also imply the existence of minimums of the rms error at certain times, answering the question we brought up in the introduction. These optimal times, t^*_{opt}, vary with $\vartheta(\Delta t)$, δ^* and ζ. Figure 1.3 shows the transitions of t^*_{opt}

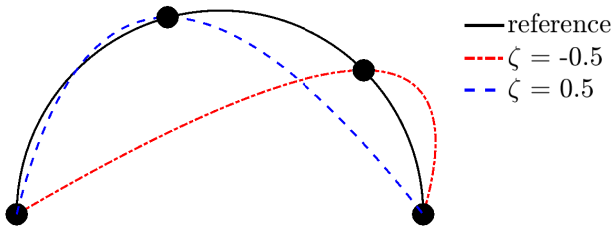

Figure 1.2: Comparison of quadratic interpolations for accelerating and decelerating particles.

from low to high δ^* for $\sigma^{*3P}_{\dot{X}_p}$ at selected $\vartheta(\Delta t)$ and ζ. The dependences on the parameters are clear – the transition switches direction when ζ changes sign; the transition occurs at a larger δ^* and becomes less steep when $\vartheta(\Delta t)$ or $|\zeta|$ increases. For $\sigma^{*3P}_{\dot{X}_p}$ shown in Figure 1.3, t^*_{opt} is approximately 0.21 for $\zeta > 0$ and 0.77 for $\zeta < 0$ when δ^* is small, and gradually collapses at $t^* = 0.5$ for large δ^*. For δ^* between 0.001 and 0.01, which is representative of most PIV systems as we have discussed in Section 1.2.4, t^*_{opt} mostly takes 0.21 or 0.77 except when the transition starts early with small $\vartheta(\Delta t)$ and $|\zeta|$.

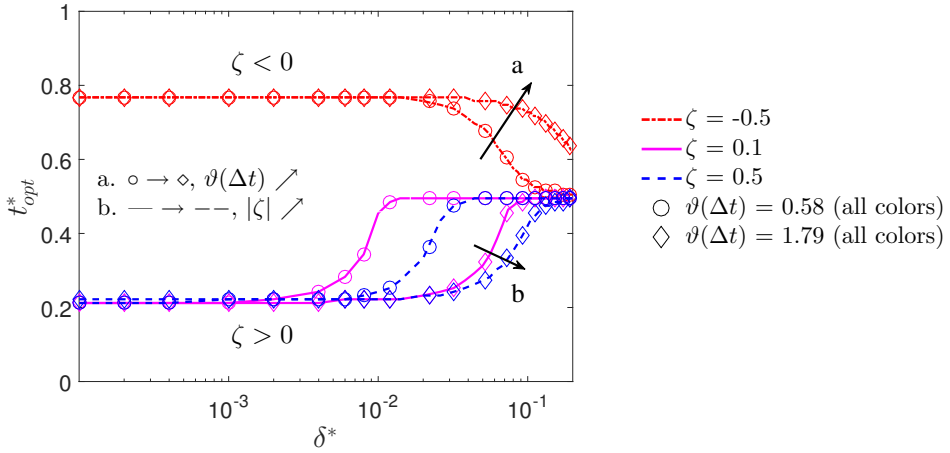

Figure 1.3: Transition of t^*_{opt} for the velocity rms error (or the velocity cost function, K_v) of 3-P.

The complete set of plots in the 4-D parameter space for position, velocity and acceleration rms errors of 3-P, 4-P INT and 4-P LSQ are included in Appendix B (Figure B.1, B.3, B.5). If we also extract the t^*_{opt} vs. δ^* curves from those plots, we observe the transition of t^*_{opt} occurs at different t^* with varying slope. The underlying reason is in fact revealed from the constitutions of the rms errors given in (1.17) and (1.20). The bias error is independent of δ^*, whereas the random error is proportional to δ^* but independent of $\vartheta(\Delta t)$ and ζ. Thereby, the total rms error is dominated by the bias error when δ^* is small, and then grows with increasing δ^* and appears nearly independent of $\vartheta(\Delta t)$ and ζ. These are evident in Figure 1.1 as well as the plots in Appendix B. Thereby, the transition of t^*_{opt} is the consequence of the random error competing with the bias error. When $\vartheta(\Delta t)$ or $|\zeta|$ is large, the bias error is significant, resulting in late and slow transitions as seen in Figure 1.3.

Furthermore, we compared different analysis methods from the perspective of bias and random error. When particle locations are measured accurately, a higher-order

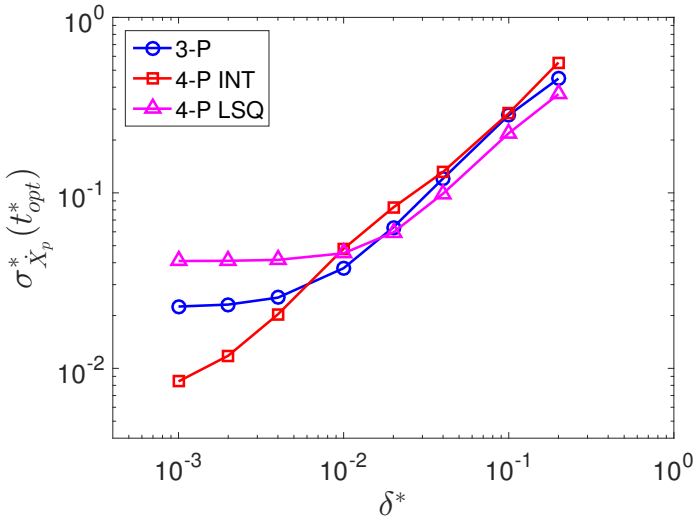

Figure 1.4: Comparison of the velocity rms error at t^*_{opt} against δ^* for different analysis methods. $\zeta = -0.5$, $\vartheta(\Delta t) = 1.51$.

method is more capable to represent the particle motion. However, since a higher-order method has more degrees of freedom, the locating noise at each particle location accumulates to generate a greater impact to the total rms error. In the context of our study, it is revealed from the growth rate of rms errors against increasing δ^*. Figure 1.4 compares the growths of velocity rms errors at $\zeta = -0.5$ and $\vartheta(\Delta t) = 1.51$ as an example to illustrate the above inferences. Clearly, 4-P INT produces the smallest bias error but the largest random error compared to the other two methods. The rapid transition to the state of $\vartheta(\Delta t)$–independent for 4-P INT is graphically evident in Figure B.3. In addition, Figure 1.4 implies 4-P LSQ is preferable for noisy measurements. These behaviors are in agreement with the experimental investigation by Ding and Adrian (2016) in which the authors compared the random and bias errors of the measured velocity and acceleration fields around an oscillating cylinder. It is worth noting that, while the preceding discussion is mainly based on the velocity rms error, they also generally apply to the position and acceleration rms errors.

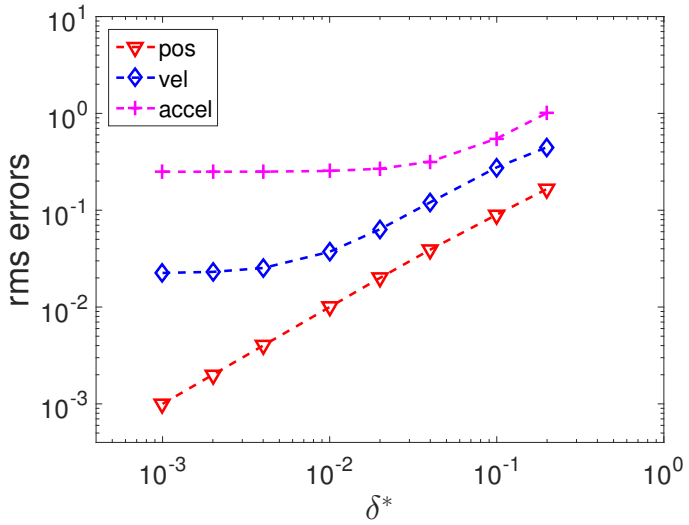

Figure 1.5: Comparison of position, velocity and acceleration rms errors of 3-P at t^*_{opt}. $\zeta = -0.5$, $\vartheta(\Delta t) = 1.51$.

Another dimension of our study is to compare the magnitudes of position, velocity and acceleration rms errors. As an example for illustration, Figure 1.5 presents those of 3-P at $\zeta = -0.5$ and $\vartheta(\Delta t) = 1.51$. It shows that rms error of acceleration is greater than that of velocity by up to an order of magnitude, and so is the rms error of velocity to that of the position. The separation in magnitude is observed for all analysis methods across the full ranges of $\vartheta(\Delta t)$ and ζ, as seen from Figure B.2, B.4, B.6 in Appendix B (note the different color scales used). These plots are the rms errors at t^*_{opt} so that the data are compressed into a 3-D space. Christensen and Adrian (2002) also proved magnified acceleration rms error from their analyses showing the acceleration noise embodied the fluctuating random and bias error from both PIV cameras. This result is important for the designs of PIVA/PTVA experiments and the interpretation of measured acceleration fields. In general, acceleration measurements are more sensitive to displacement error and appear noisier than the simultaneous velocity fields. To achieve satisfactory accuracy of acceleration, one needs to extend Δt to reduce δ^* as much as allowed by other limitations.

In Figure B.2, B.4 and B.6, the axes of δ^* use logarithmic scale intended to amplify the range $0.001 \leq \delta^* \leq 0.01$, which is representative of most PIV systems. Within this range, $\sigma^*_{X_p}$ is up to about 0.01, $\sigma^*_{\dot{X}_p}$ is up to about 0.1, and $\sigma^*_{\ddot{X}_p}$ is mostly below 0.4, except when ζ is close to -0.5 and $\vartheta(\Delta t)$ approaches 3, $\sigma^{*3\mathrm{P}}_{\ddot{X}_p}$ and $\sigma^{*4\mathrm{P\,LSQ}}_{\ddot{X}_p}$ rise up to about 1.

1.4 Optimal Times to Evaluate Velocity and Acceleration

As discussed in the introduction, the uncertainties of velocity and acceleration involve not only the magnitude and direction, but where to assign the measured vectors. In the context of our PTV study, that means a fair measure of the uncertainties needs to take into account the rms error of position as well. In this regard, we define two cost functions

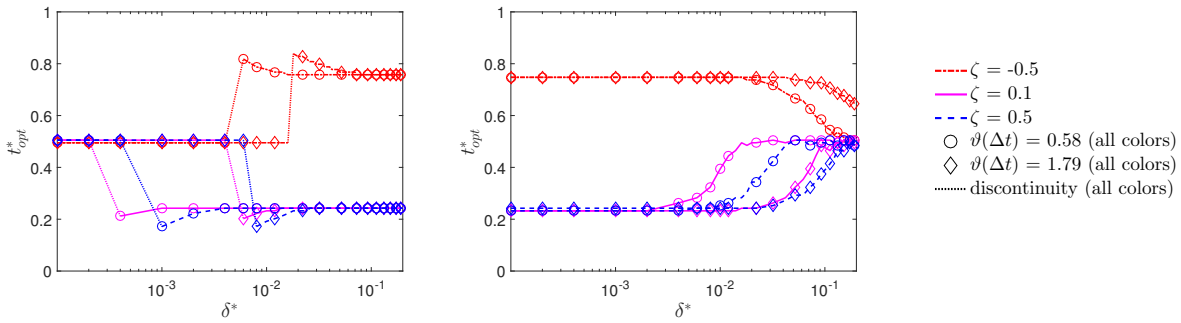

(a) 4-P INT (b) 4-P LSQ

Figure 1.6: t^*_{opt} of K_v for different analysis methods.

for velocity and acceleration, respectively,

$$K_v = \eta\sigma^*_{X_p} + (1-\eta)\sigma^*_{\dot{X}_p}, \tag{1.23}$$

and

$$K_a = \eta\sigma^*_{X_p} + (1-\eta)\sigma^*_{\ddot{X}_p}. \tag{1.24}$$

The weighting factor η is set to be 0.5 to equally emphasize their importances. Consequently, the t^*_{opt}s to evaluate velocity and acceleration are the times minimizing K_v and K_a, respectively.

In fact, due to the considerable separation of magnitude, the t^*_{opt} of K_v coincides with that of the velocity, and so does the t^*_{opt} of K_a with that of the acceleration. We have already discussed the t^*_{opt} of K_v for 3-P in Figure 1.3. Figure 1.6(a) shows the t^*_{opt} of K_v for 4-P INT. As δ^* increases, t^*_{opt} starts at 0.5 and moves to 0.24 for $\zeta > 0$ and 0.76 for ζ<0, with the transitions appearing in the form of discontinuities. We checked the discontinuity was not an artifact due to insufficient sampling rate by asymptotically adjusting δ^* near the jump and observing t^*_{opt}. The t^*_{opt} of K_v for 4-P LSQ, shown in Figure 1.6(b), appears nearly identical to that of 3-P in Figure 1.3 as they are both quadratic methods. An

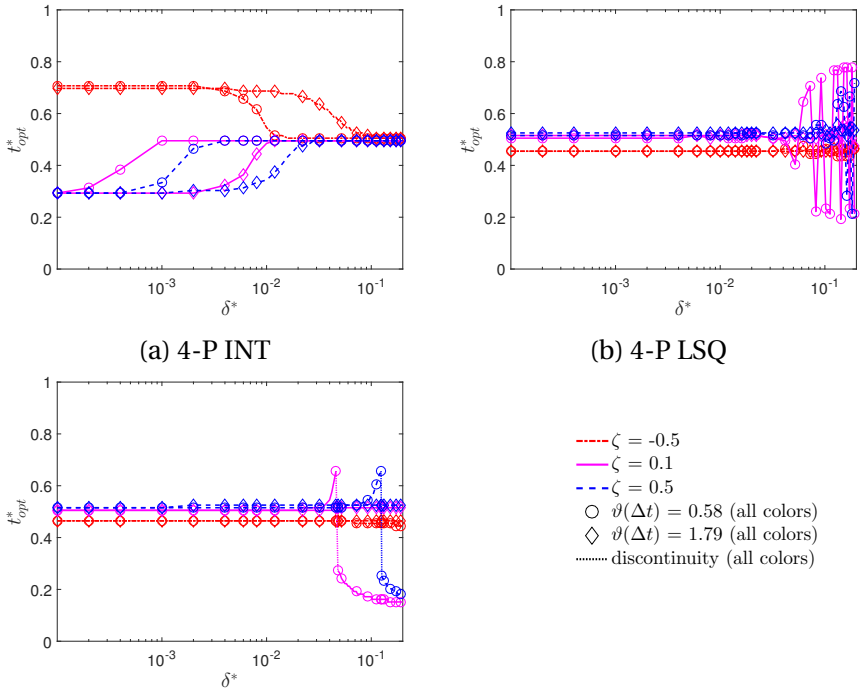

(a) 4-P INT

(b) 4-P LSQ

(c) 3-P

Figure 1.7: t^*_{opt} of K_a for different analysis methods.

exception is that t^*_{opt} at low δ^* is close to 0.23 ($\zeta > 0$) or 0.75 (ζ<0), slightly differing from that of 3-P.

Figure 1.7(a) presents the t^*_{opt} of K_a for 4-P INT, in which t^*_{opt} is 0.3 for $\zeta > 0$ and 0.7 for ζ <0 initially and then collapses to 0.5. The dependence on $\vartheta(\Delta t)$ and ζ are similar to what we have discussed for Figure 1.3. The transitions of K_a for 4-P LSQ and 3-P exhibit some interesting behaviors, as seen in Figure 1.7(b) and 1.7(c). The transitions take the form of bifurcation or discontinuity. When $\delta^* \leq 0.02$, the t^*_{opt}s of K_a for 4-P LSQ and 3-P are close to 0.5, a simple and unified result to be used in experiments. This also implies the acceleration bias error by lower-order methods could be quite dominant so that the transition does not occur until a large δ^*.

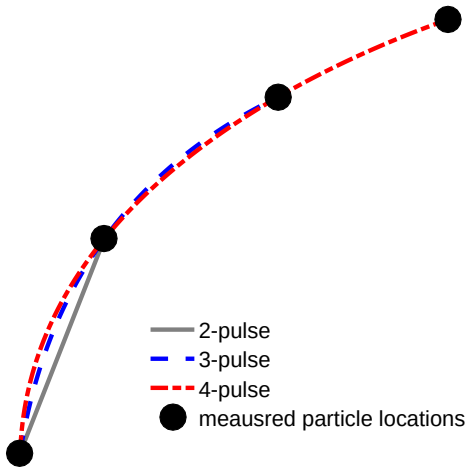

Figure 1.8: Particle trajectory measured by 2-P and N-P PTVA with extended time delays.

1.5 Dynamic Range

1.5.1 Velocity

In this section, we study the improvements of *DVR* and *VDSR* by N-P PTVA compared to 2-pulse PTV. The results in previous sections have indicated δ^* plays a key role in the total rms error. Thereby, the comparisons of dynamic ranges in this section are on the basis of extended time delays intended to reduce δ^*. Suppose a 2-pulse PTV employs a time delay of $\Delta\tau$. Then we set the time delays of 3- and 4-P PTVA to be $2\Delta\tau$ and $3\Delta\tau$, respectively. The corresponding trajectories are continuations of the circular path (the reference) between the first two pulses, as illustrated in Figure 1.8. From the extended time delay, we expect to have reduced δ^* and increased $|\zeta|$ and $\vartheta(\Delta t)$. Table 1.2 summarizes the calculations of corresponding parameters for N-P PTVA. We restrict $\vartheta(\Delta\tau)$ below 0.78 and $|\zeta^{2P}|$ below 0.16 such that the parameters of 4-P PTVA do not exceed the limits listed in Table 1.1.

The *DVR* in the context of our PTVA study is given by

$$DVR = \frac{u_{max} M_0}{\sigma_{\dot{X}_p}} = \frac{u_{max} M_0 \Delta t}{\sigma^*_{\dot{X}_p} R\vartheta(\Delta t)}, \tag{1.25}$$

where M_0 is the lateral magnification; $\sigma_{\dot{X}_p}$ is calculated at a representative location in the field of view. We set the comparison in the situation when one applies both 2-P and N-P PTVA to measuring a flow field concurrently. Thus, u_{max} and M_0 cancel out in the *DVR* ratio with respect to $DVR^{2\mathrm{P}}$:

$$DVR^{*NP} = \frac{DVR^{NP}}{DVR^{2\mathrm{P}}} = \frac{(N-1)\vartheta(\Delta\tau)}{\vartheta[(N-1)\Delta\tau]} \frac{\sigma^{*2\mathrm{P}}_{\dot{X}_p}}{\sigma^{*NP}_{\dot{X}_p}}. \tag{1.26}$$

Likewise, we define the *VDSR* to be

$$VDSR = \frac{L_x}{2\sigma_{X_p}} = \frac{L_x}{2\sigma^*_{X_p} R\vartheta(\Delta t)} \tag{1.27}$$

implying two neighboring vectors are at least $2\sigma_{X_p}$ apart. Then the *VDSR* ratio is

$$VDSR^{*NP} = \frac{VDSR^{NP}}{VDSR^{2\mathrm{P}}} = \frac{\vartheta(\Delta\tau)}{\vartheta[(N-1)\Delta\tau]} \frac{\sigma^{*2\mathrm{P}}_{X_p}}{\sigma^{*NP}_{X_p}} \tag{1.28}$$

The rms errors of 2-pulse PTV, $\sigma^{*2\mathrm{P}}_{\dot{X}_p}$ and $\sigma^{*2\mathrm{P}}_{X_p}$, were calculated with the same method described in Section 1.2.1 assuming the estimated trajectory is a straight line between two measured particle locations. The optimal time of 2-pulse PTV was found to be 0.5, which is in agreement with Adrian (1995) and Wereley and Meinhart (2001). $\sigma^{*NP}_{\dot{X}_p}$ and

				Example		
	$\vartheta(\Delta t)$	ζ	δ^*	$\vartheta(\Delta t)$	ζ	δ^*
2-P	$\vartheta(\Delta\tau)$	$\zeta^{2\mathrm{P}}$	$\delta^{*2\mathrm{P}}$	0.78	0.16	4.0e-03
3-P	$\vartheta(2\Delta\tau) = \frac{2\vartheta(\Delta\tau)}{1+\zeta^{2\mathrm{P}}} + \frac{4\vartheta(\Delta\tau)\zeta^{2\mathrm{P}}}{1+\zeta^{2\mathrm{P}}}$	$\zeta^{3\mathrm{P}} = 2 * \zeta^{2\mathrm{P}}$	$\delta^{*3\mathrm{P}} = \delta^{*2\mathrm{P}} \frac{\vartheta(\Delta\tau)}{\vartheta(2\Delta\tau)}$	1.78	0.32	1.8e-03
4-P	$\vartheta(3\Delta\tau) = \frac{3\vartheta(\Delta\tau)}{1+\zeta^{2\mathrm{P}}} + \frac{9\vartheta(\Delta\tau)\zeta^{2\mathrm{P}}}{1+\zeta^{2\mathrm{P}}}$	$\zeta^{4\mathrm{P}} = 3 * \zeta^{2\mathrm{P}}$	$\delta^{*4\mathrm{P}} = \delta^{*2\mathrm{P}} \frac{\vartheta(\Delta\tau)}{\vartheta(3\Delta\tau)}$	2.99	0.48	1.0e-03

Table 1.2: Calculation of the parameters for N-P PTVA with extended time delays.

$\sigma_{X_p}^{*NP}$ at the t_{opt}^* of K_v are used for the comparisons, and they are readily obtainable from the results in Section 1.3 and 1.4.

Figure 1.9 shows DVR^*, $VDSR^*$ and their products for varying δ^* and flow conditions. Each data point displayed here is calculated with the analysis method that yields the smallest K_v at t_{opt}^*. Different methods are marked with different symbols. Data in the shaded region show the improvement for δ^* achievable by current 2-pulse PIV systems, i.e. δ^{*2P} = 0.004 ... 0.01, as discussed in Section 1.2.4. Within this range, when the particle trajectory is nearly a straight line with constant velocity (Figure 1.9(a)), the overall performance, characterized by the product of DVR^* and $VDSR^*$ (Adrian, 1997), is improved by about a half order of magnitude. With the presence of moderate curvature (Figure 1.9(b)) or acceleration (Figure 1.9(c)), the ratio increases to an order of magnitude, especially when δ^{*2P} gets close to 0.004. Further increases of $|\zeta^{2P}|$ and $\vartheta(\Delta\tau)$ result in

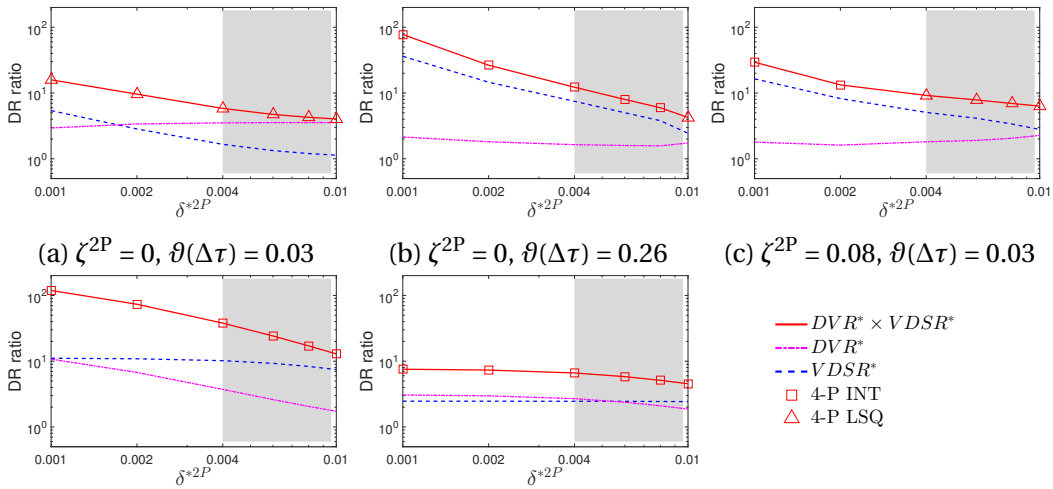

(a) $\zeta^{2P} = 0$, $\vartheta(\Delta\tau) = 0.03$ (b) $\zeta^{2P} = 0$, $\vartheta(\Delta\tau) = 0.26$ (c) $\zeta^{2P} = 0.08$, $\vartheta(\Delta\tau) = 0.03$

(d) $\zeta^{2P} = -0.16$, $\vartheta(\Delta\tau) = 0.52$ (e) $\zeta^{2P} = 0.16$, $\vartheta(\Delta\tau) = 0.78$

Figure 1.9: *DVR* and *VDSR* ratios for varying δ^* and flow conditions. Data in the shaded region show the improvements for δ^* achievable by current 2-pulse PIV systems.

a more significant improvement of up to 50 times, as seen from Figure 1.9(d). If future camera technology allows δ^{*2P} to reach 0.001, the overall performance could be enhanced by up to two orders of magnitude as indicated in Figure 1.9(b) and 1.9(d). Interestingly, Figure 1.9(e) shows reduced overall performance improvement when the strong ζ^{2P} and $\vartheta(\Delta\tau)$ lead to very large $\vartheta(3\Delta\tau)$ (see the example in Table 1.2). It suggests that, to gain the most improvement from the additional pulses, the time delay of 4-P PTVA needs to be properly adjusted to avoid strongly curved trajectories ($\vartheta(\Delta t) \sim 3$) constantly occurring in the field of view. Moreover, the results in Figure 1.9 imply that the best performance is achieved by either 4-P INT or 4-P LSQ, and the latter one is advantageous when the trajectory is close to a straight line (Figure 1.9(a) and 1.9(c)), or δ^* is relatively high (Figure 1.9(b) and 1.9(c)). However, the 3-P PTVA could be a less expensive option whose performance in velocity and acceleration measurements is comparable to a 4-P system under some circumstances. An example PIVA work is (Ding and Adrian, 2016), in which the authors also outlined some other considerations for choosing a 3-P or 4-P system besides the regards of dynamic range and rms error. In addition, it is evident that the *VDSR* has a greater potential than the *DVR* to significantly contribute to the improvement of overall performance. Typically, the *DVR* ratio is under 5, whilst the *VDSR* ratio could be up to 50-100.

1.5.2 Acceleration

For acceleration measurements, we use some example numbers to calculate the dynamic ranges. We define the dynamic acceleration range (*DAR*) as the ratio of the

maximum acceleration to the acceleration rms error,

$$DAR = \frac{a_{max} M_0}{\sigma_{\ddot{X}_p}} = \frac{a_{max} M_0}{\sigma^*_{\ddot{X}_p} 2R\vartheta(\Delta t)/\Delta t^2} = \frac{A^*_{max}}{\sigma^*_{\ddot{X}_p}} \tag{1.29}$$

wherein

$$A^*_{max} = \frac{a_{max} M_0 \Delta t^2}{2R\vartheta(\Delta t)} \tag{1.30}$$

is the normalized maximum acceleration. As we discussed in Section 1.2.4, the acceleration scale $\frac{2R\vartheta(\Delta t)}{\Delta t^2}$ is set to be in the same order of the maximum acceleration, so here we choose $A^*_{max} = 3$ as an example to calculate *DAR*.

The acceleration dynamic spatial range (*ADSR*), similar to *VDSR*, characterizes the number of independent acceleration measurements that can be made across the linear dimension of the field. The *ADSR* in our calculation is defined as

$$ADSR = \frac{L_x}{2\sigma_{X_p}} = \frac{L_x / R\vartheta(\Delta t)}{2\sigma^*_{X_p}}. \tag{1.31}$$

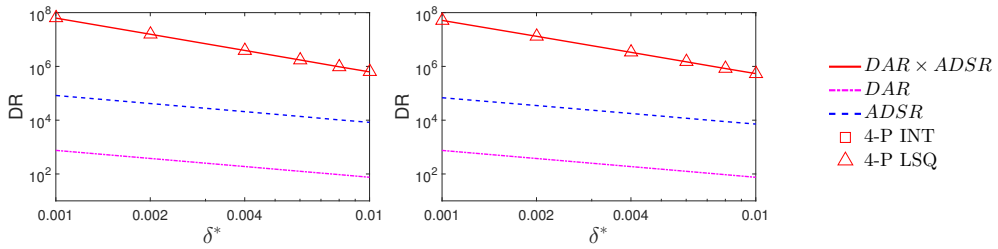

(a) $\zeta = 0$, $\vartheta(\Delta t) = 0.03$ (b) $\zeta = -0.5$, $\vartheta(\Delta t) = 0.03$

(c) $\zeta = 0$, $\vartheta(\Delta t) = 1.0$ (d) $\zeta = 0.5$, $\vartheta(\Delta t) = 3.0$

Figure 1.10: Example *DAR* and *ADSR* for varying flow conditions and locating noise.

It is important to note that, although the *ADSR* is of the same form as the *VDSR* in (1.27), the $\sigma^*_{X_p}$ in (1.31) and the $\sigma^*_{\ddot{X}_p}$ in (1.29) are evaluated at the t^*_{opt} of K_a. The numerator in (1.31) is the ratio of the linear dimension of the field to the length of the trajectory. We use $L_x/R\vartheta(\Delta t) = 100$ as an example for our calculations, which indicates a trajectory length of 40 pixels if the imaging sensor is 4,000-pixel wide.

Figure 1.10 shows example numbers of *DAR* and *ADSR*. Noticeably, the *ADSR* is always greater than the *DAR* by about two to three orders of magnitude. When a particle moves along a nearly straight pathline with no acceleration (Figure 1.10(a)), the *ADSR* ranges from 10^4 to 10^5 when δ^* varies from 0.01 to 0.001; meanwhile, the corresponding *DAR* is between 10^2 and 10^3. If we compare Figure 1.10(b) and 1.10(c) to Figure 1.10(a), it indicates that the presence of strong velocity variation has a negligible impact on *DAR* and *ADSR*, whereas even a moderate increase of $\vartheta(\Delta t)$ could cause reductions of both *DAR* and *ADSR* by a factor of 2 to 3 at the low δ^* end ($\delta^* \approx 0.001$). In other words, the curvature of a particle trajectory, i.e. the centripetal acceleration, is more difficult to be captured by polynomial fits. Further increases of $|\zeta|$ and $\vartheta(\Delta t)$ (Figure 1.10(d)) reduce *DAR* below 10 and *ADSR* below 10^4.

1.6 Summary and Conclusions

We have theoretically studied the performance and optimization of N-pulse PTVA (N = 3 or 4). Using a circular pathline as the reference trajectory, we quantified the normalized rms errors in position, velocity and acceleration for varying flow conditions and particle locating noise. The results indicate elevated rms errors for strong curvature and velocity variation as well as large locating noise. The investigation of bias and random errors of different analysis methods suggests 4-P INT is advantageous when δ^* is low to

produce the smallest bias, whereas 4-P LSQ is capable to reduce the random error but at the cost of strong bias. The acceleration error is more significant than the simultaneous velocity error. Enhancement of acceleration accuracy requires employing an extended time delay, and further enhancement may rely on the development of camera technology for improved image signal-to-noise ratio.

Cost functions combining the uncertainty of position with that of velocity and acceleration were used to find the optimal times for velocity and acceleration measurements. When the locating noise increases, the optimal times exhibit transitions as the consequence of the random error gradually dominating the total rms error.

With the normalized rms errors, we calculated the ratios of *DVR* and *VDSR* between N-pulse and 2-pulse PTVA on the basis of extended time delays. For locating noise achievable by current 2-pulse PIV systems, the 4-P PTVA can improve the overall performance by 10 to 50 times, except when the trajectory is nearly straight with negligible velocity variation. If future camera technology reduces the locating noise by a factor of 4 to 5, we showed the overall improvement could be up to two orders of magnitude. The contribution of *VDSR* to the overall performance improvement is greater than that of *DVR*. In addition, 4-P LSQ is preferable for large locating noise and small curvature, whereas 4-P INT yields better performance in other situations.

We propose to use *DAR* and *ADSR* to characterize the performance of N-P PTVA for acceleration measurements. The calculations using example numbers indicate the overall performance of acceleration measurement could increase by one to two orders of magnitude if the locating noise is reduced from 0.01 to 0.001. Moreover, accurate measurement of the centripetal acceleration appears to be more challenging for a polynomial fit compared to the tangential acceleration.

The present work provides guidances for experimentalists to optimize their PIVA/PTVA measurements. It is worth mentioning that our methodology of studying the optimization problem can be extended to experiments employing more light pulses (Martinez *et al.*, 2015) or different fitting models (Wagner *et al.*, 2012).

Acknowledgments

The authors would like to acknowledge the financial support by ONR under Phase II STTR contract N00014-14-C-0095 through Spectral Energies LLC.

Chapter 2

N-PULSE PARTICLE IMAGE VELOCIMETRY-ACCELEROMETRY FOR UNSTEADY FLOW-STRUCTURE INTERACTION[2]

ABSTRACT

Flow-structure interaction experiments are a major area of application of instruments capable of simultaneously measuring instantaneous fields of velocity and acceleration. An N-pulse particle image velocimeter-accelerometer (N-P PIVA) employing bursts of N pulses, where N=3 or 4, and operating in the high-image-density particle seeding mode is described and demonstrated in the context of a representative flow-structure interaction experiment. The instrument employs two double-pulsed lasers and a high-resolution, fast-framing camera to acquire successive particle images having time separations small enough to perform good interpolation or finite differencing. The interrogation procedure locates the same group of particles at each pulse time using multiple cross-correlations, and a predictor-corrector algorithm enhances the strength of the cross-correlations by centering the windows on the particle groups at each time. Data from 2-, 3- and 4-pulse systems are compared to assess their relative performance. Measurements from the 4-pulse method with interpolation have smaller mean bias errors than the 3-pulse method with interpolation or the 4-pulse method with least squares, but larger random error. A flow-structure experiment was performed in liquid surrounding a horizontal cylinder suspended by two thin, flexible, vertical rods from a slider block driven horizontally and

[2]This chapter is reformatted from an article co-authored with Dr. Ronald J. Adrian and published in Measurement Science and Technology (Ding and Adrian, 2016).

sinusoidally. The value of the Keulegan-Carpenter number is $KC = 4.85$ and the frequency parameter (or Stokes number) is $\beta = 7.2$. To make measurements close to the surface of the cylinder, a method using near-wall transformation and correlation analysis on a transformed grid is developed. Image processing used to determine the position, velocity and acceleration of the center of the cylinder is described. These measurements, together with the N-P PIVA data allow complete evaluation of each term in the exact, stationary control surface formulation of the fluid force applied to the cylinder surface (Noca, 1997; Noca *et al.*, 1997, 1999; Unal *et al.*, 1997), demonstrating the ability to measure unsteady fluid force on the cylinder

Keywords: particle image velocimetry (PIV), particle image velocimetry and accelerometry (PIVA), N-pulse PIVA, flow-structure interaction, moving cylinder

2.1 Introduction

N-pulse particle image velocimetry-accelerometry (N-pulse PIVA or N-P PIVA) is a generalization of the fundamental double-pulse particle image velocimetry (PIV or more precisely 2-P PIV) method that has been standard for more than two decades. As a class, N-P PIVA contains N-P PIV, wherein acceleration is not measured; time-resolved PIV (T-R PIV), wherein many frames in a sequence of images are recorded either cinematically or video-graphically to create a movie of a time-varying velocity field; and long-time multi-pulse particle tracking in which single particles are tracked over long trajectories. In either case the image density may be low enough to track individual particles (particle tracking velocimetry, or PTV) or high enough to track groups of particles by cross-correlation (PIV).

Surprisingly, the modern time-resolved PTV is predated by the work of Nayler and Frazer (1917) almost one century ago. Modern time-resolved work follows very similar lines, except that all methods are computerized and virtually all experiments use videographic recording, with the exception of the cinematic PIV experiment by Lin *et al.* (1995). T-R PTV has been employed widely in measurements of three-dimensional volumetric velocity fields (Malik *et al.*, 1993; Virant and Dracos, 1997; Robinson and Rockwell, 1993; Nishino *et al.*, 1989), and it has proved to be very effective for the Lagrangian tracking of particles over long-periods using experimental setups similar to T-R PIV/T-R PTV (Virant and Dracos, 1997; La Porta *et al.*, 2001; Mordant *et al.*, 2004; Ferrari and Rossi, 2008; Rossi and Lardeau, 2011). Given a particle's trajectory, both velocity and acceleration of the fluid can be measured in the pure Lagrangian sense, to the extent that the particle is imbedded in the fluid without slipping. The Lagrangian acceleration field can also be found by using high image density velocity measurements from two double-pulsed PIV systems plus the equation for the substantial or material derivative,

$$\frac{\mathrm{D}}{\mathrm{D}t} = \frac{\partial}{\partial t} + \boldsymbol{u} \cdot \nabla \tag{2.1}$$

Velocity fields at two slightly different times are measured to get the Eulerian acceleration, $\partial \boldsymbol{u}/\partial t$ (Perret *et al.*, 2006), and the material derivative is found by adding the $\boldsymbol{u} \cdot \nabla \boldsymbol{u}$ term (Christensen and Adrian, 2002). Note that measurements performed in a frame moving with velocity $\boldsymbol{u}$ require no correction for the second term (Liu and Katz, 2006).

Alternatively, high image density PIV can also measure Lagrangian acceleration by determining the trajectory from multi-pulse images of *groups* of particle images. The small groups of particle images act as markers of the fluid they are imbedded in. Tracking the group by cross-correlation allows reconstruction of the group's trajectory, and subsequent differentiations yield velocity and acceleration of the group (Lynch and Scarano, 2014). This transition from PTVA to PIVA is a conceptually simply matter of replacing

a single particle with a small group of closely neighboring particles. But, a group of particles deforms with the fluid, whereas a single particle does not.

Any measurement of acceleration requires three or more pulses, so in effect all PIVA and PTVA instruments are N-pulse devices of some order. Rather than the long series of images from T-R PTVA or T-R PIVA, it is possible to make good measurements of acceleration employing only 3- or 4- pulses (Adrian, 2010; Haranandani, 2011; Lynch and Scarano, 2013; Ding, 2014), or more (Martinez *et al.*, 2015).

Ground breaking work by Noca (1997); Noca *et al.* (1997, 1999); Unal *et al.* (1997) showed how the total unsteady fluid force on a body could be evaluated knowing the fluid velocity and acceleration in a control volume. Their finding materially elevated the importance of measuring acceleration in flow-structure research. The slow framing rates of film cameras severely limited the maximum measurable velocity, so they are seldom used. Digital cameras frame faster, and make it easy to record and off-load long sequences of images for PIV interrogation and analysis. If pairs of images are interrogated from a TR-PIV time series, acceleration can be measured by finite differences, provided that the time between frames is small enough (Hain and Kähler, 2007; Sciacchitano *et al.*, 2012 among others). Currently, fast digital cameras having more than one-megapixel format frame up to 25 kHz (corresponding to maximum velocities of order 5 m/s if the maximum displacement between pulses is restricted to be less than 0.2 mm). In faster flows dual-frame PIV cameras can reduce the inter-frame time below one-microsecond, allowing up to 200 m/s velocity, but without continuous time resolution owing to the limited off-load speeds of these cameras. These considerations make systems using 3-, 4-, or even more pulses attractive.

N-pulse PIVA provides benefits that may be more significant than the measurement of acceleration. Based on the observation that neither the spatial resolution nor the dy-

namic velocity range had increased significantly for more than a decade, it was proposed that an innovation was needed to get more information from the images. Specifically, the extra information could be obtained by adding light pulses to achieve significantly improved performance (Adrian, 2010). Relative to the standard double-pulse PIV, it was hypothesized that additional pulses would: 1) improve spatial resolution; 2) increase dynamic velocity range; and 3) add the capability to measure fluid acceleration. The proposed innovation extended PIVA to 3- or 4-pulses.

Until recently, the optimization and potential performance of N-P PIV has been evaluated by analyzing the simpler case of N-pulse particle *tracking* velocimetry-accelerometry (N-P PTVA), wherein the multiple pulses mark the locations of a single particle along its trajectory. Analyses of uncertainty of velocity and acceleration measurements made by N-P PTVA operating over a wide range of conditions and operating parameters (pattern of the pulses, time between first and last pulses, noise in the particle image, curvature of the particle pathline, acceleration along the pathline, and maximum velocity) have been analyzed extensively (Haranandani, 2011; Westerweel *et al.*, 2013; Ding, 2014; Ding and Adrian, 2017). The results show performance significantly superior to double-pulse PTV. For example, when the pathline has small curvature but large acceleration along it, the velocity error and position error can be reduced up to one order of magnitude. Based on the performance results from the aforementioned analyses of 3-P and 4-P PTVA, 3-P and 4-P PIVA using cross-correlation to determine displacements also appear promising. Contemporaneously with the PTVA studies (Westerweel *et al.*, 2013; Ding, 2014) the feasibility of 4-pulse PIVA using cross-correlation methods was demonstrated experimentally by Lynch and Scarano (2014) in an air flow separated from a reward facing step.

The present work applies 3-pulse and 4-pulse PIVA to simultaneous measurements of velocity and acceleration fields in flow around an oscillating cylinder, with adaptations for high image density correlation interrogation and measurements close to the accelerating fluid-solid interface. Our purpose is to compare the performance of 3- and 4-pulse PIVA in an interesting unsteady flow-structure interaction experiment using optimization concepts based on the results by Westerweel *et al.* (2013); Ding (2014) and to demonstrate a powerful tool for investigating such flows.

2.2 Experimental Apparatus and Data Acquisition

The test section, shown in Figure 2.1(a), consists of a 355.6 mm (L)× 203.2 mm (W)× 235.0 mm(H) aquarium and a pendulum comprised of a transparent Plexiglas cylinder (diameter D = 25.4 mm, span b = 114.3 mm) supported by two threaded Nylon 6/6 rods (4-40 thread) from above. The cylinder is immersed in fluid and positioned in the center. The elastic rods are 177.8 mm long (from the hinge base to the center of the cylinder) with 71.4 mm immersed the fluid. The distance between the two rods is 91.9 mm. To illuminate both sides of the cylinder,the working fluid is a refractive-index-matching (RIM) solution made with 30.35% sodium iodide (NaI), 14.57% water and 55.08% glycerin by weight, matching the refractive index of Plexiglas of 1.49. The RIM solution has a density of 1.42 g/mL and a kinematic viscosity of 60 cSt. The pendulum is driven by a step motor (VXM) controlled translation slider and oscillates sinusoidally. Figure 2.1(b) compares the positions of the driving slider and the cylinder as measured from direct imaging. The slider oscillates with a peak-to-peak amplitude of 38.1 mm and period T_0 = $1/f_0$ = 1.496 s. The cylinder oscillates with the same period but with a slightly larger amplitude of 39.2 mm and a phase delay of $3\pi/5$; i.e. $\varphi_c(t) = \varphi(t) - 3\pi/5$, where φ_c

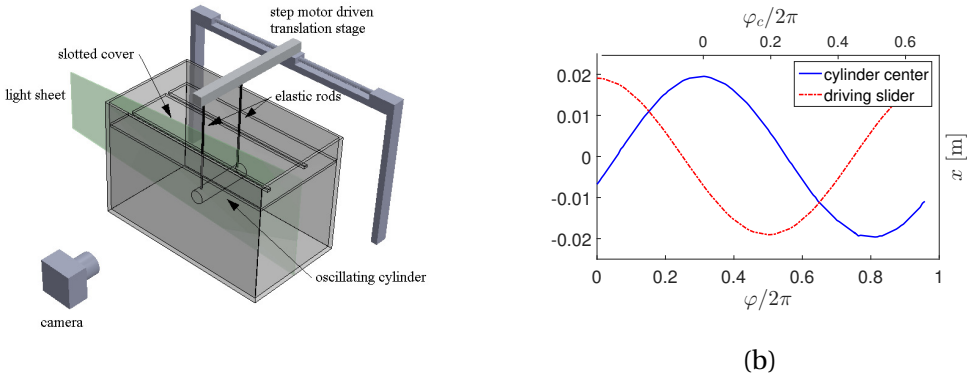

Figure 2.1: (a) Test section. (b) Positions of the driving slider and the cylinder. φ and φ_c are the phases of the driving slider and the cylinder, respectively, and $\varphi_c(t) = \varphi(t) - 3\pi/5$.

and φ denote the phase of cylinder and driving slider, respectively ($\varphi = 0$ is defined when the driving slider is at its right-most position). The Keulegan-Carpenter number, $KC = 2\pi A/D$, of the cylinder oscillation is 4.85, where A is the oscillation semi-amplitude and D is the cylinder diameter. The Reynolds number based on the maximum velocity of the cylinder is 35, and thus the frequency parameter (or Stokes number) is $\beta = Re/KC = 7.2$. To avoid the surface wave that could affect the cylinder oscillation, the liquid surface is covered by a plastic plate with two slots, along which the elastic rods can move freely.

Our 3- and 4-pulse PIVA system hardware consists of four Nd:YAG lasers (Quantel) and a high speed CMOS camera (Vision Research Phantom v641) that serves as a convenient surrogate for the 3- or 4-frame camera envisioned for true N-P PIVA. The four lasers are triggered independently and their beams are aligned collinearly by precise beam-combining optics to achieve 95% overlap at the test section. Pulse energies exceed 100mJ/pulse for good particle image signal-to-noise ratio. The illumination system is well-suited for moderate to high-speed flows due to the combination of great timing

flexibility and high pulse energy, capabilities not normally found in high-repetition-rate lasers. The camera collects up to 1,450 fps at the full resolution of 2560×1600 pixels. A section of 2560×1440 pixels is selected in the present experiment to ensure full image illumination by the laser. The light sheet is perpendicular to the cylinder and positioned at the midspan. PIVA images are captured at $f\# = 8$ with magnification 0.145.

Figure 2.2 presents the timing diagram of our experiment. Two BNC565 pulse/delay generators (#1 and #2) trigger flashlamps and Q-switches, respectively, firing four laser pulses with 10 ms apart. Another BNC box (#3) is set as the master to synchronize laser pulses and camera exposures with the phases of the pendulum oscillation. That is, at the beginning of each half cycle ($\varphi = 0$ and $\pi/2$), BNC#3 receives a signal from the step motor driver, and send signals to BNC #1 and #2 to fire lasers. Meanwhile, four channels of BNC #3 trigger the camera for four fast exposures with the four light pulses centered at each one. By setting all BNC channels to burst mode of eight pulses, the flow field is sampled by four fast frames at every phase, i.e. $\varphi = 0$, $\pi/8$, $2\pi/8$,...,$15\pi/8$, within each cycle. Hereafter, we use t_i, $i = 1,2,3,4$, to denote the time instants of the four pulses, and the total time delay $\Delta t = t_4 - t_1 = 30$ ms.

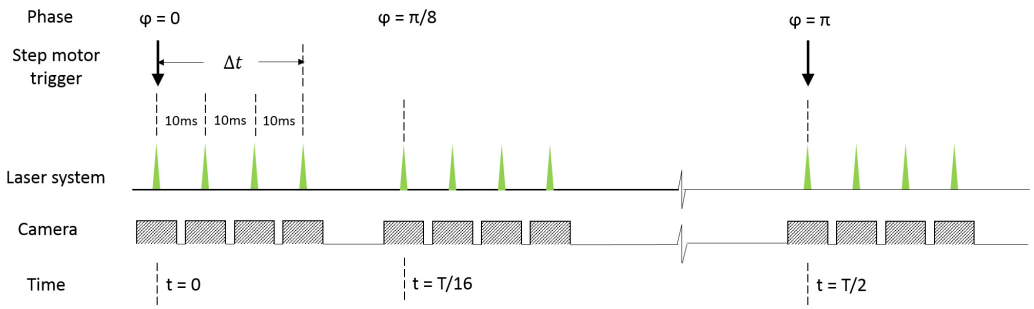

Figure 2.2: Timing diagram of 4-P PIVA measurement. Four fast frames are captured at each phase.

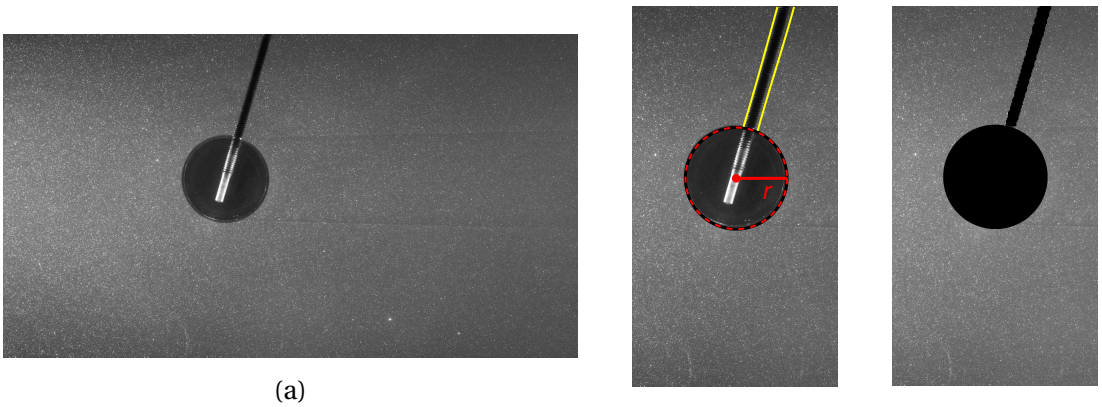

(a) (b) (c)

Figure 2.3: Segmentation of the solid region (cylinder and rod) from particle images. (a) Original particle image. (b) Detection of the cylinder circular contour (red dashed line) and the boundaries of the region blocked by the rod (yellow line). (c) Image with the solid region masked.

2.3 Position, Velocity and Acceleration of the Cylinder

A typical side-view image of the particles and the moving cylinder is shown in Figure 2.3(a). The RIM solution enables illumination of the entire field of view. The slightly dim region behind the cylinder is caused by attenuation of the light intensity when passing through the cylinder. The particle image signal-to-noise ratio decreases gradually from left to right due to divergence of the light sheet. A Circular Hough Transform (CHT) method (Atherton and Kerbyson, 1999) is adopted to detect the contour of the cylinder/light sheet cross-section with speed and accuracy. Figure 2.3(b) shows the result of the cylinder detection, in which the cross-section is given by its center and radius. The region blocked by the elastic rod is segmented by Otsu's thresholding algorithm (Otsu, 1975), followed by third-order polynomial fit to the left and right boundaries. It should be noted that the thresholding process can be accelerated if performed only within a prescribed region above the cylinder. In addition, the region for CHT searching the circle

can also be limited within the area over which the cylinder oscillates, further decreasing the processing time. Figure 2.3(c) shows the segmented image with the solid region masked.

The cylinder trajectory is measured by tracking the centers, as shown in Figure 2.4(a). The trajectory follows a "figure-eight" pattern with a slight left-right asymmetry possibly due to imperfect mounting of the pendulum. Curve fitting is performed for the cylinder center positions with the following Fourier series model up to the third harmonic,

$$\hat{\boldsymbol{x}}_c(t) = \boldsymbol{a}_0 + \sum_{k=1}^{3} [\boldsymbol{a}_i cos(k\omega t) + \boldsymbol{b}_i sin(k\omega t)], \tag{2.2}$$

where $\omega = 2\pi / T$. In the x-direction, the amplitude of the second and third harmonics (k = 2, 3) are less than 0.5% of that of the fundamental frequency (k = 1); in the y-direction, the strongest harmonic occurs at k = 2, and the amplitude of k = 3 is less than 1.5% of

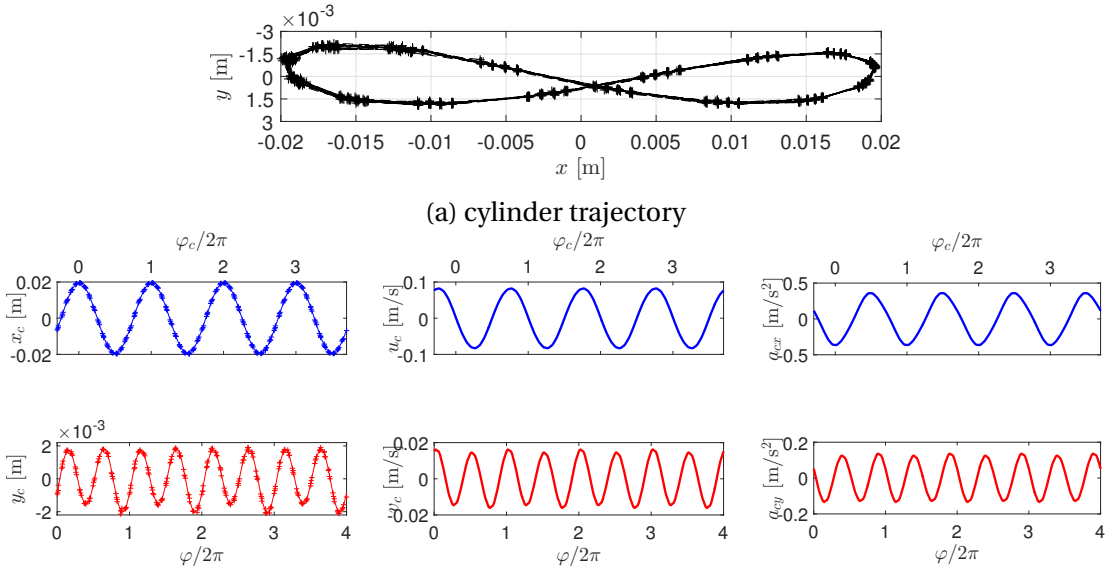

(a) cylinder trajectory

(b) position (c) velocity (d) acceleration

Figure 2.4: Tracking of the cylinder motion. "+": center positions obtained from CHT; "—" curve fitting. (a) cylinder oscillation trajectory over four periods. (b) cylinder position vs. time. (c) velocity vs. time. (d) acceleration vs. time. Blue is for x-component and red for y-component. Both φ_c and φ are indicated on the time axes.

that. The cylinder velocity, (u_c, v_c), and acceleration, (a_{cx}, a_{cy}), are then calculated by differentiating $\hat{\boldsymbol{x}}_c(t)$, and the results are shown in Figure 2.4(b) – 2.4(d). The maximum magnitudes of velocity occur when the cylinder is moving through the center of its trajectory, whereas the maximum magnitudes of acceleration occur when the cylinder is turning to the opposite direction at the left- and right-most positions of the trajectory.

2.4 Velocity and Acceleration Fields of the Fluid

2.4.1 N-pulse PIVA Analysis

The particle-filled fluid region with particles is processed using adaptive window-based cross-correlation to track the same groups of particles in four consecutive frames at t_1, t_2, t_3 and t_4. The iterative image deformation technique proposed by Scarano (2001) is applied to improve the accuracy. The 3-pulse analysis correlates the images from pulse 2 to 1, and from pulse 2 to 4, yielding two displacement vectors, $\Delta\boldsymbol{x}_{21}$ and $\Delta\boldsymbol{x}_{24}$, with both starting points located at the window center of pulse 2. The window-averaged trajectory is then estimated by a second-order polynomial fitted to the three positions, $\Delta\boldsymbol{x}_{21}$, $\boldsymbol{0}$, and $\Delta\boldsymbol{x}_{24}$. The strategy of performing cross-correlation starting from the middle frame (pulse 2) avoids the possible weak correlation signals due to in-plane and out-of-plane loss of pairs (Adrian and Westerweel, 2011) if otherwise correlating from pulse 1 to 2, and from pulse 1 to 4. The use of pulse 1,2,4 for triple-pulse analysis instead of pulse 1,2,3 is to (1) have the same Δt as quadruple-pulse analysis for a valid comparison of their performances; and (2) reduce the random noise level by using a longer Δt (Ding and Adrian, 2017). The 4-pulse analysis estimates the trajectory by fitting a polynomial to four positions, $\Delta\boldsymbol{x}_{21}$, $\boldsymbol{0}$, $\Delta\boldsymbol{x}_{23}$ and $\Delta\boldsymbol{x}_{24}$.

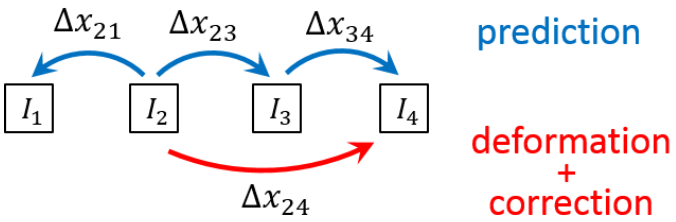

Figure 2.5: Schematic of the interrogation scheme for window-based 4-pulse PIVA analysis

We investigate two fitting methods – third-order polynomial and second-order polynomial by least squares, referred to as 4-pulse with interpolation and 4-pulse with least squares, respectively. The latter intends to reduce the influence of the random errors embedded in displacement measurements. $\Delta\boldsymbol{x}_{21}$ and $\Delta\boldsymbol{x}_{23}$ are measured directly by cross-correlation with iterative image deformation. The measurement of $\Delta\boldsymbol{x}_{24}$ employs a predictor-corrector interrogation scheme (Figure 2.5), similar to fluid tracking correlation (FTC) for TRPIVA (Lynch and Scarano, 2013). Vector fields $\Delta\boldsymbol{x}_{34}$ are first measured on the same grid as $\Delta\boldsymbol{x}_{23}$, and then interpolated onto a grid defined by the ending points of $\Delta\boldsymbol{x}_{23}$ yielding $\Delta\boldsymbol{x}'_{34}$. We use $\Delta\boldsymbol{x}_{23} + \Delta\boldsymbol{x}'_{34}$ as the initial prediction for $\Delta\boldsymbol{x}_{24}$, which is then corrected by two iterations of deformation and update using images of pulse 2 and 4. The velocity and acceleration of triple- and quadruple-pulse analyses are calculated by differentiating the time-dependent trajectories at $t = t_2$, and assigned to the window centers at pulse 2, yielding vectors on regular grids. More accurate estimates of the velocity and acceleration may be achieved by assigning each vector obtained by cross-correlation to the centroid of the particle group and calculating velocity and acceleration at the optimal times proposed by Ding and Adrian (2017) from their N-P PTVA simulation. However, the calculations of the vorticity, viscous stress tensor, and many other quantities require data interpolation on grid points, which may bring in extra error to an unknown degree.

The present method of assigning vectors to window centers and evaluating velocity and acceleration at $t = t_2$ is a convenient and near-optimum strategy.

2.4.2 Treatment of the Near-Wall Region

The aforementioned schemes were employed to measure the flow fields far away from the moving cylinder surface. In our early tests, tracking near-wall particle groups by N-P PIVA analysis using the digital mask technique of Gui *et al.* (2000) produced significant numbers of invalid vectors, an effect attributed to the difficulty of properly performing deformation interpolation near the moving curved surface. Near-wall particle images and the surface are often distorted undesirably during the iterations of image deformation. This problem appears more severe for N-pulse analysis that searches three or four consecutive frames for matching particle groups. To achieve accurate measurement close to the surface, we follow the same strategy as in Nguyen *et al.* (2010)

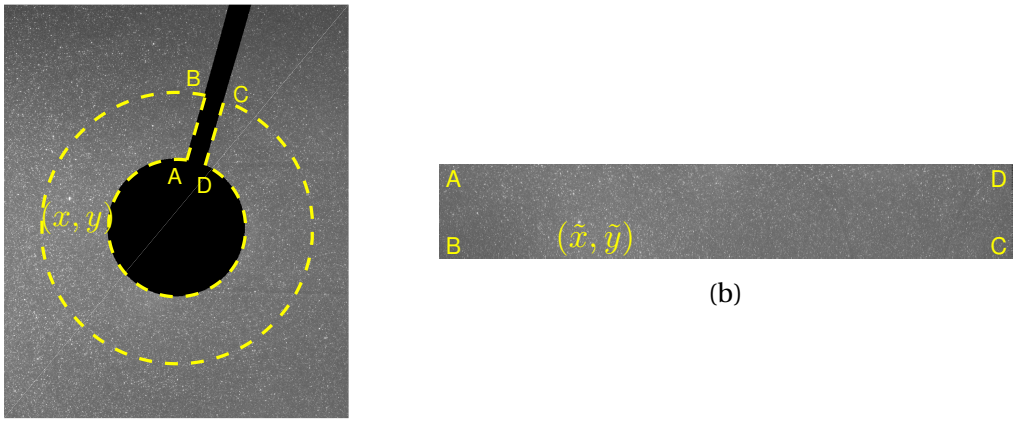

(a) (b)

Figure 2.6: (a) A circular band to be transformed near the surface, outlined by the yellow dashed line. (b) The resulting rectangle in the transformed domain. Corresponding corners are labeled with A, B, C and D.

and Jeon and Sung (2011) that transforms the near-wall region to a rectangle, which is more amenable to N-P PIVA analysis with image deformation. The transformation method proposed here is simple but more general for various applications.

Near-wall region transformation. Local tangent and normal coordinate systems sometimes fail to describe the local geometry, especially if the region to be transformed is bounded by another object or by the boundaries of the image. To be more flexible for various geometries, the proposed method maps the four corners of a prescribed near-wall region in the physical domain to the four corners of a rectangle in the transformed domain. Figure 2.6(a) shows a circular band to be transformed in the vicinity of the cylinder with an interior boundary $\widehat{AD}$ and an exterior boundary $\widehat{BC}$. The corresponding corners after transformation, labeled A, B, C and D, are shown in Figure 2.6(b). The transformation is mathematically represented by a vector function $\boldsymbol{F}$, relating the physical domain (x, y) to the transformed domain $(\tilde{x}, \tilde{y})$,

$$(x, y) = \boldsymbol{F}(\tilde{x}, \tilde{y}), \qquad \text{or} \qquad (\tilde{x}, \tilde{y}) = \boldsymbol{F}^{-1}(x, y). \tag{2.3}$$

The length of $\widehat{AD}$ and $\widehat{BC}$ are denoted l_1 and l_2, respectively, and the transformed rectangle has a length of $\tilde{l}$ and a width of $\tilde{w}$. Then the transformation function $\boldsymbol{F}$ is

$$\boldsymbol{F}(\tilde{x}, \tilde{y}) = (1 - \frac{\tilde{y}}{\tilde{w}})\boldsymbol{H}_1(\frac{\tilde{x}}{\tilde{l}} l_1) + \frac{\tilde{y}}{\tilde{w}}\boldsymbol{H}_2(\frac{\tilde{x}}{\tilde{l}} l_2), \tag{2.4}$$

in which $\boldsymbol{H}_1$ and $\boldsymbol{H}_2$ calculate the positions along $\widehat{AD}$ and $\widehat{BC}$ where the cumulative lengths are equal to $\frac{\tilde{x}}{\tilde{l}} l_1$ and $\frac{\tilde{x}}{\tilde{l}} l_2$, respectively. In practice, $\widehat{AD}$ and $\widehat{BC}$ are represented by a series of discrete point positions, and the cumulative length is estimated by adding the straight distances between neighboring points. $\boldsymbol{H}_1$ and $\boldsymbol{H}_2$ are then fitted to relate the cumulative length to the point positions using cubic-spline. For pixelized digital images, the transformation function $\boldsymbol{F}^*$ of the $(\tilde{m}, \tilde{n})^{th}$ pixel in the transformed image with $\tilde{M} \times \tilde{N}$

pixels can be written as

$$\boldsymbol{F}^*(\tilde{m},\tilde{n}) = (1-\frac{\tilde{y}^*}{\tilde{N}})\boldsymbol{H}_1(\frac{\tilde{x}^*}{\tilde{M}}l_1) + \frac{\tilde{y}^*}{\tilde{N}}^*\boldsymbol{H}_2(\frac{\tilde{x}^*}{\tilde{M}}l_2), \tag{2.5}$$

where $(\tilde{x}^*,\ \tilde{y}^*) = (\tilde{m}-0.5,\ \tilde{n}-0.5)$ is the center of the $(\tilde{m},\tilde{n})^{th}$ pixel. Consequently, the intensity of the $(\tilde{m},\tilde{n})^{th}$ pixel in the transformed image, $I_{trans}(\tilde{m},\tilde{n})$, is interpolated as

$$I_{trans}(\tilde{m},\tilde{n}) = I_{phys}(\boldsymbol{F}^*(\tilde{m},\tilde{n})), \tag{2.6}$$

where the I_{phys} is computed with a user-preferred interpolation method, such as bilinear, or cubic-spline (present work), for example. The resolution of the transformed image needs to be comparable to that in the physical domain to avoid loss of intensity information. The near-wall band should be relatively narrow to avoid strong distortion in the transformed image due to significant magnification variation. Meanwhile, it should allow at least 6-8 vector spacings for reliable interrogation and validation of PIVA. It is worth noting that, although the foregoing description is based on the current geometry, this transformation method can be easily applied to arbitrarily shaped surfaces, provided they are smooth enough to prevent extreme distortion around kinks.

Displacement vector inverse transformation. Displacement fields $\Delta\boldsymbol{x}_{21}$, $\Delta\boldsymbol{x}_{23}$ and $\Delta\boldsymbol{x}_{24}$ in the transformed domain are measured by window-based N-P PIVA analysis as described in section 2.4.1. Displacement vectors in the physical domain are then obtained by inverse transformation. Note that the starting and ending points of a vector need to be transformed by different transformation functions. That is, if $\boldsymbol{F}_a$ and $\boldsymbol{F}_b$ denote the transformation for the starting and ending frames in cross-correlation analysis, respectively, the corresponding vector, $\boldsymbol{u}_{phys}$, in the physical domain is

$$\boldsymbol{u}_{phys} = \boldsymbol{F}_b(\tilde{x}_b,\tilde{y}_b) - \boldsymbol{F}_a(\tilde{x}_a,\tilde{y}_a), \tag{2.7}$$

where $(\tilde{x}_a,\tilde{y}_a)$ and $(\tilde{x}_b,\tilde{y}_b)$ are the starting and ending points respectively for a vector in the transformed domain.

Data interpolation onto Cartesian grid. Figure 2.7 illustrates the three regions of the field that we treat differently in the analysis. The entire field is divided into two mutually exclusive partitions – the interpolation region (IR) that covers the solid phase (cylinder + rod) and its vicinity, and the outer region (OR) that occupies the rest of the field. The near-wall region (NWR) is where we perform the transformation and the displacement vector inverse transformation, overlapping with IR and OR. The velocity and acceleration of NWR are calculated in the physical domain using the displacement vectors obtained from inverse transformation. The resulting vectors are distributed in a polar-type grid around the cylinder, whereas the vectors in OR are on a Cartesian grid. To achieve the vectors on a uniform Cartesian grid throughout the field, we perform interpolation (Matlab v4 algorithm) in IR using the velocity and acceleration data from NWR and OR. Note that the overlap between OR and NWR assures smooth interpolation at the boundary between the polar-type grid and Cartesian grid.

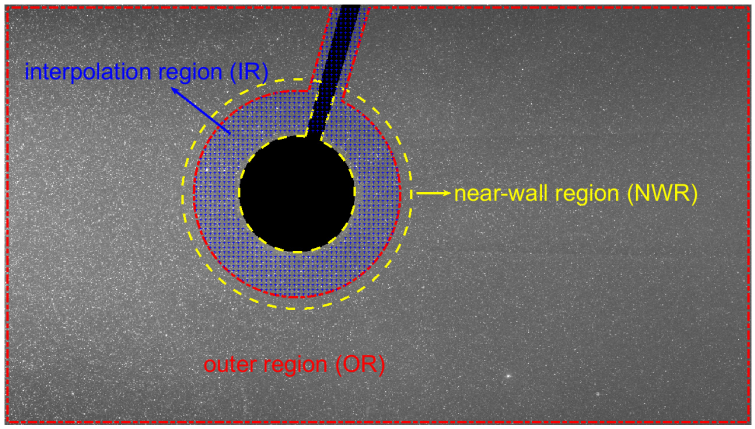

Figure 2.7: Illustration of data interpolation and region assembly. Velocity and acceleration data in NWR (yellow dashed line) are on a polar-type grid, whereas the data in OR (red dash-dot line) are on a Cartesian grid. Interpolation is performed in IR using the NWR and OR data to achieve a uniform Cartesian grid throughout the field.

2.4.3 Instantaneous and Phase Averaged Velocity and Acceleration

Velocity and acceleration fields are measured at fixed phases in each cycle with final interrogation window size 2.2 mm × 2.2 mm and vector spacing 1.1 mm. Figure 2.8 compares the instantaneous velocity and acceleration fields from different analysis methods at $\varphi_c/2\pi = 0.7$ ($\varphi/2\pi = 0$), when the cylinder is accelerating in the positive x-direction. The surrounding fluid circulates around the cylinder, and recirculates in the downstream wake. Pronounced centripetal acceleration occurs on the top and the bottom of the cylinder due to strongly curved streamlines. The comparison is among different analyses – 2-pulse, 3-pulse, 4-pulse with interpolation, and 4-pulse with least squares. The 2-pulse velocity field is conventionally calculated from $\frac{\Delta \boldsymbol{x}_{23}}{(t_3 - t_2)}$. All velocity fields are almost identical and smoothly varying, while the acceleration fields manifest observable differences, implying acceleration is more sensitive to measurement noise. 4-pulse analysis with interpolation produces the noisiest acceleration field, which is also evident from the root-mean-square (rms, with respect to the averaged field at each phase) acceleration fields shown in Figure 2.9. Considering the flow is phase-locked and non-turbulent, the rms fields primarily reveal the level of random error. The N-P PTVA simulation conducted by Ding and Adrian (2017) also shows that 4-pulse with interpolation presents larger random error than 3-pulse with interpolation because the normalized particle locating errors of four particles accumulate when they are large. In the present experiment, this can be equivalently interpreted as the accumulation of normalized displacement random errors (normalized by the total displacement during Δt) when measuring $\Delta \boldsymbol{x}_{21}$, $\Delta \boldsymbol{x}_{23}$ and $\Delta \boldsymbol{x}_{24}$. In the region far from the cylinder where the fluid is slightly disturbed by the oscillating cylinder, the normalized displacement random error is significant, making the acceleration field of 4-pulse with interpolation

noisier than the 3-pulse. The comparisons in Figure 2.8 and 2.9 also show that the 4-pulse analysis with least squares is capable of suppressing random error, yielding slightly better results than the 3-pulse analysis. The larger rms acceleration around the cylinder implies the transformation and interpolation of the near-wall treatment could introduce additional noise. It is worth mentioning that, for flows with strong 3-D motion and turbulence, the random error of 3-pulse analysis is expected to grow more rapidly than the 4-pulse analysis when performing planar PIVA measurements. This is because the correlation signal is weakened by greater loss of pairs during longer inter-frame time given the same Δt. Shortening Δt is risky for 3-pulse measurements because the normalized displacement random error is inversely proportional to the total time delay.

While the forgoing discussion implies that the 4-pulse analysis with least squares has the advantage of smaller random error and better cross-correlation signals, the comparison of the mean bias error presented in Figure 2.10 suggests otherwise. The mean bias is calculated by taking the magnitude of the mean acceleration measured by 4-pulse analysis with interpolation as our 'ground truth' data. This is because earlier work (Lynch and Scarano, 2013; Ding and Adrian, 2017) has shown that higher-order fitting estimates curved trajectories more accurately, regardless of noise. The results in Figure 2.10 are the differences between the other fields and the ground truth field normalized by the full scale acceleration of the field (≈ 0.7 m/s^2). It is noticed in Figure 2.9 that the interpolation in the region blocked by the rod introduces additional random error. Thus, to objectively assess the bias error generated from different analysis methods only, Figure 2.10 presents the mean bias error in the lower half of the field. Clearly 4-pulse analysis with least squares and 3-pulse analysis both present non-negligible bias error. The largest bias, up to 10% of the full scale, occurs underneath the cylinder where streamlines are strongly curved and centripetal acceleration is considerable. It is also evident that the

4-pulse analysis with least squares reduces the random error at the cost of larger bias error than the 3-pulse analysis.

Phase-averaged velocity and acceleration fields are calculated using quadruple-pulse analysis with interpolation over 105 periods. A half cycle is presented in Figure 2.11. From $\varphi_c/2\pi = 0.7$ to 0.825, when the cylinder quickly passes through the center, the wake recirculation region elongates with attenuating vorticity intensity. Two counter rotating vortices are formed symmetrically about the cylinder advancing direction. The vortex pair stays attached to the cylinder, as seen at $\varphi_c/2\pi = 0.95$, and it stops developing until the cylinder reaches the right-most position. At $\varphi_c/2\pi = 0.95$, right after the cylinder reverses, the cylinder collides with the vortex induction, forming a stagnation point. The vortices in the former wake are mixed and cancelled by the newly-formed boundary layer with vorticity of the opposite sign. The fluid adjacent to the leading and trailing surfaces of the cylinder always accelerates and decelerates synchronously with the cylinder. The strongest centripetal acceleration of the fluid curving around the cylinder at the top and the bottom occurs when the cylinder reaches its velocity maximum. The KC number and β number of present experiment ($KC = 4.85$, $\beta = 7.2$) belong to flow regime A* proposed by Tatsuno and Bearman (1990) for cylinder in-line oscillation, in which no vortex shedding occurred in accordance with the velocity fields described above. However, secondary streaming reported by the authors is not observed in the present work.

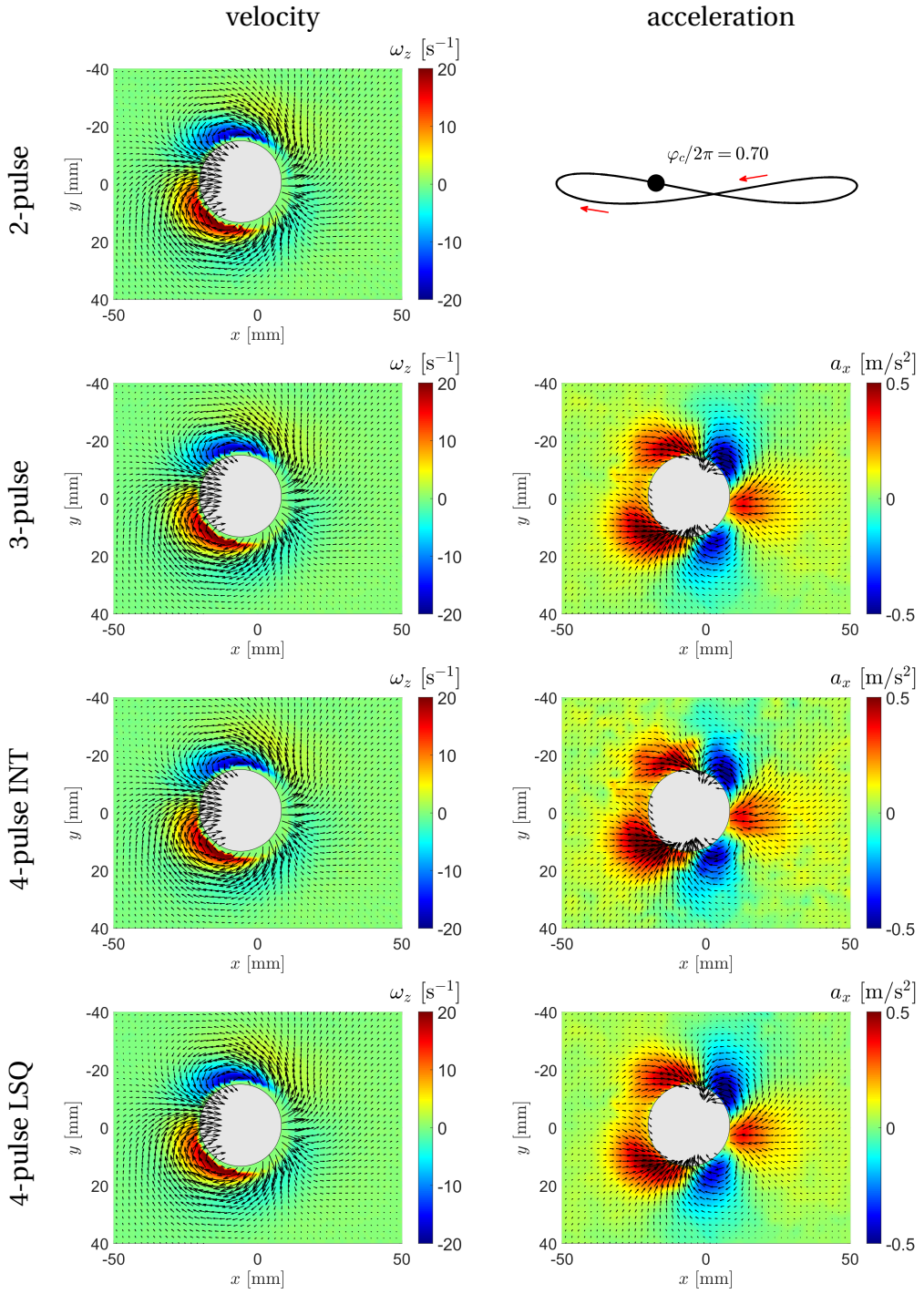

Figure 2.8: Instantaneous velocity and acceleration fields showing every other vector at $\varphi_c/2\pi = 0.7$ ($\varphi/2\pi = 0$) from 2-, 3-, and 4-pulse PIVA analyses. Colors in the velocity fields represent the vorticity. Colors in the acceleration fields represent the x-component of acceleration. The inset indicates the cylinder location at $\varphi_c/2\pi = 0.7$.

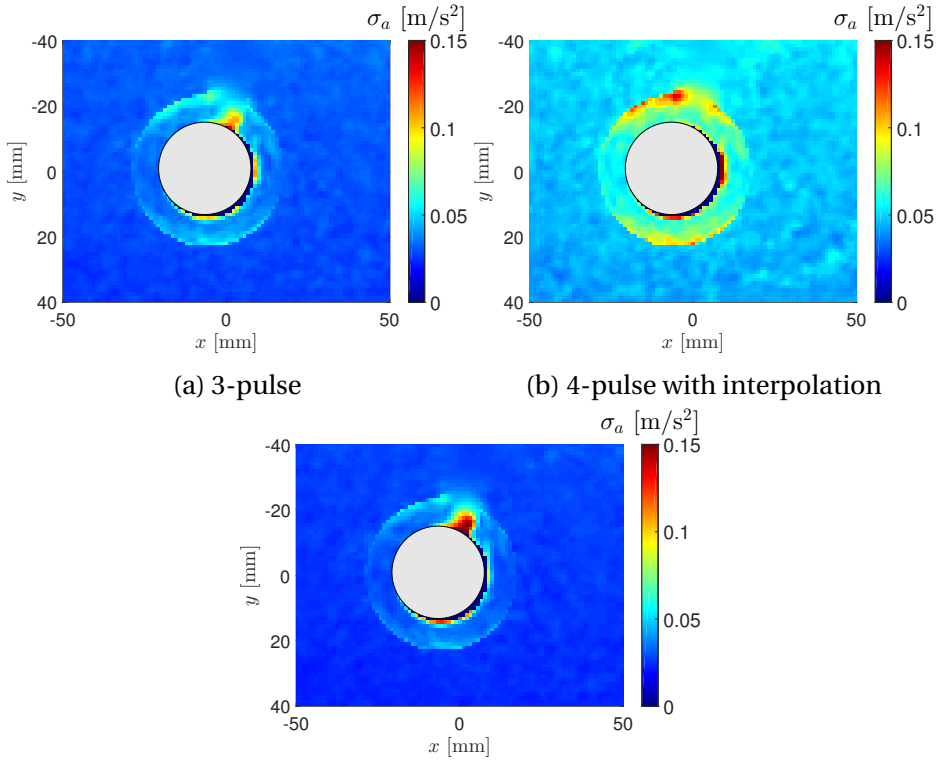

(a) 3-pulse

(b) 4-pulse with interpolation

(c) 4-pulse with least squares

Figure 2.9: Comparison of the rms acceleration from different analysis methods at $\varphi_c/2\pi = 0.7$ ($\varphi/2\pi = 0$).

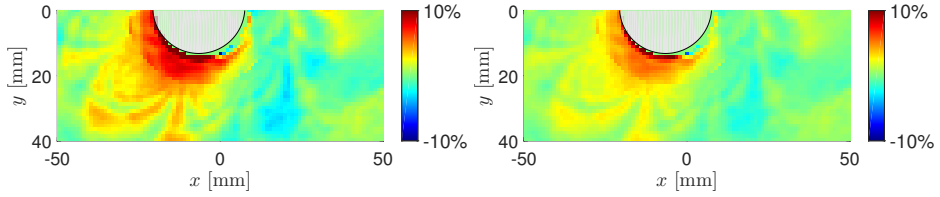

(a) 4-pulse with least squares

(b) 3-pulse

Figure 2.10: Comparison of the mean bias acceleration with respect to the 4-pulse analysis with interpolation at $\varphi_c/2\pi = 0.7$ ($\varphi/2\pi = 0$). The mean bias errors are calculated as $\left(|\boldsymbol{a}|_{4\text{p,intp}} - |\boldsymbol{a}|_{4\text{p,lsq}}\right)$ and $\left(|\boldsymbol{a}|_{4\text{p,intp}} - |\boldsymbol{a}|_{3\text{p}}\right)$, and they are normalized by the full scale acceleration of the field (≈ 0.7 m/s^2).

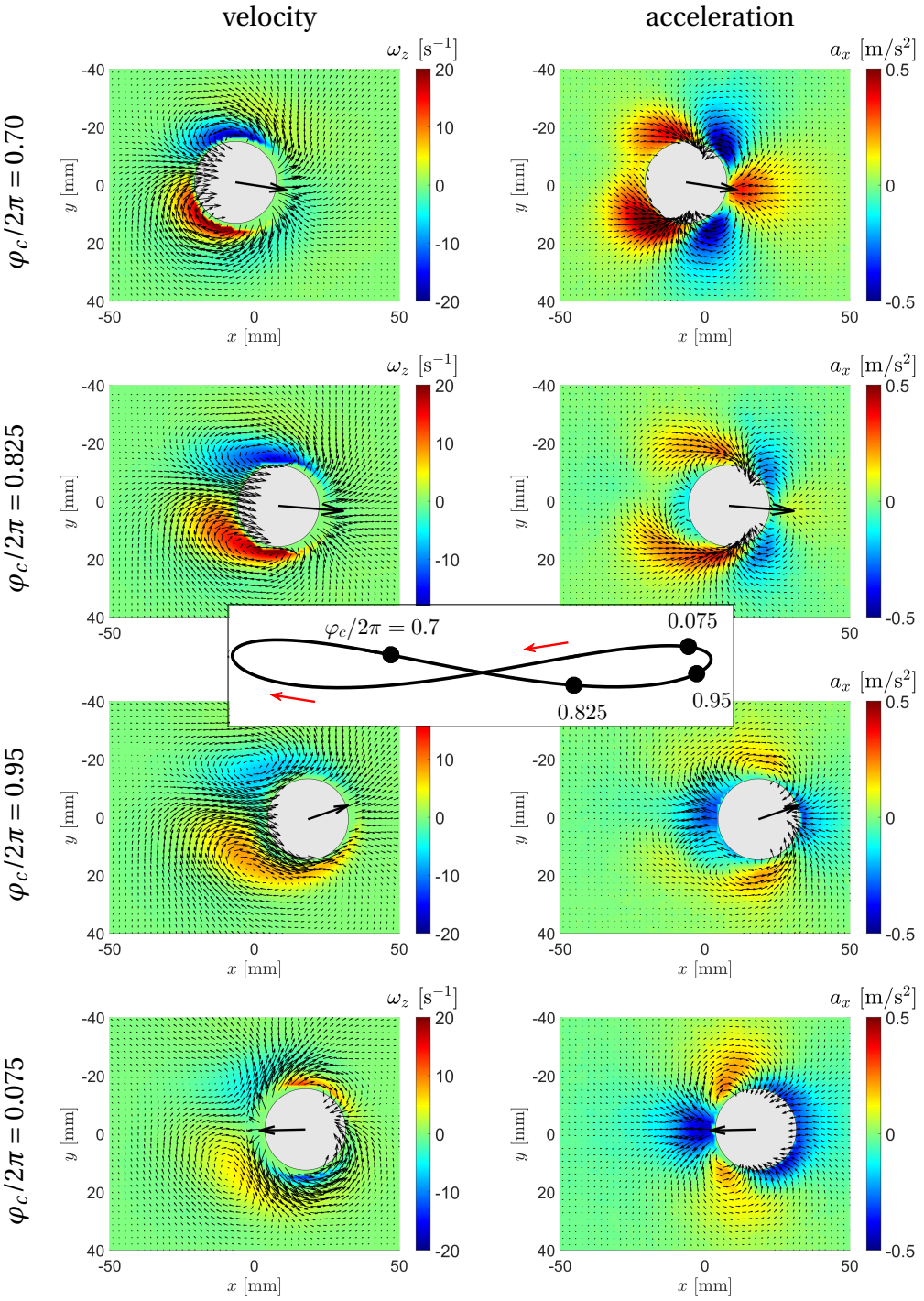

Figure 2.11: Phase averaged velocity and acceleration fields showing every other vector at $\varphi_c/2\pi = 0.7, 0.825, 0.95, 0.075$. The inset indicates corresponding locations of the cylinder. Bold black vectors at the cylinder center indicate the direction along which the cylinder moves.

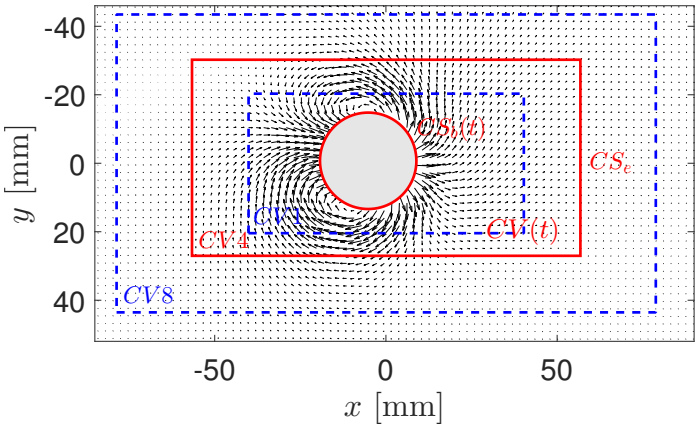

Figure 2.12: Control volume $CV(t)$ bounded by an interior surface, $CS_b(t)$, following the cylinder, and an exterior surface, CS_e. Parametric study of the force measurement is conducted by varying $CS_e(t)$ between $CV1$ and $CV8$.

2.5 Force Evaluation by 4-P PIVA Data and Control Volume Approach

Noca (1997) showed that the fluid force acting on a body can be evaluated with an exact control volume formulation that involves only velocity fields and their derivatives. Figure 2.12 shows the configuration of the control volume, $CV(t)$, in the present work. The interior surface, $CS_b(t)$, follows the moving cylinder surface; the exterior surface, $CS_e(t)$, enclosing the cylinder oscillation trajectory, is either fixed or moving with the cylinder. The flow at $Re = 35$ and $KC = 4.85$ is assumed to be two-dimensional over most of the cylinder (Tatsuno and Bearman, 1990) so that the measurements in the mid-plane are representative of the three-dimensional flow. Applying the formulation to our case, the total fluid force on the cylinder is the sum,

$$\boldsymbol{F} = \boldsymbol{F}_{\text{vol}} + \boldsymbol{F}_{\text{mf}} + \boldsymbol{F}_{\text{str}}. \tag{2.8}$$

The volume term,

$$\boldsymbol{F}_{\text{vol}} = -\frac{d}{dt}\int_{CV(t)} \rho \boldsymbol{u} dV, \tag{2.9}$$

is the time rate of change of the momentum in the control volume. The term of momentum flux on $CS_e(t)$ is

$$\boldsymbol{F}_{\mathrm{mf}} = -\oint_{CS_e(t)} \rho \boldsymbol{n} \cdot (\boldsymbol{u} - \boldsymbol{u}_s) \boldsymbol{u} dS \tag{2.10}$$

wherein $\boldsymbol{u}_s$ is the velocity of a surface element dS on $CS_e(t)$. The last term, the stress term, is

$$\boldsymbol{F}_{\mathrm{str}} = \oint_{CS_e(t)} \left[\frac{1}{2} |\boldsymbol{u}|^2 \boldsymbol{n} - u_n (\boldsymbol{x} \times \boldsymbol{\omega}) - \left(\boldsymbol{x} \cdot \frac{\partial \boldsymbol{u}}{\partial t} \right) \boldsymbol{n} + x_n \frac{\partial \boldsymbol{u}}{\partial t} + \nu (\boldsymbol{x} \cdot \nabla^2 \boldsymbol{u}) \boldsymbol{n} - \nu x_n \nabla^2 \boldsymbol{u} + \frac{\boldsymbol{T}_n}{\rho} \right] \rho dS, \tag{2.11}$$

wherein $()_n = \boldsymbol{n} \cdot ()$. $\boldsymbol{T}$ is the viscous stress tensor, $\boldsymbol{\omega}$ the vorticity, ν the kinematic viscosity of the working fluid, and $\boldsymbol{x}$ the position vector. It can be shown that $\boldsymbol{F}_{\mathrm{str}}$ is equal to the surface integral of the pressure and viscous stress on $CS_e(t)$ (Noca, 1997). Note that dV has the dimension of area, and dS has the dimension of length when evaluating sectional force in the plane of the PIVA measurement. The original force equation in Noca (1997) had another term describing the momentum flux on the interior control surface; this term vanishes in our case as $\boldsymbol{u} = \boldsymbol{u}_s$ on $CS_b(t)$.

N-P PIVA data allow for the complete evaluation of each term in (2.9) – (2.11). In our analysis, the volume term, $\boldsymbol{F}_{\mathrm{vol}}$, is estimated by fitting a parabola to the volume integrals of three successive velocity fields $\boldsymbol{u}(t_i) = \dfrac{\Delta \boldsymbol{x}_{i,i+1}}{t_{i+1} - t_i}$, i = 1,2,3, and differentiating at $t = t_2$. The displacement fields $\Delta \boldsymbol{x}_{i,i+1}$ are obtained by performing cross-correlation of neighboring frames with iterative image deformation. The momentum flux, $\boldsymbol{F}_{\mathrm{mf}}$, is evaluated using the velocity fields from the 4-pulse analysis with least squares for less random error. The stress term, $\boldsymbol{F}_{\mathrm{str}}$, is evaluated using central differencing in space for $\boldsymbol{\omega}$, $\boldsymbol{T}$, and $\nabla^2 \boldsymbol{u}$, and central differencing in time for $\dfrac{\partial \boldsymbol{u}}{\partial t}$, i.e. $\dfrac{\boldsymbol{u}_{34} - \boldsymbol{u}_{12}}{t_3 - t_1}$.

Fluid forces acting on the cylinder surface are computed using (2.9) – (2.11), and they are normalized by the maximum cylinder velocity in the x-direction, $u_{c,max}$, to calculate

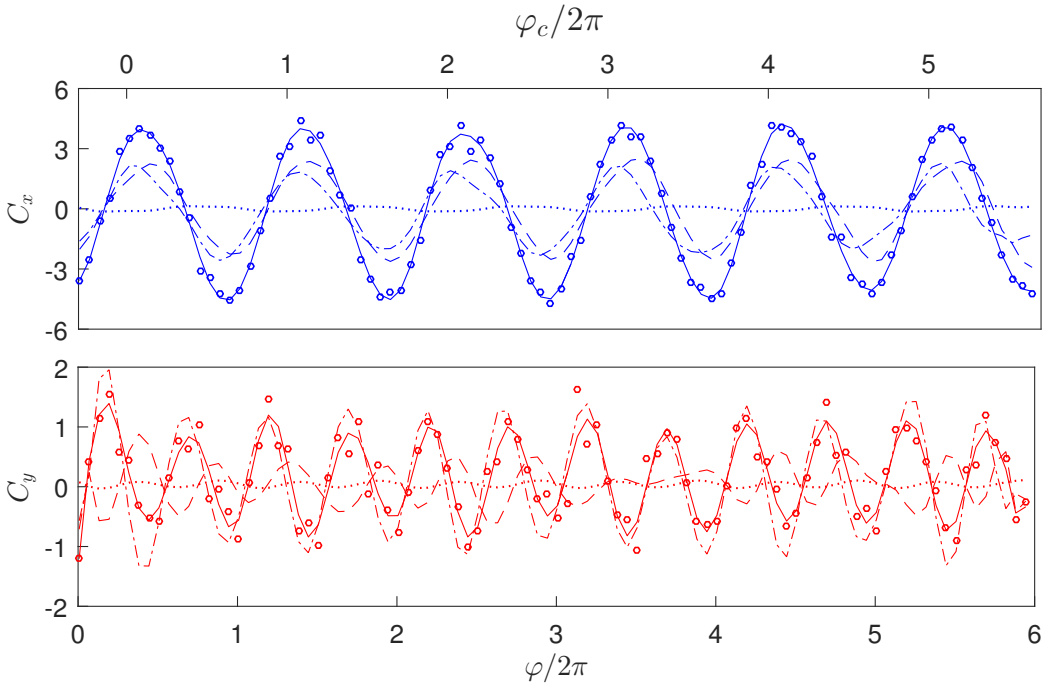

Figure 2.13: Instantaneous $x-$ and $y-$direction force coefficients and contributions from each term calculated with $CV4$ (fixed) shown in Figure 2.12. ◯, unfiltered total force; —, filtered total force; – –, filtered volume term; $\cdots$, filtered momentum flux; – · –, filtered stress term. Filtered data use a 10th-order Butterworth low-pass filter with cut-off frequency $f_c = 2$ Hz. Note the different scales used for y axes.

force coefficients,

$$C_\alpha(t) = \frac{F_\alpha(t)}{\frac{1}{2}\rho D u_{c,max}^2}, \tag{2.12}$$

where the subscript α denotes directions (x or y) or different terms (volume term, momentum flux, stress term). A 10th-order Butterworth low-pass filter with cutoff frequency $f_c = 2$ Hz is applied to attenuate fluctuations at high frequencies. Note that the cylinder oscillates at $f_0 = 0.68$ Hz, and the sampling frequency of the force measurement is $f_s = 10.84$ Hz. Results calculated using $CV4$ (fixed) are presented in Figure 2.13. In the x-direction, the unfiltered total force is smooth and stable in amplitude. The volume term and the stress term are comparable in amplitude, and they exhibit slight phase shifts of opposite sign with respect to the total force. The momentum flux on CS_e is negligibly

small as the disturbance is confined within close vicinity of the cylinder. The force in the y-direction is noisier than that in the x-direction, which is probably due to the fact that the flow field is dominated by flow in the x-direction so that measurements in the y-direction encounter larger normalized displacement random error. The stress term of the y-direction appears in phase with the total force, whilst the volume term shows an approximately 150° phase shift. Figure 2.14 plots the variations in amplitude of each force term as well as the total force when increasing the size of fixed control volume from $CV1$ to $CV8$ (Figure 2.12). The peak-to-peak amplitudes are calculated by averaging over $m = 6$ cycles, i.e.

$$A_\alpha(CV) = \frac{\pi}{mT}\int_0^{mT} \left|F_\alpha^*(t;CV)\right| dt, \tag{2.13}$$

where $F_\alpha^*(t;CV)$ denotes the filtered force data for control volume CV. It is evident that the total force amplitudes stay almost unaltered for both directions, in accordance with the results from Noca (1997); Noca *et al.* (1999). For the x-direction, moving CS_e outwards causes an increase in the amplitude of the stress term and a decrease for the volume term. In the y-direction, as the stress term and volume term are out of phase, the amplitudes both increase, canceling each other. The momentum flux terms stay small, and present a slightly decreasing trend in both directions. In addition, for the scenario of $CS_e(t)$ moving with the cylinder, we calculated the total force amplitudes of $CV1$ to $CV5$, which show consistency with the results of fixed CS_e. Figure 2.15 (left) presents the power spectra of the total force coefficients presented in Figure 2.13. The strongest harmonics occur at $fT_0 = 1$ and $fT_0 = 2$ for the x- and y-direction, respectively. The rest of the spectra appear likely to be white noise, albeit there may exist weak signals at $fT_0 = 3, 4, \ldots$. The signal-to-noise ratios (SNR), shown in Figure 2.15 (right), are calculated between the summed square of the force coefficients (or equivalently the integral of the power spectrum) and the summed square of the noise by excluding the first three harmonics.

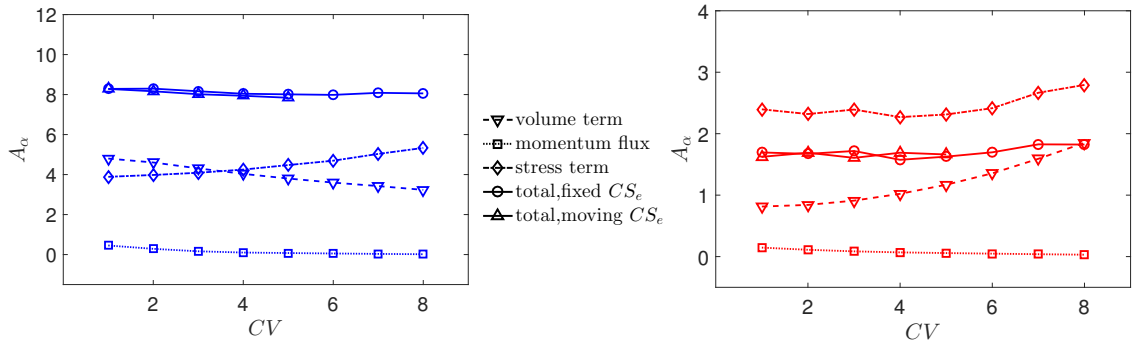

(a) x-direction (b) y-direction

Figure 2.14: Peak-to-peak amplitudes of each force term with increasing control volume.

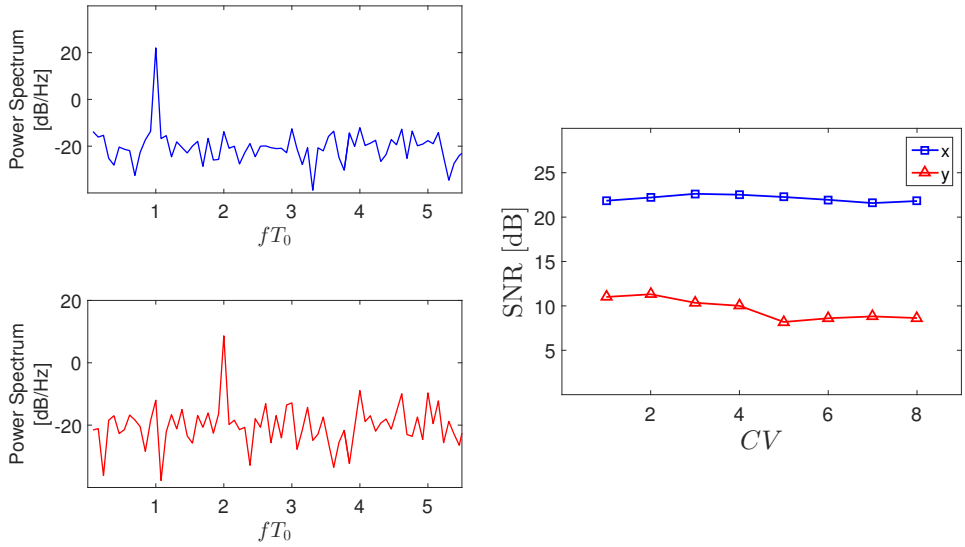

Figure 2.15: Power spectra of C_x (left top) and C_y (left bottom) plotted in Figure 2.13. The SNR is the ratio between the summed square of the signal and that of the noise. The computation of the noise excludes the first three harmonics in the power spectrum.

The decrease of SNR in the y-direction suggests that it may be disadvantageous to set up the control volume including a significant part of the undisturbed field where large normalized displacement random error exists, although it may make the viscous stress and the momentum flux negligible.

The in-line force per unit length acting on an oscillating cylinder in stationary fluid can be characterized by Morison equation (Morison *et al.*, 1950),

$$F = -\frac{1}{2}\rho D C_d \left|u_c\right| u_c - \frac{1}{4}\pi\rho D^2 C_i \frac{du_c}{dt} \tag{2.14}$$

where u_c is the cylinder velocity, and C_d and C_i are drag and added mass coefficients, respectively. Calculation of C_d and C_i using the x-direction force data computed from the phase-averaged fields yields $C_d = 2.95$, $C_i = 1.51$. Other experiments and numerical simulations studying C_d and C_i (in the case of oscillatory flow around a fixed cylinder, C_i is replaced by the inertia coefficient $C_m = C_i + 1$) for in-line oscillation of a cylinder at low β numbers can be found in Bearman *et al.* (1985) ($\beta = 196$); Lin *et al.* (1996) ($\beta = 76$); Dütsch *et al.* (1998) ($\beta = 20, 35$); Iliadis and Anagnostopoulos (1998) ($\beta = 34, 53$). Our results at $KC = 4.85$ and $\beta = 7.2$ are compared to those in literature at $KC = 5$ in Figure 2.16. Clearly our results constitute reasonable continuations of the increasing trends for C_d and C_i when β gets smaller, albeit the small-amplitude oscillation superimposed in the y-direction adds uncertainties to the comparison. Future assessment of the force accuracy could be achieved by adding force sensors to our facility or redesigning the experiment for more direct comparisons with experiments in the literature, but neither are within the scope of the present work.

The supplementary material of this article includes a movie that shows simultaneous fluid velocity and acceleration fields, cylinder velocity and acceleration traces, and the force exerted on the cylinder, providing a clear picture of the outcomes from N-P PIVA. An immediate and important observation from the movie is that the maximum force along the x-direction occurs slightly after the maximum acceleration and before the maximum velocity of the cylinder. In other words, the peak force is the combined contribution by the added mass force and the traction forces in the boundary layer. At this moment, the

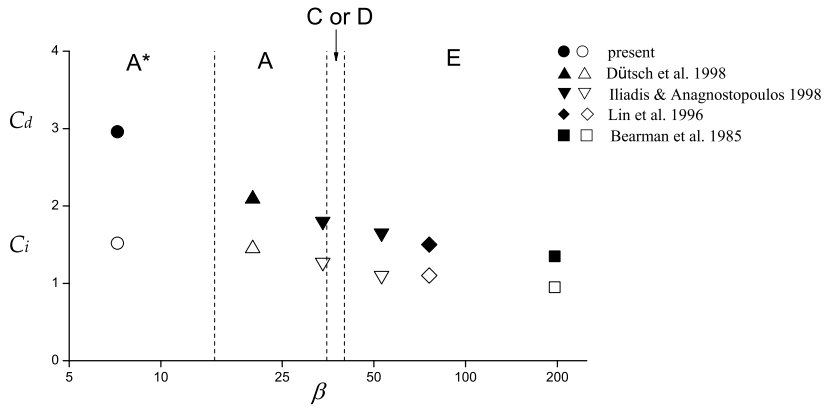

Figure 2.16: C_d and C_i of the present measurement at $KC = 4.85$ and $\beta = 7.2$ compared with other works in literature at $KC = 5$ and $\beta = 20 - 196$. Dark symbols are C_d and white ones are C_i. Flow regimes proposed by Tatsuno and Bearman (1990) are marked along β.

field shows bulk acceleration in the opposite direction of the force, and the velocity field indicates the initiation of the viscous boundary layer roll-up after the cylinder reverses direction, which later forms vortex pairs.

2.6 Summary and Conclusions

The N-pulse particle image velocimeter-accelerometer is intended to establish a new generation of PIVA instruments by increasing the velocity dynamic range, improving the spatial resolution and adding the capability to measure instantaneous acceleration fields. These improvements are accomplished by adding one or two additional light pulses to extract information sufficient to construct an estimate of the fluid trajectory over a short time. As in Liu and Katz (2006) and Lynch and Scarano (2014), small groups of particles are tracked by cross-correlation. The tracking procedure employs iterative image deformation and a predictor-corrector interrogation scheme to enhance detectability of the cross-correlation peaks.

The feasibility of employing the planar 3- or 4-pulse PIVA method in an unsteady flow-structure interaction experiment has been demonstrated, and the results are encouraging. The experiment concerned a horizontally driven cylinder supported in liquid by elastic rods. The cylinder interacted strongly with the surrounding fluid. In addition to the driving frequency and the eddy shedding frequency, the flexibility of the support rods introduced a third, pendulum frequency. The cylinder's motion and the velocity and acceleration fields of the fluid motion are measured after isolating their respective images by segmentation. Velocity and acceleration near to the wall of the moving cylinder are resolved well by means of a special treatment employing image transformation, a method considered to be more adaptable to various boundary geometries than previously reported procedures. Comparisons of the rms and mean bias of the instantaneous fields obtained by the different methods of analysis indicate that the 3-pulse analysis and 4-pulse analysis with least squares produce less random error than 4-pulse analysis with interpolation at the cost of larger mean bias. The choice between 3- and 4-pulse systems is a trade-off between performance, cost and flexibility. It is worth noting that 3D measurements such as tomographic PIV/PTV, 3D PTV eliminate the problem of out-of-plane motion. Removing this restriction should make the 3-pulse method more amenable to challenging 3D measurements.

Phase-averaged velocity and acceleration fields are calculated, highlighting the processes occurring in the oscillating flow. The formation of a pair of attached counter-rotating vortices, the stagnation point after the cylinder reverses direction, and the canceling of the vortex pair by the newly-formed boundary layer are clearly resolved.

Measuring the force on the moving cylinder has been conducted with considerable success using 4-P PIVA data and a control volume approach. The behaviors of each force term are studied. It is shown that the contribution of the momentum flux on the

exterior control surface is small compared to the volume term and the stress term, and the amplitudes of the latter two vary monotonically with increasing control volume size. The decrease in SNR implies that it is disadvantageous to set up an exterior control surface in the very remote region of the cylinder. The drag and added mass coefficients, C_d and C_i, are measured to be 2.96 and 1.52, respectively. They are compared to measurements and simulations in the literatures at $KC = 5$ and $\beta = 20 - 196$, showing reasonable continuations of the increasing trends for C_d and C_i.

A movie integrating simultaneous measurements of fluid motion, cylinder motion, and fluid force is presented as supplementary material.

The current work successfully demonstrates 3-pulse and 4-pulse PIVA has the potential to be a successful and highly informative tool for simultaneous velocity, acceleration and force measurements in fluid-structure interaction experiments.

Acknowledgement

The assistance by Mr. Ali Moradi in setting up the step motor and the cylinder pendulum is sincerely acknowledged. The authors would also like to acknowledge the support of Dr. Paisan Atsavapranee (Navy) and Dr. Ron Joslin (ONR). This project is funded by ONR under Phase II STTR contract N00014-14-C-0095 through Spectral Energies LLC.

Chapter 3

HIGH-ACCURACY CAMERA REGISTRATION FOR MULTI-CAMERA PLANAR N-PULSE PIVA[3]

ABSTRACT

N-pulse particle image velocimetry-accelerometry (PIVA) is a new-generation PIV developed to improve the performance of current 2-pulse PIV systems. Its applications to high-speed flows require high-accuracy registration of multiple cameras viewing the same object space. Five registration methods are described in this work, including two global methods, one local method and two advanced ones combining the global and local procedures. Numerical test with synthetic particle images and experimentally extracted disparity fields demonstrates the two advanced methods are capable to reduce the mean residual disparity down to 0.001 pixel, which is substantially lower than the residuals reported in the literature. We also discussed the mechanism of the residual disparity for different registration methods by comparing their topologies. In addition, a sensitivity study of the rms residual shows superior performances of the two advanced methods subjected to increasing noise level. Experimentally, a 3-pulse PIVA measurement of an impinging air jet was conducted to validate the proposed registration procedures. We calculated the mean centerline acceleration and the divergence of the acceleration estimate, both of which imply significant improvement in measurement quality after correcting the registration error. This work opens a way to employing multiple cameras

[3]This chapter is reformatted from a manuscript prepared for publication in Measurement Science and Technology.

for N-pulse PIVA to accurately measure velocity, acceleration and pressure of high-speed flows.

Keywords: camera registration, N-pulse PIVA, multi-camera PIVA, acceleration, impinging jet, high-speed flow

3.1 Introduction

N-pulse PIVA extends the conventional 2-pulse PIV by employing bursts of N pulses ($N >= 3$), aiming at improving the performance of PIV systems (Westerweel *et al.*, 2013; Ding and Adrian, 2016, 2017). The superior capability of N-pulse systems, including time-resolved systems, as a tool for enhancing measurement accuracy, measuring higher-order quantities (acceleration, force, etc.) and understanding complex flow phenomena has been demonstrated by many researchers (Schanz *et al.*, 2016; Lynch and Scarano, 2014; Unal *et al.*, 1997; La Porta *et al.*, 2001, among others).The implementation of multiple pulsing relies on high-frame-rate cameras and high-repetition-rate light sources (lasers or LEDs). One way to achieve a very short time delay (~10 μs) between successive light pulses is to combine multiple independently triggered Nd:YAG lasers by beam-combing optics. If one carefully aligns the optics, the spatial overlap between the beams is typically around 95% (Murphy and Adrian, 2010). This translates to about 5% loss-of-pairs in correlation analysis or particle tracking, which is well acceptable in terms of the valid detection probability given sufficient seeding density (Keane and Adrian, 1990). A single CW laser or Nd:YLF laser is an alternative option, but the recorded images usually suffer from high noise level due to streaky particle images (CW laser) or insufficient pulse energy (Nd:YLF laser).

On the other hand, it is relatively difficult to achieve a very short interframe time for an N-pulse imaging system. One option is to use a single high-speed video camera with the advantage of easy setup. But the low frame rate often limits its applications towards high speed flows. Currently, high-speed cameras available on the market can typically frame up to 20 kHz at one-megapixel format, corresponding to flow velocities in the order of 5 m/s if the maximum displacement is restricted to be under 0.2 mm. Faster flows require the sacrifice in format (i.e. reduced pixel resolution) or continuous time resolution if dual-frame PIV cameras are used to record images. A better option to achieve both image format and continuous time resolution is to combine multiple cameras viewing the same field of view. This can be realized by a beam-splitting camera with multiple imaging channels (Ding, 2014; Murphy and Adrian, 2010) or multiple high-speed video cameras/PIV cameras with external beam splitters and polarizers (Christensen and Adrian, 2002; Liu and Katz, 2006). In these multi-camera setups, registration is a critical step to align images from different cameras that belong to the same object space. Unsuccessful registration results in systematic error in PIV cross-correlation analysis, which could significantly affect the accuracy of velocity and especially acceleration. In a previous work by the author (Ding, 2014), a residual registration error of 0.02 pixel, which is usually acceptable for velocity, led to an acceleration error of 1,500 m/s^2, compared to the full scale acceleration 20,000 m/s^2 of the flow.

Different procedures and accuracies for registering cameras have been reported in the literature. Mechanical registration typically yields the residual misalignment between two cameras in the order of 1 pixel (Bian *et al.*, 2010; Christensen and Adrian, 2002). Self-calibration is considered to be a registration procedure for stereo-PIV (SPIV) and tomographic PIV (TPIV) in the sense that it refines the mapping function to have the images from the same particle back-projected to a common point in the measurement

plane (SPIV)/volume (TPIV). The outcomes of self-calibration are the elimination of systematic error due to misalignment between the light sheet and the calibration target for SPIV (Wieneke, 2005) and the enhancement of reconstruction quality for TPIV (Wieneke, 2008). The residual disparity reported by Wieneke (2005, 2008) for self-calibration is in the order of 0.1 pixel. As a matter of fact, reliable acceleration/pressure measurements from PIV data require the residual registration error to be in the order of 0.01 pixel or even lower. In this regard, Liu and Katz (2006) proposed a local deformation method to align vectors measured from different cameras, and their test with synthetic images showed the method was able to reduce the registration residual down to 0.01 pixel. However, this method did not address the problem of correcting the registration error when PIV cross-correlation is performed across cameras, which is necessary for many advanced interrogation algorithms (Hain and Kähler, 2007; Sciacchitano *et al.*, 2012; Lynch and Scarano, 2013, among others).

In this work, we aim to further improve the accuracy of registration towards 0.001-pixel residual. The proposed procedures apply to the scenario when cross-correlation is performed across cameras in a planar N-pulse PIVA system. Section 3.2 will discuss two possible camera configurations in an N-pulse system and compare their advantages and disadvantages. Several registration methods will be described in Section 3.3, and their performances are assessed using synthetic images in Section 3.4. A 3-pulse PIVA experiment measuring the mean acceleration field of an impinging air jet is used to validate the registration methods, and the results and discussions will be presented in Section 3.5.

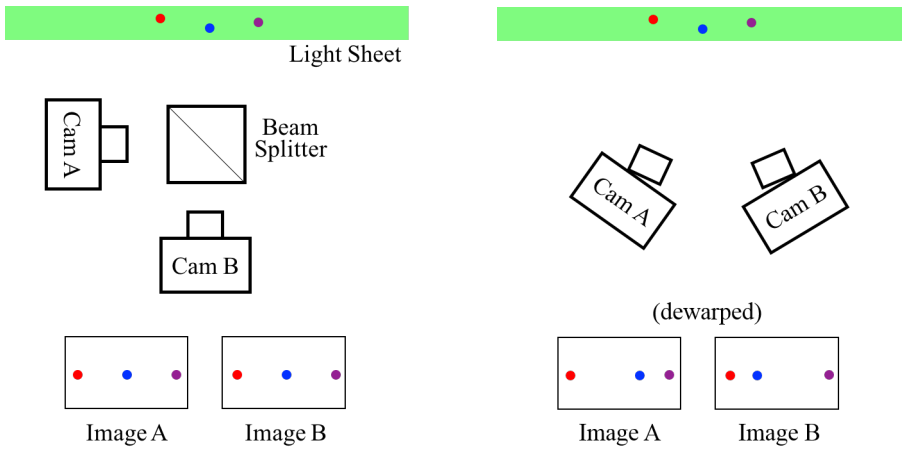

(a) Collinear configuration (b) Angular configuration

Figure 3.1: Schematics of camera configurations and corresponding recorded/dewarped images. In each case, only two cameras are displayed to illustrate a multi-camera system for simplicity.

3.2 Camera Configuration

To have the multiple cameras in a N-pulse imaging system view the same object space, it is necessary to consider special optical arrangements and camera configurations. Figure 3.1 illustrates two possible ways to set up the cameras. The collinear configuration in Figure 3.1(a) features all cameras viewing the flow perpendicularly by means of one or more beam splitters (and mirrors). If one carefully aligns the cameras and the optics, the magnifications are nearly identical for all cameras and uniform over the field of view. Particle images captured by different cameras at the same time are also nearly identical. Any small systematic discrepancy that indicates the residual misalignment can be corrected by the methods described later in this paper. Thus, images acquired with this collinear configuration are well suitable for cross-correlation and particle tracking analyses across cameras. Examples of the collinear configuration include Murphy and Adrian (2010); Christensen and Adrian (2002); Liu and Katz (2006) among others. The

drawback of this configuration may be the increasing complexity in aligning multiple cameras and optics with increasing number of pulses. Another issue may be that the collinear configuration does not allow a correction of magnification error arising from the misalignment between the calibration target and the mid-plane of light sheet. However, this issue can be compensated by employing an additional camera at a different angle following Discetti and Adrian (2012).

In contrast, the angular configuration, depicted in Figure 3.1(b), avoids the tedious optical alignment by arranging all cameras looking directly into the flow. The different viewing angles of the cameras allow accurate determination of the warping relation from the light sheet mid-plane to each camera by self-calibration (Wieneke, 2005). For this configuration, cross-correlation or particle tracking analysis is performed for images dewarped back to the object space. However, the real trouble in analyzing the dewarped images is the perspectives resulting in weakly correlated particle images. This is graphically explained in Figure 3.1(b) where the dewarped images of camera A and B exhibit different particle patterns at the same time due to their different perspectives. As a result, the correlation signal between image A and B becomes smeared out or completely indistinguishable with an increasing angle between the cameras or increasing light sheet thickness. Thereby, the angular configuration may be applicable only when the flow is strongly 2-D so that a very thin light sheet (<0.5 mm) can be used to illuminate the particles. In the following sections, we will discuss the registration methods in the context of the collinear configuration.

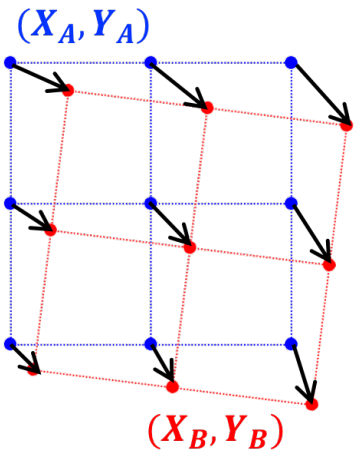

Figure 3.2: Disparity vectors characterizing the disparity field from camera A to B.

3.3 Registration Methods

The first step is to obtain the disparity field characterizing the camera misalignment. As illustrated in Figure 3.2, grids (X_A, Y_A) and (X_B, Y_B) on camera A and B respectively correspond to the same grid (x, y) defined in the object space. Due to the presence of registration error, (X_A, Y_A) and (X_B, Y_B) do not possess the same spatial location of respective cameras. Here, we define the vectors connecting corresponding grid points to be the disparity vector field. Note a disparity field is defined with directional information.

There are two common ways to obtain a disparity field. The first one is to explicitly measure disparity vectors by correlating particle images recorded on different cameras at the same time, while the second way is by imaging a calibration target inserted in the test section. For the image dewarping method introduced later in this section, the information obtained from the calibration target is used to dewarp particle images back to the object space. This means the latter method implicitly reveals the disparity fields from the warping functions. In addition, the latter method is presumably less accurate

than the first one with a degree depending on the adopted warping function model, quality of the calibration target, etc. However, it may become useful when acquiring a large number of densely seeded particle images is not feasible for some experiments, e.g. shock tube measurements.

3.3.1 Global Fitting (GF) Method

Suppose P+1 cameras are employed in an N-pulse imaging system and denoted by indices 0, 1, ..., P; An object grid (x, y) corresponds to an image grid (X_i, Y_i) for the i-th camera where $i = 0, 1, ..., P$. The global fitting method then follows these steps:

(a) **Select a reference camera using which to determine the magnification/mapping relation.** Without loss of generality, camera 0 is set to be the reference for later discussions. In practice, the camera with the least number of optics in its imaging path can be used as the reference as it presumably has the smallest distortion.

(b) **Obtain disparity fields $\boldsymbol{d}_{0i}$, $i = 1, 2, ..., P$.** Here, the subscript '$0i$' indicates the direction of the disparity fields, i.e. from the reference camera to others. Disparity fields are measured by correlating simultaneously recorded particle images and ensemble averaging the correlation maps (Meinhart *et al.*, 2000) for fast convergence.

(c) **Fit transformation functions $\mathcal{G}_{0i}$, $i = 1, 2, ..., P$.** $\mathcal{G}_{0i}$ adopts a form with reciprocal terms:

$$(X_i, Y_i) = \mathcal{G}_{0i}(X_0, Y_0) = \frac{\boldsymbol{a}_{1,i}}{X_0^2} + \frac{\boldsymbol{a}_{2,i}}{X_0 Y_0} + \frac{\boldsymbol{a}_{3,i}}{Y_0^2} + \frac{\boldsymbol{a}_{4,i}}{X_0} + \frac{\boldsymbol{a}_{5,i}}{Y_0} + \boldsymbol{a}_{6,i} + \boldsymbol{a}_{7,i} X_0 + \boldsymbol{a}_{8,i} Y_0 + \boldsymbol{a}_{9,i} X_0^2 + \boldsymbol{a}_{10,i} X_0 Y_0 + \boldsymbol{a}_{11,i} Y_0^2 \tag{3.1}$$

which has proved to perform superiorly based on our test compared to a polynomial model. Coincidentally, a similar transformation that involves negative exponents

is often implemented by the image processing community for image registration (Brown, 1992).

(d) **Transform the flow images recorded on camera** $1,2,...,P$**.** Pixel intensities are interpolated with proper interpolation schemes (Astarita and Cardone, 2005) onto a grid calculated using $\mathscr{G}_{0i}$. In this way, camera $1,2,...,P$ are registered with respect to camera 0.

(e) **Perform PIVA or PTVA analysis** with transformed images in the image space, and calculate the quantities in the object space using the magnification/mapping relation determined for camera 0.

3.3.2 Image Dewarping (ID) Method

With this method, cameras are registered during the process of image dewarping. The warping function for each camera is first determined by inserting a calibration target into the test section. We adopted in this work the pinhole camera model (Tsai, 1987) for the warping function. PIVA or PTVA analysis is then carried out with dewarped flow images in the object space. As discussed earlier, the performance of this method depends on the warping function model, quality of the calibration target , etc.

3.3.3 Local Correction (LC) Method

The GF and ID methods globally register the images before cross-correlation or particle tracking . In contrast, this third method corrects the registration error locally for a measured displacement vector. As illustrated in Figure 3.3, for a camera pair A and B, a particle (or a small group of particles) at $\boldsymbol{x}_A$ on camera A moves to $\boldsymbol{x}_B$ on camera B

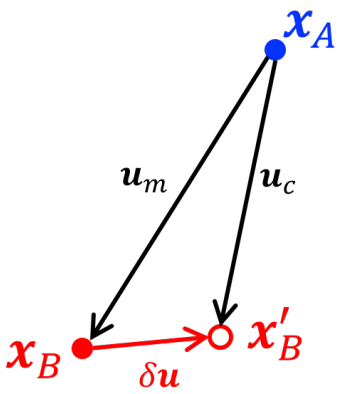

Figure 3.3: A local correction $\delta \boldsymbol{u}$ applied to a measured displacement vector $\boldsymbol{u}_m$ from camera A to B.

during two successive pulses. If there exists misalignment between A and B, it would embed into the measured displacement vector, $\boldsymbol{u}_m = \boldsymbol{x}_B - \boldsymbol{x}_A$. With the knowledge of the disparity field, a correction vector $\delta \boldsymbol{u}$ is possible to calculate. It is preferable to use the *inverse* disparity field $\boldsymbol{d}_{BA}$, which is in the direction opposite to that of the displacement measurement, to interpolate at $\boldsymbol{x}_B$ for $\delta \boldsymbol{u}$. The benefit of doing so is the interpolation can be performed with gridded data for high accuracy and reduced computational cost. If disparity field $\boldsymbol{d}_{AB}$ is used otherwise, one needs to perform scattered data interpolation that may be less reliable. Note $\boldsymbol{d}_{AB}$ and $\boldsymbol{d}_{BA}$ in fact represent the same disparity information but are sampled on different grids with opposite directions, making it nontrivial to optimize the cross-correlation analysis for determining the disparity field. Consequently, the corrected displacement vector is obtained as $\boldsymbol{u}_c = \boldsymbol{u}_m + \delta \boldsymbol{u}$.

3.3.4 Global Fitting/Local Correction (GF/LC) Method

For the GF method, because we empirically choose a model for $\mathscr{G}_{0i}$ to transform images, it is always expected to have some residual disparity $\boldsymbol{d}'$ after transformation. $\boldsymbol{d}'$

may still be detrimental with a degree depending on the initial disparity and adopted transformation function. To further enhance the registration accuracy, the LC method can be combined with the GF method to correct $\boldsymbol{d}'$, which is implemented as follows. After step (c) of the GF procedure, the simultaneously recorded images are transformed using $\boldsymbol{\mathcal{G}}_{0i}$ and cross-correlated to calculate $\boldsymbol{d}'$. Displacement vectors measured with the transformed flow images are then corrected for the residual disparity $\boldsymbol{d}'$ using the LC method.

3.3.5 Image Dewarping/Local Correction (ID/LC) Method

Likewise, the $\boldsymbol{d}'$ after image dewarping can be corrected by the LC method too. The implementation is also similar – determine $\boldsymbol{d}'$ by correlating the simultaneously recorded images after dewarping. Displacement vectors measured with the dewarped flow images are then corrected for the residual disparity $\boldsymbol{d}'$ using the LC method.

3.4 Synthetic Image Test

We assessed the performances of the registration methods by simulations using synthetic particle images. The particle images have a mean diameter of $d_\tau = 3$ pix. The seeding density was set to be 20 particles per 32-by-32-pixel window, corresponding to approximately 0.02 *ppp* (particle per pixel). The particle physical diameter d_p follows a log-normal distribution with $\mu_{d_p} = 1$ and $\sigma_{d_p} = 0.2$ (arbitrary unit) to allow nonuniform particle image intensities ($\propto d_p^2$). These images were generated in pairs with predefined flow fields and distorted based on realistic disparity fields. We tested three flows given by the following displacement fields:

(1) Stagnation flow (FF1): $u = \lambda(x_p - l_x/2)$; $v = \lambda(l_y - y_p)$ with $\lambda = 3/160$;

(2) Sinusoidal flow (FF2): $u = u_{max}\sin(4\pi y_p/l_y)$ with $u_{max} = 12$ pix; $v = 0$;

(3) Vortex (FF3): $u_\theta = \dfrac{r}{b}e^{-\frac{r}{a}}$ with $r = \sqrt{x_p^2 + y_p^2}$, $a = 256$ pix and $b = 8$ pix;

wherein $l_x = 960$ pix and $l_y = 640$ pix are the linear dimensions of the field of view. All relevant variables are in pixel units. Two disparity fields, referred to as 'DF1' and 'DF2', were extracted from the experimental data of a beam-splitting camera (see Figure 3.7 in Section 3.5) and used to distort the image pairs. For each flow field and disparity field, 250 image pairs were analyzed with an in-house PIV code combined with the proposed registration methods. In order to test the local correction, 500 pairs of simultaneously recorded images (i.e. identical image pairs) were distorted and analyzed to determine the inverse (residual) disparity fields for the LC, GF/LC and ID/LC methods. We compared the resulting displacement fields to the PIV results from 250 undistorted image pairs, intended to eliminate the systematic error associated with the PIV algorithm and study merely the residual disparities.

Table 3.1 lists the statistics of the residual disparity in the x-direction for each flow field and disparity field (the results in the y-direction are very similar). The residual disparity field, $\boldsymbol{d}''$, is defined to be the differential of the displacement vectors resulting from the distorted and undistorted image pairs, respectively. We calculated the $\mu_{|d_x''|}$ in Table 3.1 by first averaging over the 250 image pairs to obtain $\overline{d_x''}$ and then over the field of view using $\left|\overline{d_x''}\right|$, i.e.

$$\mu_{|d_x''|} = \underset{FOV}{\text{avg}} \left|\overline{d_x''}\right| = \underset{FOV}{\text{avg}} \left|\frac{1}{250}\sum_{k=1}^{250} d_{x,k}''\right| \tag{3.2}$$

Likewise, the field root-mean-square (rms) $\sigma_{d_x''}^{\text{FOV}}$ is computed as

$$\sigma_{d_x''}^{\text{FOV}} = \underset{FOV}{\text{rms}} \left(\frac{1}{250}\sum_{k=1}^{250} d_{x,k}''\right) \tag{3.3}$$

whereas the ensemble rms $\sigma^{\mathrm{ENS}}_{d''_x}$ is given by

$$\sigma^{\mathrm{ENS}}_{d''_x} = \operatorname*{avg}_{FOV} \left[\frac{1}{249} \sum_{k=1}^{250} \left(d''_{x,k} - \overline{d''_x} \right)^2 \right]^{-\frac{1}{2}} \tag{3.4}$$

to show the spread associated with the randomness in particle distribution. Clearly, the two advanced methods (GF/LC, ID/LC) yield the lowest residual disparity with $\mu_{|d''_x|}$ and $\sigma^{\mathrm{FOV}}_{d''_x}$ in the order of 0.001 pixel. The $\mu_{|d''_x|}$ and $\sigma^{\mathrm{FOV}}_{d''_x}$ for the GF and ID methods are approximately 0.01 pixel, whereas the performance of the LC method is slightly better with reduced $\mu_{|d''_x|}$ and $\sigma^{\mathrm{FOV}}_{d''_x}$. $\sigma^{\mathrm{ENS}}_{d''_x}$ is in the order of 0.01 pixel and very similar for all registration methods, implying the random particle distribution predominantly causes the data spread.

	GF			LC			ID		
	$\mu_{\lvert d''_x\rvert}$ ($\times 10^{-2}$pix)	$\sigma^{\mathrm{FOV}}_{d''_x}$ ($\times 10^{-2}$pix)	$\sigma^{\mathrm{ENS}}_{d''_x}$ ($\times 10^{-2}$pix)	$\mu_{\lvert d''_x\rvert}$ ($\times 10^{-2}$pix)	$\sigma^{\mathrm{FOV}}_{d''_x}$ ($\times 10^{-2}$pix)	$\sigma^{\mathrm{ENS}}_{d''_x}$ ($\times 10^{-2}$pix)	$\mu_{\lvert d''_x\rvert}$ ($\times 10^{-2}$pix)	$\sigma^{\mathrm{FOV}}_{d''_x}$ ($\times 10^{-2}$pix)	$\sigma^{\mathrm{ENS}}_{d''_x}$ ($\times 10^{-2}$pix)
FF1/DF1	1.058	1.290	0.787	0.591	0.732	0.758	0.872	1.056	0.786
FF2/DF1	1.063	1.295	1.708	0.605	0.726	1.680	0.878	1.066	1.708
FF3/DF1	1.067	1.298	0.869	0.522	0.608	0.838	0.875	1.067	0.869
FF1/DF2	0.982	1.159	0.790	0.595	0.734	0.760	1.182	1.281	0.790
FF2/DF2	1.010	1.197	2.398	0.599	0.702	2.372	1.206	1.325	2.398
FF3/DF2	0.986	1.163	0.877	0.513	0.595	0.841	1.188	1.301	0.877

	GF/LC			ID/LC		
	$\mu_{\lvert d''_x\rvert}$ ($\times 10^{-2}$pix)	$\sigma^{\mathrm{FOV}}_{d''_x}$ ($\times 10^{-2}$pix)	$\sigma^{\mathrm{ENS}}_{d''_x}$ ($\times 10^{-2}$pix)	$\mu_{\lvert d''_x\rvert}$ ($\times 10^{-2}$pix)	$\sigma^{\mathrm{FOV}}_{d''_x}$ ($\times 10^{-2}$pix)	$\sigma^{\mathrm{ENS}}_{d''_x}$ ($\times 10^{-2}$pix)
FF1/DF1	0.083	0.105	0.787	0.079	0.099	0.786
FF2/DF1	0.144	0.179	1.708	0.141	0.175	1.708
FF3/DF1	0.084	0.105	0.869	0.081	0.102	0.869
FF1/DF2	0.078	0.098	0.790	0.079	0.098	0.790
FF2/DF2	0.198	0.248	2.398	0.197	0.248	2.398
FF3/DF2	0.083	0.104	0.877	0.083	0.103	0.877

Table 3.1: Statistics of the residual disparity $\boldsymbol{d}''$, given in Equation (3.2) – (3.4), for different registration methods, flow fields and disparity fields.

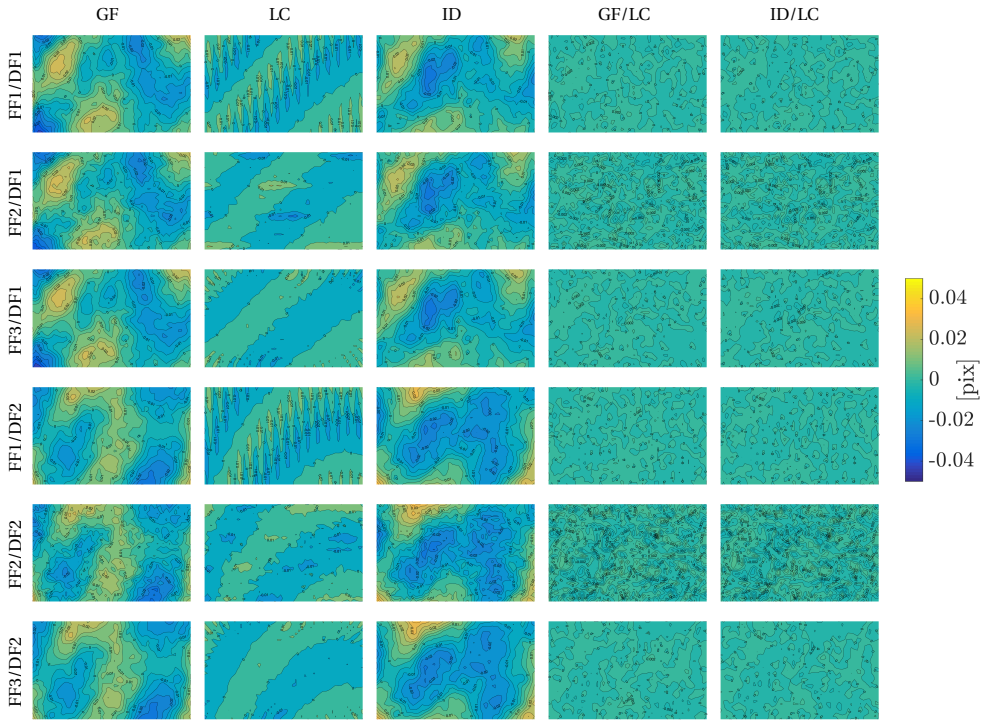

Figure 3.4: Contours of mean residual disparity $\overline{d''_x}$.

To thoroughly understand the mechanism of the residual disparity $\boldsymbol{d''}$, we examined and compared the topologies of $\overline{d''_x}$ for different flow fields and disparity fields using their contour plots presented in Figure 3.4. It is evident that the $\overline{d''_x}$ of GF and ID are dependent on the tested disparity fields and registration methods, but nearly independent of the flow fields. Thereby, it indicates the incapability of the transformation/warping function to fully represent the disparity field is responsible for the residual. On the other hand, the $\overline{d''_x}$ of the LC method exhibit a correlation with the flow field, but do not alter much for the two disparity fields. Possibly, the systematic error of the local interpolation scheme (cubic-spline interpolation was implemented in this work) varying as a function of the sub-pixel displacement contributes to most of the residual disparity. For the two advanced methods, the overall magnitude significantly decreases. The topologies are

mostly flow-dependent, which is consistent with the observation from the LC method as they both apply LC in the final step.

Furthermore, we studied the sensitivity of $\boldsymbol{d}''$ subjected to random noise present in measuring the initial disparity field. Five noise levels ranging from 0.1% to 10% of the maximum disparity magnitude (about 2.5 pix in the simulation) were tested. For each noise level, 100 Gaussian random noise fields were generated. For the GF and ID method, the noise fields were added to the disparity vectors/calibration target images before fitting the transformation/warping function; For the LC method, the noise fields were added to the inverse disparity field. Note that the image pairs should still be distorted using the exact disparity fields (DF1 or DF2). Figure 3.5 shows the rms residual of different registration methods against increasing noise level. The rms's were calculated over the 100 independent noise fields followed by averaging over the field of view. Clearly, the LC method is the most sensitive to noise as the noise propagates into the local

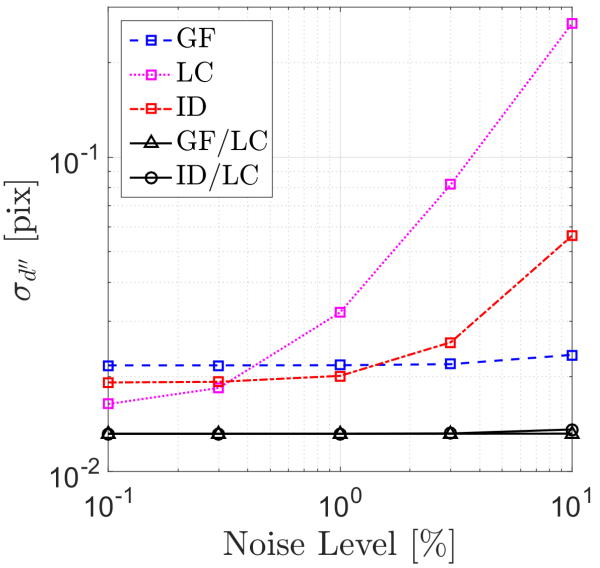

Figure 3.5: Residual disparity rms subjected to increasing noise level.

correction vector ($\delta \boldsymbol{u}$) without a suppressing mechanism. In contrast, the GF and ID methods are able to alleviate the impact of noise as the transformation/warping function is determined using analytical models in the least square sense. The best performance is achieved by the two advanced methods, of which the curves stay low and flat for a wide range of noise level. It is interpreted that the GF and ID procedures correct majority of the disparity, and the LC further refines the correction. As the LC only deals with the residual arising from the GF or ID method, the resulting rms residual exhibits nearly no dependence on the noise level.

3.5 Experimental Validation

A 3-pulse PIVA experiment measuring the acceleration of an impinging air jet was conducted to validate the registration methods. Figure 3.6 shows the schematic of the experimental setup. This is an 8-pulse PIVA system with eight independently triggered Nd:YAG lasers (Quantel) and a beam splitting camera (HSFC-Pro) having four imaging channels, each of which is equipped with a CCD sensor capable of running in a PIV dual-frame mode. Three lasers were collinearly aligned by the beam combining optics to illuminate the center plane of the jet. Imaging channels C1, C2 and C3 were used to record three successive frames separately with an interframe time 30 μs. Their disparity fields, obtained by correlating 2,000 simultaneously recorded image pairs, are presented in Figure 3.7. The maximum disparity is approximately 2.5 pixels for both CCD pairs. As to the test section, the jet exited at a velocity U_J = 22.5 m/s from the nozzle with a diameter D = 21.59 mm. An impinging plate was placed at $H = 4D$ below the nozzle. The region of interest for our measurement was $3D$(w)$\times 2D$(h) above the plate.

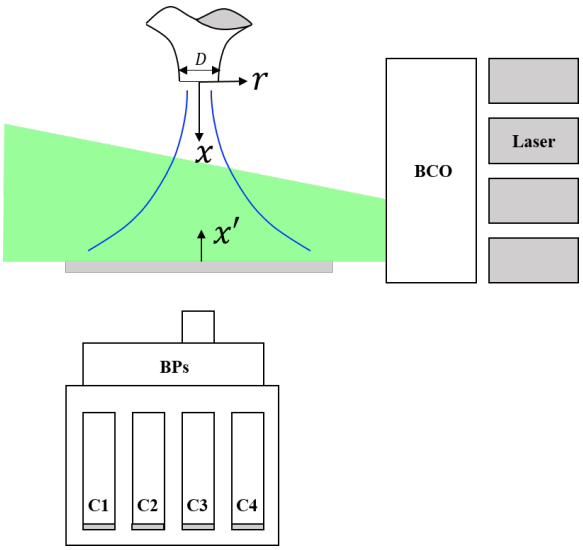

Figure 3.6: Schematic of the experimental setup. C1 - C4: Imaging channels 1-4; BPs: Beam splitters; BCO: Beam combining optics.

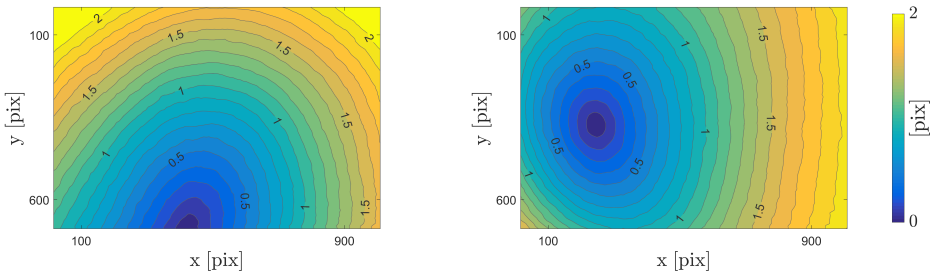

Figure 3.7: Disparity fields (magnitude) from C3 to C1 (*left*) and from C3 to C2 (*right*).

PIV images recorded by three fast frames were analyzed by an in-house PIV code featuring image deformation algorithm (Scarano, 2001), yielding displacement vectors with 3.2 mm×3.2 mm final interrogation spot and 1.6 mm vector spacing. The registration methods described in Section 3.3 were implemented to correct the registration errors. For the GF method, we chose C3 to be the reference camera as images were formed straight on C3 without reflection. For the ID method, a calibration target plate (TSI) with 20 mm dot spacing was placed in the test section to calculate the warping function for

each CCD. The residual disparity $\boldsymbol{d}'$ after transformation of the GF method has an rms of approximately 0.02 pixel, whereas that of the ID method is an order of magnitude larger, indicating the high uncertainty level of the ID method in determining the initial disparity. The material acceleration was then estimated by a 3-pulse estimator,

$$\hat{\boldsymbol{a}}_{3p} = \frac{4}{\Delta t^2}\left(\Delta \boldsymbol{x}_{23} + \Delta \boldsymbol{x}_{21}\right) \tag{3.5}$$

wherein $\Delta \boldsymbol{x}_{ij}$ denotes the displacement measured by cross-correlation from frame i to j; $\Delta t = 60\ \mu$s is the total time delay from the first to the third frame. Herein, the interrogation strategy of starting from the center frame benefits the data analysis in several aspects as discussed in Ding and Adrian (2016). As seen from Equation (3.5), the residual disparity $\boldsymbol{d}''$ embeds in the displacements and thus propagates into the acceleration measurement. Thereby, we can assess the performances of the registration methods by comparing the acceleration results.

We first looked at the mean centerline acceleration averaged over 2,000 flow fields. As the jet is statistically stationary, the mean centerline material acceleration only has contribution from the convective part. Thereby, it can be calculated by velocity u_x measured from 2-pulse PIV of frame 2 and 3:

$$\left\langle \hat{a}_{x,2p} \right\rangle_{cl} = \left\langle u_x \frac{\partial u_x}{\partial x} \right\rangle_{cl} = \frac{1}{2}\frac{\partial \langle u_x^2 \rangle_{cl}}{\partial x} \tag{3.6}$$

wherein positive x is along the mean flow direction. We evaluated the derivative by fitting a 9^{th} order polynomial to $\langle u_x^2 \rangle_{cl}$ and analytically differentiating the profile. The accuracy of the resulting acceleration profile was verified by comparing its magnitude to that obtained by finite differencing. To infer the residual disparity $\boldsymbol{d}''$ for different registration methods, we compared $\hat{\boldsymbol{a}}_{3p}$ at the centerline to $\langle \hat{a}_{x,2p} \rangle_{cl}$. The latter one was treated as the reference for two reasons: (1) As discussed in Ding and Adrian (2017),

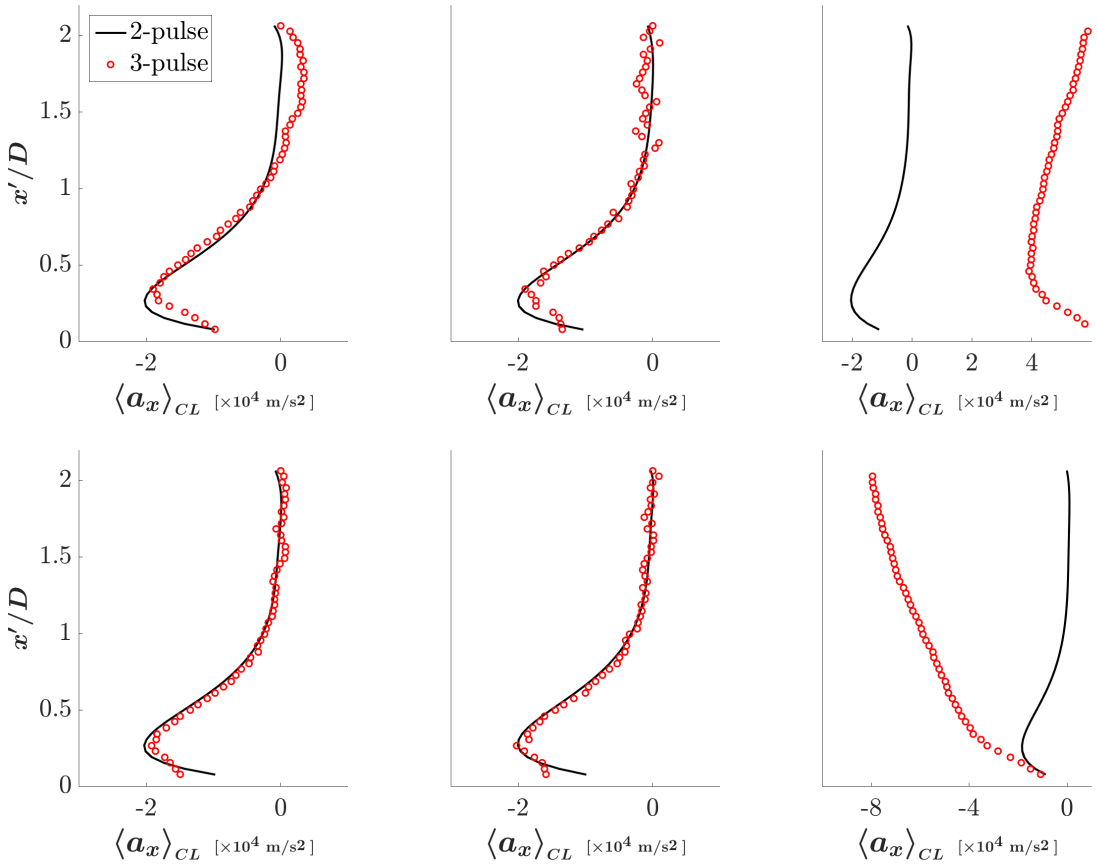

Figure 3.8: Comparisons of the mean centerline material acceleration obtained using 2-pulse PIV and 3-pulse PIA, given in Equation (3.6) and (3.5), respectively. Top left to right: GF, LC, ID; bottom left to right: GF/LC, ID/LC, no correction.

velocity is considerably less sensitive to the noise in displacement measurement; thus the influence of $\boldsymbol{d}''$ to velocities is almost negligible; (2) The noise was further suppressed by polynomial fitting.

Figure 3.8 presents comparisons of the mean centerline material acceleration obtained by the 2-pulse and the 3-pulse methods, respectively. For approximately x'/D>1.5 (x' is upward from the plate) where the flow velocity is constant, the 3-pulse estimator should yield identically zero acceleration if $\boldsymbol{d}'' = 0$ for both $\Delta\boldsymbol{x}_{21}$ and $\Delta\boldsymbol{x}_{23}$. In other words, non-zero $\hat{\boldsymbol{a}}_{3p}$ in this region indicates the residual disparity $\boldsymbol{d}''$ arising from the

registration method. (The chance of the $\boldsymbol{d}''$s for $\Delta\boldsymbol{x}_{21}$ and $\Delta\boldsymbol{x}_{23}$ cancel each other is quite rare.) Below $x'/D \approx 1.5$ where the flow starts decelerating, it is expected that deviations have contribution from $\boldsymbol{d}''$ as well as the systematic error of $\hat{\boldsymbol{a}}_{3p}$ with the magnitude depending on local flow acceleration (Ding and Adrian, 2017). It is evident from the comparisons that the GF/LC and ID/LC methods give the best match, i.e. the smallest residual disparity. The considerable near-wall discrepancies probably attribute to the limited spatial resolution of window-based PIV analysis. The acceleration estimate of the GF method is smooth but noticeably biased, while that of the LC method is noisy but the bias appears to be smaller. These observations are consistent with the mechanisms of the residual disparity we have discussed in Section 3.4. The significant bias of the ID method results from the large $\boldsymbol{d}'$ of the warping function. The comparisons imply substantial improvement over the case when no correction of registration error is performed, the result of which is also presented in Figure 3.8 for reference.

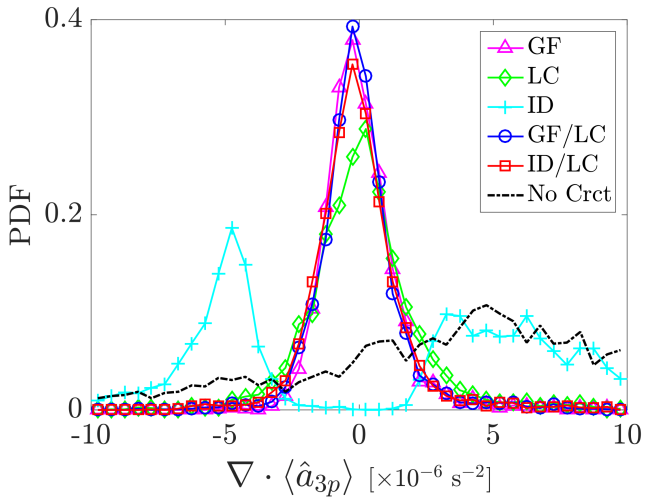

Figure 3.9: PDFs of the divergence of the 3-pulse acceleration estimate given in Equation (3.5).

In addition to the centerline acceleration, the statistics of the mean acceleration field is another indicator of the measurement quality. It can be shown from Equation (3.5) that the estimator $\hat{\boldsymbol{a}}_{3p}$ is solenoidal given $\boldsymbol{d}'' = 0$ for $\Delta\boldsymbol{x}_{21}$ and $\Delta\boldsymbol{x}_{23}$. (Note the acceleration itself is not solenoidal). Thereby, the probability density function (PDF) of $\nabla\cdot\langle\hat{\boldsymbol{a}}_{3p}\rangle$ should spread around zero, and the width of the PDF is associated with the spatial resolution and random noise level as well as the residual disparity $\boldsymbol{d}''$. In our measurement, the divergence of the mean acceleration can be computed completely using the in-plane components a_x and a_r, as the mean azimuthal acceleration is zero for an axisymmetric jet. The distributions of $\nabla\cdot\langle\hat{\boldsymbol{a}}_{3p}\rangle$ for different registration methods are plotted in Figure 3.9. We observe the PDFs of the GF/LC and ID/LC methods are more concentrated around zero compared to the LC and especially the ID methods, implying reduced $\boldsymbol{d}''$ by the two advanced methods. Interestingly, the GF method produces a comparable PDF to the two advanced methods, which means $\nabla\cdot\boldsymbol{d}''$ of the GF method is small relative to the spread due to limited measurement resolution and random noise. Again, the comparison to the PDF without correction indicates substantially enhanced measurement quality.

3.6 Summary

Accurate camera registration is critical to reliable N-pulse PIVA measurements employing multiple cameras. We have proposed and studied several registration methods in this work. The GF and ID methods globally transform or dewarp recorded images before PIV analysis, while the LC method calculates a local correction to each measured displacement vector. Two advanced methods, GF/LC and ID/LC, apply local correction to the residual disparity arising from the GF and ID procedures.

We assessed the performances of different registration methods using synthetic particle images distorted by experimentally extracted disparity fields. It was shown that the two advanced methods were able to reduce the mean disparity over the field of view down to 0.001 pixel, which is an order of magnitude lower than previously reported accuracies from the literature. The topologies of the residual disparity fields helped us understand their mechanisms, which in turn explained the rms residuals of GF/LC and ID/LC methods were nearly invariant for increasing noise in determining the initial disparity field.

The registration methods were experimentally validated by a 3-pulse PIVA measurement of an impinging air jet. The mean centerline acceleration was compared to the reference obtained by 2-pulse PIV to indicate the residual disparity. In addition, the divergence of the 3-pulse acceleration estimate was examined using the PDFs resulting from different registration methods. Both results showed substantial improvement in measurement quality by the registration procedures, and the best accuracy was achieved by GF/LC or ID/LC.

In summary, we successfully demonstrated two registration procedures (GF/LC and ID/LC) both with high accuracies. While the single-camera PIVA has to wait for future camera technology to reach a sufficiently high framing rate, the proposed registration methods enable accurate velocity, acceleration and force measurements with multi-camera N-pulse PIVA. It is also worth mentioning that, although our discussion is for planar PIVA systems, it is possible to apply similar procedures to registering multiple tomographic systems employed in N-pulse volumetric flow measurements (e.g. Lynch and Scarano, 2014; Novara *et al.*, 2016).

Chapter 4

IMPROVED N-PULSE PTVA ANALYSIS FOR PARTICLE DRAG HISTORY IN POST-SHOCK FLOWS[4]

ABSTRACT

An improved data analysis method for measuring post-shock particle drag in an 8-pulse particle tracking velocimetry-accelerometry (PTVA) experiment is described. We represent the particle drag history, $C_D(t)$, using a polynomial of order up to 3. A model for particle trajectory is then derived from the particle dynamics equation and fitted to measured particle positions to determine C_D. To assess and optimize the performance, we conducted PTVA simulations using the standard drag and an empirical drag correlation based on experimental data. The simulation results indicate a significant reduction in the rms error by the proposed method compared to two piecewise methods reported in the literature. We also find that for a realistic range of noise level the best performance in terms of the bias and random errors is achieved by lower order (quadratic or linear) $C_D(t)$ models. Potential optimizations include taking data in a low-rms-error interval in time and densely arranging the early pulses.. The experimental validation consists of the analyses of two datasets using the proposed method. We thoroughly discuss the measurement quality based on the conclusions from simulation. The noise level and the early pulse separate appear to be two important parameters for the overall accuracy. The resulting drag correlation is considerably higher than the standard drag, suggesting the necessity of a new model for unsteady drag correlation. In the end, we show the data

[4]This chapter is reformatted from a manuscript prepared for journal publication.

scattering is likely caused by the uncertainty of particle size, and propose a theoretical framework for accurate determination of drag correlation.

Keywords: N-pulse PTVA, uncertainty, particle drag, particle-shock physics, unsteady drag correlation, subcritical Mach number, particle sizing

4.1 Introduction

Particle response to shock passage has been extensively studied as a fundamentally important two-phase flow phenomenon. For a particle of mass m_p moving at velocity v_p, the governing equation of the particle dynamics, following Mei (1996), is given by

$$m_p \frac{dv_p}{dt} = F_{G-B} + F_{QS} + F_H + F_{AM} + F_{FS} + F_L \tag{4.1}$$

wherein F_{G-B} is the gravity minus the buoyance; F_{QS} is the quasi-steady force; F_H is the history term or the Basset force (Basset, 1888); F_{AM} is the added mass force; F_{FS} is the net force due to the variation of the fluid stress around the particle, which is essentially the pressure gradient in our analyses; and F_L is the lift force. Terms of interest during a particle-shock interaction are F_{QS}, F_H (viscous unsteady), and $F_{AM} + F_{FS}$ (inviscid unsteady). Since Stokes (1851) first analytically obtained the drag on a stationary sphere in an incompressible steady flow in the limit of zero Reynolds number, numerous experiments have been conducted to extend the result to finite Reynolds number up to 10^6. This led to the celebrated standard drag curve (see, e.g. Bailey, 1974) describing the quasi-steady drag coefficient of a particle as a function of the particle Reynold number,

$$Re_p = \frac{|u_f - v_p| d_p}{\nu_f} \tag{4.2}$$

wherein v_p, d_p, u_f and ν_f are the particle velocity, particle diameter, flow free-stream velocity and flow kinematic viscosity, respectively. Based on the standard drag curve,

various forms of empirical drag correlation (i.e. C_D vs. Re_p) have been fitted over a wide range of Re_p (Ingebo, 1956; Clift and Gauvin, 1970; Clift *et al.*, 1978), and Henderson (1976); Loth (2008); Parmar *et al.* (2010) extended the drag correlation to compressible flows. The added mass force arises from the fact that a particle moving through fluid at a varying velocity needs to accelerate or decelerate its surrounding fluid, resulting in an additional inviscid force. A generalized expression for the added mass force at finite Reynolds numbers was derived by Auton *et al.* (1988). The history term is associated with the retarded vorticity diffusion from the particle surface to the free-stream flow. Basset (1888) analyzed the unsteady creeping flow around a particle, and proposed to evaluate the history term with an integral kernel proportional to $t^{-1/2}$, which appeared in the famous BBO (Basset-Boussinesq-Oseen) equation and the Maxey-Riley equation (Maxey and Riley, 1983). Mei and Adrian (1992) extended the kernel to finite Reynolds numbers, and Parmar *et al.* (2011) developed a generalized BBO equation in which the history term as well as the added mass force was modified for compressible flows.

The interaction between a shock and a single particle can be considered in two regimes – the passage of the shock over the particle and the post-shock regime. During the shock passage, the particle gains a finite momentum in a typically short time scale, d_p/u_s, where u_s is the shock speed. (Based on this time scale, we can define a normalized time $\tau_s = tu_s/d_p$. Note the shock passes over the particle at $\tau_s = 1$.) The forces responsible for the impulsive increase of particle velocity when $\tau_s < 1$ are the quasi-steady force, the pressure gradient, and the unsteady forces ($F_{AM} + F_H$). Parmar *et al.* (2009) modeled all those forces but the Basset force and resolved a sharp peak in drag at approximately $\tau_s = 0.5$, agreeing with the experimental and numerical results by Sun *et al.* (2005); Skews *et al.* (2007). According to the breakdown of force terms, Parmar *et al.* (2009) attributed the sharp peak to the sudden change of pressure across the shock and the added mass force

adapted for compressible flows. In the post-shock regime ($\tau_s \gg 1$), the particle accelerates and approaches the post-shock flow velocity asymptotically. Numerous experiments measuring post-shock particle motions (Rudinger, 1970; Igra and Takayama, 1993; Suzuki *et al.*, 2005; Jourdan *et al.*, 2007; Wagner *et al.*, 2012) have observed elevated particle accelerations compared to that predicted by the standard drag, implying substantially enhanced particle drag. Compressibility and unsteadiness have been conventionally considered to be the two factors responsible for the elevation in drag. When the particle Mach number, defined with respect to the post-shock speed of sound c,

$$M_p = \frac{|u_f - v_p|}{c} \tag{4.3}$$

is below the critical Mach number ($M_{p,cr} \approx 0.6$), the flow surrounding the particle is fully subsonic and the compressibility effect is negligible. The unsteadiness of the particle, following Crowe *et al.* (1963), is characterized by a non-dimensional parameter A_c given by

$$A_c = \frac{\dot{v}_p d_p}{(u_f - v_p)^2} \tag{4.4}$$

When $A_c \ll 1$, the particle motion is usually considered to be steady or quasi-steady. For the compressibility effect, past investigations appear to have achieved a decent progress towards consistency. Some experiments isolating the compressibility effect (see Bailey and Starr, 1976; Jourdan *et al.*, 2007; Wagner *et al.*, 2012, in which A_c<0.01) reported drag correlations that are consistent under the framework of Parmar *et al.* (2009) for compressible quasi-steady drag. On the other hand, the studies of elevated drag due to the unsteadiness seem to have not reached further than experimental observations (Karanfilian and Kotas, 1978; Bordoloi *et al.*, 2017). The physical mechanism behind the elevation is still unclear, and there seems no current models or simulations able to predict it (Bordoloi *et al.*, 2017). The question of which unsteady force(s) (Basset, added mass or others) is/are responsible for the elevation needs to be answered.

Understanding the mechanism of elevated particle drag in post-shock flows remains challenging partially due to the fact that, while the elevation is experimentally evident, the data spread appears to be significant (see e.g. Figure 5 in Suzuki *et al.*, 2005, Figure 14 in Jourdan *et al.*, 2007, Figure 1 in Wagner *et al.*, 2012). Two primary reasons for the large spread are the high-noise-level nature of acceleration measurements (Christensen and Adrian, 2002; Ding and Adrian, 2017) and the uncertainty in the nominal particle diameter used in data analyses. From the noise reduction point of view, various noise filtering algorithms for PTVA were reported in the literature. Among others, Lüthi *et al.* (2005) solved an overdetermined linear system deduced from the first-order Taylor expansions of neighboring velocities for velocity spatial and temporal derivatives with reduced noise level, followed by weighted polynomial fit to further suppress noise. Mordant *et al.* (2004) employed a second-order Gaussian differentiating kernel to simultaneously filter out noise and calculate acceleration by convolving the kernel with particle position data. Voth *et al.* (2002) measured particle Lagrangian accelerations by piecewise parabolic fitting with the weight of each data point inversely proportional to the local error, thus reducing the noise propagating into acceleration estimates.

N-pulse PIVA/PTVA is a new-generation PIV developed to improve the performance of conventional 2-pulse PIV systems. Ding and Adrian (2017) theoretically showed the significant improvements in dynamic ranges by 4-pulse PTVA. An N-pulse system usually includes multiple independent pulsed lasers and cameras to provide sufficiently short inter-frame time for high-speed flows. Martinez *et al.* (2015); Bordoloi *et al.* (2017) employed an 8-pulse system in their shock tube facility measuring shock accelerated microparticles. While the 8-pulse system ensured the temporal resolution required by micron-sized particles, the limited number of particle positions raised the difficulty in their data analysis. In their early test, conventional polynomial fit to particle positions

yielded strong bias often leading to unphysical particle velocity and acceleration history. In order to thoroughly understand the particle-shock physics as our ultimate goal, we address in this work the first-order business – reliable measurement of particle drag history with an N-pulse system ($N \leq 8$). We focus on the data analysis and accuracy optimization for the experiments by Martinez *et al.* (2015); Bordoloi *et al.* (2017).

The subsequent sections are organized as the follows. The shock-tube facility and the 8-pulse data acquisition system is briefly outlined in Section 4.2. Section 4.3 describes in detail the novel curve fitting method, the performance of which is validated and assessed numerically in Section 4.4. The experimental results are presented in Section 4.5. The effect of particle size distribution on the data scattering is discussed in Section 4.6.

4.2 Experimental Setup and Data Acquisition

The details of the shock tube design and operation as well as the 8-pulse data acquisition system can be found in Martinez *et al.* (2015); Bordoloi *et al.* (2017). Some key aspects of the experimental setup are outlined here.

The experiment was conducted in a horizontal shock tube (HST) 6.5 m long with a cross-section 76.2 mm × 76.2 mm. Shock waves were generated by a diaphragmless pneumatic piston driver with high repeatability and full automation. Multiple pressure transducers were incorporated along the tube to measure the shock speed and to trigger the imaging system. Particles entered upstream and exited downstream the tube through a pipe loop driven by a low-speed fan. The seeding density was low enough to ensure no particle collisions and thus to enable us to study purely the single particle response in the post-shock flow.

The 8-pulse system consists of eight independently triggered Nd:YAG lasers and a 4-CCD high-speed framing camera. Each CCD is capable to run in a dual-frame PIV mode such that eight successive snapshots of particle positions were recorded in eight frames. An in-line shadowgraph system with a pulsed LED was integrated into the imaging system and synchronized with camera exposures to determine the accurate shock location. The shock location combined with the shock speed obtained from the pressure transducers was used to estimate the time when the shock reached each particle. An image processing procedure was implemented for accurate determinations of particle sub-pixel locations from noisy and distorted particle images.

4.3 Method Description

As discussed in the introduction, the N-pulse ($N \leq 8$) particle position data demand a reliable fitting method other than the polynomial fitting widely used in the literature. While the generality of polynomial fitting makes it a nearly universal curve fitting tool, better applicabilities to specific problems may be lost. In this regard, we introduce a novel fitting method incorporating particle dynamics for particle-shock PTVA analysis. It is based on Wagner *et al.* (2012) in which the authors derived a fitting model by integrating the equation defining the particle drag coefficient C_D:

$$\frac{\ddot{x}_p(t)}{\left[u_f - \dot{x}_p(t)\right]^2} = \kappa C_D, \tag{4.5}$$

wherein $\kappa = {}^{3\rho_f}\!/_{4\rho_p d_p}$ with ρ_f and ρ_p being particle density and post-shock fluid density, respectively; u_f is the post-shock flow velocity; $x_p(t)$ is one-dimensional particle position history; and $\dot{()}$ denotes the derivative with respect to t. In their analysis, C_D was assumed to be constant during a short time window and determined as a fitting parameter. However, to ensure C_D being constant a valid assumption in the present case with only eight

pulses, we need to set a very short inter-frame time, which undesirably result in the loss of continuous temporal resolution. Moreover, a piecewise scheme progressively using a constant C_D for each 3- or 4-pulse piece (see e.g. Bordoloi *et al.*, 2017) may yield high uncertainties due to the lack of global constraints in each piece. Thereby, we propose to use a time-resolved representation of C_D, i.e. $C_D = C_D(t)$, to derive the fitting model as follows. Suppose particle positions $x_{p,i}$ are measured at t_i, $i = 0, 1, ..., N-1$. Rewriting Equation (4.5) in terms of normalized time $t^* = (t - t_0)/T$, where $T = t_{N-1} - t_0$, gives

$$\frac{\dfrac{d^2 x_p}{dt^{*2}}}{\left(u_f T - \dfrac{dx_p}{dt^*}\right)^2} = \kappa C_D(t^*) \tag{4.6}$$

Integrate (4.6) from $t^* = 0$ to $t^* = \tau^*$:

$$\frac{1}{u_f T - \dfrac{dx_p}{dt^*}} = \frac{1}{u_f T - \dfrac{dx_p}{dt^*}\Big|_{t^*=0}} + \kappa I(\tau^*) \tag{4.7}$$

wherein $I(\tau^*) = \displaystyle\int_0^{\tau^*} C_D(t^*) dt^*$. Another integration of Equation (4.7) then yields an integral form for $x_p(t^*)$:

$$x_p(t^*) = x_{p,0} + u_f T t^* - \int_0^{t^*} \frac{d\tau^*}{\kappa I(\tau^*) + \left[\left(u_f - v_{p,0}\right) T\right]^{-1}} \tag{4.8}$$

wherein $x_{p,0}$ and $v_{p,0}$ are the particle position and velocity at $t^* = 0$, respectively. Equation (4.8) is the model we fitted to measured particle locations $x_{p,i}$ to determine $C_D(t^*)$. It has a clear physical meaning – the first two terms constitute the particle displacement as if the particle perfectly followed the post-shock flow; the integral term, which is essentially the time integral of the slip velocity $u_f - v_p$, calculates the distance of the particle

lagging behind the flow. This latter term is where the particle dynamics is involved in the form of particle drag history $C_D(t)$.

We used polynomials of different orders to represent $C_D(t^*)$:

$$C_D(t^*) = \sum_{j=1}^{\Gamma+1} j\alpha_j t^{*(j-1)}, \tag{4.9}$$

with Γ = 1, 2, 3. The coefficients α_j are determined as fitting parameters. Although other representations are possible (e.g. cubic splines), our test showed they were not advantageous over polynomials due to limited number of particle positions (N=8). With Equation (4.9), $I(\tau^*)$ can be readily calculated:

$$I(\tau^*) = \sum_{j=1}^{\Gamma+1} \alpha_j t^{*j}. \tag{4.10}$$

The least-square fitting of $x_{p,i}$ with Equation (4.8) was performed using the nonlinear algorithm reported by Coleman and Li (1996), which is conveniently provided in Matlab. Equation (4.8) was evaluated numerically during the fitting process as the analytical result of the integration is not easily obtainable.

In addition to α_j, our analyses also included $x_{p,0}$ and $v_{p,0}$ as another two fitting parameters to account for the uncertainty in determining the time when the shock starts interacting with the particle. This is necessary for our analyses because the duration of the shock passage is less than 0.1 μs during which the particle velocity dramatically increases (Parmar *et al.*, 2009).

It is worthing noting that the way we calculate C_D in Equation (4.5), in which the drag is proportional to the slip velocity, complies with the conventional definition of quasi-steady drag. However, in the case of unsteady forces existing, Equation (4.5) gives the effective drag coefficient, i.e. the drag force exerted on the particle normalized by the slip velocity square. This is necessary to be understood as the total force may also depend on the particle acceleration in the unsteady regime ($A_c \sim 1$).

To have a comparative assessment of the present method, we also implemented two other PTVA analyses similar to Voth *et al.* (2002) and Bordoloi *et al.* (2017), respectively, both of which are piecewise algorithms. For each 4-pulse piece, $\{x_{p,n},...,x_{p,n+3}\}$, n = 0, 1,..., N-4, the first piecewise analysis fits a parabola to the four positions with equal weights (the adaptive weighting by Voth *et al.* (2002) is not applicable here). Then the particle velocity and acceleration are evaluated at $(x_{p,n+1}+x_{p,n+2})/2$ by differentiating the parabola. The second piecewise analysis fits Equation (4.8) with $\Gamma = 0$, i.e. constant C_D, to each piece with α_1, $x_{p,0}$ and $v_{p,0}$ being the three fitting parameters. Note that for the nth piece $x_{p,0}$ and $v_{p,0}$ are the particle position and velocity at $t_n^* = (t_n - t_0)/T$. In the subsequent sections, these two piecewise analyses are referred to as 'piecewise polynomial (PW poly)' and 'piecewise integrated dynamic equation (PW IDE)'.

4.4 Performance Assessment

We performed PTVA simulations to assess the performance of the proposed method. The objectivity of the assessment was strengthened by testing two drag correlations shown in Figure 4.1(a):

(i) an empirical correlation beyond the quasi-steady regime based on experimental results,

$$C_D = -0.6579 + 5.382Re_p^{-\frac{1}{3}} + 99.88Re_p^{-\frac{2}{3}} - 226.3Re_p^{-1} + 436.8Re_p^{-\frac{4}{3}} \tag{4.11}$$

for $20 \lesssim Re_p \lesssim 700$. See Section 4.6 for how we obtained Equation (4.11).

(ii) the standard drag correlation in Clift and Gauvin (1970),

$$C_D = \frac{24}{Re_p}\left(1 + 0.15Re_p^{0.687}\right) + 0.42\left(1 + \frac{42500}{Re_p^{1.16}}\right)^{-1} \tag{4.12}$$

The particle position history $x_p(t)$ of each test case was calculated by integrating the C_D–Re_p correlation using initial conditions $x_{p,0} = 0$ and $v_{p,0} = 28$ m/s. We estimated $v_{p,0}$ using the force models of Parmar *et al.* (2009) at the time when the shock passed over the particle . Note the particle size and the optical setup in our experiments did not allow resolving the shock passage over a particle. Thereby, we approximated the velocity initial condition using a step at t^*=0. It is evident in Figure 4.1(b) that the empirical correlation results in stronger acceleration and the particle approaches the post-shock flow velocity faster. This also explains the empirical drag correlation in Figure 4.1(a) spans over a wider Re_p range. We set the durations of the particle trajectories such that the total particle displacements matched with that in Martinez *et al.* (2015). This ensures the position noise level to be comparable to realistic experiments (see Equation (4.15)). We also chose other simulation parameters based on the experiment by Martinez *et al.* (2015), and they are listed in Table 4.1a. In addition, we specified reasonable bounds for the parameters determined from the nonlinear least-square fittings (see Table 4.1b) to improve fitting reliabilities. The α_j bounds ensure $C_D(t^*)$ to have the correct slope and convexity.

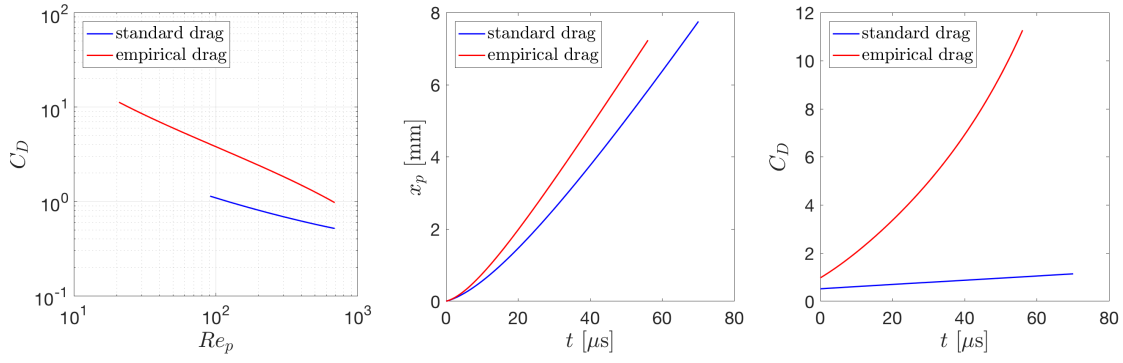

(a) drag correlation (b) particle position (c) particle drag

Figure 4.1: Simulated particle trajectories based on the two drag correlations given in Equation (4.11) and (4.12).

	Empirical	Standard
T [μs]	56	70
$\Delta x_{p,tot}$ [pix]	778.28	834.26
δ_{x_p} [pix]	0.01 – 10	
M_0 [μm/pix]	9.3	
d_p [μm]	80	
ρ_p [kg/m^3]	15	
ρ_f [kg/m^3]	1.4122	
μ_f [Pa·s]	2.0926×10^{-5}	
u_f [m/s]	155.61	

(a) simulated experimental conditions

Method	Bounds
$\Gamma = 3$	-0.2 mm $\le x_{p,0} \le$ 0.2 mm; $0 \le v_{p,0} \le$ 50 m/s; $\alpha_1, \alpha_2 \ge 0$
$\Gamma = 2$	-0.2 mm $\le x_{p,0} \le$ 0.2 mm; $0 \le v_{p,0} \le$ 50 m/s; $\alpha_1, \alpha_2, \alpha_3 \ge 0$
$\Gamma = 1$	-0.2 mm $\le x_{p,0} \le$ 0.2 mm; $0 \le v_{p,0} \le$ 50 m/s; $\alpha_1, \alpha_2 \ge 0$
PW IDE	For the first piece: -0.2 mm $\le x_{p,0} \le$ 0.2 mm; $0 \le v_{p,0} \le$ 50 m/s; For the nth piece ($n \ge 2$): $\hat{x}_p^{n-1}(t_n^*)$-0.2 mm $\le x_{p,0} \le$ $\hat{x}_p^{n-1}(t_n^*)$+0.2 mm; $0.8\hat{v}_p^{n-1}(t_n^*) \le v_{p,0} \le 1.2\hat{v}_p^{n-1}(t_n^*)$;

(b) fitting bounds

Table 4.1: Simulation parameters. $\hat{x}_p^{n-1}(t_n^*)$ and $\hat{v}_p^{n-1}(t_n^*)$ are the position and velocity estimates at t_n^* using the the $(n-1)$th piecewise fit.

To simulate an 8-pulse PTVA experiment, 8 particle positions were generated equidistantly in time along each simulated trajectory . Gaussian random noise with a standard deviation δ_{x_p} ranging from 0.01 to 10 pix was added to each particle position. 200 independent realizations were simulated for each noise level allowing us to calculate the mean bias, the random error and thus the total rms error. Here, the rms error of C_D, σ_{C_D}, is decomposed into the bias and the random error:

$$\sigma_{C_D}^2 = \langle\big(\hat{C}_D - C_{D,\text{true}}\big)^2\rangle = \underbrace{\big(\langle\hat{C}_D\rangle - C_{D,\text{true}}\big)^2}_{\text{bias}} + \underbrace{\langle\big(\hat{C}_D - \langle\hat{C}_D\rangle\big)^2\rangle}_{\text{random}} \tag{4.13}$$

wherein $\langle\,\rangle$ denotes ensemble average; ' $\hat{}$ ' indicates an estimate. In the above equation, the time dependence is not explicitly revealed for simplicity. However, one needs to bear in mind the errors vary in time along the trajectory.

In Figure 4.2, the time-averaged, normalized C_D rms error, $\overline{\sigma}_{C_D}^*$, for each analysis method is plotted against increasing noise level. $\overline{\sigma}_{C_D}^*$ is calculated by first normalizing

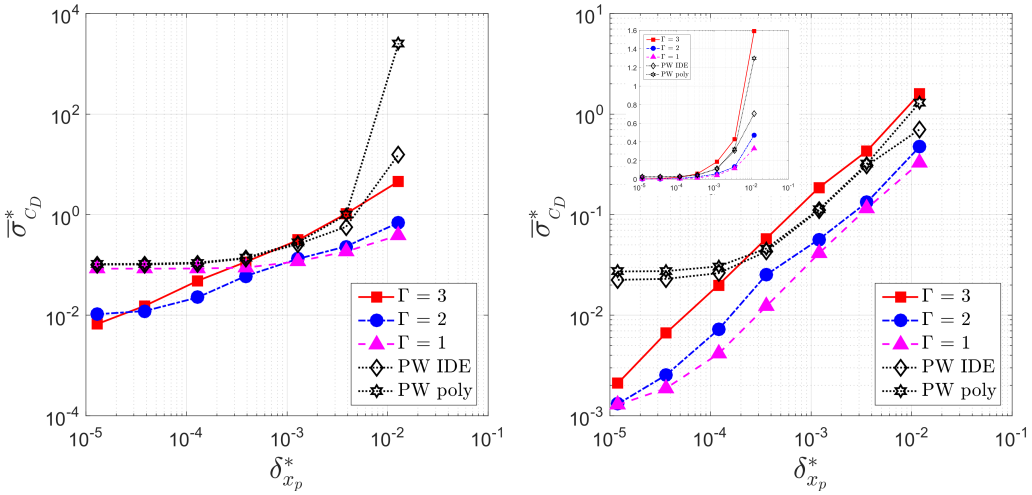

(a) empirical drag (b) standard drag

Figure 4.2: C_D rms errors with increasing locating noise. The inset in (b) uses a linear scale for the vertical axis to compare the growth rate.

σ_{C_D} with the true $C_D(t^*)$ and then averaging over $0 \le t^* \le 1$:

$$\overline{\sigma}^*_{C_D} = \int_0^1 \frac{\sigma_{C_D}(t^*)}{C_{D,\text{true}}(t^*)} dt^* \tag{4.14}$$

The noise level $\delta^*_{x_p}$ is given by the particle locating rms error δ_{x_p} normalized by the total displacement $\Delta x_{p,tot}$:

$$\delta^*_{x_p} = \delta_{x_p} / \Delta x_{p,tot} \tag{4.15}$$

It is evident from both test cases that the two piecewise analyses yield high rms errors over the entire range of $\delta^*_{x_p}$. At small $\delta^*_{x_p}$ where bias error dominates, the constancy of C_D (PW IDE) or acceleration (PW poly) within each 4-pulse piece leads to strong bias; when $\delta^*_{x_p}$ increases, the piecewise methods produce rapidly increasing rms errors due to the lack of global constraints in each piecewise fit. In contrast, the continuous, time-resolved representations of C_D used in the proposed method exhibit reduced rms errors. At large $\delta^*_{x_p}$, lower order models (Γ = 1, 2) are able to suppress random noise, whereas the cubic model (Γ = 3), similarly to the piecewise methods, has a large rms error due to the

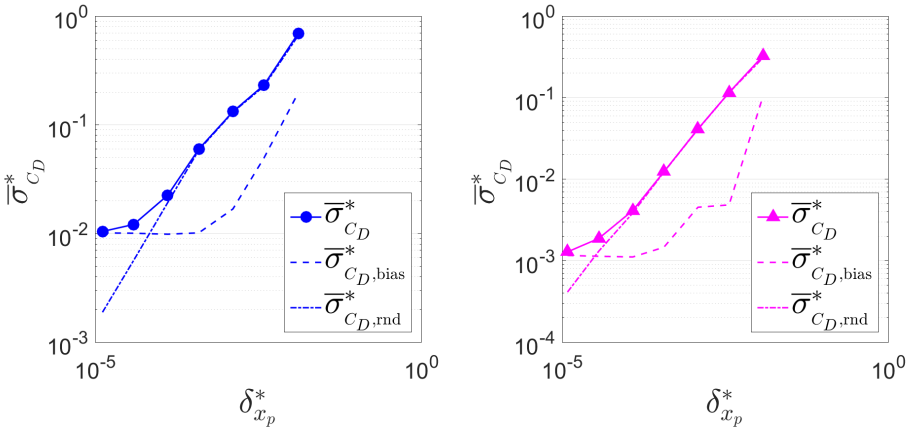

(a) empirical drag, $\Gamma = 2$ (b) standard drag, $\Gamma = 1$

Figure 4.3: Rms error decomposition – bias and random error.

increased degree of freedom. On the other hand, their performances at small $\delta^*_{x_p}$ depend on their functional forms and the shape of the true $C_D(t^*)$. As seen in Figure 4.1(c), the $C_D(t^*)$ of the empirical correlation is noticeably curvilinear, whereas the standard drag yields a nearly linear drag history. Thereby, the best performances at the lowest $\delta^*_{x_p}$ are achieved with Γ=3 and Γ=1 for the empirical correlation and the standard drag, respectively. For $\delta^*_{x_p}$ between 10^{-4} and 5×10^{-2}, corresponding to 0.1 pix $\leq \delta_{x_p} \leq$ 3 pix, an error range encountered in most PTV measurements, the preferable models are Γ=2 and Γ=1 for the empirical and the standard drag correlation, respectively. For 0.1 pix $\leq \delta_{x_p} \leq$ 3 pix, the normalized rms errors, $\overline{\sigma}^*_{C_D}$, of both test cases range approximately from 10^{-2} to 10^{-1}.

With the preferable models, Figure 4.3 presents the decomposition of the total rms errors into bias and random errors. As expected, the random error surpasses the bias error when $\delta^*_{x_p}$ increases and eventually becomes dominant. Interestingly, the bias error of either case initially stays flat and then rises up dramatically at $\delta^*_{x_p} \approx 5\times10^{-4}$, implying the nonlinearity of the fitting model. Moreover, it is necessary to isolate the bias error,

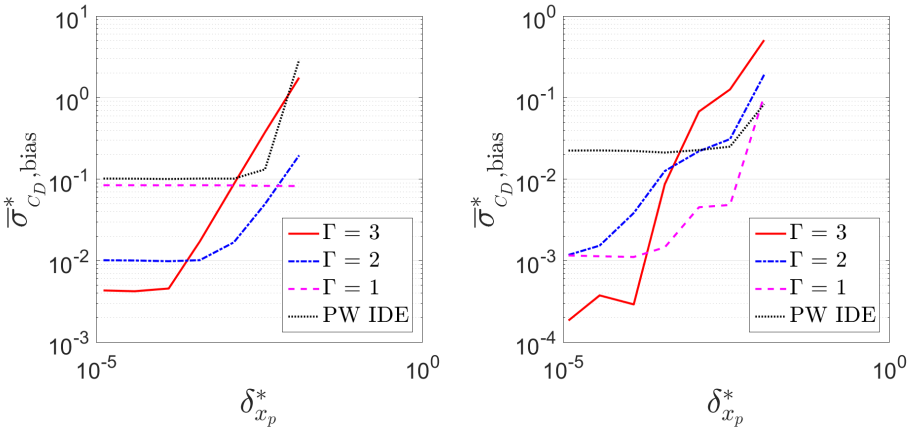

(a) empirical drag (b) standard drag

Figure 4.4: Comparison of bias errors.

which may be more meaningful for statistical studies and may provide a picture different from that of the total rms error. Figure 4.4 compares the bias errors of different fitting models. It is observed that the piecewise method has a wider plateau but its overall bias is high. The smallest bias for 0.1 pix $\leq \delta_{x_p} \leq$ 3 pix is achieved by $\Gamma = 1$ or 2 model, depending on the shape of the true $C_D(t^*)$.

The time dependences of the errors are showed in Figure 4.5 for the empirical drag correlation. (The standard drag correlation has a qualitatively similar result.) It is clear that local minimums or an interval of low rms error exist along the trajectory. The

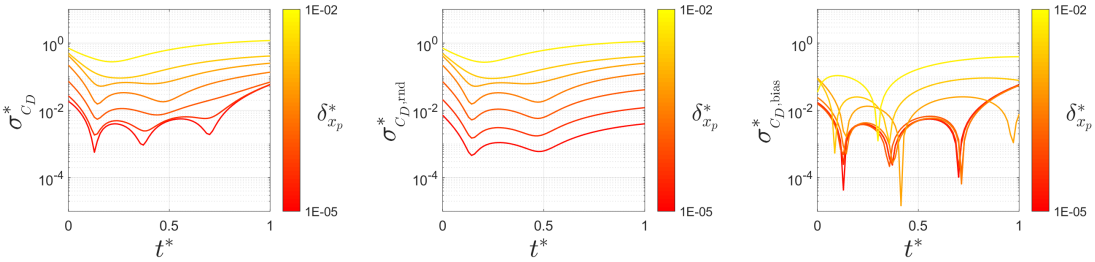

(a) rms error (b) random error (c) bias error

Figure 4.5: Time dependences of the errors for the empirical drag correlation with $\Gamma = 2$.

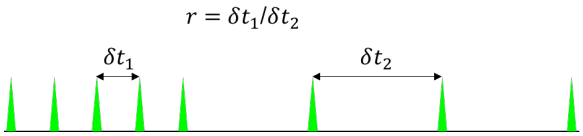

Figure 4.6: Pulse timing configuration parameterized by a single parameter r. Displayed is for r=1/3.

minimums at small $\delta^*_{x_p}$ arise from the shape of the bias error, and then gradually become aligned with those of the random error when $\delta^*_{x_p}$ increases. These observations about the local minimums are qualitatively consistent with Ding and Adrian (2017), in which the authors used the minimums to optimize velocity and acceleration evaluations. However, in the present work, we do not use them to evaluate instantaneous C_D since the drag history is of the most interest. The interval of low rms error appears approximately between $t^* = 0.2$ and 0.5 for a wide range of $\delta^*_{x_p}$, suggesting one could optionally use only a portion of $C_D(t^*)$ for improved data accuracy.

Another investigation focused on the optimization of pulse timing configuration, seeking for potential reduction of the rms error. We parameterized the pulse timing using a single parameter r defined as the ratio between the early and the late interframe times. As illustrated in Figure 4.6, the first three and the last four interframe times are set equal and denoted as δt_1 and δt_2, respectively. r is then given by $r = \delta t_1/\delta t_2$. Our preceding discussions were for a uniform pulse timing, i.e. r=1. Here, we extend the study of $\sigma^*_{C_D}$ subject to increasing noise level to $1/3 \le r \le 3$. The improvement turns out to be only noticeable at the early time, $0 \le t^* \le 0.2$. As shown in Figure 4.7(a), the reduction of $\sigma^*_{C_D}$ for 0.1 pix $\le \delta_{x_p} \le 3$ pix ($10^{-4} \le \delta^*_{x_p} \le 5 \times 10^{-2}$) is approximately 20% – 50% when r varies from 3 to 1/3. It suggests that one could possibly extend the total time duration of measurement for a reduced $\delta^*_{x_p}$ benefiting the overall accuracy, and rearrange the pulses to achieve a moderate compensation for the early time.

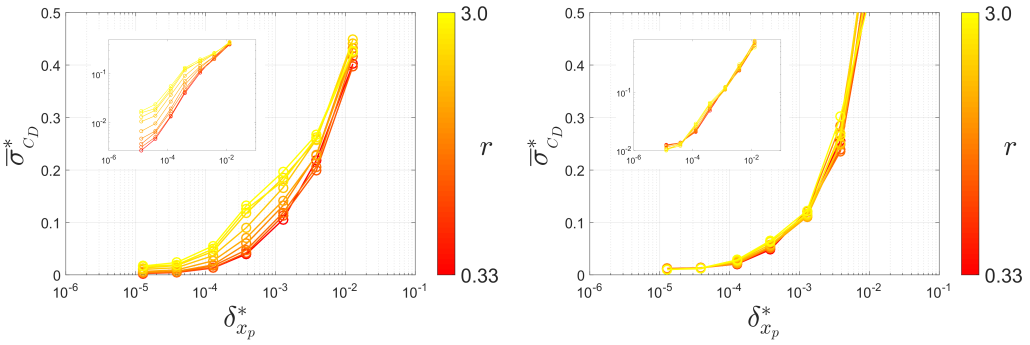

(a) $0 \le t^* \le 0.2$ (b) $0.2 \le t^* \le 1$

Figure 4.7: The rms errors of C_D at early and late times for different pulse timing configurations ($\Gamma = 2$). The inset plots use a logarithm scale for the vertical axes.

4.5 Experimental Result and Discussion

We analyzed two datasets of different particle types and experimental setups (see Table 4.2). Both datasets have the ranges of particle Mach number in the subcritical regime. The different particle diameters result in two separate Re_p ranges in our analysis. Dataset A has an averaged $\Delta x_{p,tot}$ approximately 35% greater than that of dataset B, implying an overall reduced noise level of dataset A. The ranges of A_c, estimated with $\Gamma = 2$, indicate the particle motions in our experiment are significantly beyond the quasi-steady regime (A_c<0.01, according to Crowe *et al.*, 1963). For dataset A, the 8 pulses were set uniformly with an interframe time δt indicated in the table. For dataset B, the time between the first two pulses was extended ($\Delta t_{1\text{-}2} = 4$ or 8 μs) to easily determine the particle pre-shock locations, and subsequent pulses were arranged 1 μs apart. The times of recorded particle locations with respect to $t_0 = 0$ were calculated using each particle's pre-shock location and the shock location and speed (see Bordoloi *et al.*, 2017). In our data analysis, $t_0 = 0$ corresponds to the time when the shock aligns with a particle's

	Dataset **A**	Dataset **B**
particle type	copolymer	Nylon
size range [μm]	[60,90]	[1,7]
$\overline{d}_p$ [μm]	80	4
res. [μm/pix]	9.3	2.14
ρ_p [kg/m^3]	15	1140
M_s	1.3	1.2
M_p	<0.4	<0.3
Re_p	20 - 1000	0.1-20

particle no.	δt [μs]	ρ_f [kg/m^3]	u_f [m/s]	μ_f [10^{-5}Pa·s]	$\Delta x_{p,tot}$ [pix]	A_c
A1	5	1.412	155.61	2.093	509.92	[0.09, 0.46]
A2	7	1.409	154.82	2.091	435.03	[0.06, 0.63]
A3	7	1.409	154.82	2.091	572.25	[0.04, 0.28]
A4	10	1.411	155.35	2.092	829.01	[0.04, 0.95]
A5	10	1.411	155.35	2.092	868.54	[0.07, 1.53]
A6	10	1.411	155.35	2.092	781.20	[0.03, 0.21]
A7	10	1.411	155.35	2.092	620.65	[0.02, 0.11]
B1	1	1.254	109.27	2.022	283.36	[0.13, 0.63]
B2	1	1.257	110.06	2.024	459.69	[0.01, 5.70]
B3	1	1.259	110.57	2.024	687.91	[1e-3, 1.29]
B4	1	1.258	110.29	2.024	555.03	[0.02, 4.37]
B5	1	1.263	112.05	2.027	318.04	[0.04, 0.30]
B6	1	1.263	112.05	2.027	619.87	[1e-5, 0.93]

Table 4.2: Experimental parameters. M_s is the shock Mach number; δt is the interframe time; ρ_f, u_f and μ_f are the post-shock flow properties. A_c ranges are estimated with Γ = 2.

center. The time duration of shock passage is considered infinitesimally small due to insufficient spatial resolution (see also the discussion about the particle initial velocity in Section 4.4). Depending on which frame was synchronized with the shadowgraph system, we obtained 7 or 8 particle locations for each post-shock particle trajectory. We also removed particle location outliers by visual inspections. For the particles listed in Table 4.2, only one location (of particle B1) appeared to be an outlier. Consequently, for nearly all particles, we have 7 or 8 particle locations to perform PTVA drag analyses with the fitting models described in Section 4.4. Note the Γ = 3 model requires at least 7 data points for a least-square fit. (Particle B5 only has 6 data points due to the particle moving out of the laser sheet.)

The complete set of plots for particle position, velocity, acceleration and drag coefficient are presented in Appendix C. The results obtained by Γ = 1, 2, 3 and PW IDE

are included. Comparing them along with the conclusions from our simulation, we summarize our observations and conjectures as follows.

(1) The Γ=3 model seems to consistently overestimate C_D at the late time (approximately t^*>0.8). We tend to consider these high values of C_D to be systematic biases based on the simulation result of large bias error of Γ = 3 indicated in Figure 4.4.

(2) Some $C_D(t)$ results by the Γ = 3 model (e.g. B5, B6) and PW IDE (e.g. B2, B3, B5, B6) are apparently unphysical. It is probably associated with the high rms errors of the Γ = 3 model and PW IDE as evident in the simulation.

(3) The acceleration history curves consistently exhibit distinct peaks at small positive t, i.e. short after the shock passes over the particle. The time scales of these peaks suggest they are systematic biases rather than the peak during the shock passage predicted by Sun *et al.* (2005); Parmar *et al.* (2009). There is a tendency of the peaks occurring at relatively late times when $v_{p,0}$ is overestimated (see e.g. A1, A2, B2, B3). It is mathematically consistent with the way we calculate a_p:

$$a_p = \kappa C_D (u_f - v_p)^2 \tag{4.16}$$

in which a_p is inversely proportional to v_p at early time.

(4) The overestimated $v_{p,0}$ appears to correlate with the time between the first two pulses, $\Delta t_{1\text{-}2}$. When $\Delta t_{1\text{-}2}$ is relatively large (e.g. B2, B3, B6), we are likely to miss the strong acceleration near t = 0. It is interpreted that, with a large $\Delta t_{1\text{-}2}$, the fitting of $x_{p,i}$ loses the clamped boundary condition that constrains the early slope. The observed behaviors at the early time conceptually agree with our simulation results showing elevated rms error when the first few pulses are loosely distributed. In contrast, when $\Delta t_{1\text{-}2}$ is comparable to or smaller than the other interframe times, $a_p(t)$ results become more satisfactory (e.g. A3 – A7). In addition, the Γ = 2

model appears less sensitive to $\Delta t_{1\text{-}2}$ in terms of the early acceleration prediction compared to other models.

(5) In terms of the above discussions, the results of dataset A are generally cleaner than those of dataset B, consistent with our expectation from the low noise level of dataset A.

(6) Among the fitting models we tested in this work, the Γ=2 model appears to be the most consistent and reliable one. The Γ = 3 model and PW IDE both suffer high bias and random errors. The linear form of the Γ = 1 model may limit its wide applicability and may result in underestimated C_D, unless the noise levels in certain experiments are extremely high. This conjecture about the Γ = 2 model is in agreement with the simulation results of the empirical drag.

With the particle velocities, $C_D - Re_p$ correlation curves are readily calculated and presented in Figure 4.8. For each particle trajectory, we obtained a single $C_D - Re_p$ curve, and presented is the collection of all particles listed in Table 4.2. It is apparent that some extremely small values of C_D are predicted at the early time (i.e. large Re_p in each dataset), especially from the Γ=3 model, which is probably nonphysical. We found these unphysically small C_D values came from the particles measured with a relatively long $\Delta t_{1\text{-}2}$ (B2, B3, B6), which again prove the advantage of shortening $\Delta t_{1\text{-}2}$. The strong increasing trends of the Γ = 3 model and PW IDE at small Re_p of each dataset are clear as also evident in the $C_D(t)$ plots. It is worth to clarify that, although the continuous trend between the two datasets in the PW IDE results appears favorable, there is a lack of logical reasoning behind it. As clearly shown in Figure 4.8(f), the unsteadiness parameter A_c differs by a decade at the Re_p where the two datasets connect. Thereby, different C_D should be expected if we consider C_D is a function of both Re_p and A_c, i.e. $C_D = C_D(Re_p, A_c)$.

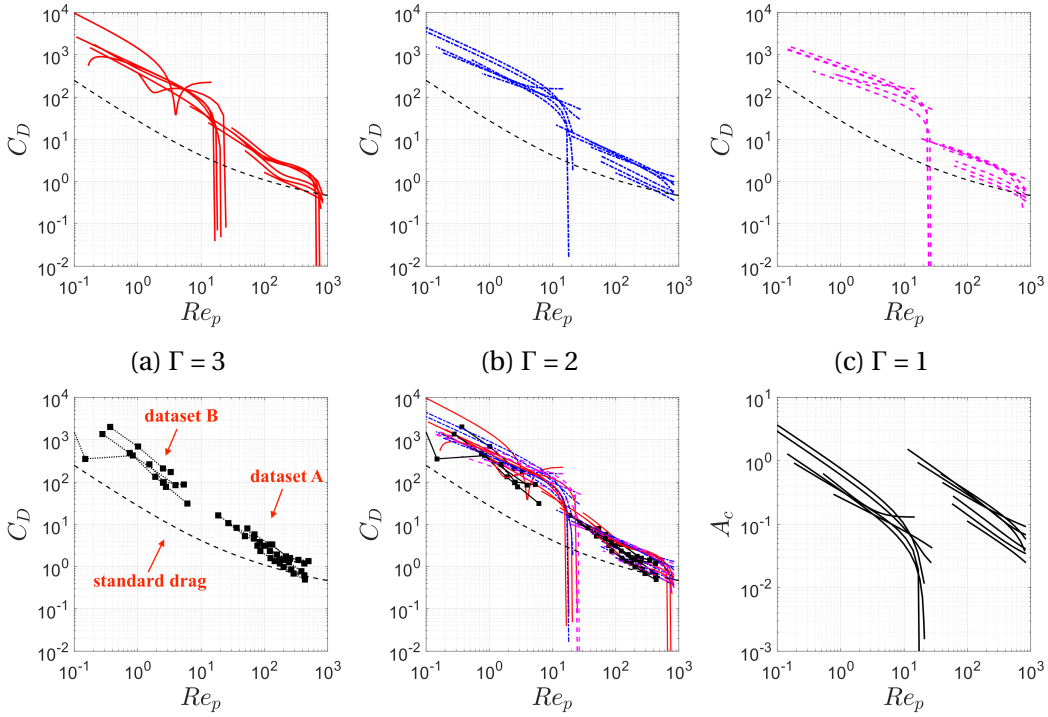

(a) $\Gamma = 3$ (b) $\Gamma = 2$ (c) $\Gamma = 1$

(d) PW IDE (e) superposed (f) A_c ($\Gamma = 2$)

Figure 4.8: $C_D - Re_p$ correlations. Each curve represents a single particle's drag history. Negative values in the PW IDE curves are ignored for logarithm-scale plots. The standard drag uses the fit by Clift and Gauvin (1970).

Based on the above discussion, we removed the early 10% (t^*<0.1) data points of C_D for the particles having unphysically small C_D at the early time (i.e. particle no. B2, B3, B6). The cleaned drag correlation is presented in Figure 4.9(a), in which the elevation relative to the standard drag is noticeable. Regarding the ranges of M_p and A_c given in Table 4.2, it is conjectured the unsteadiness is mainly responsible for the increase in drag. Karanfilian and Kotas (1978) fitted their unsteady particle drag data using an empirical model in terms of A_c and standard drag C_{DS}:

$$C_D = C_{DS}(1 + A_c)^{1.2\pm0.03} \tag{4.17}$$

for approximately 100<Re_p<5000. In spite of the different Re_p range, we examined our data in the same fashion by plotting the modified drag coefficient, $\widetilde{C}_D = C_D/(1 + A_c)^{1.2}$,

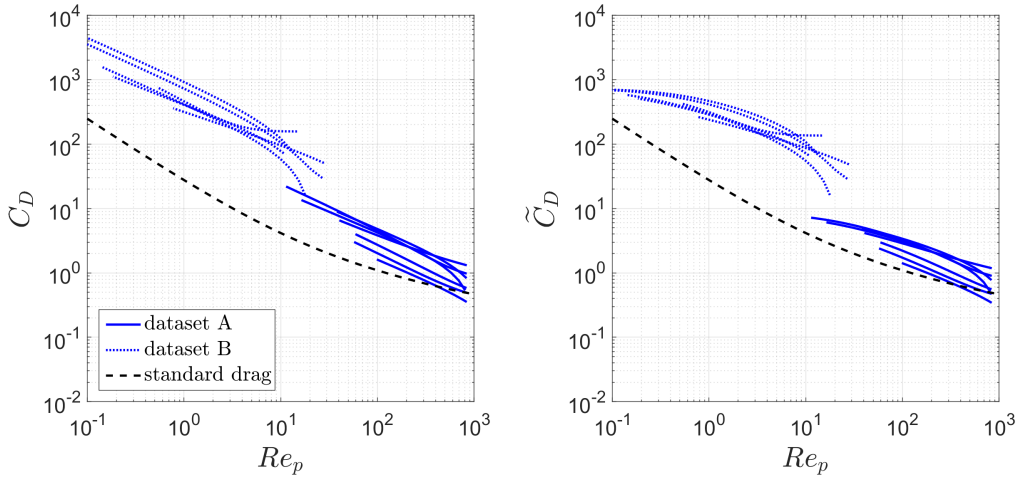

(a) cleaned drag correlation (b) modified drag coefficient

Figure 4.9: Cleaned $C_D - Re_p$ correlation after removing the early 10% data of selected particles (B2, B3, B6). The modification of C_D for unsteadiness follows Karanfilian and Kotas (1978), i.e. $\widetilde{C}_D = C_D/(1+A_c)^{1.2}$.

against Re_p (see Figure 4.9(b)). Apparently, the standard drag is not recovered, suggesting $C_D(Re_p, A_c)$ of a different form. However, the lack of accurate size measurement for each single particle prevents us from fitting the data with confidence. In the next section, we will discuss the particle size effect to the measured drag correlation and how to potentially eliminate data scattering due to particle size polydispersity.

4.6 Particle Size Effect

There is one important observation in Figure 4.8 or 4.9(a) that we have not mentioned above. That is, the C_D–Re_p curves of different particles in the logarithm-scale plot manifest translations with each other. These particles were measured under nearly the same experimental condition, so they should in principle follow an universal drag correlation after normalization. The translational scattering, which appears to be not a random

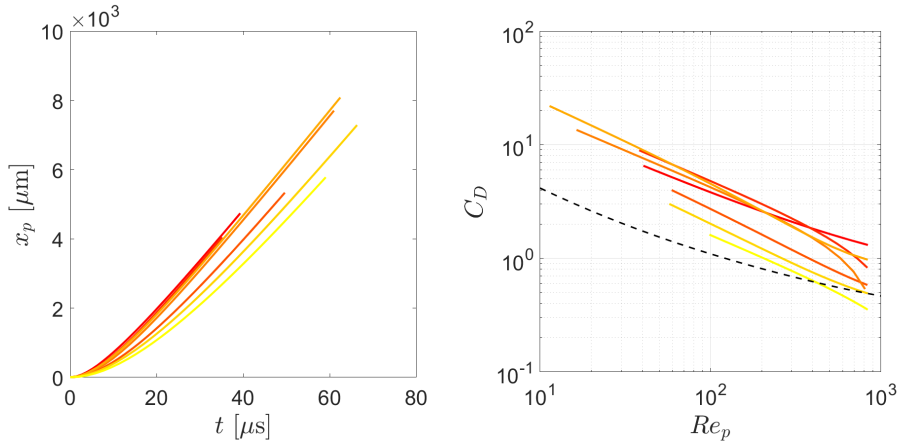

Figure 4.10: Particle position histories and corresponding drag correlations. The curves are color coded to indicate correspondences.

behavior, obviously suggests there exists an artificial mechanism causing the problem. If we examine the $C_D - Re_p$ results along with the corresponding particle position histories, as shown in Figure 4.10, we can immediately see slow-moving particles have low C_D estimates. As the particle samples are polydisperse, the slow-moving particles under the same post-shock condition should have relatively large diameters. This suggests the translational scattering may result from the fact that we used the same nominal particle diameter, i.e. the mean diameter $\overline{d}_p$ of a particle batch, in the analyses of all particles.

A further evidence of the translational scattering being caused by particle polydispersity comes from the following mathematical deduction. Suppose the ratio between the nominal diameter and a particle's true diameter is ξ, i.e.

$$\frac{d_{p,nom}}{d_{p,true}} = \xi. \tag{4.18}$$

In the fitting model (4.8), the only term involving d_p is $\kappa I(\tau^*) = \dfrac{3\rho_f}{4\rho_p d_p}\displaystyle\int_0^{\tau^*} C_D(t^*)dt^*$ in the integrand. Thereby, if d_p is scaled by ξ, then the measured C_D must also be scaled by the same factor to satisfy the same $x_p(t^*)$, i.e.

$$\frac{C_{D,meas}}{C_{D,true}} = \xi. \tag{4.19}$$

Likewise, since $Re_p \propto d_p$, we also have

$$\frac{Re_{p,meas}}{Re_{p,true}} = \xi. \tag{4.20}$$

Furthermore, if we use Φ to denote the true drag correlation in a logarithm scale:

$$\log C_{D,true} = \Phi\left(\log Re_{p,true}\right), \tag{4.21}$$

wherein 'log' is the common logarithm with base 10, then using Equation (4.19) and (4.20) it immediately follows

$$\log C_{D,meas} = \Phi\left(\log Re_{p,meas} - \log\xi\right) + \log\xi, \tag{4.22}$$

Equation (4.22) implies that the measured $C_D - Re_p$ curve is the true one translated by an offset vector $\boldsymbol{r}$ = ($\log\xi$, $\log\xi$) in a logarithm-scale plot. When ξ>1, i.e. the particle size is overestimated, the measured $C_D - Re_p$ curve appears above the true one, and it is opposite when ξ<1 (see Figure 4.11).

The above analysis in fact establishes a mapping relation between $\boldsymbol{r}$ and d_p. Since the direction of $\boldsymbol{r}$ is invariant despite the sign, we can alternatively use a scalar to express the relation for simplicity:

$$r = \log\frac{d_{p,nom}}{d_p}, \tag{4.23}$$

wherein $d_{p,true}$ is replaced by d_p to generally denote a varying d_p. Although it is difficult to determine d_p for individual particles, the particle size distribution, p_{d_p}, can be reliably measured by techniques such as direct imaging, sedimentation, laser diffraction, etc. (Crowe *et al.*, 2011). Then the probability density function (pdf) of r, p_r, can be derived:

$$p_r(r) = 2.3026 \cdot 10^{-r} d_{p,nom} \cdot p_{d_p}(10^{-r} d_{p,nom}), \tag{4.24}$$

in which $r = 0$ corresponds to $d_p = d_{p,nom}$. On the other hand, the pdf of the measured offsets, p'_r, can be determined experimentally from a big collection of $C_D - Re_p$ curves.

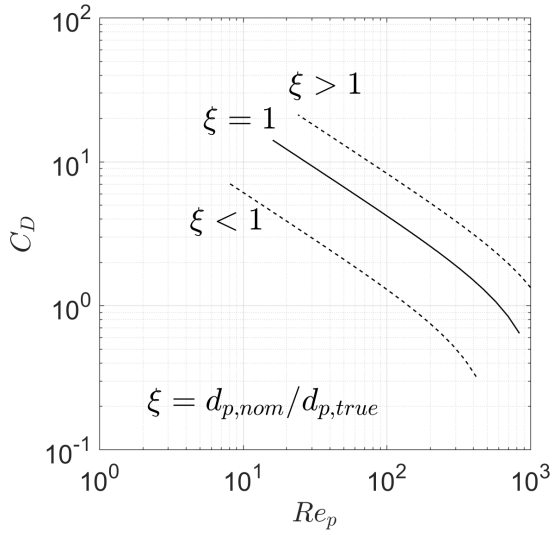

Figure 4.11: Schematic of translational scattering of the drag correlation caused by particle polydispersity.

In practice, the offsets can be measured with respect to an arbitrary reference position. Consequently, the correlation between p_r and p'_r should in principle yield the offset $\widetilde{r}$ corresponding to $d_{p,nom}$, i.e. $p'_r(\widetilde{r}) = p_r(0)$. Thus, we can obtain an accurate drag correlation free of the uncertainty due to particle size polydispersity. Note the above discussion did not take into account particle clumping due to electrostatic charge. If the clumped particles occur at a significant frequency, it requires a reasonable model of the clumping process to obtain a reliable size distribution p_{d_p}.

Finally, it is ready to explain the empirical drag correlation used in the simulation. Since the scattering is the consequence of particle size uncertainty, a correction procedure translating the $C_D - Re_p$ curves according to the particle diameter ratio is necessary. As the particle size information is unknown, we hypothetically shift all curves so that they cross a common (C_D, Re_p) position beyond the quasi-steady regime for the purpose of providing a reference to the simulation. As seen in Figure 4.12, the measured $C_D - Re_p$

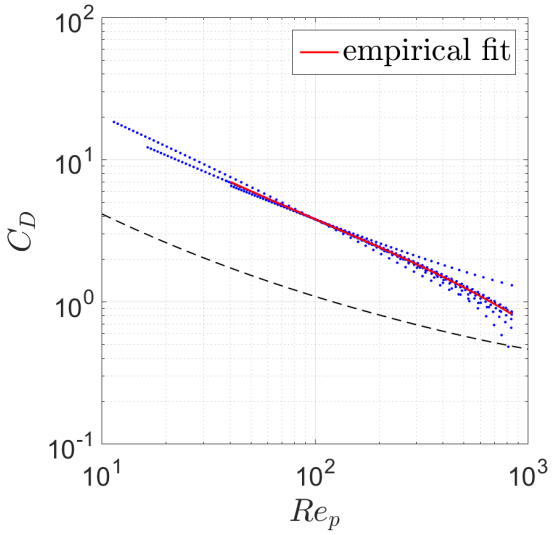

Figure 4.12: A hypothetical and empirical drag correlation based on experimental data .

curves are all brought to (C_D, Re_p) = (40, 100), and an empirical fit is obtained using the form appearing in Equation (4.11).

4.7 Summary

We reported an improved N-P PTVA ($N \leq 8$) analysis method for measuring particle drag in post-shock flows. The advantage of the method lies in the fitting model incorporating particle dynamics. The method was numerically validated by PTVA simulations using two different drag correlations. It was found, depending on the shape of the true drag correlation, the $\Gamma = 2$ or $\Gamma = 1$ model showed the best performance in terms of the total rms error, the bias and the random error within a realistic range of the noise level. The time-averaged, normalized rms error manifested in the simulation ranged between 1% to 10%. The simulation also suggested reduced rms error was achievable in a subrange of time. In addition, we demonstrated shortening the spacing of the first few pulses helped reduce the early time rms error.

Two datasets of shock-tube experiments having separate ranges of Re_p were analyzed using the proposed method. Based on the simulation results, we thoroughly discussed our observations and conjectures about the measurement quality. We found the two key parameters affecting the overall accuracy were the particle total displacement, i.e. the noise level, and the time between the first two pulses. Particles measured with a low noise level and a short $\Delta t_{1\text{-}2}$ generally yielded good results based on our conjectures. In addition, the $\Gamma = 2$ model appeared to be the most reliable one for the tested datasets. The $C_D - Re_p$ correlation estimated with $\Gamma = 2$ exhibited significant elevation relative to the standard drag, which we attributed to the flow unsteadiness. The examination using an unsteady C_D model from the literature suggested the necessity of new unsteady model as well as to understand the underlying particle-shock physics.

Last but not least, we explained how particle size polydispersity caused the translational scattering of measured $C_D - Re_p$ curves, and proposed a theoretical framework to accurately determine the drag correlation. As our ultimate goals, the new unsteady drag correlation and the unsteady particle dynamics in post-shock flows need further experimental investigations, especially the efforts on particle size distribution and dynamic particle sizing.

Chapter 5

ESTIMATION OF TURBULENCE DISSIPATION RATE AND OTHER STATISTICS FROM ENSEMBLE N-PULSE PTV DATA[5]

ABSTRACT

A novel PTV-based method for estimating turbulence isotropic dissipation rate and other statistics is presented. The method is based on the Taylor expansion of each velocity inside a resolution domain with respect to the domain center. We first derive the theoretical bases for mean velocity and mean velocity gradient, followed by the dissipation estimation utilizing the velocity differential of two closely positioned particles to infer the instantaneous flow strain rate. The mechanisms of two types of error are discussed, including the error due to finite-time averaging that leads to rms fluctuation, and the error arising from particle tracking with limited number of pulses. To validate the method and to understand the effects of different errors, a PTV simulation with synthetic turbulence is performed. It is found in the simulation that the PTV bias error is associated with the shape and length of a particle trajectory, whereas the PTV random error merely depends on the particle locating uncertainty. As a result, for the mean velocity and the mean velocity gradient, the PTV error only contributes usually negligible rms fluctuation. However, for the dissipation estimation, it constitutes a bias error inversely proportional to the square of the domain size L. On the other hand, we will show the rms fluctuation due to finite-time averaging determines the overall estimation accuracy. With the understanding of the errors, we developed a procedure of rational

[5]This chapter is reformatted from a manuscript prepared for journal publication.

analysis to reliably extract turbulence statistics. The procedure either determines an optimal L for averaging, or performs a curve fitting to the estimates at different L. Last, the method is applied to the tomographic measurement of an adverse-pressure-gradient turbulent boundary layer with $Re_\tau \approx 3000$. We successfully measured the mean velocity profile over $0.3 < y^+ < 30$ with high accuracy and high spatial resolution. The result of the mean velocity gradient is satisfactory compared to the reference obtained from a generalized Spalding's fit to the mean velocity. Finally, the isotropic dissipation rate near wall (y^+<12) is estimated with a slightly modified method to account for the strong rms fluctuation. The comparison with DNS studies at lower Reynolds numbers implies a reasonable measurement quality.

Keywords: dissipation, turbulence statistics, particle tracking velocimetry, optimization, adverse pressure gradient, turbulent boundary layer, high Reynolds number

5.1 Introduction

Dissipation rate is a key statistic for understanding turbulent kinetic energy (TKE) budget, energy cascade and turbulence scaling. Most complete turbulence studies involving the dissipation rate were in the form of direct numerical simulation (DNS) for its superior accuracy and data accessibility (Spalart, 1988; Moser *et al.*, 1999; Kaneda *et al.*, 2003; Donzis *et al.*, 2008). Reliable estimation of dissipation from experiments is yet challenging. Traditional point-wise techniques (hot wire anemometry and laser Doppler velocimetry) relied on Taylor's hypothesis that relates spatial derivatives with single-point temporal derivatives to estimate dissipation. The resulting accuracy is questionable (Dahm and Southerland, 1997), and the validity of Taylor's hypothesis is restricted despite

its overuse under a wide range of flow conditions. In addition, it is usually difficult for point-wise measurements to obtain all nine components of the rate-of-strain tensor.

With the tremendous effort in advancing particle imaging techniques over the past few decades, the opportunity of obtaining fully 3-D, high-spatial/temporal-resolution and high-accuracy turbulence data in experiments has been continuously increasing (Adrian, 1991, 2005; Adrian and Westerweel, 2011; Westerweel *et al.*, 2013; Kähler *et al.*, 2016). However, dissipation rate is still one of the most challenging quantities to be measured because of the amplification and propagation of noise during the differentiation and the square operation. Mathematically, the TKE dissipation rate is given by

$$\epsilon_T = \nu\langle u'_{i,j} u'_{i,j}\rangle + \nu\langle u'_{i,j} u'_{j,i}\rangle \tag{5.1}$$

wherein $u'_{i,j}$ is the derivative of velocity fluctuation u'_i in the x_j direction; the prime notation denotes a fluctuating quantity after subtracting the mean; and ν is the fluid kinematic viscosity. The first term on the right is the homogeneous isotropic dissipation, while the second term exists only when the flow exhibits inhomogeneity. Using the velocities measured by particle image velocimetry (PIV) to directly evaluate $\langle u'_{i,j} u'_{i,j}\rangle$ introduces two possible types of bias error. When the spacing between adjacent velocities is smaller than or comparable to Kolmogorov length scale η, the instantaneous random velocity errors result in a positive mean bias for the isotropic dissipation. This is because, despite the random error causing over- or underestimated instantaneous velocity gradient, the square operation always makes it a positive contribution to the mean. Tanaka and Eaton (2007) proposed a correction scheme for this overestimation occurring for a small mesh size utilizing the estimations at two different mesh sizes. They numerically demonstrated satisfactory accuracy for a mesh size between 0.1η and η, but did not address larger mesh sizes that are more realistically encountered. As the second type of bias error, many experimentalists have observed underestimated dissipation rate

due to insufficient spatial resolution to resolve small scale velocity fluctuations (Saarenrinne and Piirto, 2000; Sharp and Adrian, 2001; Baldi and Yianneskis, 2003; Racina and Kind, 2006; Tokgoz *et al.*, 2012; Discetti *et al.*, 2013). Among many others, Sharp and Adrian (2001) measured the dissipation rate near the tips of a Rushton turbine using planar PIV with symmetry and isotropy assumptions, and the resolved dissipation was about 70% of the full dissipation rate. Tokgoz *et al.* (2012) systematically studied the performance of tomographic PIV by measuring the dissipation rates of Taylor-Couette flows at different Reynolds numbers. From their results, the ratio between the measured dissipation and the reference dissipation, obtained from torque measurements, was about 0.5 at a moderately small shear Reynolds number (Re_s=3800), and dropped below 0.05 at Re_s=47000.

The hindrance of dissipation estimation with correlation-based PIV is the spatial averaging effect of the window-based analysis. The typical size of an interrogation spot in tomographic PIV is greater than 1 mm^3, while the length scale at which most viscous dissipation occurs is no more than 0.1 mm for moderate to high Reynolds numbers. Past studies on PIV measurements of dissipation have suggested the distance between adjacent velocity vectors to be about 3-5 η meanwhile using the smallest possible interrogation spot size (given by the valid detection probability, see Keane and Adrian, 1990) and a proper window overlap (50% or 75%) (Lavoie *et al.*, 2007; Worth *et al.*, 2010; Tokgoz *et al.*, 2012). This is apparently hard to satisfy in most experiments considering the facts: (1) when setting up a multi-camera tomographic system, the optical access required by such high magnification may not be possible in the test section; (2) the size of a particle image scales with the magnification, and large particle images prevent the use of small interrogation spots, which to some extent counteracts the benefit of using a high magnification. To compensate for the dissipation at unresolved scales, Sheng *et al.* (2000)

developed a large eddy PIV method that estimated the dissipation from the sub-grid scale (SGS) energy flux. The unresolved dissipation is somewhat recovered by the large eddy PIV, but further improved dissipation estimation is still desired (Tokgoz *et al.*, 2012).

Recent advances in particle tracking velocimetry (PTV) demonstrated its potential of surpassing the performance of correlation-based PIV. In early years, PTV suffered low data yield and high noise due to the limitations in recorded image quality, particle tracking algorithms and 3-D particle triangulation (Stanislas *et al.*, 2005, 2008). In this regard, substantial efforts have been made thanks to the development of camera technology in terms of signal-to-noise ratio, pixel resolution and framing rate. The flow information in time and space has helped materially improve the data density and accuracy of PTV measurements (Malik *et al.*, 1993; Keane *et al.*, 1995; Ohmi and Li, 2000; Fuchs *et al.*, 2017). A recent pioneering work by Schanz *et al.* (2016) utilizing iterative particle reconstructions (Wieneke, 2012) and flow temporal information opened the way to experimentally resolving turbulence small scale motions.

With these advanced PTV algorithms and the inherent advantage of PTV in spatial resolution, accurate dissipation estimation becomes promising. The high spatial resolution achieved by PTV is twofold. First, each measured velocity vector represents the velocity of the fluid material occupying the same space as the particle as if there is no particle, instead of the averaged velocity inside an interrogation spot as in PIV. Thus, high-frequency modes in a flow can be well resolved by PTV (Kähler *et al.*, 2012a). Second, the fit of a particle trajectory using successive particle positions gives accurate position history of a fluid parcel, and thus reduces the uncertainty in positioning the velocity vector. Ding and Adrian (2017) theoretically showed that N-pulse PTV was capable to reduce the positioning uncertainty by a factor of 10-50 compared to 2-pulse PTV. Furthermore, ensemble PTV recently has drawn some attentions for measuring turbulence statistics

with high resolution. The basic idea is to average PTV measurements at different times inside individual bins to get the statistical estimates at bin centers. The attractive feature of ensemble PTV is that the achievable bin size generally scales inversely with the total number of samples, and thus high resolution can be realized provided sufficiently large dataset. This ensemble PTV method has gained success in measuring mean velocity profiles (Kasagi and Nishino, 1991; Kähler *et al.*, 2012b; Schröder *et al.*, 2015) and Reynolds stress (Discetti *et al.*, 2015).

In this work, we extend the ensemble PTV method to dissipation measurement based on the fact that the differential between two closely positioned velocity vectors measured at the same time reveals the instantaneous velocity gradient. In addition, since the estimation of dissipation rate involves first estimating the mean velocity and the mean velocity gradient, we will also cover these two statistics from a rigorous mathematics point of view. It will be seen that, instead of using the ensemble PTV method in a somewhat empirical way as in previous works, this work provides rational analyses in order to optimize the accuracy. Consequently, it will become evident that, following the same line of our derivations, the ensemble PTV method also has the potential to estimate many other turbulence statistics including Reynolds stress, TKE viscous diffusion, TKE production, etc.

5.2 Theoretical Background

5.2.1 Mean Velocity

Although the validity of estimating the mean velocity by averaging particle velocities inside a subvolume (bin) seems straightforward, the derivation and discussion for the

mean velocity provide a more complete picture in terms of the truncation error, the rms error and the optimal subvolume size for averaging. We also in this section establish the notation system for the subsequent sections on the mean velocity gradient and the dissipation.

The problem is to estimate the mean velocity at a prescribed location $\boldsymbol{x}^*$ using velocity estimates from tracer particles that randomly occur in a small domain around $\boldsymbol{x}^*$ over a long period of time. Suppose, at a sampling time $t^{(q)}$, particle velocity estimates within a domain $\mathscr{D}$ centered at $\boldsymbol{x}^*$ are located at $\boldsymbol{x}^{(p,q)}$, $p = 1, ..., P^{(q)}$. The Taylor expansion of a particle velocity, $u_i^{(p,q)} = u_i(\boldsymbol{x}^{(p,q)}, t^{(q)})$, with respect to $\boldsymbol{x}^*$ is

$$u_i^{(p,q)} = u_i^* + u_{i,l}^*(x_l^{(p,q)} - x_l^*) + \frac{1}{2}u_{i,mn}^*(x_m^{(p,q)} - x_m^*)(x_n^{(p,q)} - x_n^*) + \mathscr{O}(L^3) \tag{5.2}$$

wherein Einstein notation is used, and the superscript asterisks in u_i^*, $u_{i,l}^*$, etc., indicate the quantities are taken at $\boldsymbol{x}^*$. The time dependences of asterisked variables are omitted for simplicity, and one should infer they belong to time $t^{(q)}$ in Equation (5.2) and subsequent equations. L represents the linear dimension of $\mathscr{D}$. Hereafter, our discussion assumes a cubic domain $\mathscr{D}$ with an edge length L unless otherwise specified. Some other notations frequently used in this paper are listed in Table 5.1. We now define a spatial average of a variable $\alpha^{(p,q)}$ for all $\boldsymbol{x}^{(p,q)} \in \mathscr{D}$ at $t^{(q)}$:

$$\prec \alpha^{(p,q)} \succ_{\mathscr{D}} \equiv \frac{1}{P^{(q)}} \sum_{p=1}^{P^{(q)}} \alpha^{(p,q)}. \tag{5.3}$$

The above average is denoted with curly angle brackets, as the number of particles, $P^{(q)}$, is usually a small finite number insufficient for a well converged average. We also define the long time average for a variable $\beta^{(q)}$ in its conventional way:

$$\langle \beta^{(q)} \rangle_{T\to\infty} \equiv \lim_{Q\to\infty} \frac{1}{Q} \sum_{q=1}^{Q} \beta^{(q)} \tag{5.4}$$

Notation	Description	Example
subscripts i, j	velocity component indices	u_i, u_j
subscripts l, m, n	spatial coordinate indices	x_l, x_m
superscript (q)	sampling time index	$t^{(q)}$
superscript (p,q)	the p-th estimate at time $t^{(q)}$	$u_i^{(p,q)}$
$\mathscr{D}$	resolution domain	–
$P^{(q)}$	number of estimates in $\mathscr{D}$ at time $t^{(q)}$	–
P	total number of estimates over all sampling times	–
Q	total number of sampling times	–
Q_ψ	number of sampling times given a condition ψ	$Q_{P\geq 2}$
$\prec\cdot\succ_{\mathscr{D}}$	spatial average of a variable over all estimates in $\mathscr{D}$ at a certain time	$\prec u_i^{(p,q)}\succ_{\mathscr{D}}$
$\langle\cdot\rangle_{T\to\infty}$	long time average	$\langle u_i^*\rangle_{T\to\infty}$
$\langle\cdot\rangle_T$	finite time average	$\langle u_i^*\rangle_T$
$\langle\cdot\rangle$	ensemble average	$\langle u_i^*\rangle$
α_{rms} or σ_α	rms of a variable α	u_{rms}, σ_u

Table 5.1: List of notations.

Applying the spatial average and then the long time average to Equation (5.2), we eventually obtain

$$\langle\prec u_i^{(p,q)}\succ_{\mathscr{D}}\rangle_{T\to\infty} = \langle u_i^*\rangle + \mathscr{O}(L^2) \tag{5.5}$$

The derivation of Equation (5.5) relies on several facts and assumptions explained below.

(i) The ergodicity of measured turbulent flows allows the long time average and the ensemble average are interchangeable, i.e.

$$\langle \cdot \rangle = \langle \cdot \rangle_{T \to \infty} \tag{5.6}$$

(ii) Variables evaluated at $\boldsymbol{x}^*$ behave like constants when applying the spatial average at time $t^{(q)}$. For instance,

$$\prec u_i^* \succ_{\mathscr{D}} = u_i^*, \tag{5.7}$$

$$\prec u_{i,l}^* (x_l^{(p,q)} - x_l^*) \succ_{\mathscr{D}} = u_{i,l}^* \prec x_l^{(p,q)} - x_l^* \succ_{\mathscr{D}} \tag{5.8}$$

(iii) Given a time $t^{(q)}$, $\boldsymbol{x}^{(p,q)}$ is random and independent of the flow field. Thereby, the ensemble average of the product between flow variables and spatial position variables is equal to the product of their respective averages. For instance,

$$\langle u_{i,l}^* \prec x_l^{(p,q)} - x_l^* \succ_{\mathscr{D}} \rangle = \langle u_{i,l}^* \rangle \langle \prec x_l^{(p,q)} - x_l^* \succ_{\mathscr{D}} \rangle \tag{5.9}$$

(iv) For a function

$$\Gamma(\boldsymbol{x}^{(p,q)}) = \prod_{l=1}^{3} \left(x_l^{(p,q)} - x_l^* \right)^{s_l} \tag{5.10}$$

wherein s_l is an arbitrary integer power, it can be shown that

$$\langle \prec \Gamma(\boldsymbol{x}^{(p,q)}) \succ_{\mathscr{D}} \rangle = \langle \Gamma(\boldsymbol{x}) \rangle, \qquad \forall \boldsymbol{x} \in \mathscr{D} \tag{5.11}$$

wherein we use $\boldsymbol{x}$ without the superscript (p,q) to emphasize the ensemble average is over all individual estimates in $\mathscr{D}$ regardless of $t^{(q)}$. Furthermore, the three spatial coordinates are independent to each other, so we also have, for instance,

$$\langle (x_m^{(p,q)} - x_m^*)(x_n^{(p,q)} - x_n^*) \rangle = \langle x_m^{(p,q)} - x_m^* \rangle \langle x_n^{(p,q)} - x_n^* \rangle \tag{5.12}$$

when $m \neq n$.

(v) If homogeneous seeding can be assumed, following Equation (5.11) and (5.12), we have

$$\langle (x_l - x_l^*)^{2s+1} \rangle = 0, \qquad s \in \mathbb{Z} \tag{5.13}$$

This identity is favorable as the first order term in Equation (5.2) vanishes after averaging. In addition, the second order term becomes

$$\langle u^*_{i,mm} \rangle \langle (x_m - x_m^*)^2 \rangle = \langle u^*_{i,mm} \rangle L^2/12 \tag{5.14}$$

which is absorbed into $\mathcal{O}(L^2)$ in Equation (5.5).

Equation (5.5) implies a method to estimate the mean velocity with second-order accuracy, namely the truncation error is proportional to L^2.

Moreover, if the mean gradient at x^*, i.e. $\langle u^*_{i,l} \rangle$, is known a priori, we can subtract the mean gradient term to achieve faster convergence. This is because, while in principle the term $\langle u^*_{i,l} \prec x_l^{(p,q)} - x_l^* \succ_{\mathscr{D}} \rangle$ is identically zero when homogeneous seeding is assumed, in reality with finite time averaging, it fluctuates about zero with a root-mean-square value having a positive contribution from $\langle u^*_{i,l} \rangle$. This in fact suggests an improved procedure to estimate the mean velocity:

$$\begin{aligned} \langle \prec u_i^{(p,q)} - \langle u^*_{i,l} \rangle (x_l^{(p,q)} - x_l^*) \succ_{\mathscr{D}} \rangle &= \langle u_i^* \rangle + \langle u'^*_{i,l} \rangle \langle \prec x_l^{(p,q)} - x_l^* \succ_{\mathscr{D}} \rangle + \mathcal{O}(L^2) \\ &= \langle u_i^* \rangle + \mathcal{O}(L^2) \end{aligned} \tag{5.15}$$

The rms errors related to finite time averaging will be further discussed in Section 5.3. Equation (5.15) represents a method of faster convergence to estimate the mean velocity. The implementation requires an iterative process to evaluate the mean velocity and the mean velocity gradient. The estimation of the latter one is derived in the next section.

5.2.2 Mean Velocity Gradient

Subtracting the mean velocity $\langle u_i^* \rangle$ from both sides of Equation (5.2) and multiplying the equation by $(x_{l'}^{(p,q)} - x_{l'}^*)$ gives

$$(u_i^{(p,q)} - \langle u_i^* \rangle)(x_{l'}^{(p,q)} - x_{l'}^*) = u_i'^*(x_{l'}^{(p,q)} - x_{l'}^*) + u_{i,l}^*(x_l^{(p,q)} - x_l^*)(x_{l'}^{(p,q)} - x_{l'}^*) + \mathcal{O}(L^3) \quad (5.16)$$

If we average Equation (5.16) in space and then in time as in the mean velocity derivation, with the facts and assumptions (i) – (v), if follows

$$\begin{aligned} \frac{12}{L^2}\langle \prec (u_i^{(p,q)} - \langle u_i^* \rangle)(x_{l'}^{(p,q)} - x_{l'}^*) \succ_{\mathscr{D}} \rangle_{T\to\infty} &= \frac{12}{L^2}\langle u_i'^* \rangle \langle \prec x_{l'}^{(p,q)} - x_{l'}^* \succ_{\mathscr{D}} \rangle + \langle u_{i,l}^* \rangle \delta_{ll'} + \mathcal{O}(L^2) \\ &= \langle u_{i,l'}^* \rangle + \mathcal{O}(L^2) \end{aligned} \quad (5.17)$$

wherein $\delta_{ll'}$ is the Kronecker delta arising from the identity $\langle \prec (x_l^{(p,q)} - x_l^*)(x_{l'}^{(p,q)} - x_{l'}^*) \succ_{\mathscr{D}} \rangle = \delta_{ll'} L^2/12$. Equation (5.17) implies a method to estimate the mean velocity gradient with second-order accuracy. The contribution from the mean velocity to the rms fluctuation is subtracted similarly to subtracting the mean velocity gradient for estimating the mean velocity.

It becomes clear now that the estimations of the mean velocity and the mean velocity gradient, given in Equation (5.15) and (5.17), respectively, can be implemented reciprocally and iteratively to improve their both accuracies.

5.2.3 Isotropic Dissipation Rate

We now derive the theoretical basis for estimating the isotropic dissipation rate,

$$\epsilon = \nu \langle u_{i,m}' u_{i,m}' \rangle \quad (5.18)$$

The starting point is to realize the fact that the differential between two closely positioned velocity vectors measured at the same time reveals the instantaneous strain rate. Thus,

we consider two velocity estimates at $\boldsymbol{x}^{(p,q)}$ and $\boldsymbol{x}^{(p',q)}$ at time $t^{(q)}$. Writing Equation (5.2) for both velocity estimates, and their difference is

$$u_i^{(p,q)} - u_i^{(p',q)} = u_{i,l}^{*}(x_l^{(p,q)} - x_l^{(p',q)}) + \mathcal{O}(L^2) \tag{5.19}$$

To access the fluctuating velocity gradient responsible for the dissipation rate, the mean velocity gradient is subtracted from both sides of equation (5.19):

$$u_i^{(p,q)} - u_i^{(p',q)} - \langle u_{i,l}^{*}\rangle(x_l^{(p,q)} - x_l^{(p',q)}) = u_{i,l}^{\prime *}(x_l^{(p,q)} - x_l^{(p',q)}) + \mathcal{O}(L^2). \tag{5.20}$$

For succinctness, we use $G_{\nabla u_i'}$ to denote the left side of the above equation, i.e.

$$G_{\nabla u_i'} = u_i^{(p,q)} - u_i^{(p',q)} - \langle u_{i,l}^{*}\rangle(x_l^{(p,q)} - x_l^{(p',q)}) \tag{5.21}$$

Then averaging $G_{\nabla u_i'} G_{\nabla u_i'}$ in space and time yields

$$\langle \prec G_{\nabla u_i'} G_{\nabla u_i'} \succ_{\mathscr{D}} \rangle_{T\to\infty} = \langle u_{i,m}^{\prime *} u_{i,n}^{\prime *}\rangle \langle \prec (x_m^{(p,q)} - x_m^{(p',q)})(x_n^{(p,q)} - x_n^{(p',q)}) \succ_{\mathscr{D}} \rangle + \mathcal{O}(L^4), \tag{5.22}$$

wherein the spatial average of a variable $\alpha^{(p,p',q)} = \alpha(\boldsymbol{x}^{(p,q)}, \boldsymbol{x}^{(p',q)}, t^{(q)})$ involving two estimates in $\mathscr{D}$ at the same time $t^{(q)}$ is defined as

$$\prec \alpha^{(p,p',q)} \succ_{\mathscr{D}} \equiv \frac{2}{P^{(q)}\left[P^{(q)}-1\right]} \sum_{\substack{p,p'=1 \\ p<p'}}^{P^{(q)}} \alpha^{(p,p',q)} \tag{5.23}$$

We use the following facts in combination with (i) – (v) from Section 5.2.1 to continue our derivation.

(vi) For a function

$$\Gamma(\boldsymbol{x}^{(p,q)}, \boldsymbol{x}^{(p',q)}) = \prod_{l=1}^{3} (x_l^{(p,q)} - x_l^{(p',q)})^{s_l} \tag{5.24}$$

wherein s_l is an arbitrary integer power, it can be shown that

$$\langle \prec \Gamma(\boldsymbol{x}^{(p,q)}, \boldsymbol{x}^{(p',q)}) \succ_{\mathscr{D}} \rangle_{T\to\infty} = \langle \Gamma(\boldsymbol{x}, \boldsymbol{x'}) \rangle, \qquad \forall \boldsymbol{x}, \boldsymbol{x'} \in \mathscr{D} \tag{5.25}$$

(vii) In a more general case, if the resolution domain $\mathscr{D}$ is a rectangular box of size $L_1 \times L_2 \times L_3$, we have

$$\langle \prec (x_m^{(p,q)} - x_m^{(p',q)})(x_n^{(p,q)} - x_n^{(p',q)}) \succ_{\mathscr{D}} \rangle = \delta_{mn} L_m^2/6. \tag{5.26}$$

Thereby, the homogeneous isotropic dissipation is obtained by taking the average in a cubic domain with $L_m = L$:

$$\frac{6}{L^2} \langle \prec G_{\nabla u_i'} G_{\nabla u_i'} \succ_{\mathscr{D}} \rangle_{T\to\infty} = \langle u_{i,m}'^* u_{i,m}'^* \rangle + \mathscr{O}(L^2) = \epsilon + \mathscr{O}(L^2) \tag{5.27}$$

Equation (5.27) represents a method to estimate the homogeneous isotropic dissipation with second-order accuracy.

5.3 Error Analysis

The derivations in Section 5.2 were purely theoretical in the sense that we assumed exact particle velocities and infinite-time averages. In this section, we discuss the errors encountered in situations departing from the ideal case. Three categories of error are of our interest:

(a) the errors of the mean velocity and the mean velocity gradient;

(b) the errors due to finite-time averaging;

(c) the bias and random error of PTV.

The consideration of the first category is nontrivial for the reciprocal and iterative evaluations of the mean velocity and the mean velocity gradient, as the errors would propagate from the previous iteration into the next. These errors are considered to be systematic errors fixed in each iteration, and we use $n^*_{b,\langle u_i \rangle}$ and $n^*_{b,\langle u_{i,l} \rangle}$ to denote them with the subscript 'b' implying they are bias errors. Regarding the second category, fluctuation around the true mean is introduced by finite-time averaging, for which we use $\langle \cdot \rangle_T$ to

distinguish it from the true mean. Lastly, when the errors of PTV are considered, a velocity estimate $\hat{u}_i^{(p,q)}$ contains both bias and random error, i.e.

$$\hat{u}_i^{(p,q)} = u_i^{(p,q)} + n_{b,u_i}^{(p,q)} + n_{r,u_i}^{(p,q)} \tag{5.28}$$

Consequently, with these errors taken into account, the equation of the mean velocity estimation becomes

$$\begin{aligned}\langle \prec \hat{u}_i^{(p,q)} - (\langle u_{i,l}^* \rangle - n_{b,\langle u_{i,l}\rangle}^*)(x_l^{(p,q)} - x_l^*) \succ_{\mathscr{D}} \rangle_T = \langle u_i^* \rangle + \underbrace{\left[\langle u_i^* \rangle_T - \langle u_i^* \rangle\right] + \langle u_{i,l}'^* \prec x_l^{(p,q)} - x_l^* \succ_{\mathscr{D}} \rangle_T}_{\text{(b)}} + \mathscr{O}(L^2) \\ + \underbrace{\langle \prec n_{b,u_i}^{(p,q)} \succ_{\mathscr{D}} \rangle_T + \langle \prec n_{r,u_i}^{(p,q)} \succ_{\mathscr{D}} \rangle_T}_{\text{(c)}} + \underbrace{n_{b,\langle u_{i,l}\rangle}^* \langle \prec x_l^{(p,q)} - x_l^* \succ_{\mathscr{D}} \rangle_T}_{\text{(a)}}.\end{aligned} \tag{5.29}$$

The equation for the mean velocity gradient is

$$\begin{aligned}&\tfrac{12}{L^2}\langle \prec [\hat{u}_i^{(p,q)} - (\langle u_i^* \rangle - n_{b,\langle u_i\rangle}^*)](x_{l'}^{(p,q)} - x_{l'}^*) \succ_{\mathscr{D}} \rangle_T \\ &= \langle u_{i,l'}^* \rangle + \underbrace{\frac{12}{L^2}\langle u_i'^* \prec (x_{l'}^{(p,q)} - x_{l'}^*) \succ_{\mathscr{D}} \rangle_T + \left[\langle u_{i,l'}^* \rangle_T - \langle u_{i,l'}^* \rangle\right] + \frac{12}{L^2}\langle u_{i,m}^* \prec (x_m^{(p,q)} - x_m^*)(x_{l'}^{(p,q)} - x_{l'}^*) \succ_{\mathscr{D}} \rangle_T}_{\text{(b)}} + \mathscr{O}(L^2) \\ &+ \underbrace{\frac{12}{L^2}\langle \prec n_{b,u_i}^{(p,q)}(x_{l'}^{(p,q)} - x_{l'}^*) \succ_{\mathscr{D}} \rangle_T + \frac{12}{L^2}\langle \prec n_{r,u_i}^{(p,q)}(x_{l'}^{(p,q)} - x_{l'}^*) \succ_{\mathscr{D}} \rangle_T}_{\text{(c)}} + \underbrace{\frac{12}{L^2} n_{b,\langle u_i\rangle}^* \langle \prec (x_{l'}^{(p,q)} - x_{l'}^*) \succ_{\mathscr{D}} \rangle_T}_{\text{(a)}},\end{aligned} \tag{5.30}$$

wherein $m \neq l'$. Lastly, for the dissipation estimation, with noise terms Equation (5.20) becomes

$$\begin{aligned}G_{\nabla u_i'}^{noi} &= \hat{u}_i^{(p,q)} - \hat{u}_i^{(p',q)} - (\langle u_{i,l}^* \rangle - n_{b,\langle u_{i,l}\rangle}^*)(x_l^{(p,q)} - x_l^{(p',q)}) \\ &= u_{i,l}'^*(x_l^{(p,q)} - x_l^{(p',q)}) + \mathscr{O}(L^2) + n_{br,u_i}^{(p,p',q)} + n_{b,\langle u_{i,l}\rangle}^*(x_l^{(p,q)} - x_l^{(p',q)})\end{aligned} \tag{5.31}$$

wherein

$$n_{br,u_i}^{(p,p',q)} = n_{b,u_i}^{(p,q)} + n_{r,u_i}^{(p,q)} - n_{b,u_i}^{(p',q)} - n_{r,u_i}^{(p',q)} \tag{5.32}$$

Then the equation for the isotropic dissipation estimation is

$$\frac{6}{L^2}\langle \prec G^{noi}_{\nabla u'_i} G^{noi}_{\nabla u'_i} \succ_{\mathscr{D}} \rangle_T = \langle u'^*_{i,l} u'^*_{i,l} \rangle + \underbrace{\langle u'^*_{i,l} u'^*_{i,l} \left[\frac{6}{L^2} \prec (x^{(p,q)}_l - x^{(p',q)}_l)^2 \succ_{\mathscr{D}} -1 \right] \rangle_T}_{\text{(b)1}}$$

$$+ \underbrace{\frac{6}{L^2} \langle u'^*_{i,m} u'^*_{i,n} \prec (x^{(p,q)}_m - x^{(p',q)}_m)(x^{(p,q)}_n - x^{(p',q)}_n) \succ_{\mathscr{D}} \rangle_T}_{\text{(b)2}} + \underbrace{\frac{6}{L^2} \langle \prec n^{(p,p',q)}_{br,u_i} n^{(p,p',q)}_{br,u_i} \succ_{\mathscr{D}} \rangle_T}_{\text{(c)}} + ... + \mathscr{O}(L^2) \quad (5.33)$$

wherein $m \neq n$. In Equation (5.29), (5.30) and (5.33), error terms are labeled according to their corresponding categories. Note the argument in (iii) does not hold for finite-time averaging, so the relevant terms in the above equations are not separated into respective means. The terms of category (b) listed above are all zero-mean, so their contributions are in the form of rms fluctuations. Categories (b) and (c) are the focus of subsequent discussions, and errors of category (a) are dependent on these two error sources.

5.3.1 Error from Finite-Time Averaging

The ensemble and the long-time averages appearing in Section 5.2 were assumed to be the true means in the limit of infinite number of recordings. In realistic data analysis, an average is always evaluated within finite time, making the estimated mean deviate from the true mean. Generally, the rms of the mean estimate of a random variable ξ using N independent samples is given by

$$\sigma_{\langle \xi \rangle_T} = \sigma_\xi / \sqrt{N} \quad (5.34)$$

In our data analysis, the number of velocity fields that can be used for averaging is a function of the domain size L and the seeding density C, i.e. number of particles per unit volume. More specifically, the number of velocity estimates in $\mathscr{D}$ is a random variable following the Poisson distribution, and the probability of κ velocity estimates occurring

in $\mathscr{D}$ at time $t^{(q)}$ is given by

$$\text{Prob}\left\{\text{number of } u_i^{(p,q)} = \kappa \;\middle|\; \boldsymbol{x}^{(p,q)} \in \mathscr{D}\right\} = \frac{\Lambda^\kappa}{\kappa!} e^{-\Lambda} \tag{5.35}$$

wherein $\Lambda = CL^3$ is the mean number of velocity estimates in $\mathscr{D}$. Therefore, as the average operations in the mean velocity and the mean velocity gradient estimation require at least one velocity estimate in $\mathscr{D}$, the number of velocity fields for averaging is

$$Q_{P\geq 1} = Q(1 - e^{-\Lambda}) \tag{5.36}$$

with Q denoting the total number of velocity fields. Likewise, the dissipation estimation requires at least two velocity estimates in $\mathscr{D}$ at the same time, so the number of velocity fields for averaging is

$$Q_{P\geq 2} = Q(1 - e^{-\Lambda} - \Lambda e^{-\Lambda}) \tag{5.37}$$

With the above knowledge, the rms of $\left[\langle u_i^* \rangle_T - \langle u_i^* \rangle\right]$ in Equation (5.29) is readily obtained:

$$\left[\langle u_i^* \rangle_T - \langle u_i^* \rangle\right]_{rms} = (u_i^*)_{rms} / \sqrt{Q_{P\geq 1}} \tag{5.38}$$

Furthermore, plugging Equation (5.36) into the above and considering $1 - e^{-\Lambda} \approx \Lambda$ for $\Lambda \ll 1$, Equation (5.38) becomes

$$\left[\langle u_i^* \rangle_T - \langle u_i^* \rangle\right]_{rms} = \begin{cases} (u_i^*)_{rms} / \sqrt{Q}, & \text{for } \Lambda \gg 1 \\ (u_i^*)_{rms} / \sqrt{QCL^3}, & \text{for } \Lambda \ll 1 \end{cases} \tag{5.39}$$

For the first-order term $\langle u_{i,l}'^* \prec x_l^{(p,q)} - x_l^* \succ_{\mathscr{D}} \rangle_T$ in Equation (5.29), we need to take into account the spatial average in $\mathscr{D}$ that effectively reduces the rms by adding samples. For the rms of $\prec x_l^{(p,q)} - x_l^* \succ_{\mathscr{D}}$, when $\Lambda \gg 1$, a reasonable estimate is by considering it as a finite-sample average with Λ samples, i.e.

$$\left[\prec x_l^{(p,q)} - x_l^* \succ_{\mathscr{D}}\right]_{rms} \approx \left[x_l^{(p,q)} - x_l^*\right]_{rms} / \sqrt{\Lambda}; \tag{5.40}$$

when $\Lambda \ll 1$, as only those velocity fields with at least one velocity estimates occurring in $\mathscr{D}$ are used, the rms of $\prec x_l^{(p,q)} - x_l^* \succ_{\mathscr{D}}$ should approach $\left[x_l^{(p,q)} - x_l^*\right]_{rms}$. Therefore, we can define an effective mean occurrence $\widetilde{\Lambda}$:

$$\widetilde{\Lambda} = \begin{cases} \Lambda, & \text{if } \Lambda > 1 \\ 1, & \text{if } \Lambda < 1 \end{cases} \tag{5.41}$$

and we have

$$\left[\langle u_{i,l}'^* \prec x_l^{(p,q)} - x_l^* \succ_{\mathscr{D}} \rangle_T\right]_{rms} = \frac{\left(u_{i,l}'^*\right)_{rms}\left[\prec x_l^{(p,q)} - x_l^* \succ_{\mathscr{D}}\right]_{rms}}{\sqrt{Q_{P\geq 1}}} \approx \frac{\left(u_{i,l}'^*\right)_{rms}\left[x_l^{(p,q)} - x_l^*\right]_{rms}}{\sqrt{Q_{P\geq 1}\widetilde{\Lambda}}} \tag{5.42}$$

wherein the repeated l does not imply summation. The derivation of the above relation uses the following identity about the rms of the product of two independent random variables u and v:

$$\sigma_{uv}^2 = \sigma_u^2 \langle v \rangle^2 + \sigma_v^2 \langle u \rangle^2 + \sigma_u^2 \sigma_v^2 \tag{5.43}$$

The validity of the approximation in Equation (5.42) is confirmed by a numerical test with Q = 1e05, and the result is presented in Figure 5.1 (more details about the numerical simulation can be found in Section 5.4). We see the model agrees satisfactorily well with the numerical result for a wide range of Λ. Furthermore, if we plug Equation (5.36) and (5.41) into Equation (5.42), then we get

$$\left[\langle u_{i,l}'^* \prec x_l^{(p,q)} - x_l^* \succ_{\mathscr{D}} \rangle_T\right]_{rms} = \begin{cases} \left(u_{i,l}'^*\right)_{rms} / \sqrt{12QCL}, & \text{for } \Lambda \gg 1 \\ \left(u_{i,l}'^*\right)_{rms} / \sqrt{12QCL}, & \text{for } \Lambda \ll 1 \end{cases} \tag{5.44}$$

i.e. two identical relations for large and small Λ.

The preceding derivations have used the mean velocity equation as the example, inferring those error terms of category (b) for the mean velocity gradient and the dissipation are also obtainable in a similar way.

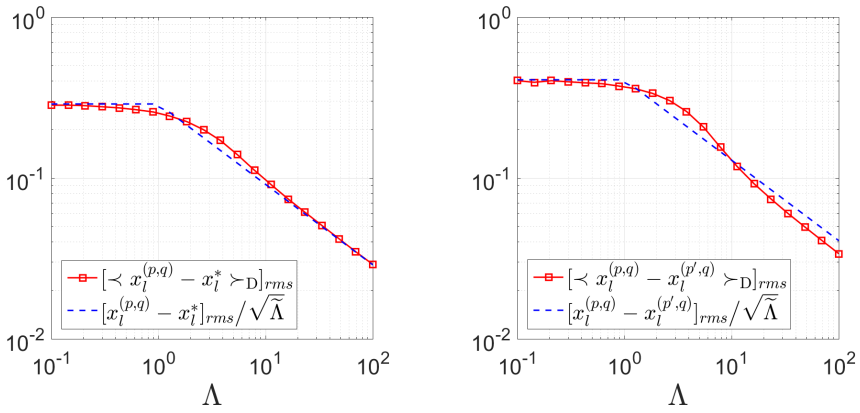

Figure 5.1: Comparison between the model and the numerical result for the rms's of the spatial-average quantities encountered in the estimations of mean velocity (left) and dissipation (right).

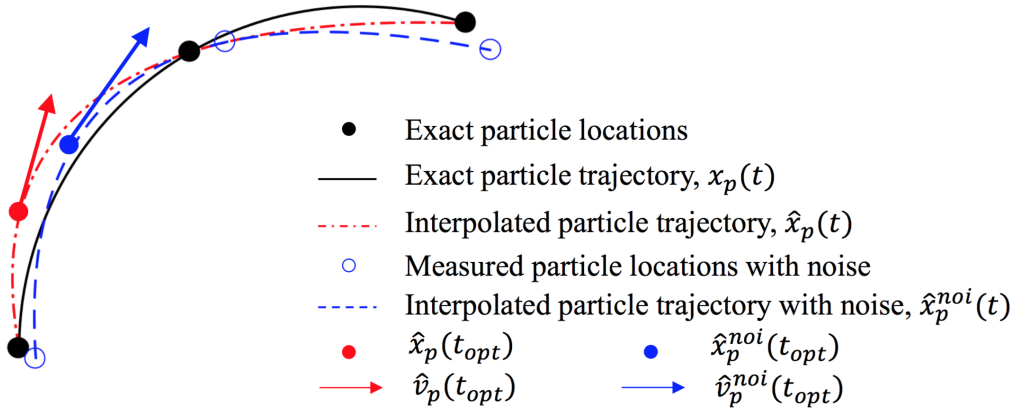

Figure 5.2: Schematic of the bias and the random error arising from PTV.

5.3.2 Error from PTV

The bias and random error of PTV stem from the discrepancy between an estimated trajectory and the true trajectory, as schematically illustrated in Figure 5.2. When exact particle locations are used to interpolate the trajectory (red curve), the resulting velocity

error is a bias error. Using the notations given in Figure 5.2, we define the bias error as

$$\boldsymbol{n}_b = \hat{\boldsymbol{v}}_p(t_{opt}) - \boldsymbol{u}[\hat{\boldsymbol{x}}_p(t_{opt}), t_{opt}]. \tag{5.45}$$

Namely, $\boldsymbol{n}_b$ is the difference between the estimated particle velocity $\hat{\boldsymbol{v}}_p$ and the fluid velocity $\boldsymbol{u}$, both of which are evaluated at the estimated particle position $\hat{\boldsymbol{x}}_p(t_{opt})$ at the optimal time t_{opt}. The optimal time is the time when the combined particle position and velocity rms error is minimized (Ding and Adrian, 2017). It is worth noting that the way we quantify the bias error, i.e. evaluating the velocity error at the estimated particle position, simplifies the error analysis by not explicitly calculating the particle position error. This is valid because, provided particle positions are random and seeding is homogeneous, the estimated particle positions are also random and homogeneously distributed. In a more strict sense following Ding and Adrian (2017), the velocity bias is given by

$$\boldsymbol{n}'_b = \hat{\boldsymbol{v}}_p(t_{opt}) - \boldsymbol{u}[\boldsymbol{x}_p(t_{opt}), t_{opt}]. \tag{5.46}$$

which is the difference between the estimated and the true particle velocity assuming no slip. Comparing $\boldsymbol{n}'_b$ to $\boldsymbol{n}_b$, it immediately follows

$$\boldsymbol{n}_b = \boldsymbol{n}'_b + [\boldsymbol{x}_p(t_{opt}) - \hat{\boldsymbol{x}}_p(t_{opt})] \cdot \nabla \boldsymbol{u}\Big|_{\hat{\boldsymbol{x}}_p(t_{opt})} + h.o.t. \tag{5.47}$$

which implies the bias error could benefit from the reduction in either the velocity error or the position error.

When particle locations are measured with noise (blue circles), the resulting velocity error contains both bias and random error. Similarly to the bias error, the random error is quantified as

$$\boldsymbol{n}_r = \hat{\boldsymbol{v}}_p^{noi}(t_{opt}) - \boldsymbol{u}[\hat{\boldsymbol{x}}_p^{noi}(t_{opt}), t_{opt}] - \boldsymbol{n}_b. \tag{5.48}$$

Hitherto, we have derived and explained how to calculate different error terms. The quantitative results of the errors will then be obtained once the flow field and the particle distribution are given. This is addressed in Section 5.4 using synthetic turbulence.

5.4 PTV Simulation with Synthetic Turbulence

5.4.1 Generation of Synthetic Turbulence

Synthetic turbulence has been employed widely as a powerful tool for studying turbulence properties and validating measurement techniques. It offers the convenience and flexibility to control turbulence parameters that are usually difficult to customize with DNS data. Perfect modeling of real turbulence is almost impossible, but it is often sufficient to have a synthetic turbulent flow only satisfy the features of most interest, e.g. spectrum, isotropy, etc. In this respect, three commonly adopted methods of generating synthetic turbulence are respectively based on random Fourier modes (Kraichnan, 1970, 1976; Fung *et al.*, 1992), random vortices (Avellaneda *et al.*, 1991; Tanaka and Eaton, 2007) and stochastic differential equations (Haworth and Pope, 1986; Careta *et al.*, 1993). In this work, we follow the random Fourier method in Kraichnan (1970) to generate synthetic turbulence fields for PTV simulations. The implementation is outlined below.

The synthetic turbulence consists of a mean velocity field in the x-direction and a small-scale fluctuating field assumed to be homogeneous and isotropic. The random fluctuating field is a superposition of N independent Fourier modes:

$$\boldsymbol{u}'(\boldsymbol{x},t) = \sum_{n=1}^{N} \left[\boldsymbol{a}_n \cos\left(\boldsymbol{\kappa}_n \cdot \boldsymbol{x} + \omega_n t\right) + \boldsymbol{b}_n \sin\left(\boldsymbol{\kappa}_n \cdot \boldsymbol{x} + \omega_n t\right)\right] \tag{5.49}$$

wherein

$$\boldsymbol{a}_n = \boldsymbol{\zeta}_n \times \boldsymbol{\kappa}_n / |\boldsymbol{\kappa}_n|, \quad \boldsymbol{b}_n = \boldsymbol{\xi}_n \times \boldsymbol{\kappa}_n / |\boldsymbol{\kappa}_n| \tag{5.50}$$

which guarantees flow incompressibility, i.e. $\boldsymbol{\kappa}_n \cdot \boldsymbol{a}_n = \boldsymbol{\kappa}_n \cdot \boldsymbol{b}_n = 0$, and the independence of $\boldsymbol{a}_n$ and $\boldsymbol{b}_n$ on the wave number $|\boldsymbol{\kappa}_n|$. $\boldsymbol{\zeta}_n$ and $\boldsymbol{\xi}_n$ are both isotropically distributed 3-D vectors with each of their component independently following a Gaussian distribution centered at zero with a standard deviation σ. $\boldsymbol{\kappa}_n$ is also isotropically distributed in the 3-D space with each component obeying a distribution satisfying a desired energy spectrum. A model spectrum from Kraichnan (1970) well serves our purpose:

$$E(\kappa) \propto \kappa^4 e^{-2\kappa^2/\kappa_0^2} \tag{5.51}$$

wherein κ_0 defines the peak. The corresponding one-dimensional spectrum $E_{11}(\kappa_1)$ is then given by

$$E_{11}(\kappa_1) \propto e^{-2\kappa_1^2/\kappa_0^2} \tag{5.52}$$

which is a Gaussian profile with a standard deviation $\kappa_0/2$. (The relation between $E(\kappa)$ and $E_{11}(\kappa_1)$ can be found in section 7.6.3 of Bernard and Wallace, 2002.) Alternatively, one could use the model spectrum proposed by Pope (2000) for a more realistic tail at large κ. Equation (5.52) suggests that each component of $\boldsymbol{\kappa}_n$ should follow a Gaussian

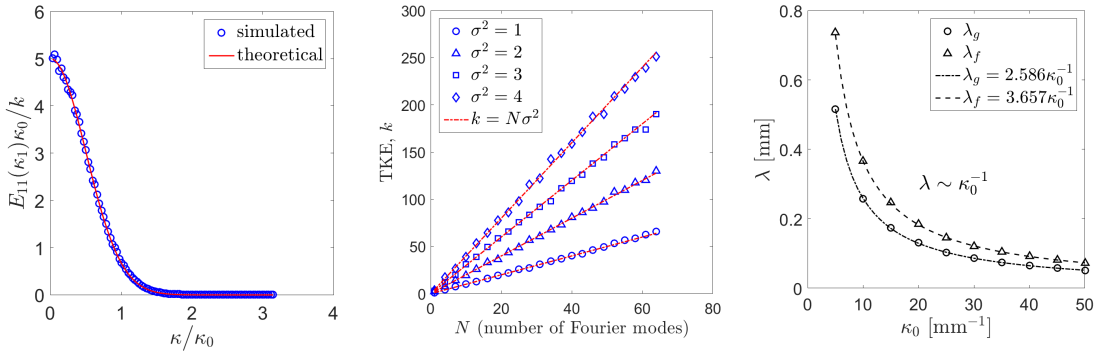

Figure 5.3: One-dimensional spectrum (left), TKE (middle) and Taylor microscale (right) of the simulated synthetic turbulence.

distribution with a standard deviation $\kappa_0/2$. This is because, with $\boldsymbol{a}_n$ and $\boldsymbol{b}_n$ given in Equation (5.50), each Fourier mode contributes equally to the turbulent kinetic energy. Therefore, $E_{11}(\kappa_1)$ is directly determined from the distribution of a single component of $\boldsymbol{\kappa}_n$. Consequently, Equation (5.49) represents a statistically isotropic synthetic turbulent flow with a well-defined energy spectrum given in Equation (5.51) or (5.52). As evident in Figure 5.3 (left), the spectrum from our simulation agrees well with the target spectrum.

The TKE, $k = 3u_{rms}^2/2$, of the synthetic turbulence is a direct consequence of the superposition of Fourier modes. Each mode has a contribution of σ^2, so the total TKE is

$$k = N\sigma^2, \tag{5.53}$$

and it immediately follows

$$u_{rms} = \sqrt{2N\sigma^2/3} \tag{5.54}$$

The TKE relation (5.53) is also confirmed by the simulation results shown in Figure 5.3 (middle). The longitudinal and transverse Taylor microscale, λ_f and λ_g, are determined numerically using their definitions:

$$\langle u_{1,1}^2 \rangle = u_{rms}^2/\lambda_g^2 = 2u_{rms}^2/\lambda_f^2 \tag{5.55}$$

and plotted against κ_0 in Figure 5.3 (right). The proportionality of Taylor microscale to κ_0^{-1},

$$\lambda_g = 2.586/\kappa_0, \tag{5.56}$$

is expected as the turbulence length scale should be only determined from the characteristic wave length. With u_{rms} and λ_g, the isotropic dissipation rate is readily calculated:

$$\epsilon = 15\nu u_{rms}^2/\lambda_g^2 \tag{5.57}$$

In addition to the length scale, the temporal evolution of the flow field is characterized by the parameter ω_n. We picked ω_n following a Gaussian distribution with a standard devia-

tion ω_0, and the resulting time-delay correlation of the velocity field is also a Gaussian function:

$$R_{u'u'}(\tau)/u_{rms}^2 = e^{-\frac{1}{2}\omega_0^2\tau^2} \tag{5.58}$$

we generated the synthetic turbulence in a cubic domain of edge length $10\lambda_g$, i.e. $x, y, z \in [-5\lambda_g, 5\lambda_g]$. The key parameters of the flow are summarized in Table 5.2. The Taylor-scale Reynolds number $Re_\lambda = u_{rms}\lambda_g/\nu$ is relative low compared to realistic turbulent flows. This is an artifact arising from u_{rms} and λ_g being two independent parameters in the random Fourier model ($u_{rms} \sim \sqrt{N\sigma^2}$, $\lambda_g \sim \kappa^{-1}$), which is typically not true for realistic turbulence (λ_g/u_{rms} is roughly proportional to $Re^{-\frac{1}{2}}$, see Pope, 2000). However, since a low Re_λ yields a large Kolmogorov length scale η ($\eta \sim \lambda_g Re_\lambda^{-1/2}$), it benefits our simulation with reduced computational cost considering, for instance, $Q_{P\geq 2}$ at $L \sim \eta \ll 1$ scales as η^6. Although a more realistic set of parameters may be employed, the present synthetic turbulence has the two most desired properties – randomness and isotropy. Therefore, it suffices for developing and validating our method to estimate turbulence statistics.

Parameter	Value
N	32
κ_0 [mm^{-1}]	10
σ [mm/s]	10
ω_0 [s^{-1}]	10
u_{rms} [mm/s]	46.2
λ_g [mm]	0.258
η [mm]	0.147
Re_λ	0.8
C [counts/mm^3]	32

Table 5.2: Simulation parameters. η and Re_λ are computed with ν = 1.5e-05 m^2/s.

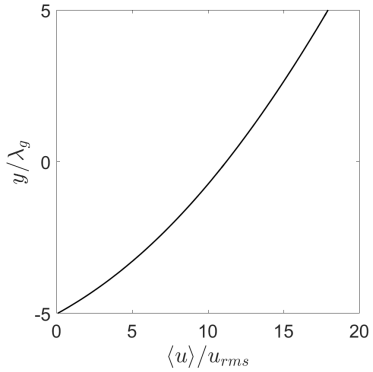

Figure 5.4: The mean velocity profile model for the simulation.

The mean velocity field is along the x-direction with a y-dependent profile, which is a logarithmic function added to a linear function, :

$$\langle u \rangle / u_{rms} = c_0 + c_1 y/\lambda_g + c_2 \log(y/\lambda_g + e^2) \tag{5.59}$$

The merit of such functional form is the ease of controlling the shape and the magnitude, as well as the mean flow field is infinitely differentiable. We picked c_0 = –3.2, c_1 = 0.6 and c_2 = 7.2 to satisfy $\langle u \rangle > 0$ for all y and $u_{rms}/\langle u \rangle \approx 0.1$ at the center. The resulting velocity profile is shown in Figure 5.4.

5.4.2 PTV Errors

To study the PTV errors in the context of PTV measurement of turbulent flows, we computed the particle tracks in the time-dependent velocity fields by numerically solving

$$\dot{\boldsymbol{x}}_p(t) = \boldsymbol{u}[\boldsymbol{x}_p(t), t] \tag{5.60}$$

wherein $\boldsymbol{x}_p$ denotes the particle position, and $\boldsymbol{u}$ is the superposition of $\boldsymbol{u}'$ and $\langle u \rangle \hat{\boldsymbol{e}}_x$ respectively given in Equation (5.49) and (5.59). Q = 1e05 independent velocity fields

were generated with an average of $C(10\lambda_g)^3 = 553$ particle tracks in each field. Particle positions were solved at four pulse times with an uniform inter-pulse time $\delta t = 0.001\omega_0^{-1}$ to simulate 4-pulse PTV measurements. Each particle track was estimated by fitting a cubic curve to the four computed particle positions. The optimal particle position and velocity were then evaluated at the one-quarter time between the first and the last pulse. Here, the determination of the optimal time t_{opt} follows the conclusion in Ding and Adrian (2017). We picked the t_{opt} value for the high noise level range because the rms error at low noise level is overall small.

We calculated the bias error for each particle track in the way described in Section 5.3.2. Figure 5.5(a) shows the pdf of each component of n_b. The symmetries of the pdfs are apparent, implying the n_{b,u_i}-related terms in Equation (5.29) and (5.30) are zero-mean and only contribute rms fluctuations. The symmetric pdfs result from the isotropic fluctuating field as well as the unidirectional homogeneous mean flow field. If the flow experiences a non-zero pressure gradient, the flow acceleration or deceleration may cause a skewed n_b distribution, as the bias error is strongly dependent on the acceleration factor of a particle trajectory (Ding and Adrian, 2017). Another observation in Figure 5.5(a) is that the width of $n_{b,u}$ distribution is smaller than those of $n_{b,v}$ and $n_{b,w}$ whose pdfs are nearly identical. If we project a particle trajectory onto the x-direction and the $y-z$ plane respectively, the dominant mode in the x-direction is a constant-velocity motion provided the particle is not near $y/\lambda_g = -5$, whereas the projection on the $y-z$ plane is a random curve with no directional preference. Thus, it is interpreted that the bias error of a nearly straight trajectory is less significant than that of a curved trajectory, which is consistent with the findings in Ding and Adrian (2017). Furthermore, as both the velocity and the position error scale with the length of a particle trajectory, the n_b distribution should also have a dependence on the mean velocity $\langle u \rangle$. In this regard,

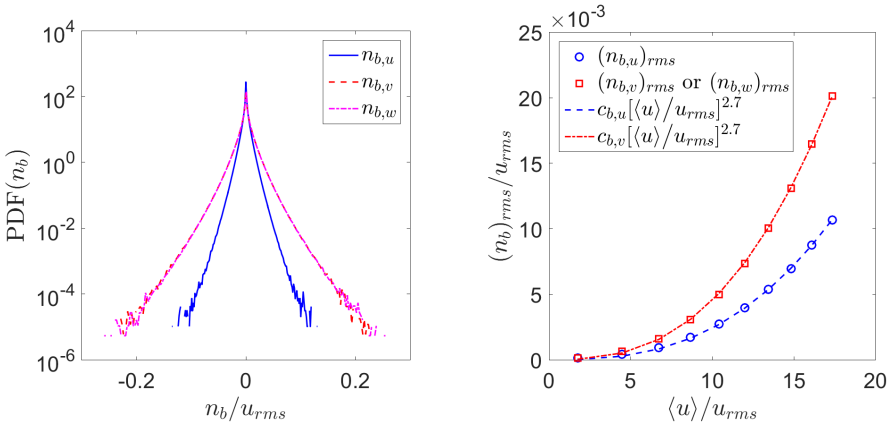

(a) pdf of n_b (b) rms of n_b

Figure 5.5: Statistics of PTV bias error. $c_{b,u}$ = 4.832e-06; $c_{b,v}$ = 9.085e-06.

we computed the rms of n_b at different y locations, and plot the result as a function of $\langle u\rangle/u_{rms}$ in Figure 5.5(b). Clearly, the rms of n_b rises with increasing $\langle u\rangle$, and for the current test case the curves follow power laws with the same exponent of approximately 2.7.

For the PTV random error resulting from the random particle locating noise, we investigated a range of locating rms error $(\delta x_p)_{rms}$ from $10^{-4}\lambda_g$ to $10^{-2}\lambda_g$, corresponding to 1.6e-03 to 1.6e-01 voxel with a reconstruction resolution of 64 vox/mm. As expected, the random error is independent of the shape and length of a particle trajectory, but rather it is a function of the locating noise $(\delta x_p)_{rms}$. The distribution of n_r has a Guassian-like pdf that retains the shape at different y positions, as illustrated in Figure 5.6(a) in form of a scatter plot. Figure 5.6(b) manifests the linear dependence of $(n_r)_{rms}$ on $(\delta x_p)_{rms}$, which again agrees with the result in Ding and Adrian (2017).

These findings of n_b and n_r are favorable for the estimations of the mean velocity and the mean velocity gradient, as the error terms of category (c) in Equation (5.29) and (5.30) are all zero-mean and only add rms fluctuations to the results. However, due to the

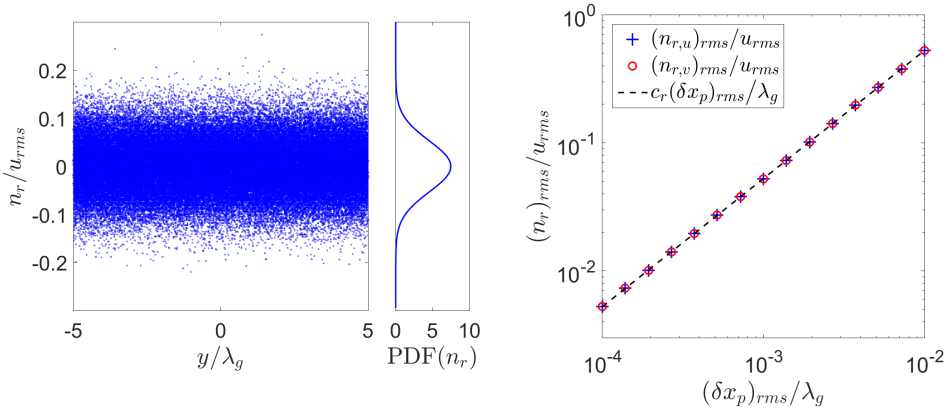

(a) pdf of n_r

(b) rms of n_r

Figure 5.6: Statistics of PTV random error. $c_r = 52.58$.

square operation in the dissipation estimation, the category (c) term in Equation (5.33) is always positive with a magnitude proportional to $(n_b)_{rms}$ and $(n_r)_{rms}$.

5.4.3 Mean Velocity and Mean Velocity Gradient

To validate our ensemble PTV method, and to further investigate the effects of different errors on the statistics, we applied the method to the synthetic turbulent flow to estimate the mean velocity and the mean velocity gradient. As both the truncation error and the finite-time-averaging error are dependent on the domain size L, we primarily present the results in terms of varying L to facilitate our discussion.

First, we look at the mean velocity with merely the finite-time-averaging errors, i.e. with $n_{b,u_i} = n_{r,u_i} = 0$. Figure 5.7 shows the estimates of $\langle u \rangle$ at $(x, y, z) = (0,0,0)$ for $0.1 \leq L/\lambda_g \leq 10$. The vertical axis represents the absolute difference between the estimated and the true mean velocity, i.e.

$$|\delta_{\langle u \rangle}| = |\langle \widehat{u} \rangle - \langle u \rangle| \tag{5.61}$$

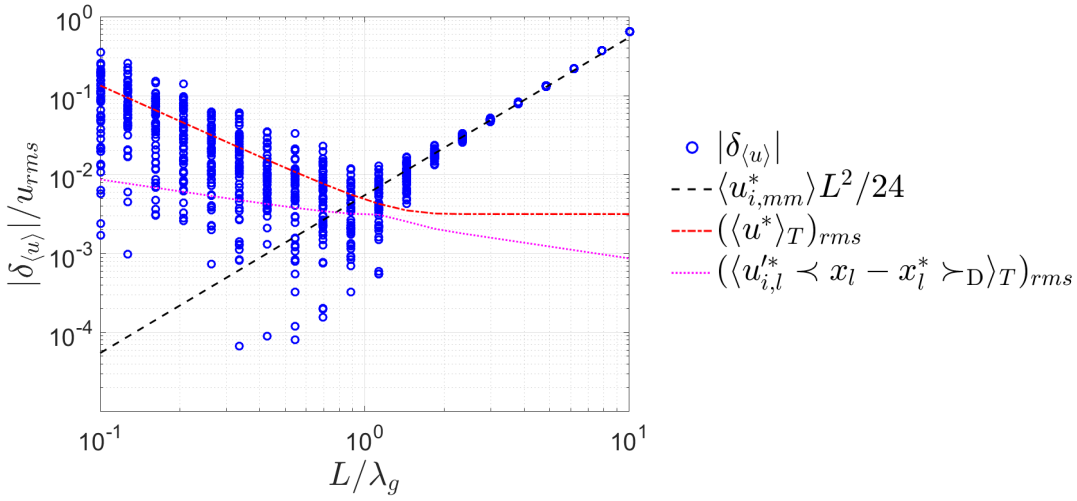

Figure 5.7: Estimates of the mean velocity at $(x,y,z) = (0,0,0)$ for varying L without PTV errors. Results from 50 independent datasets are superposed to illustrate the rms fluctuation.

The results from 50 independent datasets, each dataset having Q = 1e05 velocity fields, are superposed to illustrate the rms of $\langle\widehat{u}\rangle$. At large L, $\delta_{\langle u\rangle}$ is dominated by the truncation error $\mathcal{O}(L^2)$. As L decreases, while the truncation error keeps going down, the fluctuation of $\delta_{\langle u\rangle}$ becomes significant due to the increases in the rms's of the finite-time-averaging terms. For the mean velocity, the dominant rms fluctuation is from $\left[\langle u_i^*\rangle_T - \langle u_i^*\rangle\right]$. It stays constant at large L and then increases as $L^{-3/2}$ towards small L. The turning point occurs where $CL^3 \approx 1$, as implied in Equation (5.39). Such observation suggests an optimal domain size L_{opt} at which the ratio between the truncation error and the dominant rms fluctuation is, say, roughly 5-10. For the data presented in Figure 5.7 , $L_{opt} \approx 2\lambda_g$, and the resulting $\delta_{\langle u\rangle}$ is roughly 2% of u_{rms} and thus 0.2% of $\langle u\rangle$. Improved accuracy is achievable with larger Q and/or C since $(\langle u^*\rangle_T)_{rms}$ scales as $(QC)^{-1/2}$ as also implied in Equation (5.39).

Figure 5.8 presents the results when PTV errors are taken into account. Data of two extreme locating noise levels, i.e. the smallest and the largest $(\delta x_p)_{rms}/\lambda_g$, are displayed. With the discussions and results in Section 5.3.1 and 5.4.2, the rms fluctuations arising from the PTV bias and random error are calculable. Specifically, for both $\Lambda \gg 1$ and $\Lambda \ll 1$,

$$(\langle \prec n_{r,u} \succ_{\mathscr{D}} \rangle_T)_{rms} = \frac{(n_{r,u})_{rms}}{\sqrt{Q_{P\geq 1}\widetilde{\Lambda}}} \approx \frac{(n_{r,u})_{rms}[(\delta x_p)_{rms}]}{\sqrt{QCL^3}}, \tag{5.62}$$

and

$$(\langle \prec n_{b,u} \succ_{\mathscr{D}} \rangle_T)_{rms} \approx \frac{(n_{b,u})_{rms}(L)}{\sqrt{QCL^3}}, \tag{5.63}$$

both of which scale as $L^{-3/2}$. Note the dependence of $(n_{r,u})_{rms}$ on $(\delta x_p)_{rms}$ and the dependence of $(n_{b,u})_{rms}$ on L. The former is given in Figure 5.6(b), whereas the latter requires a deduction using the result shown in Figure 5.5(b) and the mean velocity profile (5.59). It is evident that, with the 4-pulse PTV algorithm, the bias error fluctuation is negligibly small. The random error fluctuation strongly depends on the locating noise level, but it is not an influential factor until $(\delta x_p)_{rms}$ exceeds $0.01\lambda_g$ (0.16 vox), which

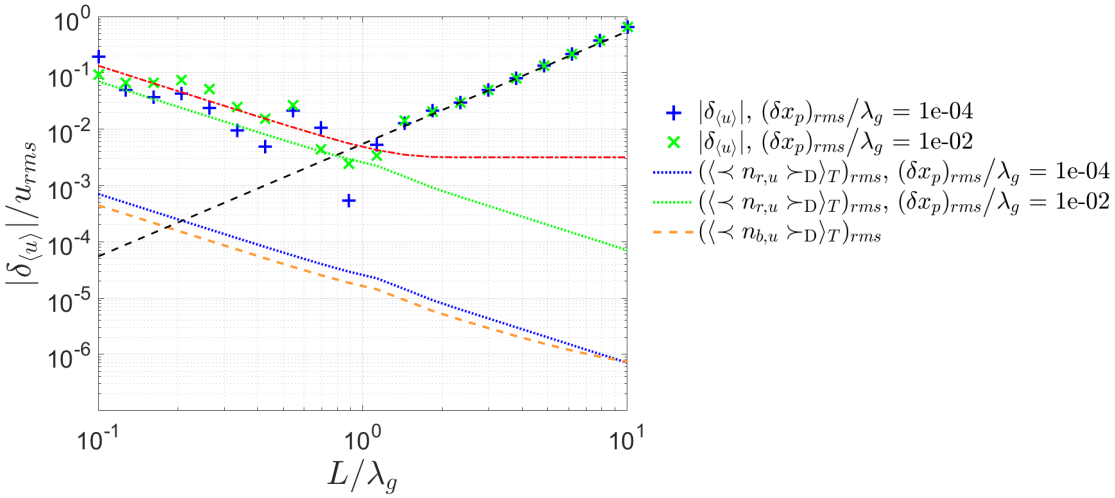

Figure 5.8: Estimates of the mean velocity at $(x, y, z) = (0, 0, 0)$ for varying L with the PTV errors taken into account.

is considered to be a fairly large number in most experiments. Thereby, the simulation results suggest that the rms fluctuations arising from PTV errors are not prominent for mean velocity estimation, especially when particle positions are accurately determined using advanced algorithms (e.g. Wieneke, 2012; Schanz *et al.*, 2012).

In addition to evaluating the mean velocity at L_{opt}, another way to achieve high accuracy is by utilizing the well-behaved truncation error as a function of L. Based on preceding derivations, when L falls in the range where the rms fluctuations are negligible, the estimated mean velocity can be expressed using only the true mean plus the truncation error:

$$\langle \widehat{u} \rangle = \langle u \rangle + a_2 L^2 + a_4 L^4 + h.o.t, \tag{5.64}$$

which clearly suggests us to excavate an accurate $\langle \widehat{u} \rangle$ by determining the coefficient a_{2n}. This can be done by fitting the following model to $\langle \widehat{u} \rangle$:

$$\langle \widehat{u} \rangle (L_i) = \sum_{n=0}^{\mathcal{N}} a_{2n} L_i^{2n} \tag{5.65}$$

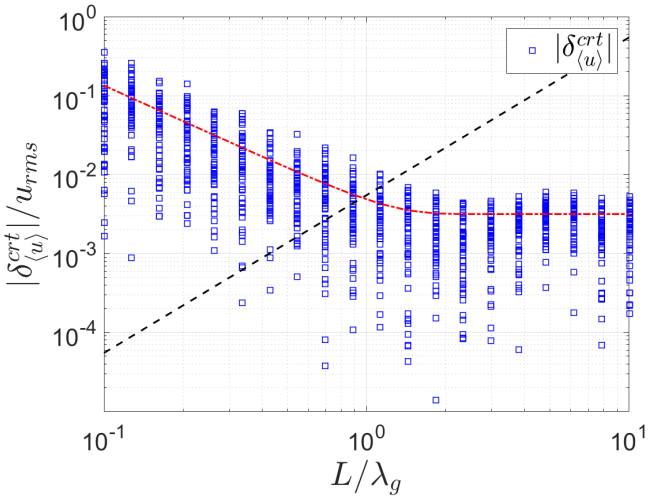

Figure 5.9: Estimates of the mean velocity after correction. Results from 50 independent datasets are superposed to illustrate the rms fluctuation.

wherein L_i is picked from the range with low rms fluctuation, which in our case corresponds to $L > 2\lambda_g$. For the L range shown in Figure 5.7, it suffices to use $\mathcal{N} = 2$, but a higher order may be necessary for an extended L range. Clearly, a_0 determined from Equation (5.65) can be the new $\langle\widehat{u}\rangle$. However, our implementation uses a different model derived from Equation (5.65):

$$\Delta\langle\widehat{u}\rangle(L_i) = \langle\widehat{u}\rangle(L_{i+1}) - \langle\widehat{u}\rangle(L_i) = \sum_{n=1}^{\mathcal{N}} a_{2n}(L_{i+1}^{2n} - L_i^{2n}) \tag{5.66}$$

This allows us to get a good sense of the rms fluctuation level as the noise stands out when compared to the difference of the estimates at two adjacent L_i. The new estimate at L_i is then obtained:

$$\langle\widehat{u}\rangle^{crt}(L_i) = \langle\widehat{u}\rangle(L_i) - \sum_{n=1}^{\mathcal{N}} a_{2n}L_i^{2n} \tag{5.67}$$

wherein we use a superscript '*crt*' to indicate the new estimate after the correction procedure.

The new $\langle\widehat{u}\rangle$ after correction is presented in Figure 5.9. It is seen that $\delta_{\langle u\rangle}^{crt}$ is approximately aligned with $(\langle u^*\rangle_T)_{rms}$, which is what we expect after subtracting the systematic truncation error. $\delta_{\langle u\rangle}^{crt}$ at large L represents the achievable accuracy, which is comparable to $u_{rms}/\sqrt{Q}$. In addition, one could further reduce the uncertainty by averaging $\langle\widehat{u}\rangle^{crt}$ over the same L range used in the data fitting, i.e. $L > 2\lambda_g$ for the present case. The resulting rms of $\delta_{\langle u\rangle}^{crt}$ is approximately 0.15% of u_{rms}, which is an order of magnitude lower than the $\delta_{\langle u\rangle}$ at L_{opt}. Note the above correction procedure works only when a fitting model for the truncation error can be inferred with confidence from flow properties. The tested synthetic turbulence is ideal in terms of homogeneity and isotropy. Realistic flows may result in more complicated shapes of the truncation error with varying L. Under those circumstances, it may still be advantageous to use L_{opt} to evaluate $\langle\widehat{u}\rangle$. This is further illustrated in Section 5.5 with experimental data.

A similar analysis for the mean velocity gradient yields quantitatively consistent conclusions. Figure 5.10 (top) presents $\langle\widehat{u_{1,2}}\rangle$ for $0.33 \leq L/\lambda_g \leq 10$. The observations are similar to those in the mean velocity plot, except the dominant rms fluctuation has a steeper increase towards small L. It stems from the zero-th order term in the Taylor's expansion, i.e. the fluctuating velocity u'^*, being divided by L to reveal the velocity

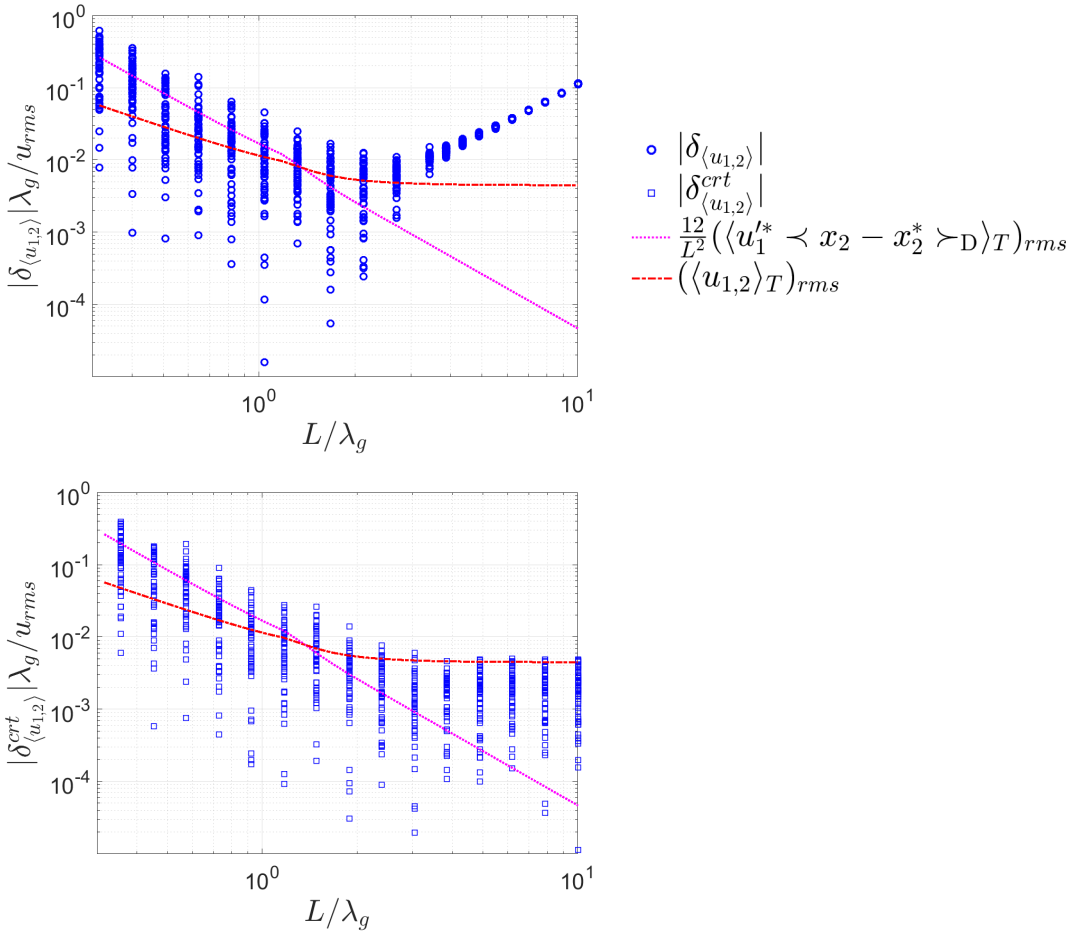

Figure 5.10: Estimates of the mean velocity gradient before (top) and after (bottom) correction. Results from 50 independent datasets are superposed to illustrate the rms fluctuation

gradient. The dominant rms fluctuation is given by

$$\frac{12}{L^2}(\langle u_1'^* \prec x_2^{(p,q)} - x_2^* \succ_{\mathscr{D}} \rangle_T)_{rms} \approx \frac{12}{L^2}\frac{(u_1'^*)_{rms} L/\sqrt{12\widetilde{\Lambda}}}{\sqrt{Q_{P\geq 1}}} \approx \frac{\sqrt{12}(u_1'^*)_{rms}}{\sqrt{QCL^{5/2}}} \tag{5.68}$$

for both $\Lambda \gg 1$ and $\Lambda \ll 1$, which scales as $L^{-5/2}$. Figure 5.10 also indicates $L_{opt} \approx 4\lambda_g$, and $|\delta_{\langle u_{1,2}\rangle}|$ at L_{opt} is approximately 2% of u_{rms}/λ_g and 1% of $\langle u_{1,2}\rangle$. After a similar correction procedure as for $\langle \widehat{u} \rangle$, the rms of $|\delta^{crt}_{\langle u_{1,2}\rangle}|$ drops slightly below $(\langle u_{1,2}\rangle)_{rms}$ at large L, which is possibly because, in our data fitting, the spacing between adjacent L_i for the mean velocity gradient was smaller than that of the mean velocity. Nevertheless, $(\delta^{crt}_{\langle u_{1,2}\rangle})_{rms}$ and $(\langle u_{1,2}\rangle)_{rms}$ are comparable at large L, consistent with the observation for the mean velocity estimation.

In virtue of the preceding discussions on the rms fluctuation, it now becomes more convincing that the mean velocity and the mean velocity gradient need to be subtracted for the estimations of the mean velocity gradient and the mean velocity, respectively, as seen in Equation (5.15) and (5.17). Namely, by removing their contributions to the

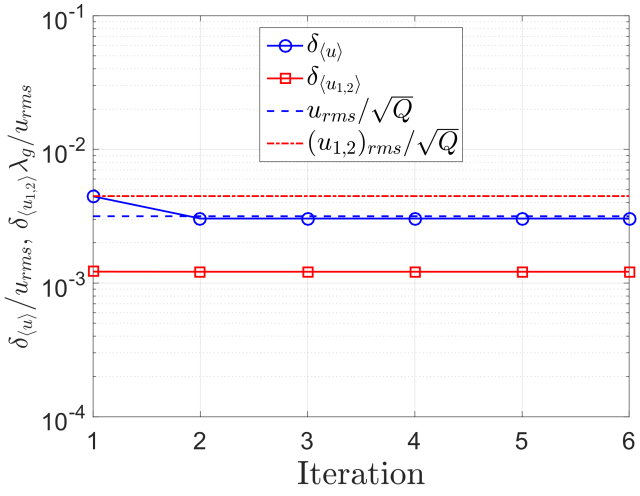

Figure 5.11: Estimates of mean velocity and mean velocity gradient with the reciprocal and iterative strategy.

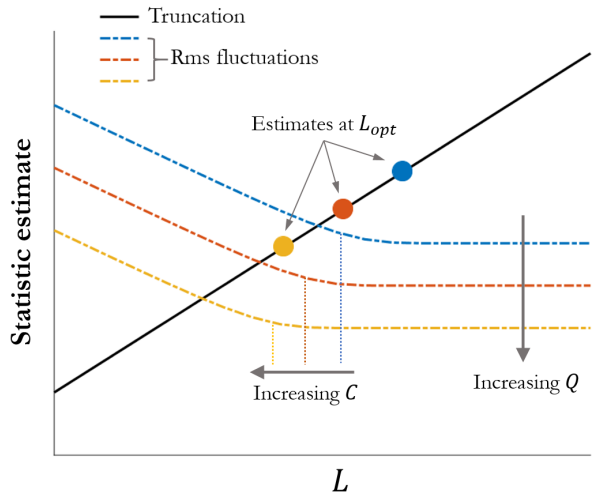

Figure 5.12: Schematic of the effect of rms fluctuation on estimation accuracy. Displayed is in logarithm scale.

rms fluctuation, improved accuracies could be achieved with the same Q and C. In this regard, we tested the reciprocal and iterative strategy for evaluating $\langle u \rangle$ and $\langle u_{1,2} \rangle$. Note, for the tested synthetic turbulence, $\langle u_{1,2} \rangle$ is the only non-zero mean gradient; for realistic flows with other non-zero gradients of velocity, Equation (5.15) actually implies all $\langle u^*_{i,l} \rangle$ terms need to be evaluated and subtracted. We started the process from evaluating $\langle u \rangle$ without subtracting $\langle u_{1,2} \rangle$, and then iteratively evaluate $\langle u_{1,2} \rangle$ and $\langle u \rangle$. The results of six iterations are shown in Figure 5.11, in which we observe the initial improvement of the mean velocity estimate. Again, $\delta_{\langle u \rangle}$ and $\delta_{\langle u_{1,2} \rangle}$ are comparable to $u_{rms}/\sqrt{Q}$ and $(u_{1,2})_{rms}/\sqrt{Q}$, respectively.

Thus far, our discussion has implied the rms fluctuation arising from finite time averaging plays a key role in determining the overall accuracy. Although this is quite an intuitive conclusion, our analysis provides a quantitative and elaborated explanation of the mechanism, which is schematically summarized in Figure 5.12. The turning point in the plot, at which the rms fluctuation starts rising, is approximately given by $C^{-1/3}$. Thus,

as the seeding density C increases, the turning point moves towards small L, and so does L_{opt}. When Q increases, the rms fluctuation overall attenuates, so the estimate can be evaluated at a smaller L_{opt} with an improved accuracy. Additionally, a large Q is beneficial considering the accuracy achieved after the correction procedure is comparable to the level of rms fluctuation at large L.

5.4.4 Isotropic Dissipation Rate

The fundamental difference of the estimation of dissipation rate compared to first-order statistics, e.g. $\langle u \rangle$ and $\langle u_{1,2} \rangle$, is that the PTV errors are amplified and not averaged out due to the square operation. This is evident in Equation (5.33), in which the category (c) term, scaling as L^{-2}, is the square of the combined error from two particles. Figure 5.13 presents the estimates of dissipation rate at different noise levels with Q = 1e05. When the noise level is negligible, as seen in Figure 5.13(a), the dependence on L is similar to what we observed in the mean velocity result. That is, the truncation error decreases when L gets smaller until the rms fluctuation becomes dominant. Here, the dominant rms fluctuations, i.e. the rms's of the (b)1 and (b)2 term in Equation (5.33), increase as L^{-3}. With an elevated noise level, as seen in Figure 5.13(b), the shape of $|\delta_\epsilon|$ changes significantly, and it follows a L^{-2} trend at small L. This adds complexity to the strategy of accurately determining ϵ: with very small noise level, it is still possible to pick an optimal L to evaluate ϵ; However, when the noise level is prominent, a correction procedure, similar to that for the mean velocity estimation but with a modified fitting model, is required. The consideration for choosing a proper fitting model is twofold. First, it needs to incorporate an L^{-2} term to account for prominent PTV error. Second, it is noticed that the truncation error of dissipation estimate deviates rapidly from the leading order term

L^2. This is attributed to the cross products between lower- and higher-order terms during the square operation. Therefore, we add more truncation terms to the fitting model:

$$\Delta\hat{\epsilon}(L_i) = \hat{\epsilon}(L_{i+1}) - \hat{\epsilon}(L_i) = a_{-2}(L_{i+1}^{-2} - L_i^{-2}) + \sum_{n=1}^{\mathcal{N}} a_{2n}(L_{i+1}^{2n} - L_i^{2n}) \tag{5.69}$$

with $\mathcal{N} = 4-8$, and the dissipation estimate at L_i after correction is

$$\hat{\epsilon}^{crt}(L_i) = \hat{\epsilon}(L_i) - a_{-2}L_i^{-2} - \sum_{n=1}^{\mathcal{N}} a_{2n}L_i^{2n} \tag{5.70}$$

As reported in numerous literatures, accurate estimation of dissipation rate is much more difficult than mean velocity and mean velocity gradient. Based on our test results, there seems no universal rule for the implementation of the proposed framework using ensemble PTV data. However, we would discuss a few empirical rules that help improve the performance most of the time.

(1) The most powerful way to improve the accuracy is to increase the total number of velocity fields, Q.

When the PTV error is negligibly small, as the case in Figure 5.13(c), the benefit of a large Q is similar to what we have discussed in Section 5.4.3, i.e. it allows using a smaller L_{opt} to obtain a more accurate $\hat{\epsilon}$. When the PTV error is significant, as the case in Figure 5.13(d), a large Q improves the reliability of the curve fitting in the correction procedure. This is demonstrated in Figure 5.14, in which the enhanced smoothness of $\Delta\hat{\epsilon}$ is apparent with an increasing Q.

(2) When the PTV error is not significant, one should set $a_{-2} = 0$ in the fitting model given in Equation (5.69) to reduce uncertainty. For instance, it suffices to use only the positive-exponent terms for the case shown in Figure 5.13(c).

(3) When $\Delta\hat{\epsilon}$ is noisy, perform the curve fitting in the region with relatively less noise. For instance, in Figure 5.14(a), only the data of $L_i/\lambda_g > 10^{0.25}$ could be used for the curve fitting.

(4) While it is difficult to claim an optimal $\mathcal{N}$, one could possibly obtain a robust estimate of the dissipation rate by observing the trend of $\hat{\epsilon}$ over a range of $\mathcal{N}$, or by a histogram-based method explained below.

Besides the fitting model (5.69) primarily used in our analysis, we also tested a simple

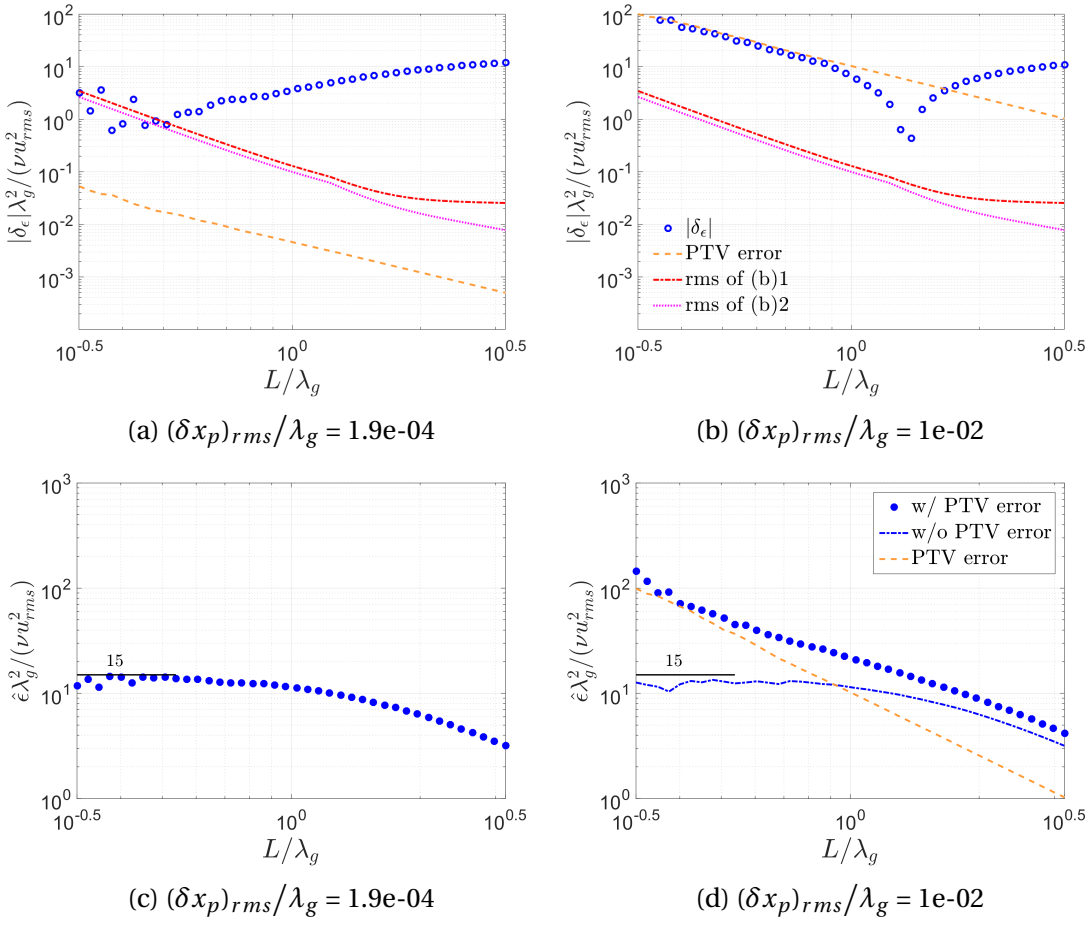

(a) $(\delta x_p)_{rms}/\lambda_g$ = 1.9e-04 (b) $(\delta x_p)_{rms}/\lambda_g$ = 1e-02

(c) $(\delta x_p)_{rms}/\lambda_g$ = 1.9e-04 (d) $(\delta x_p)_{rms}/\lambda_g$ = 1e-02

Figure 5.13: Dissipation estimates at different noise levels. The curves of 'PTV error ' , '(b)1' and '(b)2' are given in Equation (5.33). Top: $|\delta_\epsilon|$; bottom: $\hat{\epsilon}$. The true dissipation rate 15 (after normalization) is indicated.

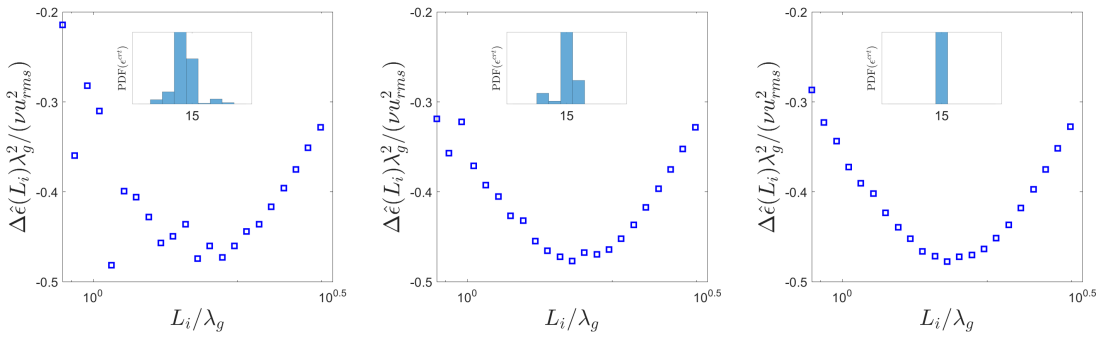

(a) Q = 1e05 (b) Q = 1e06 (c) Q = 1e07

Figure 5.14: Effect of Q on the smoothness of $\Delta\hat{\epsilon}$ and the pdf of $\hat{\epsilon}^{crt}$. The pdfs are calculated using all data points displayed in their respective figures.

version similar to that of the mean velocity given in Equation (5.65):

$$\hat{\epsilon}(L_i) = a_0 + a_{-2}L_i^{-2} + \sum_{n=1}^{\mathcal{N}} a_{2n}L_i^{2n}, \tag{5.71}$$

and used a_0 as $\hat{\epsilon}^{crt}$ (one single a_0 for each $\mathcal{N}$). Figure 5.15 displays a_0 as a function of $\mathcal{N}$ for three different cases. Here, we remove the $a_{-2}L^{-2}$ term for the low-noise-level case in Figure 5.15(a), but retain it for the other two cases in which the PTV error is influential. It is observed that the most accurate estimate of the dissipation rate occurs approximately at an optimal order, $\mathcal{N}_{opt}$, where the curve changes its geometric property. In Figure 5.15(b), it is the inflection point of the curve, while in 5.15(a) and 5.15(c) they correspond to the turning points. This is probably not a coincidence, but rather it arises from the mechanisms responsible for the shapes of the two segments (below and beyond $\mathcal{N}_{opt}$) being different. With small $\mathcal{N}$, the model is incapable to predict the rapid deviation from L^2, so the estimates asymptotically approach the true value when increasing $\mathcal{N}$; passing $\mathcal{N}_{opt}$, the high-order polynomial model starts adapting itself to the imbedded noise, which leads to the different geometry of the curve. Note this model combined with the reasoning from the curve geometry sometimes works better than the model in Equation

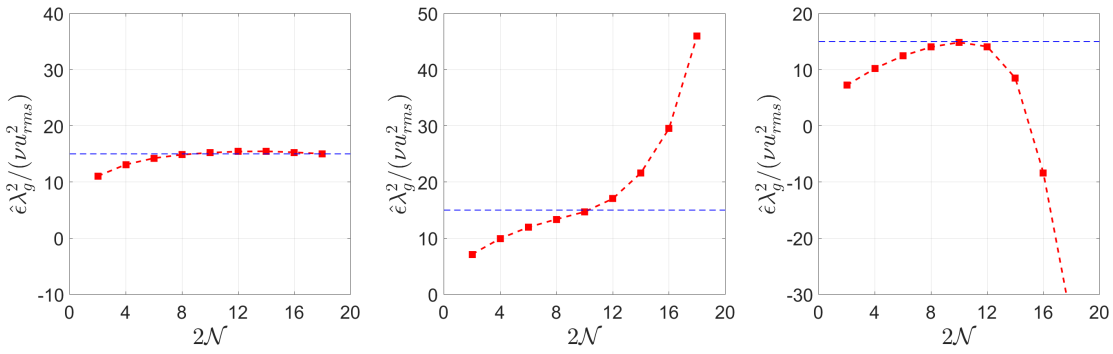

(a) $(\delta x_p)_{rms}/\lambda_g$ = 1.9e-04 (b) $(\delta x_p)_{rms}/\lambda_g$ = 3.7e-03 (c) $(\delta x_p)_{rms}/\lambda_g$ = 1e-02

Figure 5.15: Dissipation estimates with varying $\mathcal{N}$ using the fitting model (5.71). For the low-noise-level case in (a), the term $a_{-2}L^{-2}$ is removed. The true dissipation rate 15 (after normalization) is indicated.

(5.69), especially when the noise level is considerable. This is probably because, without using $\Delta\hat{\epsilon}$, the noise appears relatively small, which helps improve the fitting reliability.

Another strategy to extract the dissipation rate, possibly more robust, is to locate the peak in the histogram of $\hat{\epsilon}^{crt}(L_i)$. With the correction procedure described by Equation (5.69) and (5.70), at each L_i, we obtain a new estimate $\hat{\epsilon}^{crt}(L_i)$. Marching over $\mathcal{N} = 4-8$, the statistics of $\hat{\epsilon}^{crt}(L_i)$ turns out to be informative about the true dissipation rate. In our implementation, the final estimate of dissipation is the averaged $\hat{\epsilon}^{crt}(L_i)$ within the highest bin. According to our test, a bin width of $\nu u_{rms}^2/\lambda_g^2$ works well. The corresponding histograms of the data shown in Figure 5.14 are presented in the insets. The change in the peak location and the data spread with increasing Q is a good indication of improved measurement quality. Note the histogram in Figure 5.14(a) was calculated using all $\Delta\hat{\epsilon}$ data points shown in the figure, including the noisy range $L_i/\lambda_g < 10^{0.25}$. As a result, the histogram has a peak at $\hat{\epsilon}^{crt}\lambda_g^2/(\nu u_{rms}^2) = 14$, which leads to an error of approximately 7% of the true dissipation. This can certainly be improved by using only the data points in $L_i/\lambda_g > 10^{0.25}$, as we suggested above.

Employing the above discussed empirical rules, the achievable accuracy in our simulation with Q = 1e05 is within 2% of the true dissipation rate, which can be further improved with a larger Q.

5.5 Experiment in APG-TBL

5.5.1 Experimental Setup and Data Acquisition

A tomographic PIV experiment was conducted in the Eiffel-type atmospheric wind tunnel at Bundeswehr University in Munich. The wind tunnel has a 22-m-long test section with a 2×2 m^2 cross section. A 7-m-long steel model consisting of two s-shaped sections and a 4-m-long flat plate was mounted vertically to the side wall to form three zones with, respectively, favorable pressure gradient (FPG), zero pressure gradient (ZPG) and adverse pressure gradient (APG). (See the sketch in Figure 5.16) The main stream velocity was set to 5 m/s to avoid noticeable vibration of the wind tunnel. A flexible tube with a line of holes and connected to a Laskin nozzle at the tunnel entrance was attached to the same side wall vertically at the beginning of the test section to provide a satisfactory seeding density downstream near wall.

The data was taken in the APG zone through a glass window precisely flushed to the steel wall. As shown in Figure 5.17, four high-speed cameras (LaVision Imager Pro HS), each equipped with a 2x teleconverter and a Scheimpflug mount, were employed to simultaneously record particle images from different angles. A 768-by-552-pixel subregion of each imaging sensor was used to capture images for the sake of sufficient framing rate. Camera calibration was done by traversing a calibration target (Edmund Optics) along

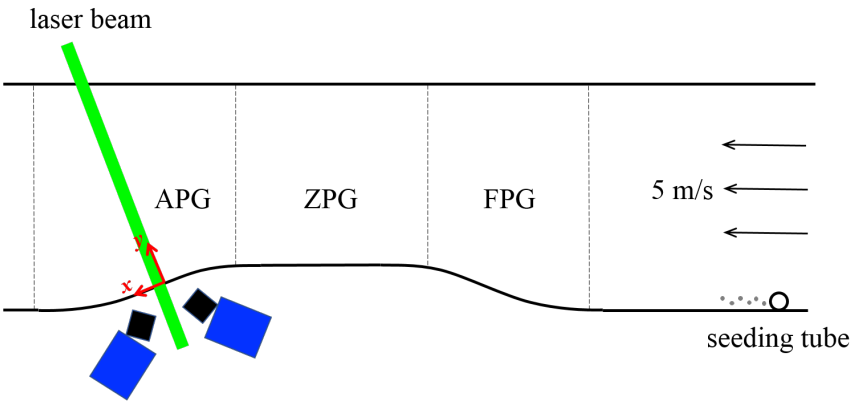

Figure 5.16: Schematic of the experimental setup.

Figure 5.17: Camera configuration of the tomographic TBL measurement.

the wall-normal direction in 0.25-mm steps covering a distance of 4.25 mm from the wall. The calibration dots are 0.5 mm in diameter with a spacing of 1 mm. The mapping function was calculated using the third-order polynomial model proposed in Soloff *et al.* (1997). A registration procedure using recorded particle images (Wieneke, 2008) was implemented to reduce the mean residual disparity to below 0.05 pixel. The magnification, estimated from the mapping function, was approximately 0.75, corresponding to 70

pix/mm. A high-repetition-rate Nd:YLF laser was set up on the opposite side of the test section to emit a laser beam perpendicular to the glass window. The cross sectional area of the beam is approximately 8 mm (x) × 2 mm (z). A total of 10 datasets, each containing 10000 recordings of the turbulent boundary layer, was obtained at a framing rate of 9 kHz.

5.5.2 Data Processing

Due to the limited laser pulse energy at the high repetition rate (9 kHz), the particle image signal-to-noise ratio was not ideal. Therefore, we preprocessed the recorded images to enhance their quality. The historical mean was first removed from each image in the sequence, followed by adding back 12 intensity counts. This is nearly equivalent to subtracting the historical minimum that is usually applied to remove the background, except it is more robust for those pixels having at least one extremely low reading. (We observed an extremely low reading likely occurred after an over exposure.) The intensity level of each image was then normalized with respect to the first frame. In addition, we subtracted the sliding minimum using a 3×3 kernel, and convolved the images with a 3×3 Gaussian kernel to recover particle tails.

The rest of the data processing consisted of two parts: (1) 3-D particle position reconstruction and (2) particle tracking. We reconstructed the particle positions in the measurement volume primarily following the algorithm reported in Fuchs *et al.* (2016), which combines tomographic reconstruction and 3-D particle triangulation to materially reduce the percentage of ghost particles. The implementation of the algorithm is outlined as follows, in which the criterion for determining a ghost particle is slightly modified compared to the original one.

With the preprocessed images, 3-D intensity distributions were reconstructed by surface segmentation technique inside a volume of 4 mm (x) × 4 mm (y) × 1.875 mm (z) with a 64 vox/mm reconstruction resolution. Reconstructed particles were then located by convolving each reconstruction volume with a 5×5×5 Gaussian blob. On the other hand, individual particle images were identified on recorded images using a 5×5 Gaussian template. With particles identified in both the image space and the objective space, if a reconstructed particle is projected onto all four cameras, on each camera, there should be one matched particle image. Here, If a particle image is only associated with an unique reconstructed particle, we call this an unique matching; if there are multiple reconstructed particles corresponding to the same particle image, we call it an ambiguous matching. In the original work by Fuchs *et al.* (2016), the authors proposed to completely reject a reconstructed particle if it had more than two ambiguous matchings. Such criterion succeeded to reduce the percentage of ghosts to below 1%. However, it also caused the percentage of correctly reconstructed particles to drop quickly with an increasing image density. This is because, in principle, a ghost reconstruction has ambiguous matchings on all cameras, but not vice versa. Therefore, in our implementation, we retained a reconstructed particle either when it had at least two unique matchings, or when the projected particle location was the nearest to the matched particle image on at least three cameras. Finally, the 3-D position of each retained reconstructed particle was calculated by triangulation from four matched particle images.

Each particle was then tracked over four successive frames. The non-iterative particle tracking algorithm developed by Fuchs *et al.* (2017), combined with predictors based on flow spatial and temporal information, was adopted to yield reliable result with light computational burden. For the first two frames, the instantaneous velocity field was initially estimated on a coarse grid, which allowed us to define a reasonable search

volume for each particle in the second frame. Out of all possible candidates within the search volume, the correct match was then determined if the resulting displacement was the closest to the peak of the histogram collecting all possible displacements of all neighboring particles. Here, the neighbors of a particle of interest are defined inside an ellipsoid that is 1.25 mm wide in both the x and z direction and 0.25 m high in the y direction. For frame 3 and 4, the process was similar except the search volume was a sphere of a 0.6-mm diameter around the position predicted from the already measured particle displacement.

An example field of 4-pulse particle tracks is presented in Figure 5.18. An average of 127 particle tracks were obtained for each velocity field, which translates to a seeding density of 4.23 particles/mm^3. Particle velocities and the positions to assign velocity vectors were calculated with the method described in Section 5.4.2. With a total of 100000

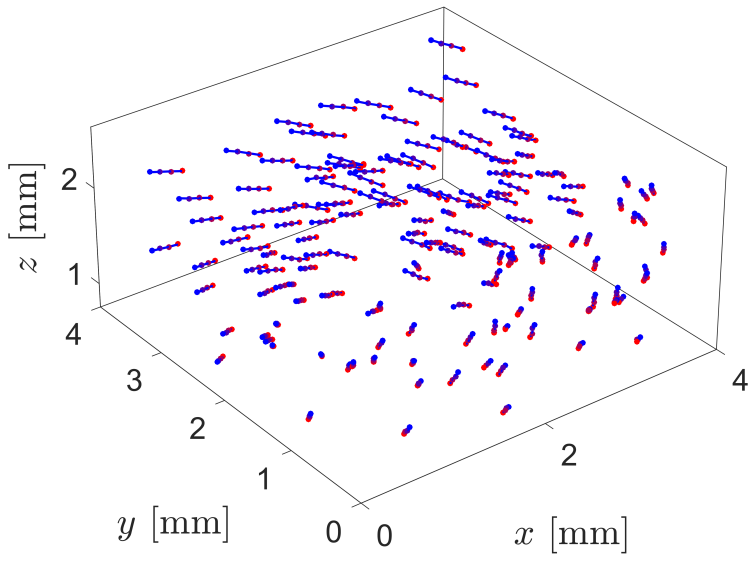

Figure 5.18: An example field of 4-pulse particle tracks. Particle positions are color coded from blue to red to indicate the time order.

recordings, we obtained $Q = 25000$ velocity fields for averaging. We used these data to estimate the mean velocity, the mean velocity gradient and the isotropic dissipation rate, which are discussed in later sections.

5.5.3 Seeding Homogeneity

To examine the extent to which the assumption of homogeneous seeding holds, Figure 5.19 presents the distribution of estimated particle location, $\hat{\boldsymbol{x}}_p$, i.e. the location to assign a velocity vector. Due to the fact that a particle track is identified only if all four particle positions occur within the reconstruction box, the boundaries essentially act as filters modifying near-boundary distributions. For instance, near $x = 4$mm, we observe decreasing number of velocity vectors when the averaged trajectory length increases towards $y = 4$ mm. The explanation is also schematically illustrated in Figure 5.20. Such issue is less severe near $x = 0$ mm since each velocity vector is evaluated at the one-quarter time along a trajectory. The rapid drop near $y = 4$ mm is due to the top boundary sifts out those particle tracks with positive v-components. However, these boundary effects can be a trivial matter considering the data near boundaries can be discarded. In contrast, the inhomogeneous seeding near $y = 0$ mm, as evident in Figure 5.19(a), is more problematic for estimating near-wall statistics. It probably arises from the diffusion occurring when tracer particles travel from the upstream seeding tube to a far downstream location. In this regard, a special near-wall treatment will be discussed later. It is also noticed that, away from the boundaries, the pdf of $\hat{y}_p$ is slightly convex downwards, which may be an artifact in our data processing. Further investigation is needed to fully understand the cause. In Figure 5.19(b), the distribution in the z-direciton reveals the laser intensity profile, which appears to be nearly a parabola. Note only the z-direction dimension of

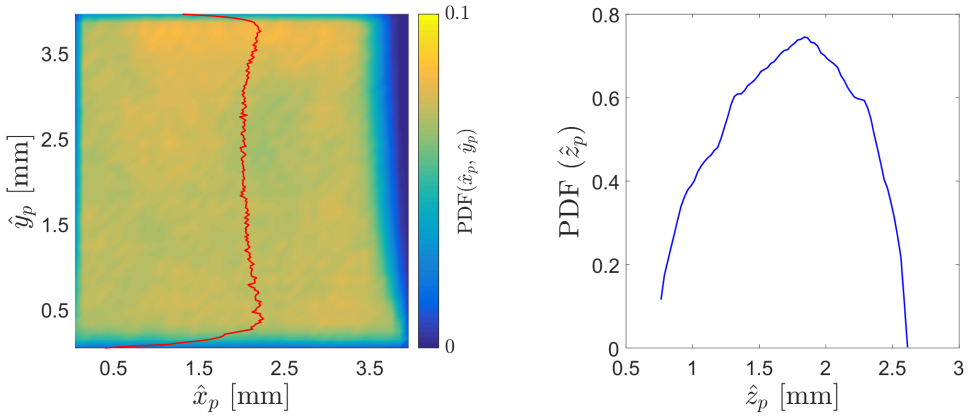

(a) joint pdf of $\hat{x}_p$ and $\hat{y}_p$

(b) pdf of $\hat{z}_p$

Figure 5.19: Distribution of estimated particle location, $\hat{\boldsymbol{x}}_p$. The red curve in (a) represents the pdf of $\hat{y}_p$.

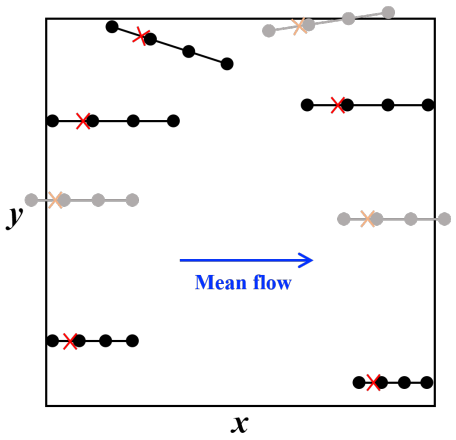

Figure 5.20: Schematic of the boundary effect causing inhomogeneous near-boundary distribution. Identified and unidentified particle tracks are drawn in black and gray, respectively. Each red cross denotes the location to assign the velocity vector, which is the one-quarter point in time.

the reconstruction volume is close to the actual laser beam thickness. For the x- and y-direction, the reconstruction was well within the illuminated volume.

The aforementioned inhomogeneity of $\hat{\boldsymbol{x}}_p$ certainly introduces errors to the statistical estimates, which will be discussed along with the results in the subsequent sections.

5.5.4 Mean Velocity and Mean Velocity Gradient

Using the ensemble of particle velocities, we estimated the mean velocity and the mean velocity gradient for 0.02 mm $\leq y \leq$ 3.9 mm at x = 2 mm and z = 1.6875 mm, i.e. along the wall-normal axis of symmetry of the reconstruction volume. The evaluation was an iterative and reciprocal process as described in Section 5.4.3. Figure 5.21 (left) presents a typical result of the dependence of $\langle \widehat{u} \rangle$ on varying domain size after two iterations. It was obtained by using a domain with $L_x = 2L_y$ and L_z = 1.875 mm and centered at each $\boldsymbol{x}^*$, intended to include more particles for reduced rms fluctuation. Using the full thickness in the z-direction in principle does not affect the truncation error considering all spanwise

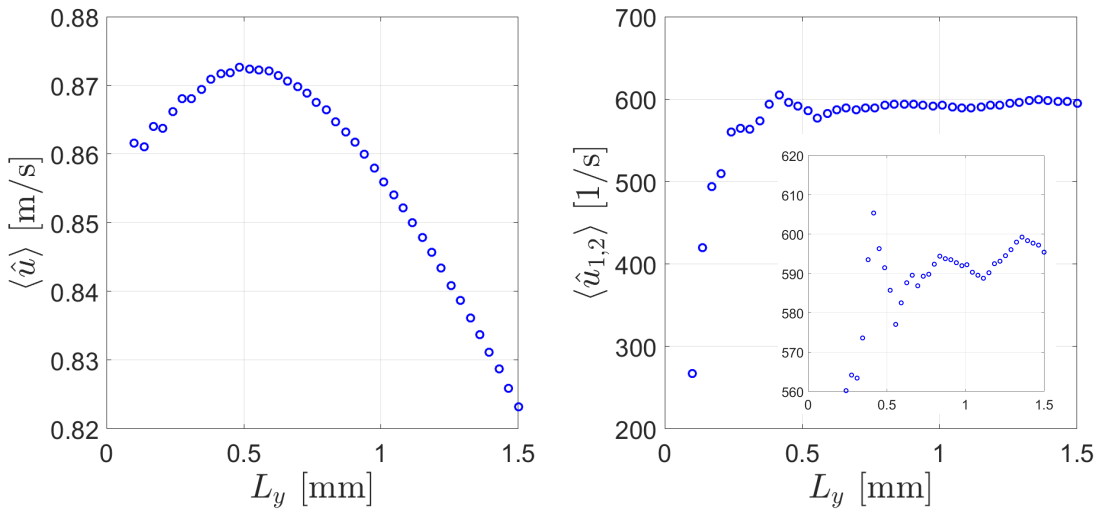

Figure 5.21: Estimates of the streamwise mean velocity (left) and the wall-normal mean velocity gradient (right) using a resolution domain of varying size centered at $\boldsymbol{x}^*$ = (2, 1, 1.6875) mm. The domain size is given by $L_x = 2L_y$ and L_z = 1.875 mm.

derivatives are zero. It is observed that the rms fluctuation becomes influential below approximately $L_y = 0.2$ mm. Beyond this point, the smoothness of the curve suggests a systematic variation of the truncation error with increasing L_y. The trend at large L_y is quadratic, agreeing with the theory and the simulation result. However, the increase in the region $0.1 < L_y < 0.5$ is not predicted, and it appears to result from a linear dependence on L_y. The possibility of the inhomogeneity of $\hat{\boldsymbol{x}}_p$ causing $\langle u^*_{1,2} \prec y^{(p,q)} - y^* \succ_{\mathscr{D}} \rangle_T$ to vary linearly with L_y was ruled out as the estimation with the actual distribution of $\hat{\boldsymbol{x}}_p$ (see Figure 5.19) did not give matched order of magnitude. Thus, without fully understanding the functional form of the truncation error, we did not perform the correction scheme described in Section 5.4.3. Instead, the mean velocity estimate was taken at the smallest L_y below which the rms fluctuation starts amplifying. We observed from our data that $L_{y,opt} = 0.2$ mm was a good universal choice for this purpose.

A typical result of the mean velocity gradient estimate, $\langle \widehat{u_{1,2}} \rangle$, is displayed in Figure 5.21 (right). The rapid change at small L_y was indeed seen from the simulation, but the behavior of the truncation error is again puzzling. So we also take $\langle u_{1,2} \rangle$ at an optimal L_y, which appears to be approximately 0.75 mm, as shown in the inset in Figure 5.21 (right). Note the measurement noise is amplified during differentiation, so the estimation of mean velocity gradient has to use an L_y larger than that of the mean velocity.

The above strategy is only applicable to the region away from the wall, as decreasing L_y from both sides of $\boldsymbol{x}^*$ is not feasible for y near zero. To this regard, we adopted a special near-wall treatment utilizing the linear velocity profile in the viscous sublayer with a single-sided domain. More specifically, the resolution domain is above y^* with a height of $L_y/2$. As a result of that, the first-order term is no longer zero-mean, but instead increases linearly with L_y with a slope equal to $\langle u^*_{1,2} \rangle$. Moreover, the linear term $\langle u^*_{1,2} \prec y^{(p,q)} - y^* \succ_{\mathscr{D}} \rangle_T$ is the only non-zero truncation term as the linearity of $\langle u \rangle$ in the

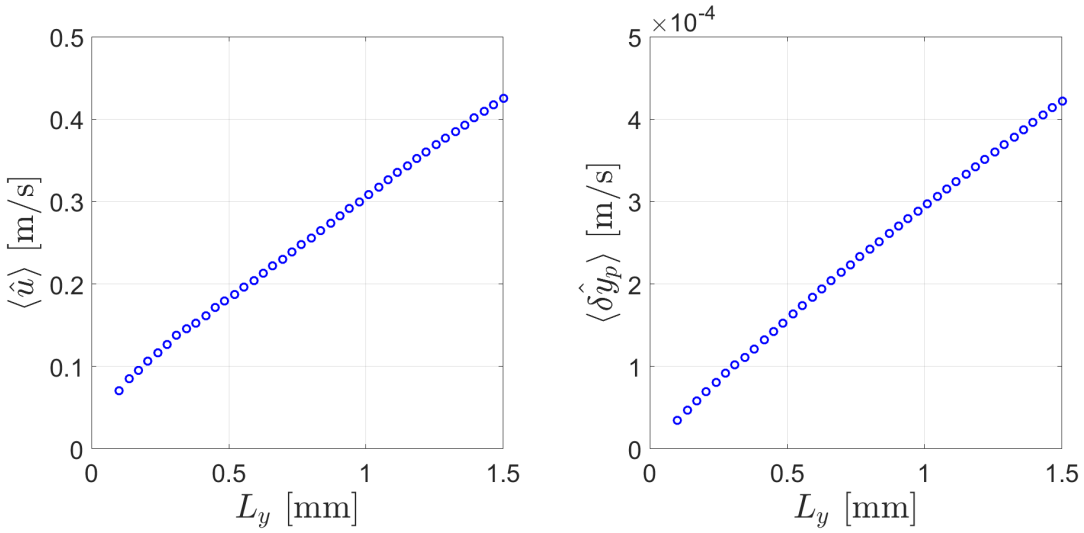

Figure 5.22: Estimates of the mean velocity at $y = 0.02$ mm (left) and the corresponding mean deviation in the y-direction (right) using a single-sided domain (i.e. $y^{(p,q)} \geq y^*$).

viscous sublayer ensures higher-order derivatives to be zero. Figure 5.22 (left) shows the dependence of $\langle \widehat{u} \rangle$ on L_y using such a single-sided domain at $y^* = 0.02$ mm. The trend is linear except for the small distortion near $L_y = 0$, which appears to be mostly attributed to the inhomogeneous near-wall seeding. This is supported in Figure 5.22 (right) with the plot of the actual mean deviation, $\langle \delta \widehat{y}_p \rangle = \langle \prec y^{(p,q)} - y^* \succ_{\mathscr{D}} \rangle_T$, calculated from the experimental data. It is apparent the inhomogeneous near-wall seeding causes the curve to slightly depart from a straight line. The above discussion in fact suggests that $\langle u^* \rangle$ and $\langle u^*_{1,2} \rangle$ in the viscous sublayer can be estimated respectively from a_1 and a_2 in the following fit:

$$\langle \widehat{u} \rangle = a_1 + a_2 \langle \delta \widehat{y}_p \rangle \tag{5.72}$$

We applied this strategy for $0.02 \text{ mm} \leq y \leq 0.28$ mm, which later will be seen to correspond to $0.32 \leq y^+ \leq 2.37$. The strategy of using an optimal L_y is otherwise applied.

Compiling the results obtained in the two different regions with the above discussed rational analysis, Figure 5.23 (left) presents the mean streamwise velocity for 0.02 mm

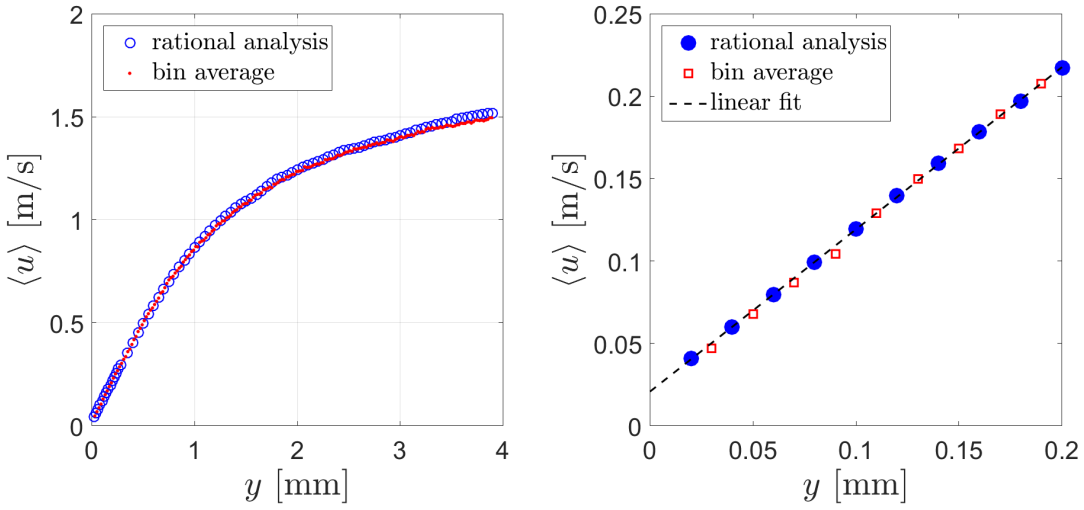

Figure 5.23: Comparison with the bin-average method and the linear profile in the viscous sublayer.

$\leq y \leq 3.9$ mm. The result is compared to that calculated by a bin-average method (Kähler *et al.*, 2012b), in which the reconstruction volume was divided into 0.02 mm bins in the wall-normal direction, and all velocity estimates within each bin were averaged to estimate the mean at the bin center. The noticeable discrepancy occurs at $y > 2$ mm, which we believe is primarily related to the the second-order truncation term of the x-direction. This is because, as the full span in the x-direction is used for bin averaging, the truncation term $\langle u^*_{1,11} \prec (x^{(p,q)} - x^*)^2 \succ_{\mathscr{D}} \rangle_T$ is more significant than that in our rational analysis. In addition, as seen in Figure 5.23 (right), the result of the bin-average method in the viscous sublayer appears to be slightly noisier compared to the smooth linear profile obtained by the rational analysis.

As a bonus of the high-resolution mean velocity measurement in the viscous sublayer, the friction velocity u_τ is directly measured from the slope of the linear profile:

$$u_\tau = \left[\nu \langle u_{1,2} \rangle \Big|_{y^+<5} \right]^{-\frac{1}{2}} \tag{5.73}$$

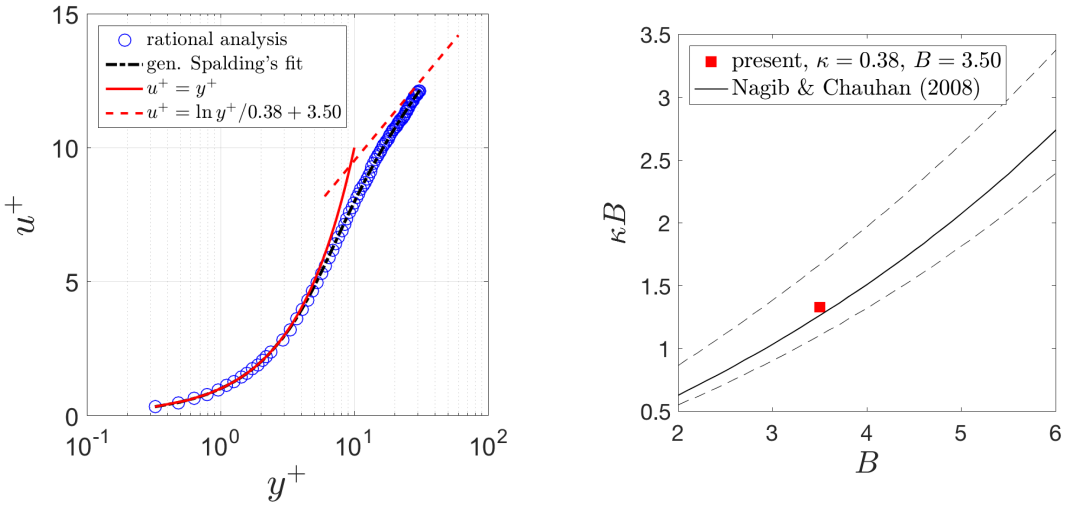

Figure 5.24: Mean velocity profile in wall units. The determined von Kármán coefficients are compared to the empirical fit given in Nagib and Chauhan (2008). The dashed lines in the right figure indicate the data spread in the original plot.

The linear fit is plotted in Figure 5.23 (right) on top of the mean velocity data, in which we see the fit is nearly perfect. It is also noticed the linear line intersects with the horizontal axis at $y \approx -0.02$ mm, which indicates the first y-position in our calibration was in fact approximately 20 μm above the actual wall. This is a fairly reasonable error when we manually pushed the calibration target against the glass window. Consequently, the mean velocity profile is plotted in wall units in Figure 5.24 after shifting the wall-normal coordinate to the actual wall position, i.e.

$$y^+ = (y + y_{shift})u_\tau/\nu \tag{5.74}$$

The resulting y^+ ranging from 0.3 to 30 primarily falls in the viscous sublayer and the buffer layer. To determine the von Kármán coefficients κ and B as a validation of our measurement, we computed a generalized Spalding's fit (Spalding, 1961):

$$y^+ = u^+ + e^{-\kappa B}\left[e^{\kappa u^+} - 1 - \kappa u^+ - (\kappa u^+)^2/2 - (\kappa u^+)^3/3! - (\kappa u^+)^4/4!\right] \tag{5.75}$$

The result, $\kappa = 0.38$ and $B = 3.50$, is compared to the empirical fit given in Nagib and

Chauhan (2008):

$$\kappa B = 1.6\left(e^{0.1663B} - 1\right), \tag{5.76}$$

which was calculated based on a comprehensive collection of experiment results of wall-bounded turbulence covering a wide range of pressure gradient. As evident in Figure 5.24 (right), our result agrees with the empirical fit very well and is well within the data spread shown in the original plot (Figure 5 in Nagib and Chauhan, 2008).

The estimated mean velocity gradient $\langle u_{1,2} \rangle$ is presented in Figure 5.25, along with the derivative of the generalized Spalding's fit as a reference. The estimates in the region where we take $\langle \widehat{u_{1,2}} \rangle$ at the optimal L_y, i.e. $y^+ > 2.37$, are in good agreement with the reference, except the noticeable discrepancy at $y^+ > 25$. Two reasons are possibly responsible for that: (1) The measurement noise becomes relatively prominent as the magnitude of $u^+_{1,2}$ gets small at large y^+; A larger dataset would help alleviate this prob-

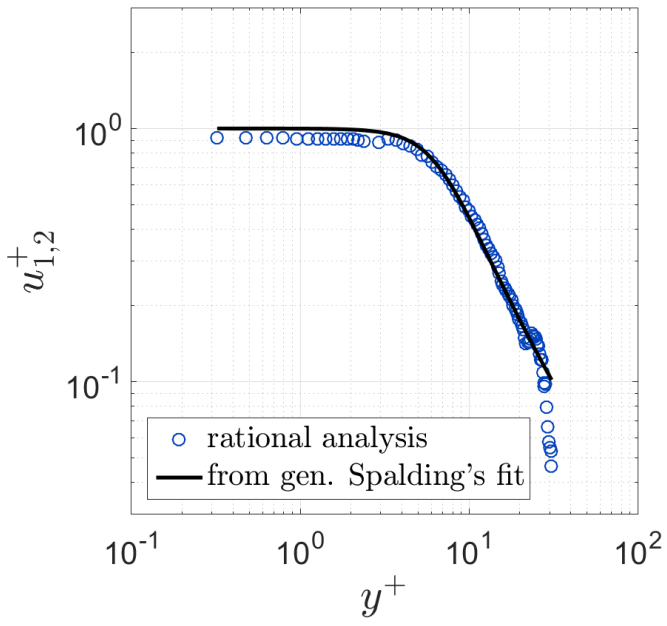

Figure 5.25: Mean velocity gradient $\langle u_{1,2} \rangle$ in wall units.

lem; (2) The inhomogeneous distribution of $\hat{\boldsymbol{x}}_p$ near the top boundary adds extra bias error, making the result less reliable than that away from the boundary. Additionally, a systematic underestimation of about 10% is revealed in the near-wall region where we inferred $\langle\widehat{u_{1,2}}\rangle$ from the slope of $\langle\widehat{u}\rangle$ when varying the size of a single-sided domain. While the mechanism of the underestimation is not yet fully understood, one potential source of error arises from the fact that a Taylor series expansion is not always globally converged. In other words, when we express a velocity far from the wall using a Taylor series expansion with respect to a near-wall location, extra terms other than the Taylor series may be needed.

It is worth mentioning that, besides $\langle u_{1,2}\rangle$, other non-zero mean velocity gradients in an APG-TBL include $\langle u_{1,1}\rangle$, $\langle u_{2,1}\rangle$ and $\langle u_{2,2}\rangle$. However, because the flow near wall ($y^+ <$ 30) almost fully adapts itself to the boundary geometry, those three gradients are too small to be estimated given the size of the current dataset. A rough estimate of $\langle u_{1,1}\rangle$ (and thus $\langle u_{2,2}\rangle = -\langle u_{1,1}\rangle$) by computing the mean streamwise velocity profiles at x = 1.8, 1.9, ..., 2.2 mm showed $\langle u_{1,1}\rangle$ increased from 0 to about 20 s^{-1} when moving from the wall to the top boundary. As a comparison, $\langle u_{1,2}\rangle$ is about 1000 s^{-1} at the wall and drops to about 100 s^{-1} at $y^+ \approx 30$.

5.5.5 Near-Wall Dissipation Rate

Because not all the mean velocity gradients can be reliably measured in the present experiment, we will only focus on the estimate of isotropic dissipation rate below $y^+ < 12$, where the only mean gradient that needs to be considered is $\langle u_{1,2}\rangle$. This is because of the homogeneity and symmetry of the mean field in the spanwise direction, as well as $\langle u_{1,1}\rangle = -\langle u_{2,2}\rangle = 0$ as the flow is nearly parallel to the boundary for the y^+ range considered.

In addition, the contribution from x-direction derivatives, i.e. $\langle u'_{i,1} u'_{i,1} \rangle$, was neglected in our dissipation estimation considering the pressure gradient is not strong enough to make $\langle u'_{i,1} u'_{i,1} \rangle$ near wall comparable to other terms. Therefore, we have evaluated the following 6 terms:

$$\langle u'_{1,2} u'_{1,2} \rangle + \langle u'_{1,3} u'_{1,3} \rangle + \langle u'_{2,2} u'_{2,2} \rangle + \langle u'_{3,2} u'_{3,2} \rangle + \langle u'_{2,3} u'_{2,3} \rangle + \langle u'_{3,3} u'_{3,3} \rangle \tag{5.77}$$

These terms are all closely related to the flow structures in the TBL. The first term arises from the strong near-wall shear; the second term is associated with the near-wall alternating high and low speed streaks; and the last fours terms have their roots in the quasi-streamwise vortices.

In our data processing, the 6 terms were grouped into different directions of derivative. For each direction, we analyzed the dependence of the dissipation estimate on L varying merely along that direction, which was intended to reduce the rms fluctuation by averaging over more particles. When the domain size varies in a single direction, say, y, the equation for estimating dissipation, i.e. Equation (5.33), becomes

$$\frac{24}{L_y^2} \langle \prec G^{noi}_{\nabla u'_i} G^{noi}_{\nabla u'_i} \succ_{\mathscr{D}} \rangle_T = \langle u'^*_{i,2} u'^*_{i,2} \rangle + \frac{\Pi}{L_y^2} + \mathscr{O}(L^2) \tag{5.78}$$

wherein Π incorporates the PTV error, $\langle \prec n^{(p,p',q)}_{br,u_i} n^{(p,p',q)}_{br,u_i} \succ_{\mathscr{D}} \rangle_T$, and the contributions from the other two directions, $\langle u'^*_{i,1} u'^*_{i,1} \rangle L_x^2 + \langle u'^*_{i,3} u'^*_{i,3} \rangle L_z^2$. Note, since L_x and L_z are fixed, the dissipation estimate from Equation (5.78) scales as L_y^{-2} at small L_y. This is verified in Figure 5.26 showing the estimate of dissipation with varying L_y. The result was calculated at y = 0.1 mm with L_x = 3 mm, L_z = 1.6 mm, and L_y decreasing from the side above y = 0.1 mm. The L_y^{-2} dependence at small L_y is evident, and the curve after subtracting the Π/L_y^2 term appears to approach the true value before it gets noisy. Because of the relatively high noise level, as well as the undetermined functional form of the truncation error, the strategy to extract the dissipation from the experimental data slightly differs

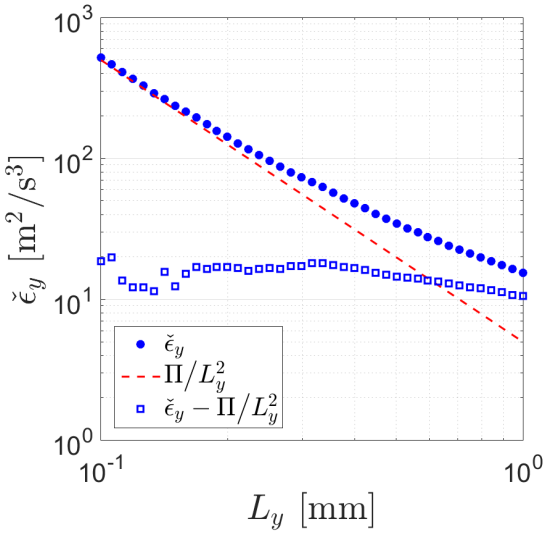

Figure 5.26: Estimation of the y-direction dissipation $\check{\epsilon}_y$ with varying L_y. $\check{\epsilon}_y$ is obtained from Equation (5.78).

from the fitting method described in Section 5.4.4. Thus, we first determined Π by fitting the following model to the data points of $L_y \lessapprox 0.25$ mm:

$$\check{\epsilon}_y = b_1 + b_2/L_y^2 \tag{5.79}$$

wherein $\check{\epsilon}_y$ stands for the estimate for the y-direction dissipation given in Equation (5.78). Note b_1 is not a reliable estimate of $\langle u'^*_{i,2} u'^*_{i,2} \rangle$ due to its sensitivity to noise. A rational estimation was then made from $\check{\epsilon}_y - \Pi/L_y^2$. It was found that the noise level imbedded in the $\check{\epsilon}_y - \Pi/L_y^2$ curve varied at different y, so we have chosen the median of the data over approximately 0.4 mm $< L_y <$ 0.7 mm to be a good estimate of the dissipation.

Marching over y from 0.05 to 1.5 mm with the above described strategy for both the y and the z-direction, we obtained a profile of the isotropic dissipation rate accounting for the majority of dissipation occurring near wall. The result after scaled with u_τ^4/ν is presented in Figure 5.27, and it is compared to other results from the literature. The

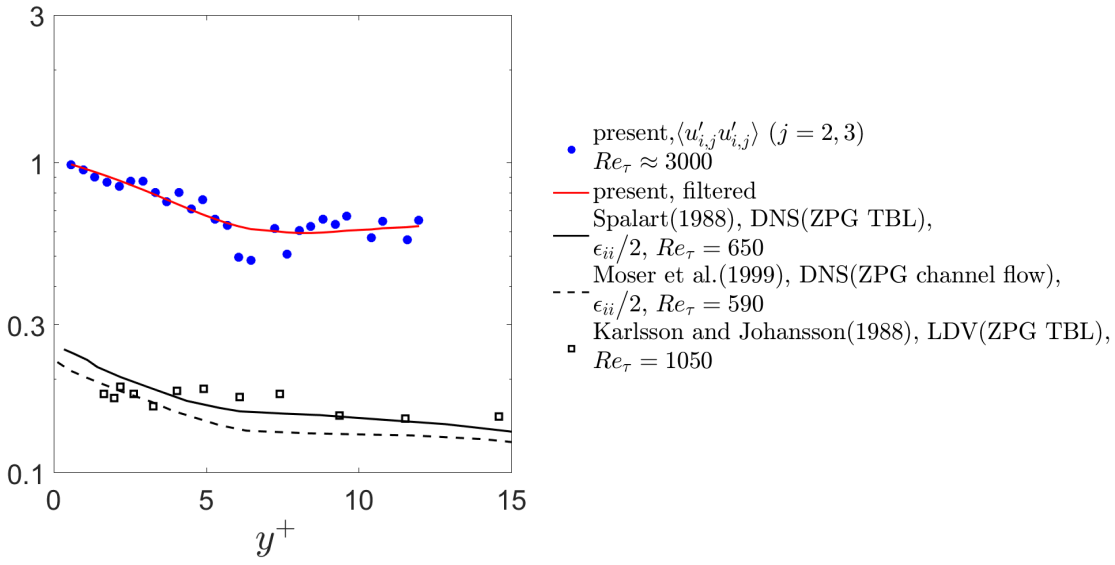

Figure 5.27: Isotropic dissipation estimate scaled with u_τ^4/ν for 0.5< y^+ <12. The DNS and LDV results are taken from Bernard and Wallace (2002).

friction Reynold number in our experiment, $Re_\tau \approx 3000$, was estimated based on the boundary layer thickness in another experiment conducted in the same facility under similar flow conditions (Reuther *et al.*, 2015). The dissipation data was smoothed by a Butterworth low-pass filter with a cut-off frequency at 1/20 of the sampling frequency. The DNS results from Spalart (1988) and Moser *et al.* (1999) represent the full isotropic dissipation rate, i.e.

$$\epsilon_{ii}/2 = \langle u'_{i,m}u'_{i,m}\rangle \tag{5.80}$$

wherein Einstein notation is used, and ϵ_{jk} is the dissipation tensor. Although our result is only compared to low-Reynolds-number flows due to the lack of simulations and experiments matching the current Re_τ, the comparison is qualitatively favorable. The plateau starting at $y^+ \approx 6$ is consistently observed at different Re_τ. The rapid increase of dissipation near wall (y^+ <5) is well resolved, and it appears to follow the same law as in the low-Reynolds-number cases except with a larger magnitude. The LDV measurement

by Karlsson and Johansson (1988) was not capable to resolve the dissipation profile close to the wall, and it probably underestimated the near-wall dissipation considering the Re_τ is about twice of those of the DNS studies. It is not clear how the adverse pressure gradient in the present experiment modifies the dissipation profile, which, however, is probably not observable in the y^+ range considered (Lee and Sung, 2008).

5.6 Summary

We presented a novel method for extracting turbulence statistics from ensemble PTV data. The common starting point for different statistics is the Taylor expansion of each velocity vector inside a resolution domain with respect to the domain center. We showed that manipulations of the Taylor expansion equation lead to the approaches for many turbulence statistics. The focus of the present work is the mean velocity, the mean velocity gradient and the isotropic dissipation rate. The theoretical bases for some other statistics are provided in Appendix D, including Reynolds stress, TKE production, TKE viscous diffusion, and inhomogeneous dissipation rate.

We theoretically derived the equations for the mean velocity, the mean velocity gradient and the dissipation rate, identifying the leading order truncation terms. The mechanisms of two error sources were discussed, including the rms fluctuation arising from the finite-time averaging, and the random and bias error associated with the particle tracking analysis.

A PTV simulation with synthetic turbulence was designed to validate the PTV-based method and to assess the effects of different errors. The synthetic turbulence consists of random Fourier modes matching a well-defined power spectrum. The flow parameters including TKE and the Taylor microscales in both space and time are easy controlled.

The PTV errors were studied by generating trajectories of randomly located particles following the synthetic turbulent flow. We found the PTV bias error had a dependence on the geometry of a trajectory, whereas the PTV random error was merely determined by the rms particle locating noise. As a result, the PTV error translates to rms fluctuation with zero mean for the mean velocity and the mean velocity gradient, and the fluctuation amplitude is usually negligible. However, because of the square operation in calculating the dissipation, the PTV error presents as a positive bias that could be significant at small domain size L. This observation, combined with the underestimation at large L due to the negative truncation terms, manifests the challenge for dissipation measurement. On the other hand, the rms fluctuation arising from finite-time averaging competes with the decreasing truncation terms when L decreases. We have demonstrated both theoretically and numerically that the finite-time averaging results in growing rms fluctuation towards small L. Thus, the amplitude of the rms fluctuation, scaling inversely with the total number of velocity fields Q and the seeding density C, determines the optimal L to evaluate the mean velocity and the mean velocity gradient, as well as the dissipation rate if the PTV error is sufficiently small. In other words, Q and C are two decisive factors for the overall measurement accuracy. In addition, we demonstrated the benefit of reciprocally and iteratively evaluating the mean velocity and the mean velocity gradient as a pair to reduce the rms fluctuation for both of them.

With the thorough understanding of different errors, we proposed to extract statistics by means of a correction method that involves fitting a model to the statistic estimates at different L. This correction method can yield improved accuracy provided good knowledge of the functional forms of the truncation terms and the PTV error. For the dissipation estimation with considerable PTV error, a fitting model incorporating an L^{-2} term to account for the PTV error at small L succeeded to yield an accurate dissipation

result. We also discussed in depth the empirical rules regarding the optimization of the correction method.

The proposed method for estimating turbulence statistics was applied to a tomographic measurement of an APG-TBL with $Re_\tau \approx 3000$. Particles were identified inside a small volume above the wall with an algorithm combining 3-D triangulation and surface segmentation to avoid ghost reconstructions, and were tracked over four successive pulses for reduced PTV error. We successfully measured the streamwise mean velocity profile over $0.3 < y^+ < 30$ with high spatial resolution by a rational analysis for the optimal L. As a benefit of the high spatial resolution, we also directly measured the friction velocity u_τ from the near-wall velocity data. The determined von Kármán coefficients agree well with an empirical fit based on a comprehensive collection of experimental results, indicating excellent measurement accuracy. The mean velocity gradient was also estimated with satisfactory accuracy, which can be certainly improved given a larger dataset. Lastly, the isotropic dissipation was estimated for $y^+ <12$ using 6 dominant terms neglecting the streamwise terms. A special strategy was implemented to enable the estimation of dissipation in each direction (the direction of the derivative), and meanwhile to account for the noticeable rms fluctuation due to limited number of samples. The near-wall dissipation profile was then compared to DNS and LDV results of ZPG-TBL with lower Re_τ. The consistency revealed from the plateau position and the sharp increase near wall favorably implies reasonable measurement quality.

Chapter 6

OTHER INVESTIGATIONS

6.1 Surface Segmentation for Tomographic PIV

6.1.1 Introduction

Tomographic PIV (tomo-PIV) is a 3-D flow measurement technique that employs multiple cameras, typically 4 to 6, to view the same volume of interest from different angles. The volumetric intensity distribution is reconstructed using the multiplicative algebraic reconstruction technique (MART), and the 3D3C velocity field is calculated by 3-D cross-correlation (Elsinga *et al.*, 2006; Westerweel *et al.*, 2013).

Since the first publication on tomo-PIV (Elsinga *et al.*, 2006), related works aiming at improving its performance have explosively emerged. These include but not limited to, correcting mapping function errors (Wieneke, 2008), reducing computational burden (Atkinson and Soria, 2009; Worth and Nickels, 2008; Discetti and Astarita, 2012b), and attenuating or eliminating ghost particles using temporal information (Novara *et al.*, 2010; Schanz *et al.*, 2016). The latter two categories are critical for tomo-PIV when applied to a large measurement volume. An example of the high computational cost of tomo-PIV can be found in Discetti and Astarita (2012b), in which the reported processing time for a 64^3-voxel volume with a 20 vox/mm resolution and a source density (Adrian and Westerweel, 2011) $N_s = 0.3$ is about an hour using the standard MART and about 20 minutes using an optimized MART. In a realistic experiment, the measurement volume is often in the order of $20 \times 20 \times 20$ mm^3 with a reconstruction resolution up to 64 vox/mm, and thousands

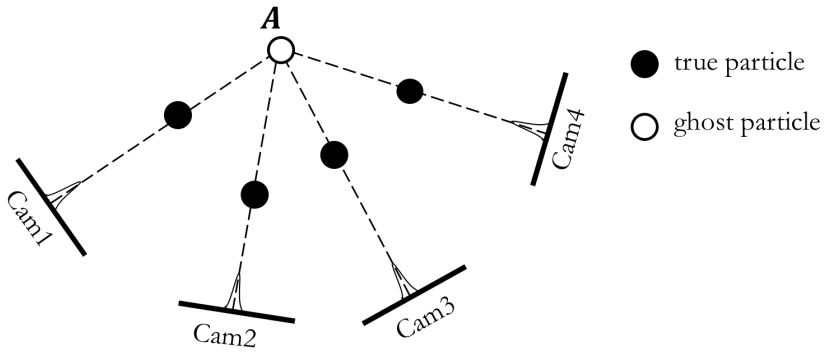

Figure 6.1: Formation of ghost particles.

of realizations are required to get good convergence of statistics. All these considerations make the data processing of tomo-PIV extremely challenging. On the other hand, the high percentage of ghost particles is another obstacle that prevents tomo-PIV from being a reliable technique to resolve small scale motions (Elsinga *et al.*, 2011). The mechanism of generating ghost particles is illustrated in Figure 6.1. When every line of sight of a point A in the measurement volume intersects with a true particle, a ghost particle is formed at A during reconstruction. The intensities of ghost particles are likely to be attenuated during MART iterations (Atkinson and Soria, 2009), and the existence of a particle over multiple successive frames can be used to reduce the ghost particle percentage.

While the majority of previous efforts have attempted to improve tomo-PIV for a large measurement volume, surface segmentation was proposed by Ziskin *et al.* (2011) as a fast and accurate method for 3-D flow measurement in a thin slab. The work presented in this section is a continuous development of surface segmentation towards improved accuracy, reduced processing time and application to curvilinear-coordinate reconstruction.

6.1.2 Working Principle

Surface segmentation directly reconstructs the volumetric intensity distribution without MART iterations. As illustrated in Figure 6.2, the working principle of surface segmentation relies on the fact that each particle on a surface S in the physical domain must generate a corresponding intensity peak on every camera. If we back project recorded images with respect to S, the lines of sight of an in-surface particle would intersect at a common point on S, whereas the lines of sight of an off-surface particle intersect with S at different locations. Therefore, the product of all back-projected images with respect to S forms intensity peaks only for those particles lying on S, but filters out off-surface particles. An example of the filtering process is presented in Figure 6.3. It is clearly observed that only a small amount of particles preserve as the number of cameras increases. For realistic cases with voxelized volumes and finite particle size, the area of intersection of a particle and S is reconstructed. The working principle is applicable to any surface in the physical domain provided all lines of sight intersect with the surface only once. The intensity distribution of the entire volume can be then reconstructed by stacking reconstructed surfaces.

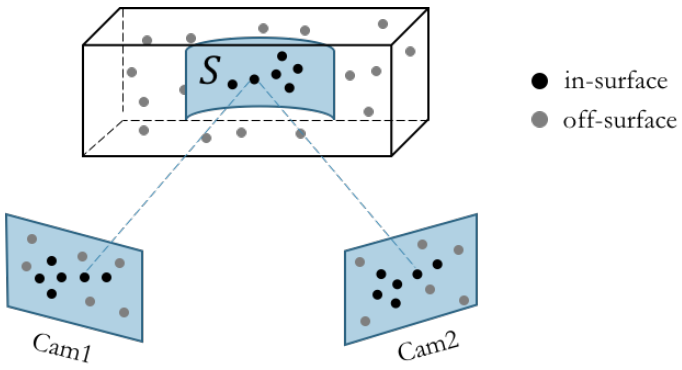

Figure 6.2: Working principle of surface segmentation.

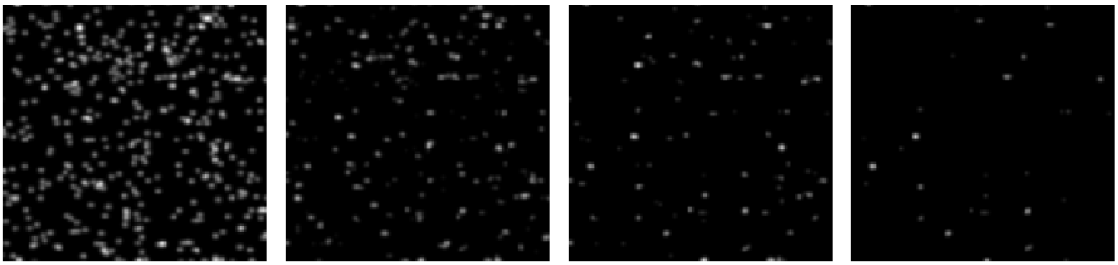

I_1 $I_1 I_2$ $I_1 I_2 I_3$ $I_1 I_2 I_3 I_4$

Figure 6.3: Filtering process of surface segmentation. I_i denotes the back-projected image from the i-th camera.

6.1.3 Ghost Particle Percentage and Reconstruction Quality in a Thin Volume

Without MART iterations, surface segmentation significantly saves the computation time but can only work with a thin volume to mitigate the issue of ghost particle. To quantitatively study the reconstruction quality for a thin volume, we simulated the reconstruction process of a 2-D volume using four line cameras. The 2-D volume, seeded with randomly distributed particles, is 20-mm long with a thickness ranging from 1 to 6 mm; each line camera is 960 pixels in length; and the reconstruction resolution is 48 pix/mm. We conducted parametric studies of the ghost particle percentage (gpp) with

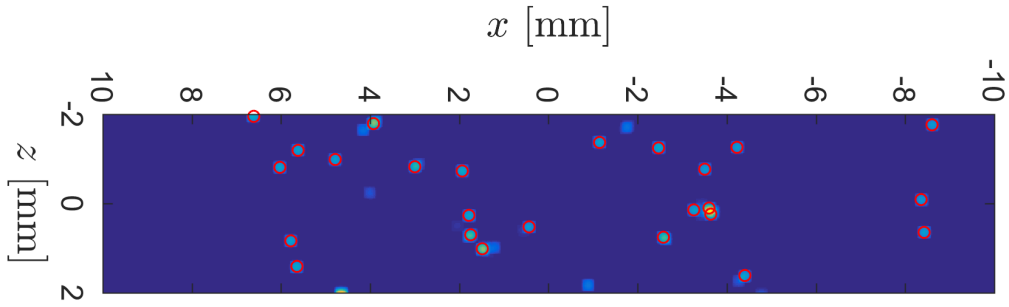

Figure 6.4: Example reconstruction of a 2-D volume. Red circles are known true particles. Particles are magnified by convolution for better visibility.

respect to true particles and the correlation coefficient Q between the reconstructed and the reference volume. An example of the reconstruction is displayed in Figure 6.4, wherein true particles are indicated by red circles and ghost particles exhibit comparable intensities.

Figure 6.5 and 6.6 present Q and gpp for varying volume thickness Δz_0 and seeding density C. The results were calculated by averaging 100 simulation realizations. If we specify an acceptable reconstruction quality to be $Q > 0.9$ and gpp < 0.3, the result suggests $\Delta z_0 < 4$ mm at $C = 15$ particles/mm^2, and a further reduced Δz_0 when increasing C. It is also noticed that gpp exponentially elevates when Δz_0 increases, implying decreasing Δz_0 is an effective way to reduce ghosts.

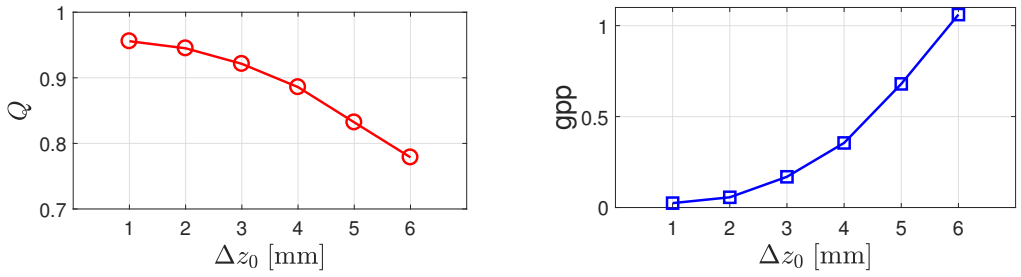

Figure 6.5: Correlation coefficient (Q) and ghost particle percentage (gpp) for varying volume thickness Δz_0. The results are calculated with $C = 15$ counts/mm^2.

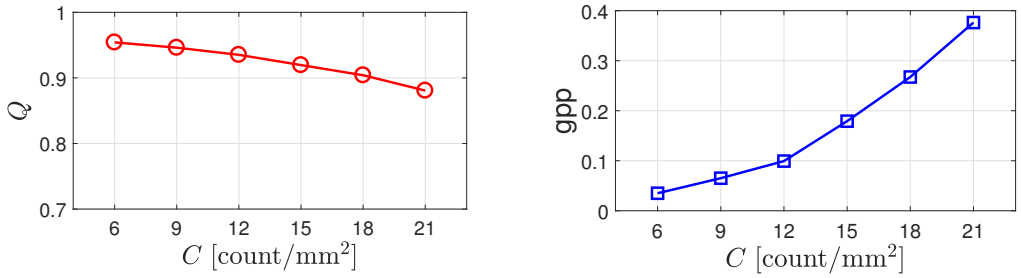

Figure 6.6: Correlation coefficient (Q) and ghost particle percentage (gpp) for varying seeding density C. The results are calculated with $\Delta z_0 = 3$ mm.

6.1.4 Surface-Based Interrogation for Volumetric Flows

As surface segmentation emphasizes the filtering process for a prescribed surface S, we also developed an interrogation strategy based on 2-D surfaces. This is another aspect of reducing the processing time for tomo-PIV by avoiding 3-D cross-correlation. In this surface-based strategy, to have sufficient particles for reliable correlation, neighboring reconstructed surfaces are summed up to form a superposed image, to which 2-D cross-correlation is performed yielding the in-plane velocity components. If this process is repeated across the volume in two orthogonal directions, we obtain the 3D3C velocity field of the measurement volume.

The number of surfaces required for reliable 2-D cross-correlation is determined by the seeding density C as well as the out-of-plane motion. For the latter, it needs to be guaranteed that less than a quarter of the particles leave the superposed image over the inter-frame time. Apparently, for flows with strong 3-D motions, the spatial resolution would be severely limited. Therefore, an iterative procedure was implemented to account for strong 3-D motion and thus to improve the spatial resolution and the velocity accuracy. The implementation is an analog to the 2-D iterative image deformation technique (Scarano, 2001), and it is outlined as follows:

(1) Cross-correlate superposed images in two orthogonal directions to predict a 3D3C vector field with a coarse grid. The initial grid size needs to comply the one-quarter rule for the out-of-plane motion (Adrian and Westerweel, 2011).

(2) Deform the volume based on the predicted vector field.

(3) Repeat the previous two steps until a good convergence is achieved for the current grid size.

(4) Repeat step (1) with a reduced grid size.

(5) Repeat step (2) to (4) until the minimum required particle number in an interrogation cell (Keane and Adrian, 1990) is reached.

To assess the performance of the surface-based interrogation strategy, we simulated a tomographic PIV measurement of a vortex ring. The measurement volume, seeded with randomly located particles, is 20 mm (x) × 20 mm (y) × 4 mm (z) with a seeding density 15 particles/mm^3. The thickness of the volume assures good reconstruction quality based on the simulation in Section 6.1.3. As depicted in Figure 6.7, four cameras are set up in the x-z plane to image the volume simultaneously. Synthetic particle images on the cameras are generated based on projected particle locations. The intensity distribution in the measurement volume is reconstructed using surface segmentation with a resolution of 48 vox/mm. The 3D3C velocity field is analyzed using the proposed surface-based interrogation strategy, and the final interrogation spot size in both directions is 1 mm × 1 mm (48 vox × 48 vox).

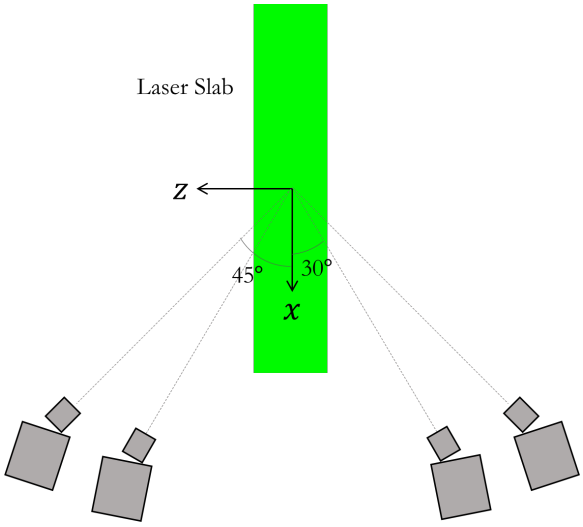

Figure 6.7: Setup of the tomo-PIV simulation of a vortex ring. The axis of revolution of the vortex ring is aligned with the z-axis.

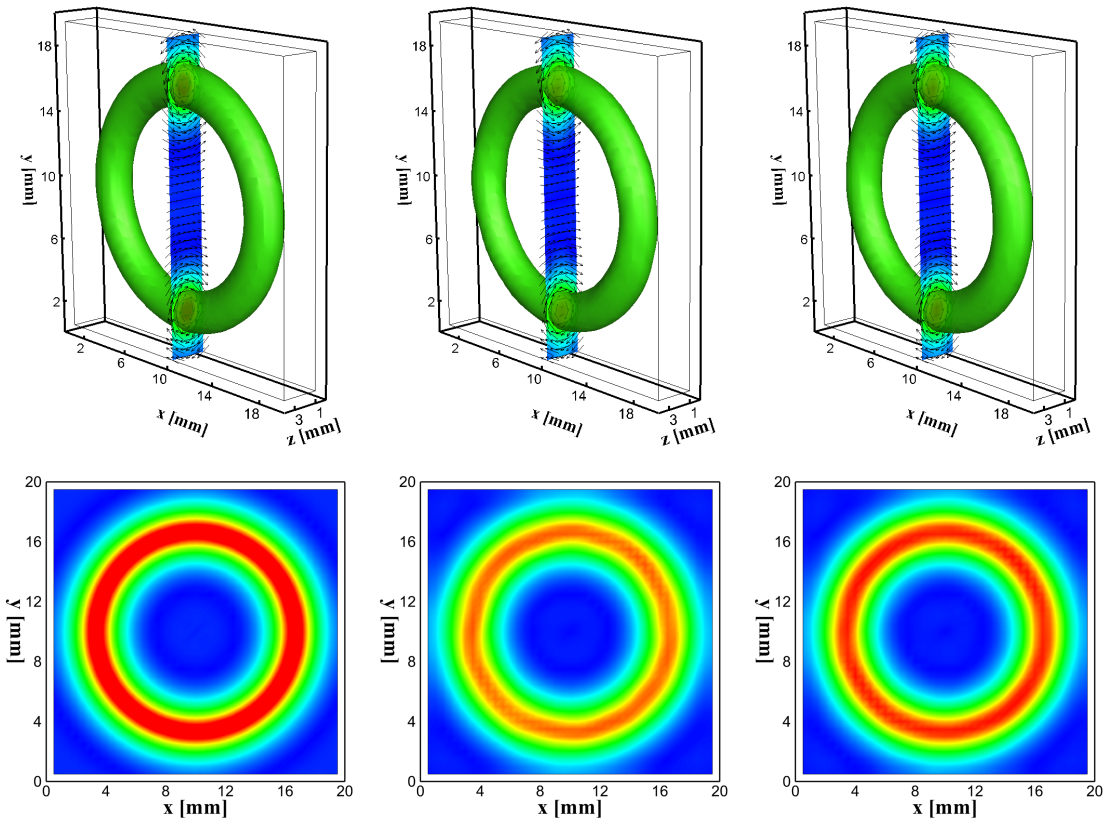

Figure 6.8: Comparison between the single-pass and the iterative analysis. Top: vorticity iso-surface (arbitrary unit); Bottom: middle z-plane vorticity contour. From left to right: reference, single-pass and iterative.

	δu_{rms} [vox]	δv_{rms} [vox]	δw_{rms} [vox]
Single-pass	0.2178	0.2100	0.2996
Iterative	0.0969	0.0843	0.1652

Table 6.1: Comparison of global rms errors between the single-pass and the iterative analysis.

Figure 6.8 presents the comparison between a single-pass analysis and the iterative analysis described above. The single-pass analysis only implements step (1) without iterative refinement. It is visually evident that the vorticity iso-surface is smoother after

the iterative analysis, which also produces smaller bias of the vorticity magnitude in the middle z-plane. Quantitatively, Table 6.1 shows the global rms errors calculated over the volume. The rms errors of u and v are reduced to below 0.1 voxel, and the rms error of w is approximately 0.15 voxel.

6.1.5 Reduction of Computational Cost

The reduction of computational cost by surface segmentation is realized in two aspects, i.e. the direct reconstruction and the surface-based interrogation, as discussed in previous sections. Following Atkinson and Soria (2009), we quantitatively compare surface segmentation with other tomo-PIV algorithms in Table 6.2. It is noticed that the reduction in reconstruction with respect to MART is considerable and the number of operations is comparable to MLOS-SMART and MLOS-SART. Additionally, the surfaced-based interrogation is approximately 25 times faster than the 3-D cross-correlation with either FFT or sparse direct correlation.

Furthermore, we studied the rms error when reducing the number of surfaces reconstructed within a fixed thickness. As the correlation analysis is performed on 2D superposed images, further reduction in computation time can be achieved by reducing the number of surfaces summed up to form the superposed image. In other words, we try to determine the minimum number of cross-sections to sufficiently sample a reconstructed particle having a 3D intensity profile. In this regard, the result in Figure 6.9 suggests the uncertainty of the measured velocity field stays constant as long as the spacing between two neighboring reconstructed surfaces is smaller than 2 voxel units.

	Operation	Example
Reconstruction		
Surf. Seg.	$120\ N_{cam}N_{vox}$	4.8e10
5 MART	$5{\times}4N_{cam}N_{vox}(8L+4)$	2.5e13
MLOS + 5 SART	$120N_{cam}N_{vox}+5(24N_{cam}+4)N_{n.z.vox}$	1.0e11
MLOS + 5 SMART	$120N_{cam}N_{vox}+5(24N_{cam}+3)N_{n.z.vox}$	1.0e11
Interrogation		
Surface-based, FFT	$2{\times}2N_I^2\log_2 N_I$	2.0e04
3D correlation, FFT	$3N_I^3\log_2 N_I$	4.9e05
3D correlation, Direct	$5\%N_I^3{\times}1\%N_I^3$	5.4e05

Table 6.2: Comparison of number of operations for surface segmentation and other tomo-PIV algorithms. Example numbers used for the calculation: N_{cam} = 4; N_{vox} = 2e08; Non-zero voxels, $N_{n.z.vox}$ = 5%N_{vox} = 1e07; Averaged length of line of sight, L = 200 vox; Interrogation spot dimension N_I = 32 vox. See details in Atkinson and Soria (2009).

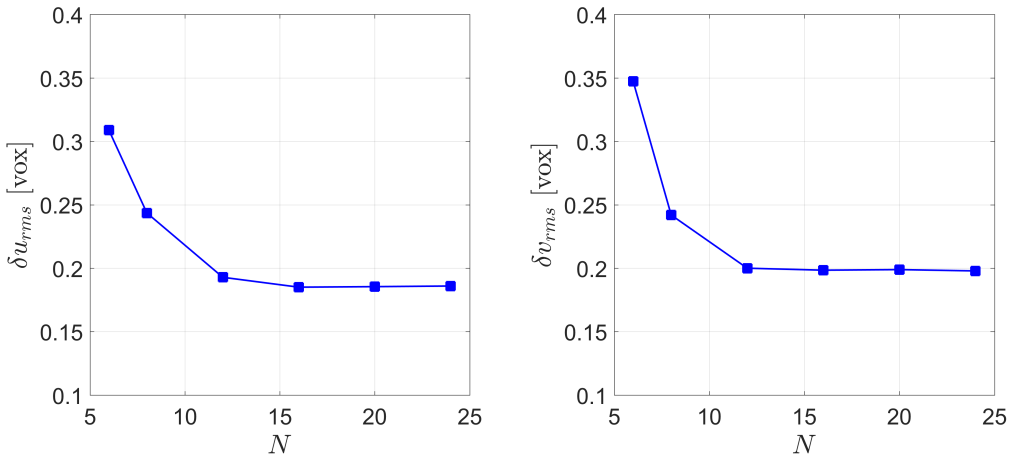

Figure 6.9: Dependence of rms errors on the number of surfaces reconstructed in a 0.5mm-thick slab. The reconstruction resolution is 48 vox/mm.

6.1.6 Towards Curvilinear Coordinate System Reconstruction

In effect, the working principle of surface segmentation allows the surface S to have an arbitrary shape provided it intersects with all lines of sight only once. For many realistic situations with flows in complex geometries, it would be necessary to extract flow information on a curvilinear surface following the local boundary geometry. Examples include Taylor-Couette flow between counter-rotating cylinders (Tokgoz *et al.*, 2012), and the flow in human carotid artery bifurcation (Buchmann *et al.*, 2011).

As an example to demonstrate the capability of surface segmentation for curvilinear coordinate system reconstruction, we simulated a tomo-PIV experiment measuring a laminar Taylor-Couette flow. As illustrated in Figure 6.10, Surface segmentation was applied to extract a mathematically prescribed azimuthal surface S. 2D interrogation of S yields excellent accuracy: the global mean velocity is 7.638 pixel with a standard deviation of 3e-04 pixel, compared to the ground-truth velocity of 7.627 pixel.

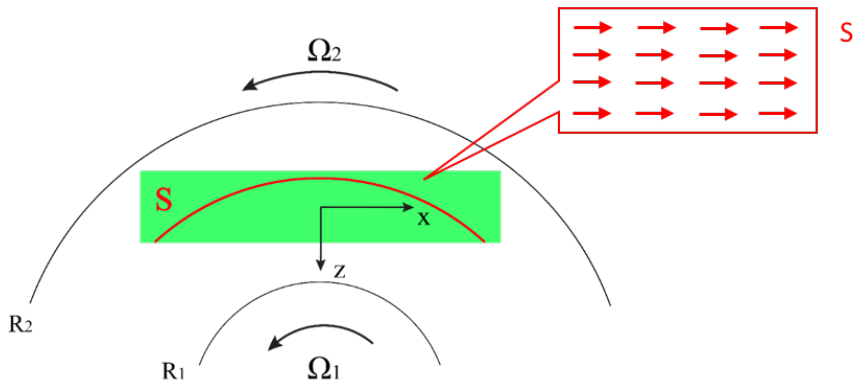

Figure 6.10: An azimuthal surface S of a laminar Taylor-Couette flow is reconstructed using surface segmentation.

6.2 Third-Order Correlation for 3-pulse PIVA

6.2.1 Introduction

In addition to the improvement achieved by PTVA analysis, N-pulse PIVA also has the potential to enhance the performance of correlation-based PIVA analysis in terms of valid detection probability. Keane and Adrian (1991) demonstrated a higher valid detection probability of displacement vectors using multiple pulsed PIV with auto-correlation compared to 2-pulse PIV. It implies an equally good measurement quality is achievable with smaller interrogation spots, i.e. enhanced spatial resolution. Follow this line, we explore the third-order cross-correlation for 3-pulse PIVA, aiming to establish a novel way to correlate N-pulse particle images with improved performance. Preliminary investigations, including the FFT implementation and the correlation peak sub-pixel interpolation, are presented in this section.

6.2.2 FFT Implementation

The third-order correlation for images I_i recorded at time t_i (i = 1, 2, 3) is defined as

$$C(\boldsymbol{r},\boldsymbol{s}) \equiv \int_{x\in W} I_1(\boldsymbol{x},t_1)\, I_2(\boldsymbol{x}+\boldsymbol{r},t_2)\, I_3(\boldsymbol{x}+\boldsymbol{s},t_3)\, d\boldsymbol{x} \tag{6.1}$$

$C(\boldsymbol{r},\boldsymbol{s})$ is a 4-D function whose highest peak contains the information of two displacement vectors, i.e. $\boldsymbol{r}_0$ between I_1 and I_2, and $\boldsymbol{s}_0$ between I_1 and I_3. With the consideration of reducing the computational cost, similar to that for the second-order correlation, we intend to develop a FFT implementation of the third-order correlation. It turns out that, if we apply 4-D Fourier transform to Equation (6.1), the right side can be written as the

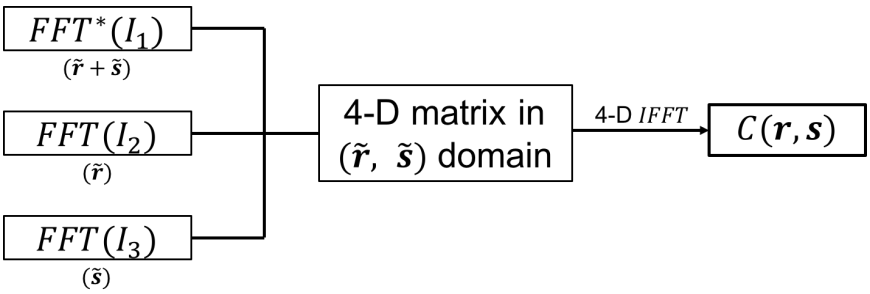

Figure 6.11: FFT implementation of the third-order correlation.

product of three 2-D Fourier transforms:

$$\mathscr{F}_{4-D}\Big[C(\boldsymbol{r},\boldsymbol{s})\Big] = \mathscr{F}^*_{2-D}\Big[I_1\Big] \times \mathscr{F}_{2-D}\Big[I_2\Big] \times \mathscr{F}_{2-D}\Big[I_3\Big] \tag{6.2}$$

Where the superscript '$*$' denotes a complex conjugate. Note that, given spatial frequency $\tilde{\boldsymbol{r}}$ and $\tilde{\boldsymbol{s}}$ respectively of I_2 and I_3, the Fourier transform of I_1 needs to be evaluated at $\tilde{\boldsymbol{r}}+\tilde{\boldsymbol{s}}$. With the fact that $\mathscr{F}^*_{2-D}\Big[I_1\Big]$ is band-limited, the FFT implementation is summarized using the flow-chart shown in Figure 6.11. The MATLAB code for computing the third-order correlation is provided in Appendix E. Regarding the reduction of computation time, a direct evaluation of the discrete version of Equation (6.1) requires $\mathscr{O}(M^6)$ multiplications for a 2-D image with $M \times M$ pixels, whereas the FFT implementation reduces that to $6M^2 \log M + 2M^4 + 4M^4 \log M \sim \mathscr{O}(4M^4 \log M)$.

6.2.3 Sub-Pixel Peak Location Interpolation

A key for PIV analysis to achieve high accuracy is the sub-pixel interpolation of correlation peaks. For the second-order correlation, a Gaussian interpolation formula is widely used to determine sub-pixel peak locations (Adrian and Westerweel 2011, Section 8.5.2). Likewise for the third-order correlation, we assume Gaussian particles to derive the sub-pixel interpolation formula for the 4-D correlation map.

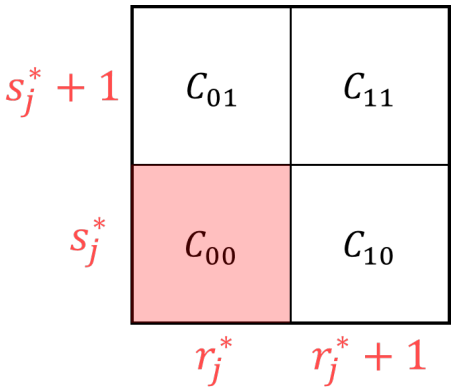

Figure 6.12: Peak location and the neighbors used for Gaussian sub-pixel interpolation. j = 1 or 2 denoting the x- or the y-direction.

The interpolation is performed separately in the x- and y-direction. That is, if we use indices (r_1, r_2, s_1, s_2) to denote the four dimensions of the correlation map, the x-direction sub-pixel displacement is calculated using only the peak value and the neighbors in the r_1 and s_1 direction, and likewise for the y-direction. As illustrated in Figure 6.12, C_{00} is the height of the highest peak occurring at a location $(r_1^*, r_2^*, s_1^*, s_2^*)$ (all are integer indices). For each direction, three neighbors are used to determine the sub-pixel location: $C_{10} = C(r_1^* + \delta_{1j}, r_2^* + \delta_{2j}, s_1^*, s_2^*)$, $C_{01} = C(r_1^*, r_2^*, s_1^* + \delta_{1j}, s_2^* + \delta_{2j})$, $C_{11} = C(r_1^* + \delta_{1j}, r_2^* + \delta_{2j}, s_1^* + \delta_{1j}, s_2^* + \delta_{2j})$, where δ_{ij} is the Kronecker delta. The sub-pixel peak location in the j-direction, $(\hat{r}_{0,j}, \hat{s}_{0,j})$, is then given by

$$\hat{r}_{0,j} = r_j^* + \frac{1}{3}\frac{\ln C_{10} + 2\ln C_{01} - 3\ln C_{11}}{\ln C_{10} + \ln C_{01} - \ln C_{00} - \ln C_{11}} \tag{6.3a}$$

$$\hat{s}_{0,j} = s_j^* + \frac{1}{3}\frac{2\ln C_{10} + \ln C_{01} - 3\ln C_{11}}{\ln C_{10} + \ln C_{01} - \ln C_{00} - \ln C_{11}} \tag{6.3b}$$

Equations (6.3a) and (6.3b) are shown to be non-biased for symmetric Gaussian particles recorded on pixels with unity fill factors.

SUMMARY

As PIV approaches its 35th anniversary, numerous efforts have been made to enable PIV to become a versatile and robust experimental tool for fluid mechanics research. The advantage of PIV over conventional point-wise techniques, such LDV and HWA, lies in its ability to offer non-intrusive and multi-point measurements of a wide range of flows. On the other hand, the desire to further improve the performance of PIV, as well as to extract more flow information from PIV, poses great challenges to the community. In this regard, a new generation of PIV, i.e. N-pulse PIVA ($N \geq 3$), has been developed aiming to break through the limitations of traditional 2-pulse PIV. As an extension of 2-pulse PIV, N-pulse PIVA employs bursts of N pulses to resolve the curvature of a particle trajectory and the velocity variation that are not accessible by the 2-pulse method.

The fundamental question of how much improvement is achievable by the additional pulses is answered in Chapter 1. The theoretical study was conducted in the form of N-pulse particle tracking (N = 3 or 4). With the understanding of the behaviors of the rms errors and the knowledge of the optimal times to evaluate particle velocity and acceleration, we compared both DVR and DSR to those obtained by 2-pulse PTV. It was shown that the overall performance, given by the product of DVR and DSR, could be enhanced by a factor of up to 10-50, or even higher when future camera technology allows more accurate determination of particle locations.

In addition to the enhanced spatial resolution and velocity accuracy, N-pulse PIVA also offers the flow unsteadiness information with high temporal resolution, and thus opens the way to direct estimation of fluid acceleration and force. This attractive capability was demonstrated in Chapter 2 in the context of unsteady flow-structure interaction. We succeeded to measure simultaneously the cylinder velocity and acceleration, the

flow velocity and acceleration, and the fluid force acting on the cylinder. The near-wall treatment for moving surfaces in fluid, as well as the interrogation strategy to track a particle cluster in N successive frames, enables N-pulse PIVA to be an informative tool for measuring complex flow-structure interaction.

Chapter 3 solved an important technical issue, i.e. multi-camera registration, for the application of N-pulse PIVA to high-speed flows. The necessity of this investigation lies in the insufficient framing rate of a single high-speed camera and the high sensitivity of acceleration to small displacement errors. It was shown that, by combining the global and local schemes, the mean residual disparity between a camera pair could be reduced to 0.001 pixel, which is sufficient for measuring acceleration by correlation analysis across cameras.

By virtue of the many advantages offered by N-pulse PIVA, the application was extended to two more challenging cases. In Chapter 4, a novel 8-pulse PTVA method was developed to extract the particle drag in a post-shock flow by a fitting model incorporating particle dynamics. We found the particle drag coefficient was substantially higher than the standard drag due to flow unsteadiness. The optimization of the 8-pulse PTVA analysis was also thoroughly discussed.

The capability of N-pulse PTV to measure turbulence statistics was demonstrated in Chapter 5. The method fully utilizes the advantage of N-pulse PTV in spatial resolution and velocity accuracy. The theoretical basis was derived from the Taylor series expansion of a velocity with respect to the point of interest, followed by the analysis of potential error sources. The performance of this PTV-based method was assessed and optimized by means of a PTV simulation with synthetic turbulence. Experimentally, we applied this method to an APG-TBL with $Re_\tau \approx 3000$, and succeeded to extract the mean velocity, the mean velocity gradient and the isotropic dissipation rate near wall. The results suggested

the superior ability of this N-pulse PTV based method compared to the correlation-based PIV analysis and point-wise techniques (LDV and HWA).

Lastly, two other investigations towards improving the performance of PIV were briefly discussed. The investigation of surface segmentation aimed to accurately measure the 3-D flow field inside a thin volume with reduced computational cost. The third-order correlation was developed to enhance the valid detection probability of particle displacement by 3-pulse correlation analysis. For both topics, preliminary results were presented to envision future explorations.

Adrian, R., "Multi-point optical measurements of simultaneous vectors in unsteady flow—a review", International journal of heat and fluid flow **7**, 2, 127–145 (1986).

Adrian, R., "Limiting resolution of particle image velocimetry for turbulent flow", Advances in Turbulence Research **1** (1995).

Adrian, R., "Dynamic ranges of velocity and spatial resolution of particle image velocimetry", Measurement Science and Technology **8**, 12, 1393 (1997).

Adrian, R. J., "Scattering particle characteristics and their effect on pulsed laser measurements of fluid flow: speckle velocimetry vs particle image velocimetry", Applied optics **23**, 11, 1690–1691 (1984).

Adrian, R. J., "Particle-imaging techniques for experimental fluid mechanics", Annual review of fluid mechanics **23**, 1, 261–304 (1991).

Adrian, R. J., "Twenty years of particle image velocimetry", Experiments in fluids **39**, 2, 159–169 (2005).

Adrian, R. J., "Next generation PIV (presentation)", in "15th International Symposium on Applications of Lasers to Fluid Mechanics, Lisbon, Portugal", (2010).

Adrian, R. J. and J. Westerweel, *Particle image velocimetry* (Cambridge University Press, 2011).

Arroyo, M. and C. Greated, "Stereoscopic particle image velocimetry", Measurement science and technology **2**, 12, 1181 (1991).

Astarita, T. and G. Cardone, "Analysis of interpolation schemes for image deformation methods in piv", Experiments in fluids **38**, 2, 233–243 (2005).

Atherton, T. J. and D. J. Kerbyson, "Size invariant circle detection", Image and Vision computing **17**, 11, 795–803 (1999).

Atkinson, C. and J. Soria, "An efficient simultaneous reconstruction technique for tomographic particle image velocimetry", Experiments in Fluids **47**, 4-5, 553 (2009).

Auton, T., J. Hunt and M. Prud'Homme, "The force exerted on a body in inviscid unsteady non-uniform rotational flow", Journal of Fluid Mechanics **197**, 241–257 (1988).

Avellaneda, M., S. Torquato and I. Kim, "Diffusion and geometric effects in passive advection by random arrays of vortices", Physics of Fluids A: Fluid Dynamics **3**, 8, 1880–1891 (1991).

Bailey, A., "Sphere drag coefficient for subsonic speeds in continuum and free-molecule flows", Journal of Fluid Mechanics **65**, 2, 401–410 (1974).

Bailey, A. and R. Starr, "Sphere drag at transonic speeds and high reynolds numbers", AIAA Journal **14**, 11, 1631 (1976).

Baldi, S. and M. Yianneskis, "On the direct measurement of turbulence energy dissipation in stirred vessels with piv", Industrial & engineering chemistry research **42**, 26, 7006–7016 (2003).

Basset, A. B., *A treatise on hydrodynamics: with numerous examples*, vol. 2 (Deighton, Bell and Company, 1888).

Bearman, P., J. Graham, M. Downie and E. Obasaju, "Forces on cylinders in viscous oscillatory flow at low keulegan-carpenter numbers", Journal of Fluid Mechanics **154**, 337-356, 14 (1985).

Belden, J., T. T. Truscott, M. C. Axiak and A. H. Techet, "Three-dimensional synthetic aperture particle image velocimetry", Measurement Science and Technology **21**, 12, 125403 (2010).

Bernard, P. S. and J. M. Wallace, *Turbulent flow: analysis, measurement, and prediction* (John Wiley & Sons, 2002).

Bian, S., S. L. Ceccio and J. F. Driscoll, "A dual-camera cinematographic piv measurement system at kilohertz frame rate for high-speed, unsteady flows", Experiments in fluids **48**, 3, 487–495 (2010).

Boillot, A. and A. Prasad, "Optimization procedure for pulse separation in cross-correlation PIV", Experiments in fluids **21**, 2, 87–93 (1996).

Bordoloi, A. D., A. A. Martinez and K. Prestridge, "Relaxation drag history of shock accelerated microparticles", Journal of Fluid Mechanics **823** (2017).

Brown, L. G., "A survey of image registration techniques", ACM computing surveys (CSUR) **24**, 4, 325–376 (1992).

Buchmann, N., C. Atkinson, M. Jeremy and J. Soria, "Tomographic particle image velocimetry investigation of the flow in a modeled human carotid artery bifurcation", Experiments in fluids **50**, 4, 1131–1151 (2011).

Careta, A., F. Sagués and J. Sancho, "Stochastic generation of homogeneous isotropic turbulence with well-defined spectra", Physical review E **48**, 3, 2279 (1993).

Charonko, J. J. and P. P. Vlachos, "Estimation of uncertainty bounds for individual particle image velocimetry measurements from cross-correlation peak ratio", Measurement Science and Technology **24**, 6, 065301 (2013).

Christensen, K. and R. Adrian, "Measurement of instantaneous eulerian acceleration fields by particle image accelerometry: method and accuracy", Experiments in Fluids **33**, 6, 759–769 (2002).

Cierpka, C., R. Segura, R. Hain and C. Kähler, "A simple single camera 3c3d velocity measurement technique without errors due to depth of correlation and spatial averaging for microfluidics", Measurement Science and Technology **21**, 4, 045401 (2010).

Clift, R. and W. Gauvin, "The motion of particles in turbulent gas streams", Proceedings of Chemeca 70 **1**, 14–28 (1970).

Clift, R., J. R. Grace and M. E. Weber, *Bubbles, drops, and particles* (Academic Press, New York, 1978).

Coleman, T. F. and Y. Li, "An interior trust region approach for nonlinear minimization subject to bounds", SIAM Journal on optimization **6**, 2, 418–445 (1996).

Crowe, C., J. Nicholls and R. Morrison, "Drag coefficients of inert and burning particles accelerating in gas streams", Symposium (International) on Combustion **9**, 1, 395–406 (1963).

Crowe, C. T., J. D. Schwarzkopf, M. Sommerfeld and Y. Tsuji, *Multiphase flows with droplets and particles* (CRC press, 2011).

Dahm, W. J. and K. B. Southerland, "Experimental assessment of taylor's hypothesis and its applicability to dissipation estimates in turbulent flows", Physics of Fluids **9**, 7, 2101–2107 (1997).

Ding, L., *Multi-pulse PTV: Evaluation on Spatial Resolution, Velocity Accuracy and Acceleration Measurement*, Master's thesis, Arizona State University (2014).

Ding, L. and R. J. Adrian, "N-pulse particle image velocimetry-accelerometry for unsteady flow-structure interaction", Measurement Science and Technology **28**, 1, 014001 (2016).

Ding, L. and R. J. Adrian, "Optimization of N-pulse particle tracking velocimetry-accelerometry (soon to be submitted, preprint upon request)", Measurement science and technology (2017).

Discetti, S. and R. J. Adrian, "High accuracy measurement of magnification for monocular piv", Measurement Science and Technology **23**, 11, 117001 (2012).

Discetti, S., N. Agüera, G. Cafiero and T. Astarita, "Ensemble 3d ptv for high resolution turbulent statistics", in "11th international symposium on particle image velocimetry, Santa Barbara, CA USA, September", pp. 14–16 (2015).

Discetti, S. and T. Astarita, "Fast 3d piv with direct sparse cross-correlations", Experiments in fluids **53**, 5, 1437–1451 (2012a).

Discetti, S. and T. Astarita, "Fast 3d piv with direct sparse cross-correlations", Experiments in fluids **53**, 5, 1437–1451 (2012b).

Discetti, S. and T. Astarita, "A fast multi-resolution approach to tomographic piv", Experiments in fluids **52**, 3, 765–777 (2012c).

Discetti, S., I. B. Ziskin, T. Astarita, R. J. Adrian and K. P. Prestridge, "Piv measurements of anisotropy and inhomogeneity in decaying fractal generated turbulence", Fluid Dynamics Research **45**, 6, 061401 (2013).

Donzis, D., P. Yeung and K. Sreenivasan, "Dissipation and enstrophy in isotropic turbulence: Resolution effects and scaling in direct numerical simulations", Physics of Fluids **20**, 4, 045108 (2008).

Dütsch, H., F. Durst, S. Becker and H. Lienhart, "Low-reynolds-number flow around an oscillating circular cylinder at low keulegan–carpenter numbers", Journal of Fluid Mechanics **360**, 249–271 (1998).

Elsinga, G., R. Adrian, B. Van Oudheusden and F. Scarano, "Three-dimensional vortex organization in a high-reynolds-number supersonic turbulent boundary layer", Journal of Fluid Mechanics **644**, 35–60 (2010).

Elsinga, G., J. Westerweel, F. Scarano and M. Novara, "On the velocity of ghost particles and the bias errors in tomographic-piv", Experiments in fluids **50**, 4, 825–838 (2011).

Elsinga, G. E., F. Scarano, B. Wieneke and B. W. van Oudheusden, "Tomographic particle image velocimetry", Experiments in fluids **41**, 6, 933–947 (2006).

Fahringer, T. W., K. P. Lynch and B. S. Thurow, "Volumetric particle image velocimetry with a single plenoptic camera", Measurement Science and Technology **26**, 11, 115201 (2015).

Ferrari, S. and L. Rossi, "Particle tracking velocimetry and accelerometry (PTVA) measurements applied to quasi-two-dimensional multi-scale flows", Experiments in Fluids **44**, 6, 873–886 (2008).

Foucaut, J., B. Miliat, N. Perenne and M. Stanislas, "Characterization of different piv algorithms using the europiv synthetic image generator and real images from a turbulent boundary layer", in "Particle Image Velocimetry: Recent Improvements", pp. 163–185 (Springer, 2004).

Fuchs, T., R. Hain and C. J. Kähler, "Double-frame 3d-ptv using a tomographic predictor", Experiments in Fluids **57**, 11, 174 (2016).

Fuchs, T., R. Hain and C. J. Kähler, "Non-iterative double-frame 2d/3d particle tracking velocimetry", Experiments in Fluids **58**, 9, 119 (2017).

Fung, J. C. H., J. C. Hunt, N. Malik and R. Perkins, "Kinematic simulation of homogeneous turbulence by unsteady random fourier modes", Journal of Fluid Mechanics **236**, 281–318 (1992).

Ganapathisubramani, B., E. K. Longmire, I. Marusic and S. Pothos, "Dual-plane piv technique to determine the complete velocity gradient tensor in a turbulent boundary layer", Experiments in Fluids **39**, 2, 222–231 (2005).

Gui, L., W. Merzkirch and R. Fei, "A digital mask technique for reducing the bias error of the correlation-based PIV interrogation algorithm", Experiments in fluids **29**, 1, 30–35 (2000).

Gui, L. and S. Wereley, "A correlation-based continuous window-shift technique to reduce the peak-locking effect in digital piv image evaluation", Experiments in Fluids **32**, 4, 506–517 (2002).

Hain, R. and C. Kähler, "Fundamentals of multiframe particle image velocimetry (piv)", Experiments in fluids **42**, 4, 575–587 (2007).

Haranandani, G., "Optimization and accuracy of 3-pulsed particle tracking velocimetry", MSE Proj. Rep., Arizona State Univ (2011).

Haworth, D. and S. Pope, "A generalized langevin model for turbulent flows", The Physics of fluids **29**, 2, 387–405 (1986).

Henderson, C. B., "Drag coefficients of spheres in continuum and rarefied flows", AIAA J **14**, 6, 707–708 (1976).

Huang, H., D. Dabiri and M. Gharib, "On errors of digital particle image velocimetry", Measurement Science and Technology **8**, 12, 1427 (1997).

Igra, O. and K. Takayama, "Shock tube study of the drag coefficient of a sphere in a non-stationary flow", Proceedings of the Royal Society of London A: Mathematical, Physical and Engineering Sciences **442**, 1915, 231–247 (1993).

Iliadis, G. and P. Anagnostopoulos, "Viscous oscillatory flow around a circular cylinder at low keulegan-carpenter numbers and frequency parameters", International journal for numerical methods in fluids **26**, 4, 403–442 (1998).

Ingebo, R. D., "Drag coefficients for droplets and solid spheres in clouds accelerating in airstreams", NACA TN 3762 (1956).

Jeon, Y. J. and H. J. Sung, "PIV measurement of flow around an arbitrarily moving body", Experiments in fluids **50**, 4, 787–798 (2011).

Jourdan, G., L. Houas, O. Igra, J.-L. Estivalezes, C. Devals and E. Meshkov, "Drag coefficient of a sphere in a non-stationary flow: new results", Proceedings of the Royal Society of London A: Mathematical, Physical and Engineering Sciences **463**, 2088, 3323–3345 (2007).

Kähler, C., U. Scholz and J. Ortmanns, "Wall-shear-stress and near-wall turbulence measurements up to single pixel resolution by means of long-distance micro-piv", Experiments in Fluids **41**, 2, 327–341 (2006).

Kähler, C. J., T. Astarita, P. P. Vlachos, J. Sakakibara, R. Hain, S. Discetti, R. Foy and C. Cierpka, "Main results of the 4th international piv challenge", Experiments in Fluids **57**, 6, 1–71 (2016).

Kähler, C. J. and J. Kompenhans, "Fundamentals of multiple plane stereo particle image velocimetry", Experiments in Fluids **29**, S070–S077 (2000).

Kähler, C. J., S. Scharnowski and C. Cierpka, "On the resolution limit of digital particle image velocimetry", Experiments in fluids **52**, 6, 1629–1639 (2012a).

Kähler, C. J., S. Scharnowski and C. Cierpka, "On the uncertainty of digital piv and ptv near walls", Experiments in fluids **52**, 6, 1641–1656 (2012b).

Kaneda, Y., T. Ishihara, M. Yokokawa, K. Itakura and A. Uno, "Energy dissipation rate and energy spectrum in high resolution direct numerical simulations of turbulence in a periodic box", Physics of Fluids **15**, 2, L21–L24 (2003).

Karanfilian, S. and T. Kotas, "Drag on a sphere in unsteady motion in a liquid at rest", Journal of Fluid Mechanics **87**, 1, 85–96 (1978).

Karlsson, R. I. and T. Johansson, "Ldv measurements of higher order moments of velocity fluctuations in a turbulent boundary layer", in "Laser Anemometry in Fluid Mechanics III (R. J. Adrian, Ed.), Ladoan- Instituto Superior Tecnico, Lisbon", pp. 273–279 (1988).

Kasagi, N. and K. Nishino, "Probing turbulence with three-dimensional particle-tracking velocimetry", Experimental thermal and fluid science **4**, 5, 601–612 (1991).

Keane, R., R. Adrian and Y. Zhang, "Super-resolution particle imaging velocimetry", Measurement Science and Technology **6**, 6, 754 (1995).

Keane, R. D. and R. J. Adrian, "Optimization of particle image velocimeters. i. double pulsed systems", Measurement science and technology **1**, 11, 1202 (1990).

Keane, R. D. and R. J. Adrian, "Optimization of particle image velocimeters: Ii. multiple pulsed systems", Measurement Science and Technology **2**, 10, 963 (1991).

Keane, R. D. and R. J. Adrian, "Theory of cross-correlation analysis of piv images", Applied scientific research **49**, 3, 191–215 (1992).

Kraichnan, R. H., "Diffusion by a random velocity field", The physics of fluids **13**, 1, 22–31 (1970).

Kraichnan, R. H., "Diffusion of passive-scalar and magnetic fields by helical turbulence", Journal of Fluid Mechanics **77**, 4, 753–768 (1976).

La Porta, A., G. A. Voth, A. M. Crawford, J. Alexander and E. Bodenschatz, "Fluid particle accelerations in fully developed turbulence", Nature **409**, 6823, 1017–1019 (2001).

Lavoie, P., G. Avallone, F. De Gregorio, G. Romano and R. Antonia, "Spatial resolution of piv for the measurement of turbulence", Experiments in Fluids **43**, 1, 39–51 (2007).

Lee, J.-H. and H. J. Sung, "Effects of an adverse pressure gradient on a turbulent boundary layer", International Journal of Heat and Fluid Flow **29**, 3, 568–578 (2008).

Lin, J.-C., P. Vorobieff and D. Rockwell, "Three-dimensional patterns of streamwise vorticity in the turbulent near-wake of a cylinder", Journal of fluids and structures **9**, 2, 231–234 (1995).

Lin, X., P. Bearman and J. Graham, "A numerical study of oscillatory flow about a circular cylinder for low values of beta parameter", Journal of Fluids and Structures **10**, 5, 501–526 (1996).

Liu, X. and J. Katz, "Instantaneous pressure and material acceleration measurements using a four-exposure piv system", Experiments in Fluids **41**, 2, 227 (2006).

Loth, E., "Compressibility and rarefaction effects on drag of a spherical particle", AIAA journal **46**, 9, 2219 (2008).

Lüthi, B., A. Tsinober and W. Kinzelbach, "Lagrangian measurement of vorticity dynamics in turbulent flow", Journal of Fluid mechanics **528**, 87–118 (2005).

Lynch, K. and F. Scarano, "A high-order time-accurate interrogation method for time-resolved piv", Measurement Science and Technology **24**, 3, 035305 (2013).

Lynch, K. and F. Scarano, "Material acceleration estimation by four-pulse tomo-piv", Measurement Science and Technology **25**, 8, 084005 (2014).

Malik, N., T. Dracos and D. Papantoniou, "Particle tracking velocimetry in three-dimensional flows", Experiments in Fluids **15**, 4-5, 279–294 (1993).

Martinez, A. A., G. C. Orlicz and K. P. Prestridge, "A new experiment to measure shocked particle drag using multi-pulse particle image velocimetry and particle tracking", Experiments in Fluids **56**, 1, 1–12 (2015).

Maxey, M. R. and J. J. Riley, "Equation of motion for a small rigid sphere in a nonuniform flow", The Physics of Fluids **26**, 4, 883–889 (1983).

Mei, R., "Velocity fidelity of flow tracer particles", Experiments in Fluids **22**, 1, 1–13 (1996).

Mei, R. and R. J. Adrian, "Flow past a sphere with an oscillation in the free-stream velocity and unsteady drag at finite reynolds number", Journal of Fluid Mechanics **237**, 323–341 (1992).

Meinhart, C. D., S. T. Wereley and J. G. Santiago, "A piv algorithm for estimating time-averaged velocity fields", Journal of Fluids engineering **122**, 2, 285–289 (2000).

Mordant, N., A. M. Crawford and E. Bodenschatz, "Experimental lagrangian acceleration probability density function measurement", Physica D: Nonlinear Phenomena **193**, 1, 245–251 (2004).

Morison, J., J. Johnson and S. Schaaf, "The force exerted by surface waves on piles", Journal of Petroleum Technology **2**, 05, 149–154 (1950).

Moser, R. D., J. Kim and N. N. Mansour, "Direct numerical simulation of turbulent channel flow up to re τ= 590", Physics of fluids **11**, 4, 943–945 (1999).

Murphy, M. J. and R. J. Adrian, "Piv space-time resolution of flow behind blast waves", Experiments in Fluids **49**, 1, 193–202 (2010).

Nagib, H. M. and K. A. Chauhan, "Variations of von kármán coefficient in canonical flows", Physics of Fluids **20**, 10, 101518 (2008).

Nayler, J. and B. Frazer, "Preliminary report upon an experimental method of investigating, by the aid of kinematographic photography, the history of eddying flow past a model immersed in water", Rep. Advisory Commit For Aeronau **1**, 1917–18 (1917).

Neal, D. R., A. Sciacchitano, B. L. Smith and F. Scarano, "Collaborative framework for piv uncertainty quantification: the experimental database", Measurement Science and Technology **26**, 7, 074003 (2015).

Nguyen, C. V., T. D. Nguyen, J. C. Wells and A. Nakayama, "Interfacial PIV to resolve flows in the vicinity of curved surfaces", Experiments in fluids **48**, 4, 577–587 (2010).

Nishino, K., N. Kasagi and M. Hirata, "Three-dimensional particle tracking velocimetry based on automated digital image processing", Journal of fluids engineering **111**, 4, 384–391 (1989).

Noca, F., *On the evaluation of time-dependent fluid-dynamic forces on bluff bodies*, Ph.D. thesis, California Institute of Technology (1997).

Noca, F., D. Shiels and D. Jeon, "Measuring instantaneous fluid dynamic forces on bodies, using only velocity fields and their derivatives", Journal of Fluids and Structures **11**, 3, 345–350 (1997).

Noca, F., D. Shiels and D. Jeon, "A comparison of methods for evaluating time-dependent fluid dynamic forces on bodies, using only velocity fields and their derivatives", Journal of Fluids and Structures **13**, 5, 551–578 (1999).

Novara, M., K. J. Batenburg and F. Scarano, "Motion tracking-enhanced mart for tomographic piv", Measurement science and technology **21**, 3, 035401 (2010).

Novara, M., D. Schanz, N. Reuther, C. J. Kähler and A. Schröder, "Lagrangian 3d particle tracking in high-speed flows: Shake-the-box for multi-pulse systems", Experiments in Fluids **57**, 8, 128 (2016).

Ohmi, K. and H.-Y. Li, "Particle-tracking velocimetry with new algorithms", Measurement Science and Technology **11**, 6, 603 (2000).

Otsu, N., "A threshold selection method from gray-level histograms", Automatica **11**, 285-296, 23–27 (1975).

Parmar, M., A. Haselbacher and S. Balachandar, "Modeling of the unsteady force for shock–particle interaction", Shock Waves **19**, 4, 317–329 (2009).

Parmar, M., A. Haselbacher and S. Balachandar, "Improved drag correlation for spheres and application to shock-tube experiments", Aiaa Journal **48**, 6, 1273–1276 (2010).

Parmar, M., A. Haselbacher and S. Balachandar, "Generalized basset-boussinesq-oseen equation for unsteady forces on a sphere in a compressible flow", Physical review letters **106**, 8, 084501 (2011).

Perret, L., P. Braud, C. Fourment, L. David and J. Delville, "3-component acceleration field measurement by dual-time stereoscopic particle image velocimetry", Experiments in Fluids **40**, 5, 813–824 (2006).

Pope, S. B., *Turbulent Flows* (Cambridge University Press, 2000).

Prasad, A. K., "Stereoscopic particle image velocimetry", Experiments in fluids **29**, 2, 103–116 (2000).

Racina, A. and M. Kind, "Specific power input and local micromixing times in turbulent taylor–couette flow", Experiments in fluids **41**, 3, 513–522 (2006).

Reuther, N., S. Scharnowski, R. Hain, D. Schanz, A. Schröder and C. Kähler, "Experimental investigation of adverse pressure gradient turbulent boundary layers by means of large-scale piv", in "11th international symposium on particle image velocimetry, Santa Barbara, CA USA, September", (2015).

Robinson, O. and D. Rockwell, "Construction of three-dimensional images of flow structure via particle tracking techniques", Experiments in fluids **14**, 4, 257–270 (1993).

Rossi, L. and S. Lardeau, "Lamination and folding in electromagnetically driven flows of specified geometries", Journal of Turbulence , 12, N6 (2011).

Rudinger, G., "Effective drag coefficient for gas-particle flow in shock tubes", Journal of Basic Engineering **92**, 1, 165–172 (1970).

Saarenrinne, P. and M. Piirto, "Turbulent kinetic energy dissipation rate estimation from piv velocity vector fields", Experiments in Fluids **29**, S300–S307 (2000).

Scarano, F., "Iterative image deformation methods in piv", Measurement science and technology **13**, 1, R1 (2001).

Scarano, F. and C. Poelma, "Three-dimensional vorticity patterns of cylinder wakes", Experiments in Fluids **47**, 1, 69 (2009).

Scarano, F. and M. L. Riethmuller, "Advances in iterative multigrid piv image processing", Experiments in Fluids **29**, 1, S051–S060 (2000).

Schanz, D., S. Gesemann and A. Schröder, "Shake-the-box: Lagrangian particle tracking at high particle image densities", Experiments in fluids **57**, 5, 70 (2016).

Schanz, D., S. Gesemann, A. Schröder, B. Wieneke and M. Novara, "Non-uniform optical transfer functions in particle imaging: calibration and application to tomographic reconstruction", Measurement Science and Technology **24**, 2, 024009 (2012).

Scharnowski, S. and C. J. Kähler, "On the effect of curved streamlines on the accuracy of piv vector fields", Experiments in Fluids **54**, 1, 1–11 (2013).

Schröder, A., R. Geisler, K. Staack, G. Elsinga, F. Scarano, B. Wieneke, A. Henning, C. Poelma and J. Westerweel, "Eulerian and lagrangian views of a turbulent boundary layer flow using time-resolved tomographic piv", Experiments in fluids **50**, 4, 1071–1091 (2011).

Schröder, A., D. Schanz, R. Geisler, M. Novara and C. Willert, "Near-wall turbulence characterization using 4d-ptv "shake-the-box"", in "11th International Symposium on Particle Image Velocimetry - PIV2015", (2015).

Sciacchitano, A., D. R. Neal, B. L. Smith, S. O. Warner, P. P. Vlachos, B. Wieneke and F. Scarano, "Collaborative framework for piv uncertainty quantification: comparative assessment of methods", Measurement Science and Technology **26**, 7, 074004 (2015).

Sciacchitano, A., F. Scarano and B. Wieneke, "Multi-frame pyramid correlation for time-resolved piv", Experiments in fluids **53**, 4, 1087–1105 (2012).

Sciacchitano, A., B. Wieneke and F. Scarano, "Piv uncertainty quantification by image matching", Measurement Science and Technology **24**, 4, 045302 (2013).

Sharp, K. and R. Adrian, "Piv study of small-scale flow structure around a rushton turbine", AIChE Journal **47**, 4, 766–778 (2001).

Sheng, J., E. Malkiel and J. Katz, "Digital holographic microscope for measuring three-dimensional particle distributions and motions", Applied optics **45**, 16, 3893–3901 (2006).

Sheng, J., E. Malkiel and J. Katz, "Using digital holographic microscopy for simultaneous measurements of 3d near wall velocity and wall shear stress in a turbulent boundary layer", Experiments in fluids **45**, 6, 1023–1035 (2008).

Sheng, J., H. Meng and R. Fox, "A large eddy piv method for turbulence dissipation rate estimation", Chemical engineering science **55**, 20, 4423–4434 (2000).

Skews, B., M. Bredin and M. Efune, "Drag measurements in unsteady compressible flow. part 2: Shock wave loading of spheres and cones", R&D J., South Afr. Inst. Mech. Eng **23**, 13–19 (2007).

Soloff, S. M., R. J. Adrian and Z.-C. Liu, "Distortion compensation for generalized stereoscopic particle image velocimetry", Measurement science and technology **8**, 12, 1441 (1997).

Spalart, P. R., "Direct simulation of a turbulent boundary layer up to rθ= 1410", Journal of fluid mechanics **187**, 61–98 (1988).

Spalding, D., "A single formula for the ' law of the wall"', Journal of Applied Mechanics **28**, 3, 455–458 (1961).

Stanislas, M., K. Okamoto, C. J. Kähler and J. Westerweel, "Main results of the second international piv challenge", Experiments in Fluids **39**, 2, 170–191 (2005).

Stanislas, M., K. Okamoto, C. J. Kähler, J. Westerweel and F. Scarano, "Main results of the third international piv challenge", Experiments in Fluids **45**, 1, 27–71 (2008).

Stokes, G. G., *On the effect of the internal friction of fluids on the motion of pendulums*, vol. 9 (Pitt Press Cambridge, 1851).

Sun, M., T. Saito, K. Takayama and H. Tanno, "Unsteady drag on a sphere by shock wave loading", Shock waves **14**, 1, 3–9 (2005).

Suzuki, T., Y. Sakamura, O. Igra, T. Adachi, S. Kobayashi, A. Kotani and Y. Funawatashi, "Shock tube study of particles' motion behind a planar shock wave", Measurement Science and Technology **16**, 12, 2431 (2005).

Tanaka, T. and J. K. Eaton, "A correction method for measuring turbulence kinetic energy dissipation rate by piv", Experiments in Fluids **42**, 6, 893–902 (2007).

Tatsuno, M. and P. Bearman, "A visual study of the flow around an oscillating circular cylinder at low keulegan–carpenter numbers and low stokes numbers", Journal of Fluid Mechanics **211**, 157–182 (1990).

Timmins, B. H., B. W. Wilson, B. L. Smith and P. P. Vlachos, "A method for automatic estimation of instantaneous local uncertainty in particle image velocimetry measurements", Experiments in Fluids **53**, 4, 1133–1147 (2012).

Tokgoz, S., G. E. Elsinga, R. Delfos and J. Westerweel, "Spatial resolution and dissipation rate estimation in taylor–couette flow for tomographic piv", Experiments in fluids **53**, 3, 561–583 (2012).

Tsai, R., "A versatile camera calibration technique for high-accuracy 3d machine vision metrology using off-the-shelf tv cameras and lenses", IEEE Journal on Robotics and Automation **3**, 4, 323–344 (1987).

Unal, M., J.-C. Lin and D. Rockwell, "Force prediction by piv imaging: a momentum-based approach", Journal of Fluids and Structures **11**, 8, 965–971 (1997).

Virant, M. and T. Dracos, "3d ptv and its application on lagrangian motion", Measurement science and technology **8**, 12, 1539 (1997).

Voth, G. A., A. la Porta, A. M. Crawford, J. Alexander and E. Bodenschatz, "Measurement of particle accelerations in fully developed turbulence", Journal of Fluid Mechanics **469**, 121–160 (2002).

Wagner, J. L., S. J. Beresh, S. P. Kearney, B. O. Pruett and E. K. Wright, "Shock tube investigation of quasi-steady drag in shock-particle interactions", Physics of Fluids (1994-present) **24**, 12, 123301 (2012).

Wereley, S. and C. Meinhart, "Second-order accurate particle image velocimetry", Experiments in Fluids **31**, 3, 258–268 (2001).

Westerweel, J., "Analysis of piv interrogation with low pixel resolution", in "Proc. SPIE Series", vol. 2005, pp. 624–635 (1993).

Westerweel, J., D. Dabiri and M. Gharib, "The effect of a discrete window offset on the accuracy of cross-correlation analysis of digital piv recordings", Experiments in fluids **23**, 1, 20–28 (1997).

Westerweel, J., G. E. Elsinga and R. J. Adrian, "Particle image velocimetry for complex and turbulent flows", Annual Review of Fluid Mechanics **45**, 409–436 (2013).

Westerweel, J., P. Geelhoed and R. Lindken, "Single-pixel resolution ensemble correlation for micro-piv applications", Experiments in Fluids **37**, 3, 375–384 (2004).

Wieneke, B., "Stereo-PIV using self-calibration on particle images", Experiments in fluids **39**, 2, 267–280 (2005).

Wieneke, B., "Volume self-calibration for 3D particle image velocimetry", Experiments in fluids **45**, 4, 549–556 (2008).

Wieneke, B., "Iterative reconstruction of volumetric particle distribution", Measurement Science and Technology **24**, 2, 024008 (2012).

Wieneke, B., "Piv uncertainty quantification from correlation statistics", Measurement Science and Technology **26**, 7, 074002 (2015).

Willert, C., "The fully digital evaluation of photographic piv recordings", Applied Scientific Research **56**, 2-3, 79–102 (1996).

Willert, C. and M. Gharib, "Three-dimensional particle imaging with a single camera", Experiments in Fluids **12**, 6, 353–358 (1992).

Willert, C. E. and M. Gharib, "Digital particle image velocimetry", Experiments in fluids **10**, 4, 181–193 (1991).

Worth, N. and T. Nickels, "Acceleration of tomo-piv by estimating the initial volume intensity distribution", Experiments in Fluids **45**, 5, 847–856 (2008).

Worth, N., T. Nickels and N. Swaminathan, "A tomographic piv resolution study based on homogeneous isotropic turbulence dns data", Experiments in Fluids **49**, 3, 637–656 (2010).

Ziskin, I., R. Adrian and K. Prestridge, "Volume segmentation tomographic particle image velocimetry", in "Proceedings of 9th international symposium on particle image velocimetry. Kobe University, Kobe, Japan", pp. 21–23 (2011).

APPENDIX A

COMPLETE EQUATIONS OF POSITION, VELOCITY AND ACCELERATION RMS ERRORS

A.1 3-P

$$\left(\sigma^{*3P}_{X_p}\right)^2 = \left(\sigma^{*3P}_{\text{bias},X_p}\right)^2 + \left(\sigma^{*3P}_{\text{rnd},X_p}\right)^2 \tag{A.1}$$

$$\begin{aligned}\left(\sigma^{*3P}_{\text{bias},X_p}\right)^2 = \Bigg\{ &\left[\frac{1}{\alpha(1-\alpha)}\frac{t'}{\Delta t} - \frac{1}{\alpha(1-\alpha)}\frac{t'^2}{\Delta t^2}\right][1-cos(\vartheta(\alpha\Delta t))] \\ &+\left(-\frac{\alpha}{1-\alpha}\frac{t'}{\Delta t} + \frac{1}{1-\alpha}\frac{t'^2}{\Delta t^2}\right)[1-cos(\vartheta(\Delta t))] - \left[1-cos(\vartheta(t'))\right]\Bigg\}^2 \Big/ \vartheta(\Delta t)^2 \\ &+\Bigg\{\left[\frac{1}{\alpha(1-\alpha)}\frac{t'}{\Delta t} - \frac{1}{\alpha(1-\alpha)}\frac{t'^2}{\Delta t^2}\right] sin(\vartheta(\alpha\Delta t)) \\ &+\left(-\frac{\alpha}{1-\alpha}\frac{t'}{\Delta t} + \frac{1}{1-\alpha}\frac{t'^2}{\Delta t^2}\right) sin(\vartheta(\Delta t)) - sin(\vartheta(t'))\Bigg\}^2 \Big/ \vartheta(\Delta t)^2\end{aligned} \tag{A.2}$$

$$\begin{aligned}\left(\sigma^{*3P}_{\text{rnd},X_p}\right)^2 = \Bigg\{ &\left(1 - \frac{1+\alpha}{\alpha}\frac{t'}{\Delta t} + \frac{1}{\alpha}\frac{t'^2}{\Delta t^2}\right)^2 + \left[\frac{1}{\alpha(1-\alpha)}\frac{t'}{\Delta t} - \frac{1}{\alpha(1-\alpha)}\frac{t'^2}{\Delta t^2}\right]^2 \\ &+\left(-\frac{\alpha}{1-\alpha}\frac{t'}{\Delta t} + \frac{1}{1-\alpha}\frac{t'^2}{\Delta t^2}\right)^2\Bigg\} \frac{\langle|\delta \boldsymbol{X}_p|^2\rangle}{R^2\vartheta(\Delta t)^2}\end{aligned} \tag{A.3}$$

$$\left(\sigma^{*3P}_{\dot{X}_p}\right)^2 = \left(\sigma^{*3P}_{\text{bias},\dot{X}_p}\right)^2 + \left(\sigma^{*3P}_{\text{rnd},\dot{X}_p}\right)^2 \tag{A.4}$$

$$\begin{aligned}\left(\sigma^{*3P}_{\text{bias},\dot{X}_p}\right)^2 = \Bigg\{ &\left[\frac{1}{\alpha(1-\alpha)} - \frac{2}{\alpha(1-\alpha)}\frac{t'}{\Delta t}\right][1-cos(\vartheta(\alpha\Delta t))] \\ &+\left(-\frac{\alpha}{1-\alpha} + \frac{2}{1-\alpha}\frac{t'}{\Delta t}\right)[1-cos(\vartheta(\Delta t))] - \left[sin(\vartheta(t'))(\dot{\vartheta}_0\Delta t + \ddot{\vartheta}_0 t'\Delta t)\right]\Bigg\}^2 \Big/ \vartheta(\Delta t)^2 \\ &+\Bigg\{\left[\frac{1}{\alpha(1-\alpha)} - \frac{2}{\alpha(1-\alpha)}\frac{t'}{\Delta t}\right] sin(\vartheta(\alpha\Delta t)) \\ &+\left(-\frac{\alpha}{1-\alpha} + \frac{2}{1-\alpha}\frac{t'}{\Delta t}\right) sin(\vartheta(\Delta t)) - \left[cos(\vartheta(t'))(\dot{\vartheta}_0\Delta t + \ddot{\vartheta}_0 t'\Delta t)\right]\Bigg\}^2 \Big/ \vartheta(\Delta t)^2\end{aligned} \tag{A.5}$$

$$\begin{aligned}\left(\sigma^{*3P}_{\text{rnd},\dot{X}_p}\right)^2 = \Bigg\{ &\left(-\frac{1+\alpha}{\alpha} + \frac{2}{\alpha}\frac{t'}{\Delta t}\right)^2 + \left[\frac{1}{\alpha(1-\alpha)} - \frac{2}{\alpha(1-\alpha)}\frac{t'}{\Delta t}\right]^2 \\ &+\left(-\frac{\alpha}{1-\alpha} + \frac{2}{1-\alpha}\frac{t'}{\Delta t}\right)^2\Bigg\} \frac{\langle|\delta \boldsymbol{X}_p|^2\rangle}{R^2\vartheta(\Delta t)^2}\end{aligned} \tag{A.6}$$

$$\left(\sigma^{*3P}_{\ddot{X}_p}\right)^2 = \left(\sigma^{*3P}_{\text{bias},\ddot{X}_p}\right)^2 + \left(\sigma^{*3P}_{\text{rnd},\ddot{X}_p}\right)^2 \tag{A.7}$$

$$\begin{aligned}\left(\sigma^{*3P}_{\text{bias},\ddot{X}_p}\right)^2 = \Bigg\{ & -\frac{2}{\alpha(1-\alpha)}\left[1-cos(\vartheta(\alpha\Delta t))\right] + \frac{2}{1-\alpha}\left[1-cos(\vartheta(\Delta t))\right] \\ & -\left[cos(\vartheta(t'))(\dot{\vartheta}_0^2 + \ddot{\vartheta}_0^2 t'^2 + 2\dot{\vartheta}_0\ddot{\vartheta}_0 t')\Delta t^2 + \ddot{\vartheta}_0 sin(\vartheta(t'))\Delta t^2\right]\Bigg\}^2 \Big/ \vartheta(\Delta t)^2 \\ & + \Bigg\{ -\frac{2}{\alpha(1-\alpha)}sin(\vartheta(\alpha\Delta t)) + \frac{2}{1-\alpha}sin(\vartheta(\Delta t)) \\ & -\left[-sin(\vartheta(t'))(\dot{\vartheta}_0^2 + \ddot{\vartheta}_0^2 t'^2 + 2\dot{\vartheta}_0\ddot{\vartheta}_0 t')\Delta t^2 + \ddot{\vartheta}_0 cos(\vartheta(t'))\Delta t^2\right]\Bigg\}^2 \Big/ \vartheta(\Delta t)^2\end{aligned} \tag{A.8}$$

$$\left(\sigma^{*3P}_{\text{rnd},\ddot{X}_p}\right)^2 = \left\{\left(\frac{2}{\alpha}\right)^2 + \left[-\frac{2}{\alpha(1-\alpha)}\right]^2 + \left(\frac{2}{1-\alpha}\right)^2\right\}\frac{\langle|\delta\boldsymbol{X}_p|^2\rangle}{R^2\vartheta(\Delta t)^2} \tag{A.9}$$

A.2 4-P INT

$$\left(\sigma^{*4P\,INT}_{X_p}\right)^2 = \left(\sigma^{*4P\,INT}_{\text{bias},X_p}\right)^2 + \left(\sigma^{*4P\,INT}_{\text{rnd},X_p}\right)^2 \tag{A.10}$$

$$\begin{aligned}\left(\sigma^{*4P\,INT}_{\text{bias},X_p}\right)^2 = \Big\{ & \boldsymbol{d}_2\cdot\boldsymbol{t}^{*4P\,INT}\left[1-cos(\vartheta(\beta\Delta t))\right] + \boldsymbol{d}_3\cdot\boldsymbol{t}^{*4P\,INT}\left[1-cos(\vartheta(\gamma\Delta t))\right] \\ & + \boldsymbol{d}_4\cdot\boldsymbol{t}^{*4P\,INT}\left[1-cos(\vartheta(\Delta t))\right] - \left[1-cos(\vartheta(t'))\right]\Big\}^2 \Big/ \vartheta(\Delta t)^2 \\ & + \Big[\boldsymbol{d}_2\cdot\boldsymbol{t}^{*4P\,INT}sin(\vartheta(\beta\Delta t)) + \boldsymbol{d}_3\cdot\boldsymbol{t}^{*4P\,INT}sin(\vartheta(\gamma\Delta t)) \\ & + \boldsymbol{d}_4\cdot\boldsymbol{t}^{*4P\,INT}sin(\vartheta(\Delta t)) - sin(\vartheta(t'))\Big]^2 \Big/ \vartheta(\Delta t)^2\end{aligned} \tag{A.11}$$

$$\begin{aligned}\left(\sigma^{*4P\,INT}_{\text{rnd},X_p}\right)^2 = \Big[& \left(1+\boldsymbol{d}_1\cdot\boldsymbol{t}^{*4P\,INT}\right)^2 + \left(\boldsymbol{d}_2\cdot\boldsymbol{t}^{*4P\,INT}\right)^2 \\ & + \left(\boldsymbol{d}_3\cdot\boldsymbol{t}^{*4P\,INT}\right)^2 + \left(\boldsymbol{d}_4\cdot\boldsymbol{t}^{*4P\,INT}\right)^2\Big]\frac{\langle|\delta\boldsymbol{X}_p|^2\rangle}{R^2\vartheta(\Delta t)^2}\end{aligned} \tag{A.12}$$

$$\left(\sigma^{*4\text{P INT}}_{\dot{X}_p}\right)^2 = \left(\sigma^{*4\text{P INT}}_{\text{bias},\dot{X}_p}\right)^2 + \left(\sigma^{*4\text{P INT}}_{\text{rnd},\dot{X}_p}\right)^2 \tag{A.13}$$

$$\begin{aligned}\left(\sigma^{*4\text{P INT}}_{\text{bias},\dot{X}_p}\right)^2 = \Bigg\{ & \boldsymbol{d}_2 \cdot \frac{d\boldsymbol{t}^{*4\text{P INT}}}{dt^*}\left[1-cos(\vartheta(\beta\Delta t))\right] + \boldsymbol{d}_3 \cdot \frac{d\boldsymbol{t}^{*4\text{P INT}}}{dt^*}\left[1-cos(\vartheta(\gamma\Delta t))\right] \\ & + \boldsymbol{d}_4 \cdot \frac{d\boldsymbol{t}^{*4\text{P INT}}}{dt^*}\left[1-cos(\vartheta(\Delta t))\right] - \left[sin(\vartheta(t'))(\dot{\vartheta}_0\Delta t + \ddot{\vartheta}_0 t'\Delta t)\right]\Bigg\}^2 \Big/ \vartheta(\Delta t)^2 \\ & + \Bigg\{ \boldsymbol{d}_2 \cdot \frac{d\boldsymbol{t}^{*4\text{P INT}}}{dt^*} sin(\vartheta(\beta\Delta t)) + \boldsymbol{d}_3 \cdot \frac{d\boldsymbol{t}^{*4\text{P INT}}}{dt^*} sin(\vartheta(\gamma\Delta t)) \\ & + \boldsymbol{d}_4 \cdot \frac{d\boldsymbol{t}^{*4\text{P INT}}}{dt^*} sin(\vartheta(\Delta t)) - \left[cos(\vartheta(t'))(\dot{\vartheta}_0\Delta t + \ddot{\vartheta}_0 t'\Delta t)\right]\Bigg\}^2 \Big/ \vartheta(\Delta t)^2 \end{aligned} \tag{A.14}$$

$$\begin{aligned}\left(\sigma^{*4\text{P INT}}_{\text{rnd},\dot{X}_p}\right)^2 = \Bigg[& \left(\boldsymbol{d}_1 \cdot \frac{d\boldsymbol{t}^{*4\text{P INT}}}{dt^*}\right)^2 + \left(\boldsymbol{d}_2 \cdot \frac{d\boldsymbol{t}^{*4\text{P INT}}}{dt^*}\right)^2 \\ & + \left(\boldsymbol{d}_3 \cdot \frac{d\boldsymbol{t}^{*4\text{P INT}}}{dt^*}\right)^2 + \left(\boldsymbol{d}_4 \cdot \frac{d\boldsymbol{t}^{*4\text{P INT}}}{dt^*}\right)^2\Bigg] \frac{\langle|\delta \boldsymbol{X}_p|^2\rangle}{R^2\vartheta(\Delta t)^2} \end{aligned} \tag{A.15}$$

$$\left(\sigma^{*4\text{P INT}}_{\ddot{X}_p}\right)^2 = \left(\sigma^{*4\text{P INT}}_{\text{bias},\ddot{X}_p}\right)^2 + \left(\sigma^{*4\text{P INT}}_{\text{rnd},\ddot{X}_p}\right)^2 \tag{A.16}$$

$$\begin{aligned}\left(\sigma^{*4\text{P INT}}_{\text{bias},\ddot{X}_p}\right)^2 = \Bigg\{ & \boldsymbol{d}_2 \cdot \frac{d^2\boldsymbol{t}^{*4\text{P INT}}}{dt^{*2}}\left[1-cos(\vartheta(\beta\Delta t))\right] \\ & + \boldsymbol{d}_3 \cdot \frac{d^2\boldsymbol{t}^{*4\text{P INT}}}{dt^{*2}}\left[1-cos(\vartheta(\gamma\Delta t))\right] + \boldsymbol{d}_4 \cdot \frac{d^2\boldsymbol{t}^{*4\text{P INT}}}{dt^{*2}}\left[1-cos(\vartheta(\Delta t))\right] \\ & - \left[cos(\vartheta(t'))(\dot{\vartheta}_0^2 + \ddot{\vartheta}_0^2 t'^2 + 2\dot{\vartheta}_0\ddot{\vartheta}_0 t')\Delta t^2 + \ddot{\vartheta}_0 sin(\vartheta(t'))\Delta t^2\right]\Bigg\}^2 \Big/ \vartheta(\Delta t)^2 \\ & + \Bigg\{ \boldsymbol{d}_2 \cdot \frac{d^2\boldsymbol{t}^{*4\text{P INT}}}{dt^{*2}} sin(\vartheta(\beta\Delta t)) + \boldsymbol{d}_3 \cdot \frac{d^2\boldsymbol{t}^{*4\text{P INT}}}{dt^{*2}} sin(\vartheta(\gamma\Delta t)) + \boldsymbol{d}_4 \cdot \frac{d^2\boldsymbol{t}^{*4\text{P INT}}}{dt^{*2}} sin(\vartheta(\Delta t)) \\ & - \left[-sin(\vartheta(t'))(\dot{\vartheta}_0^2 + \ddot{\vartheta}_0^2 t'^2 + 2\dot{\vartheta}_0\ddot{\vartheta}_0 t')\Delta t^2 + \ddot{\vartheta}_0 cos(\vartheta(t'))\Delta t^2\right]\Bigg\}^2 \Big/ \vartheta(\Delta t)^2 \end{aligned} \tag{A.17}$$

$$\begin{aligned}\left(\sigma^{*4\text{P INT}}_{\text{rnd},\ddot{X}_p}\right)^2 = \Bigg[& \left(\boldsymbol{d}_1 \cdot \frac{d^2\boldsymbol{t}^{*4\text{P INT}}}{dt^{*2}}\right)^2 + \left(\boldsymbol{d}_2 \cdot \frac{d^2\boldsymbol{t}^{*4\text{P INT}}}{dt^{*2}}\right)^2 \\ & + \left(\boldsymbol{d}_3 \cdot \frac{d^2\boldsymbol{t}^{*4\text{P INT}}}{dt^{*2}}\right)^2 + \left(\boldsymbol{d}_4 \cdot \frac{d^2\boldsymbol{t}^{*4\text{P INT}}}{dt^{*2}}\right)^2\Bigg] \frac{\langle|\delta \boldsymbol{X}_p|^2\rangle}{R^2\vartheta(\Delta t)^2} \end{aligned} \tag{A.18}$$

See Equation (1.19) for the definitions of $\boldsymbol{t}^{*4\text{P INT}}$ and $\boldsymbol{d}_i$.

APPENDIX B

PLOTS OF POSITION, VELOCITY AND ACCELERATION RMS ERRORS

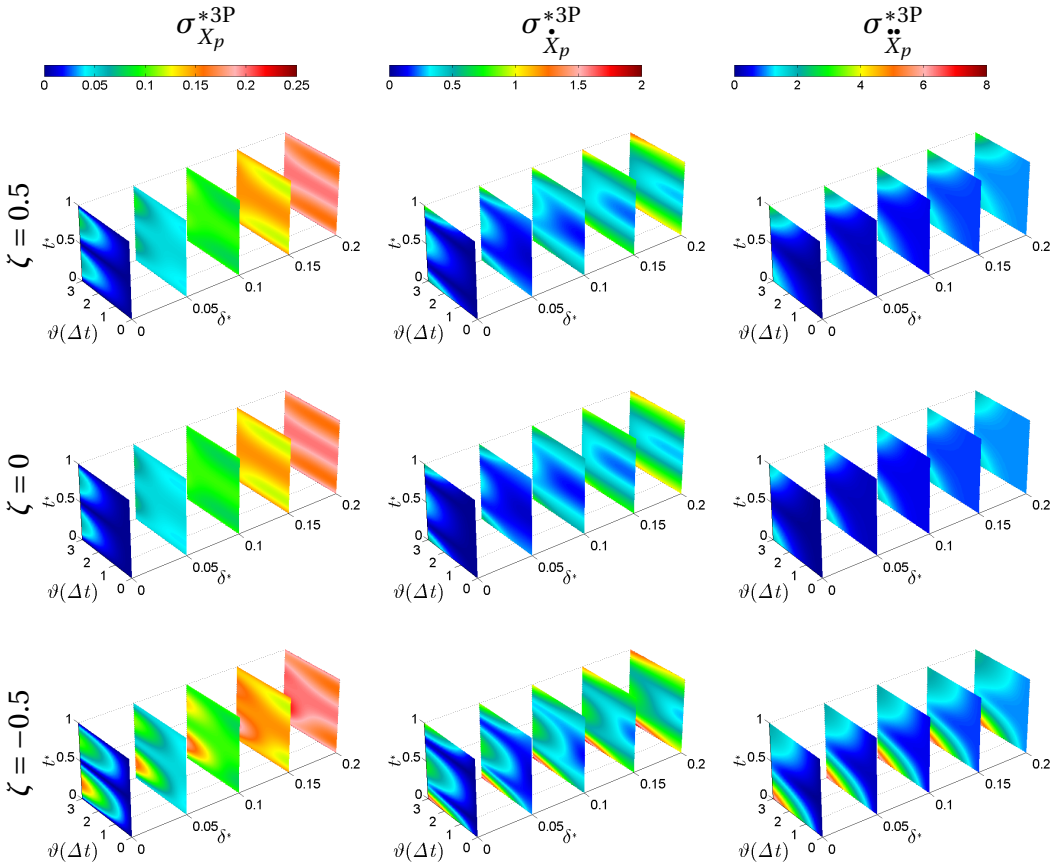

Figure B.1: Position, velocity and acceleration rms errors of 3-P in 4-D space.

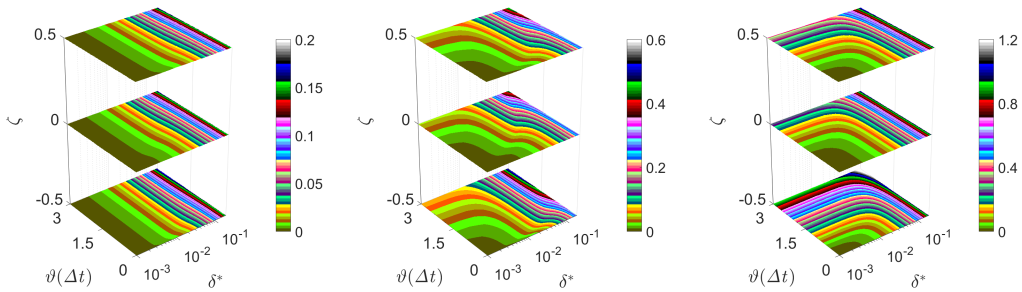

(a) position (b) velocity (c) acceleration

Figure B.2: Rms errors of 3-P at optimal times.

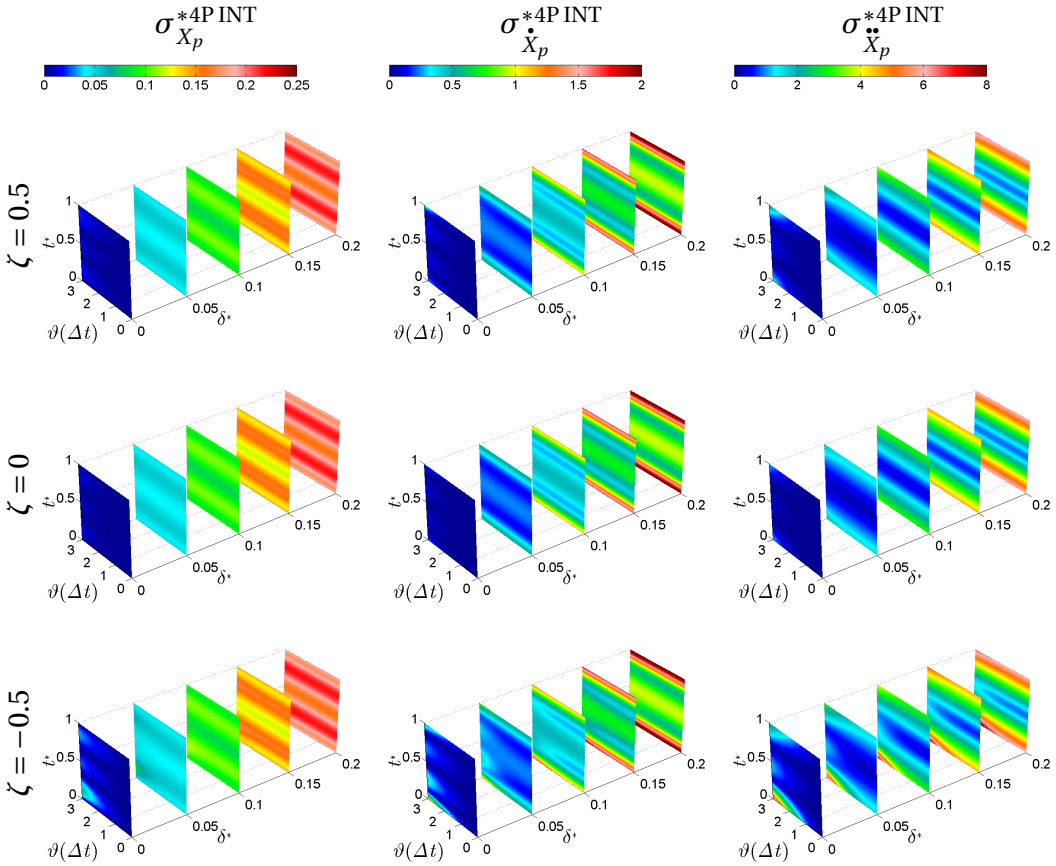

Figure B.3: Position, velocity and acceleration rms errors of 4-P INT in 4-D space.

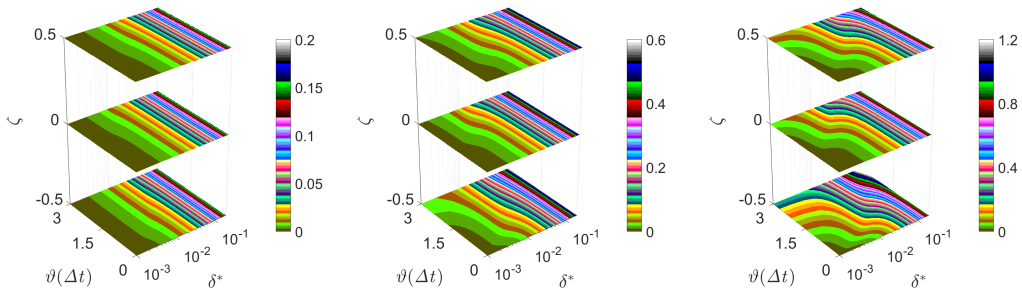

(a) position (b) velocity (c) acceleration

Figure B.4: Rms errors of 4-P INT at optimal times.

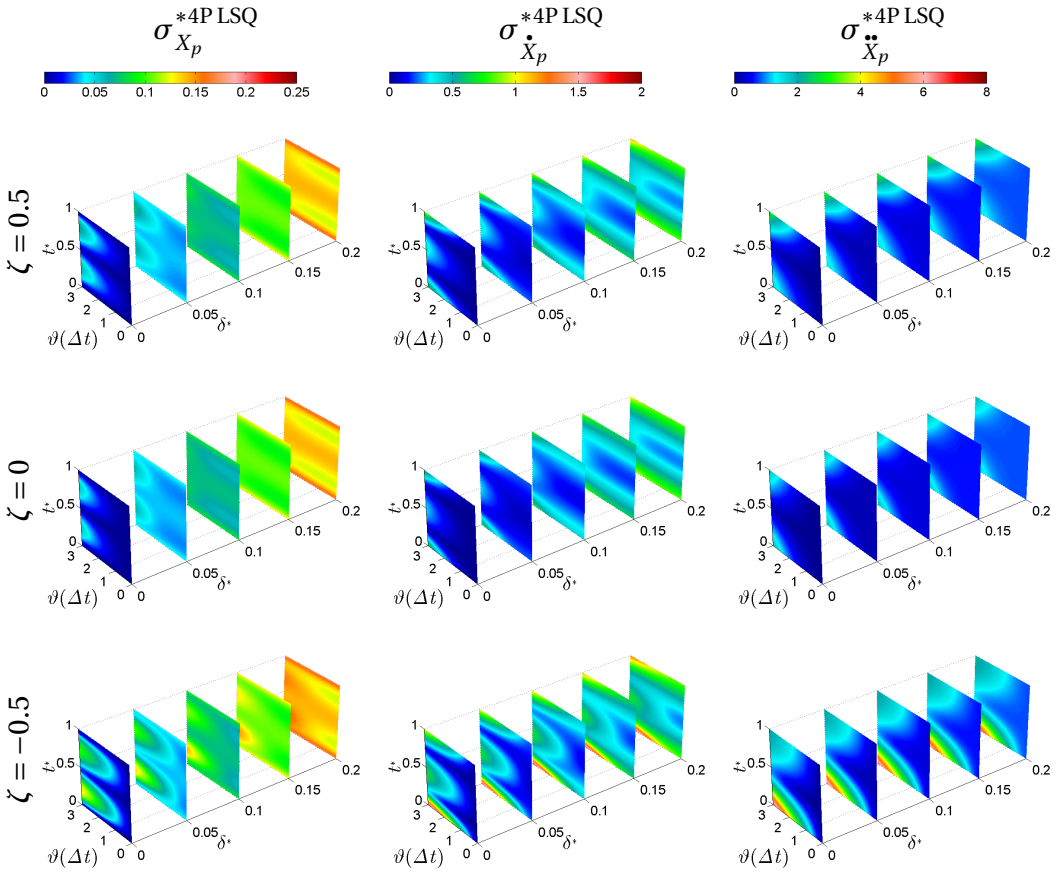

Figure B.5: Position, velocity and acceleration rms errors of 4-P LSQ in 4-D space.

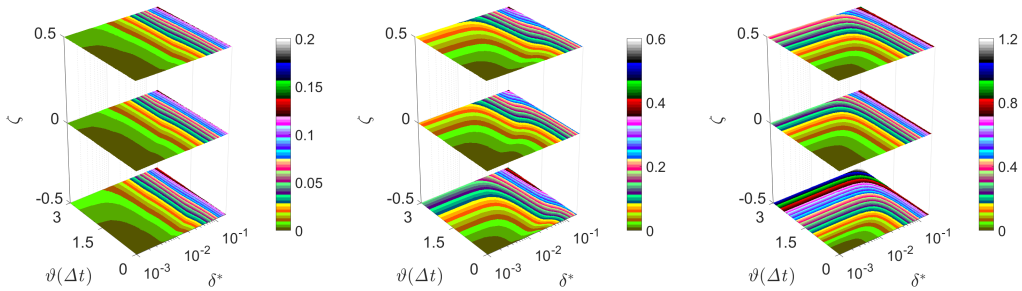

(a) position (b) velocity (c) acceleration

Figure B.6: Rms errors of 4-P LSQ at optimal times.

APPENDIX C

PLOTS OF PARTICLE DRAG MEASUREMENTS

particle no. A1
particle no. A2
particle no. A3
x_p [μm]
v_p [m/s]
a_p [m/s^2]
C_D
t [μs]
$x_{p,m}$
u_f
$\Gamma = 3$
$\Gamma = 2$
$\Gamma = 1$
PW IDE

particle no. A4
particle no. A5
particle no. A6
x_p [μm]
v_p [m/s]
a_p [m/s^2]
C_D
t [μs]
$x_{p,m}$
u_f
$\Gamma = 3$
$\Gamma = 2$
$\Gamma = 1$
PW IDE

particle no. A7
particle no. B1
particle no. B2
x_p [μm]
v_p [m/s]
a_p [m/s²]
C_D
t [μs]
$x_{p,m}$
u_f
Γ = 3
Γ = 2
Γ = 1
PW IDE

particle no. B3
particle no. B4
particle no. B5
x_p [μm]
v_p [m/s]
a_p [m/s^2]
C_D
t [μs]
$x_{p,m}$
u_f
$\Gamma = 3$
$\Gamma = 2$
$\Gamma = 1$
PW IDE

particle no. B6
x_p [μm]
t [μs]
$x_{p,m}$
$\Gamma = 3$
$\Gamma = 2$
$\Gamma = 1$
PW IDE
v_p [m/s]
u_f
a_p [m/s^2]
C_D

APPENDIX D

THEORETICAL BASIS FOR ESTIMATING OTHER TURBULENCE STATISTICS FROM ENSEMBLE PTV DATA

D.1 Reynolds stress and TKE production

In this section, it will be seen that some manipulations of equation (5.2) will allow us to estimate the Reynolds stress tensor,

$$R_{ij} = \langle u_i' u_j' \rangle \tag{D.1}$$

Given the Reynolds decomposition,

$$u_i = \langle u_i \rangle + u_i' \tag{D.2}$$

we subtract the mean velocity , $\langle u_i^* \rangle$, from both sides of equation (5.2), and multiply it with a similar equation written for u_j. The result is averaged in $\mathscr{D}$ and then in time, which eventually gives us

$$\langle \prec [u_i^{(p,q)} - \langle u_i^* \rangle][u_j^{(p,q)} - \langle u_j^* \rangle] \succ_{\mathscr{D}} \rangle_{T\to\infty} = \langle u_i'^* u_j'^* \rangle + \mathscr{O}(L^2) \tag{D.3}$$

The derivation of (D.3) utilizes the facts and assumptions (i) – (v) discussed in Section 5.2. Thus, we obtain a method of second-order accuracy to estimate the Reynolds stress tensor.

Furthermore, an improvement is achievable by a procedure similar to subtracting the mean velocity gradient in the estimation of mean velocity (see Section 5.2.1 and 5.4.3). The truncation term $\mathscr{O}(L^2)$ in (D.3) can be further expanded:

$$\left[\langle u_{i,m}^* \rangle \langle u_{j,m}^* \rangle + \langle u_{i,m}'^* u_{j,m}'^* + \frac{1}{2} u_i'^* u_{j,mm}'^* + \frac{1}{2} u_j'^* u_{i,mm}'^* \rangle \right] \langle (x_m^{(p,q)} - x_m^*)^2 \rangle \tag{D.4}$$

Clearly, this implies the mean velocity gradients, $\langle u_{i,m}^* \rangle$ and $\langle u_{j,m}^* \rangle$, can be subtracted to reduce the truncation error. Thus, we define a new variable $F_{u_i'}$:

$$F_{u_i'} = u_i^{(p,q)} - \langle u_i^* \rangle - \langle u_{i,l}^* \rangle (x_l^{(p,q)} - x_l^*), \tag{D.5}$$

and then the improved procedure to estimate $R_{i,j}$ is described by the following equation:

$$\begin{aligned}\langle \prec F_{u_i'} F_{u_j'} \succ_{\mathscr{D}} \rangle_{T\to\infty} &= \langle u_i'^* u_j'^* \rangle + \langle u_{i,m}'^* u_{j,m}'^* + \frac{1}{2} u_i'^* u_{j,mm}'^* + \frac{1}{2} u_j'^* u_{i,mm}'^* \rangle \frac{L^2}{12} + \mathscr{O}(L^4) \\ &= \langle u_i'^* u_j'^* \rangle + \mathscr{O}(L^2) \end{aligned} \tag{D.6}$$

This is a method similar to that proposed in Discetti *et al.* (2015), in which the authors considered subtracting up to the second-order derivative of mean velocity by fitting a quadratic curve/surface to the mean velocity profile. Additionally, the TKE production, $\langle u_{i,j} \rangle R_{ij}$, is also obtained from the estimation of the mean velocity gradient and the Reynolds stress.

D.2 TKE viscous diffusion

A further step from equation (D.6) leads to estimating the TKE viscous diffusion, $\nu\nabla^2 K$, where $K = \langle u_i' u_i'/2 \rangle$. Let $i = j$, evaluate (D.6) with two different edge lengths, L and ηL, satisfying $\eta > 1$ and $(\eta^2 - 1)/12 \sim (\eta^4 - 1)/80$. Then $R_{i,j}$ is canceled out by calculating their difference:

$$\langle \prec F_{u_i'} F_{u_i'} \succ_{\mathscr{D}} \rangle_{T\to\infty}\Big|_{\eta L} - \langle \prec F_{u_i'} F_{u_i'} \succ_{\mathscr{D}} \rangle_{T\to\infty}\Big|_{L} = \langle u_{i,m}'^* u_{i,m}'^* + u_i'^* u_{i,mm}'^* \rangle \frac{(\eta^2-1)L^2}{12} + \mathscr{O}\left(\frac{(\eta^4-1)L^4}{80}\right) \tag{D.7}$$

Given the identity

$$u_{i,m}' u_{i,m}' + u_i' u_{i,mm}' = \frac{\partial}{\partial x_m}\left(u_i' \frac{\partial u_i'}{\partial x_m}\right) = \frac{\partial^2 (u_i' u_i'/2)}{\partial x_m^2}, \tag{D.8}$$

we have the following from (D.7):

$$\frac{12}{(\eta^2-1)L^2}\left[\langle \prec F_{u_i'} F_{u_i'} \succ_{\mathscr{D}} \rangle_{T\to\infty}\Big|_{\eta L} - \langle \prec F_{u_i'} F_{u_i'} \succ_{\mathscr{D}} \rangle_{T\to\infty}\Big|_{L}\right] = \nabla^2 K + \mathscr{O}(L^2) \tag{D.9}$$

Thus, we have obtained a method of second-order accuracy to estimate the TKE viscous diffusion.

D.3 Inhomogeneous dissipation

For the inhomogeneous dissipation rate, the terms we need are

$$\langle u'_{i,j}u'_{j,i}\rangle = \langle u'^2_{1,1}\rangle + \langle u'^2_{2,2}\rangle + \langle u'^2_{3,3}\rangle + 2\langle u'_{1,2}u'_{2,1}\rangle + 2\langle u'_{1,3}u'_{3,1}\rangle + 2\langle u'_{2,3}u'_{3,2}\rangle \tag{D.10}$$

The first three terms also appear in the homogeneous isotropic dissipation, which in fact can be obtained from equation (5.22). The strategy is to vary the size of $\mathscr{D}$ in the corresponding direction for each component, similar to how we obtained the TKE diffusion. For instance, if we keep $L_y = L_z = L$, and evaluate (5.22) for $i = 1$ twice using $L_x = L$ and $L_x = \eta L$ ($\eta > 1$), then we will be able to estimate $\langle u'^2_{1,1}\rangle$ by calculating their difference, i.e.

$$\frac{6}{(\eta^2-1)L^2}\left[\langle \prec G^2_{\nabla u'_1} \succ_{\mathscr{D}}\rangle_{T\to\infty}\Big|_{L_x=\eta L} - \langle \prec G^2_{\nabla u'_1} \succ_{\mathscr{D}}\rangle_{T\to\infty}\Big|_{L_x=L}\right] = \langle u'^2_{1,1}\rangle + \mathscr{O}(L^2) \tag{D.11}$$

For the other three terms on the right side of equation (D.10), It is observed that they are generated by the following operation:

$$\langle \prec \sum_{\substack{i,j=1\\ i<j}}^{3}\left[(x_i^{(p,q)} - x_i^{(p',q)})G_{\nabla u'_i}\right]\left[(x_j^{(p,q)} - x_j^{(p',q)})G_{\nabla u'_j}\right] \succ_{\mathscr{D}}\rangle_{T\to\infty} \tag{D.12}$$

wherein repeated i and j do not imply summations. If we use a cubic domain $\mathscr{D}$, given equation (5.20), the above eventually becomes

$$\left(\langle u'_{1,1}u'_{2,2}\rangle + \langle u'_{1,1}u'_{3,3}\rangle + \langle u'_{2,2}u'_{3,3}\rangle + \langle u'_{1,2}u'_{2,1}\rangle + \langle u'_{1,3}u'_{3,1}\rangle + \langle u'_{2,3}u'_{3,2}\rangle\right)\frac{L^4}{36} + \mathscr{O}(L^6) \tag{D.13}$$

As the fluctuating velocity field is solenoidal, the first three terms in (D.13) can be calculated using equation (D.11) and the following identity

$$\langle u'_{1,1}u'_{2,2}\rangle + \langle u'_{1,1}u'_{3,3}\rangle + \langle u'_{2,2}u'_{3,3}\rangle = -\frac{1}{2}\left(\langle u'^2_{1,1}\rangle + \langle u'^2_{2,2}\rangle + \langle u'^2_{3,3}\rangle\right) \tag{D.14}$$

Thereby, the last three terms in equation (D.10) are obtained:

$$\frac{36}{L^4}\langle \prec \sum_{\substack{i,j=1 \\ i<j}}^{3} \left[(x_i^{(p,q)} - x_i^{(p',q)}) G_{\nabla u_i'} \right] \left[(x_j^{(p,q)} - x_j^{(p',q)}) G_{\nabla u_j'} \right] \succ_{\mathscr{D}} \rangle_{T\to\infty} + \frac{1}{2}\Big(\langle u_{1,1}'^2 \rangle + \langle u_{2,2}'^2 \rangle + \langle u_{3,3}'^2 \rangle \Big)$$

$$= \langle u_{1,2}' u_{2,1}' \rangle + \langle u_{1,3}' u_{3,1}' \rangle + \langle u_{2,3}' u_{3,2}' \rangle + \mathscr{O}(L^2) \tag{D.15}$$

Consequently, combining Equation (D.11) and (D.15), we have derived a method of second-order accuracy for estimating the inhomogeneous dissipation.

APPENDIX E

MATLAB CODE FOR COMPUTING THIRD-ORDER CORRELATION

```
% MATLAB function 'triple_corr' computes the third-order
% correlation of three images I1, I2 and I3

function C = triple_corr(I1, I2, I3)

[N,M] = size(I1);
[x1,y2,x3,y4] = ndgrid(1:M,1:N,1:M,1:N);

% Compute the indices at which the band-limited and
% periodic spectrum of I1 has the corresponding frequency
% numbers given the frequency number of I2 and I3
xi = x1+x3-1;
xi(xi>M) = xi(xi>M)-M;
yi = y2+y4-1;
yi(yi>N) = yi(yi>N)-N;

% Compute the 2-D Fourier transform of each image
FI1 = conj(fft2(I1));
FI2 = fft2(I2);
FI3 = fft2(I3);

% Construct and compute the 4-D correlation map
Ind = sub2ind([N,M],yi(:),xi(:));
repFI1 = reshape(FI1(Ind),[M,N,M,N]);
repFI2 = permute(repmat(FI2,[1,1,M,N]),[2,1,3,4]);
repFI3 = permute(repmat(shiftdim(FI3,-2),[M,N,1,1]),[1,2,4,3]);
C = ifftn(repFI1.*repFI2.*repFI3);
C = fftshift(C);

end
```

APPENDIX F

REPORT FOR DOCTORAL DISSERTATION DEFENSE

ASU Graduate College
Arizona State University

ANNOUNCEMENT AND REPORT FOR DOCTORAL DISSERTATION DEFENSE

Within 10 days of the defense, a copy of this form must be submitted to the Graduate College with the appropriate level of pass or fail noted and a brief description of corrections that need to be made (Sections B & C). Please read the subsequent procedures page for instructions for completing the official, original signed form.

SECTION A

"I verify that I have conducted this research and scholarship in accordance with ASU academic integrity, copyright and research on human and animal subjects' policies. I understand that failure to comply with these polices could lead to sanctions including revocation of my degree. My submission of this document to formatting affirms that I have prepared this final document in accordance with both the selected style guide and the *Format Manual*."

STUDENT		ASU I.D. NO.
Liuyang Ding		1204338546
DEGREE		**MAJOR**
Doctor of Philosophy		Mechanical Engineering
DOCUMENT TITLE		
Fundamentals and Applications of N-pulse Particle Image Velocimetry-accelerometry: Toward Advanced Measurements of Complex Flows and Turbulence		
DATE OF DEFENSE	**TIME**	**PLACE (Building and Room)**
Tuesday, January 30, 2018	12:00 PM	ENGRC 490

LEVEL OF PASS OR FAIL

- (•) **Pass:** Only minor format corrections need to be made (e.g., typographic errors, pagination).
- **Pass with minor revisions:** Extensive format/editorial corrections and/or minor substantive changes need to be made (e.g., rewrite some text, correct grammatical errors).
- **Pass with major revisions:** Extensive substantive changes need to be made (e.g., chapter rewrite).
- **Fail:** The overall execution of the study is flawed or the candidate's performance in the oral examination is seriously deficient.

SECTION B (To be completed by the Committee Chair or Co-Chair)

Preliminary Examination Results: (•) Pass ( ) Pass with minor revisions ( ) Pass with major revisions ( ) Fail

REVISIONS NEEDED (To be completed by Committee Chair or Co-Chair)
No revisions were requested by the committee.

SECTION C (Examination Results)

PASS	FAIL	NAME	SIGNATURE	PASS	FAIL	NAME	SIGNATURE
✓		CHAIR or CO-CHAIR Ronald Adrian	Ronald J Adrian			CHAIR or CO-CHAIR	
✓		MEMBER Yulia Peet		✓		MEMBER Marcus Herrmann	
✓		MEMBER David Frakes		✓		MEMBER Huei-Ping Huang	
		MEMBER				MEMBER	

SECTION D (Final Approval of Document (To be signed by Committee Chair or Co-Chair)

MY NAME AND SIGNATURE CERTIFIES THAT ALL REVISIONS NOTED ABOVE HAVE BEEN COMPLETED	DATE
RONALD J ADRIAN Ronald J Adrian	1.29.18

APPENDIX G

PERMISSION TO USE PUBLISHED WORK

Dr. Ronald J. Adrian, the co-author of the published journal article 'N-pulse particle image velocimetry-accelerometry for unsteady flow-structure interaction' (Ding and Adrian, 2016), has permitted the use of the full paper in Chapter 2.